

Structure and Function
of the Ca^{2+} dependent
 K^{+} channel AKT1 from *A. thaliana*

Inaugural Dissertation

zur Erlangung des Doktorgrades
der Mathematisch-Naturwissenschaftlichen Fakultät
der Heinrich-Heine-Universität Düsseldorf

vorgelegt von
Alexandra Bork
aus Frankfurt am Main

Düsseldorf, Mai 2023

aus dem Institut für Biochemie
der Heinrich-Heine-Universität Düsseldorf

Gedruckt mit der Genehmigung der
Mathematisch-Naturwissenschaftlichen Fakultät der
Heinrich-Heine-Universität Düsseldorf

Berichtersteller:

1. Prof. Dr. Lutz Schmitt
2. Prof. Dr. Georg Groth

Tag der mündlichen Prüfung: 14.08.2023

*“Every morning you have two choices:
Continue to sleep with your dreams
or wake up and chase them.”*

-Carmelo Anthony-

Abstract

Plants play essential roles for all living matter on earth, be it in the compensation of CO₂ or as food source for humans and animals. Hence the understanding of plants themselves and their nutrition is of high interest. If a nutrient runs low in the soil, plants as sessile organisms have to adapt to these changes. This study focused on a membrane protein of the model plant *Arabidopsis thaliana* that was found to be involved in the K⁺ uptake under low K⁺ conditions in the soil, namely the voltage gated K⁺ channel AKT1. Upon *in planta* and *Xenopus* oocyte experiments the protein kinase CIPK23 and the plasma membrane associated Ca²⁺ sensor proteins CBL1 and 9 were found as upstream regulators of AKT1 and essential for AKT1 mediated K⁺ uptake. Upon K⁺ deprivation spatio temporal specific Ca²⁺ signatures are triggered. The increasing cytosolic Ca²⁺ concentrations are sensed by CBL1 and 9, which thereupon recruit CIPK23 to the plasma membrane. Upon a complex phosphorylation pattern the activity of the K⁺ channel gets promoted.

This project aimed towards the structural and functional analysis of the components involved in AKT1 mediated K⁺ uptake. By getting to know the structure and interaction between the components a better understanding in the adaption mechanisms under low K⁺ conditions should be obtained. A first step towards this aim was the establishment of heterologous expression and subsequent purification procedures for the multi domain membrane protein AKT1 as well as the cytosolic CIPK23 and the membrane associated CBL1. Therefore, the well established procaryotic expression host *Escherichia coli*, the eukaryotic expression host *Saccharomyces cerevisiae* as well as wheat germ based cell free expression was attempted.

The AKT1 channel showed expression in *S. cerevisiae* ΔPP for both expression after plasmid transformation as well as after homologous recombination of the *akt1* gene into the *pdr5* locus of the *S. cerevisiae* ΔPP genome. Confocal fluorescence microscopic analysis of yeast cells expressing either N- or C-terminally His-GFP tagged AKT1 fusion proteins showed that the position of the tag determined the localization of the channel. N-terminally tagged AKT1 was found in the plasma membrane, while the C-terminally tagged channel remained in inner compartments of the yeast cell. The isolation of AKT1 membranes did yield in degradation and no membranes containing full length AKT1 could be obtained. Expression of CIPK23 in *E. coli* was shown to work, but purification resulted in degradation despite different conditions tested. Hence, the genes for both AKT1 and CIPK23 were cloned into vectors suitable for wheat germ based cell free expression. Both proteins could be produced in full length. For AKT1 initial purification success could be obtained, while the CIPK23 protein showed severe aggregation.

The expression of the Ca²⁺ sensor CBL1 in *E. coli* Rosetta pLysS and subsequent purification via an N-terminal StrepII tag could be established in this study. In contrary to the already established purification protocols for CBL2 and CBL4, multi angle light scattering analysis showed that CBL1 was present in higher oligomeric states unless BriJ35 detergent was added during the purification procedure. CBL1 could be purified in sufficient amounts for subsequent analysis of its binding affinities for Ca²⁺, Mn²⁺ and Mg²⁺ by isothermal titration calorimetry. Besides Ca²⁺, Mn²⁺ and Mg²⁺ were found to be of interest since the EF hand 4 of the related CBL4 was found to bind Mn²⁺ and some calmodulin variants can bind Mg²⁺ besides Ca²⁺. This ITC analysis resulted in 3 potential binding sites for Ca²⁺ and Mn²⁺ respectively and 1 potential binding site for Mg²⁺. Upon the creation of mutants that impaired Ca²⁺ binding (E → Q at the conserved -Z coordinate), the determined K_D and ΔH values could be assigned to the different EF hands. EF hand 2 was found to be impaired for Ca²⁺ binding, while for the other 3 EF hands an *in vivo* binding model was postulated. Mg²⁺ binding is found not to be relevant. The *in vivo* binding behavior

for Mn^{2+} could not be clarified beyond doubt, but a possible *in vivo* impact cannot be excluded. Especially the findings for the CBL1 can be used as basis for the analysis of the remaining CBL proteins and will be helpful to decipher the Ca^{2+} signatures and their impact on the plant in the future.

Zusammenfassung

Pflanzen spielen eine essentielle Rolle für alle Lebewesen auf der Erde, sei es durch die Fixierung von CO_2 oder als Nahrungsquelle. Daher ist es von großem Interesse die Pflanzen selbst und ihre Ernährung zu verstehen. Wenn ein Nährstoff im Boden zur Neige geht, müssen Pflanzen als sesshafte Organismen sich an diese Veränderungen anpassen. Diese Arbeit konzentrierte sich auf ein Membranprotein aus der Modellpflanze *Arabidopsis thaliana*, welches an der K^+ -Aufnahme unter niedrigen K^+ -Bedingungen im Boden beteiligt ist, nämlich den spannungsgesteuerten K^+ -Kanal AKT1. Durch *in planta* und *Xenopus* Oozyten Experimente wurden die Proteinkinase CIPK23 und die Plasmamembran-assoziierten Ca^{2+} -Sensorproteine CBL1 und 9 als vorgeschaltete Regulatoren von AKT1 identifiziert, die für die durch AKT1 vermittelte K^+ -Aufnahme essentiell sind. Bei K^+ -Mangel werden räumlich und zeitlich spezifische Ca^{2+} -Signaturen ausgelöst. Die steigenden cytosolischen Ca^{2+} -Konzentrationen werden von CBL1 und 9 detektiert, welche daraufhin CIPK23 an die Plasmamembran rekrutieren. Durch ein komplexes Phosphorylierungsmuster, welches AKT1, CIPK23 und CBL1/9 involviert, wird die Aktivität des K^+ -Kanals gesteuert.

Ziel dieses Projekts war die strukturelle und funktionale Analyse der an der AKT1-vermittelten K^+ -Aufnahme beteiligten Komponenten. Durch die Bestimmung der Struktur und der Interaktionen zwischen den Komponenten soll ein besseres Verständnis der Anpassungsmechanismen unter niedrigen K^+ -Bedingungen erreicht werden. Ein dahingehend erster Schritt war die Etablierung heterologer Expressions- und anschließender Reinigungsverfahren für das Multidomänen-Membranprotein AKT1 sowie das cytosolische CIPK23 und das membranassoziierte CBL1. Dazu wurde der etablierte prokaryotische Expressionswirt *Escherichia coli*, der eukaryotische Expressionswirt *Saccharomyces cerevisiae* sowie die zellfreie Expression auf der Basis von Weizenkeimlingen herangezogen.

Der AKT1-Kanal konnte in *S. cerevisiae* ΔPP sowohl nach Plasmid-Transformation als auch nach homologer Rekombination des akt1-Gens in den pdr5-Lokus des *S. cerevisiae* ΔPP -Genoms exprimiert werden. Konfokale Fluoreszenz-Mikroskopie der Hefezellen, welche entweder N- oder C-terminal His-GFP-markierte AKT1-Fusionsproteine exprimierten, zeigten, dass die Position der Markierung Einfluss auf die Lokalisierung des Kanals hat. N-terminal markiertes AKT1 befand sich in der Plasmamembran, während der C-terminal markierte Kanal in inneren Kompartimenten der Hefezelle verblieb. Bei der Isolierung von AKT1-haltigen Membranen kam es zu einer Degradation des Proteins. Es konnten keine Membranen präpariert werden, welche AKT1 in voller Länge enthielten. Es zeigte sich, dass die Expression von CIPK23 in *E. coli* möglich ist, aber die Reinigung führte trotz verschiedener getesteter Bedingungen zu einer Degradation des Proteins. Auf Grund dessen wurden die für AKT1 als auch für CIPK23 codierenden Gene in spezielle Vektoren kloniert, welche für die zellfreie Expression geeignet sind. Beide Proteine konnten so in voller Länge hergestellt werden. Für AKT1 konnte ein erster Reinigungserfolg erzielt werden, während CIPK23 eine starke Aggregation aufwies.

Die Expression des Ca^{2+} -Sensors CBL1 in *E. coli* Rosetta pLysS und die anschließende Reinigung über eine N-terminale StrepII-Markierung konnte in dieser Arbeit etabliert werden. Im Gegensatz zu den bereits etablierten Reinigungen für CBL2 und CBL4 zeigte die Mehrwinkel-Lichtstreuungsanalyse (MALS), dass CBL1 in höheren oligomeren Zuständen vorlag, wenn nicht während der Reinigung das Detergens Brij35 zugesetzt wurde. CBL1 konnte so in ausreichenden Mengen gereinigt werden, um im Anschluss seine Bindungsaffinitäten für Ca^{2+} , Mn^{2+} und Mg^{2+} mittels isothermer Titrationskalorimetrie zu analysieren. Neben Ca^{2+} waren auch Mn^{2+} und Mg^{2+} von Interesse, da festgestellt wurde, dass die EF-Hand 4 des verwandten CBL4 Mn^{2+} binden kann und einige Calmodulin-Varianten neben Ca^{2+} auch

Mg²⁺ binden können. Die ITC-Analyse zeigte 3 potenzielle Bindungsstellen für Ca²⁺ bzw. Mn²⁺ und 1 potenzielle Bindungsstelle für Mg²⁺ auf. Durch die Erzeugung von EF Hand Mutanten, welche die Ca²⁺-Bindung je einer EF Hand beeinträchtigten (E → Q an der konservierten -Z-Koordinate), konnten die ermittelten K_D und ΔH Werte den verschiedenen EF-Händen zugeordnet werden. Anhand dessen wurde festgestellt, dass EF Hand 2 kein Ca²⁺ bindet, während für die anderen 3 EF Hände ein *in vivo* Bindungsmodell postuliert wurde. Die Mg²⁺ Bindung erwies sich als nicht relevant. Das *in vivo*-Bindungsverhalten für Mn²⁺ konnte nicht zweifelsfrei geklärt werden, ein möglicher *in vivo* Einfluss kann jedoch nicht ausgeschlossen werden. Insbesondere die Ergebnisse für CBL1 können als Grundlage für die Analyse der übrigen CBL-Proteine dienen und werden in Zukunft bei der Entschlüsselung der Ca²⁺-Signaturen und deren Auswirkungen auf die Pflanze hilfreich sein.

Table of Content

Abstract	I
Zusammenfassung.....	III
Table of Content	V
List of Figures.....	VII
List of Tables	VIII
List of Abbreviations	IX
Introduction.....	1
Minerals in Plants - Micro- and Macronutrients	1
Ca ²⁺ signaling in plants as initial response to nutrient deprivation.....	3
Potassium uptake in plants	4
The shaker-like voltage gated K ⁺ channel AKT1.....	6
Shaker channels vs. plant voltage gated K ⁺ channels – structural features	6
The transmembrane domain.....	7
The cyclic nucleotide binding domain	12
The Ankyrin Repeat Domain.....	14
The regulation of AKT1 uptake via the silent shaker subunit AtKC1	16
Regulation of AKT1 by phosphorylation via CIPK23	17
The CBL interacting protein kinase CIPK23	18
CIPK23 is a serine/threonine protein kinase	18
Structural insights into CBL interacting protein kinases.....	19
Regulation of the CIPK kinase activity	21
The calcineurin B-like proteins CBL1 and 9	22
The EF hand Ca ²⁺ binding motif	23
Calcineurin-B like proteins.....	24
Insights into the 3D structure of calcineurin-B like proteins.....	25
The regulation of the voltage gated K ⁺ channel AKT1.....	26
Aim of Studies.....	27
Chapters.....	28
Chapter 1 – The voltage gated K ⁺ channel AKT1 from <i>Arabidopsis thaliana</i>	29
Chapter 2 - The CBL interacting protein kinase CIPK23.....	62
Chapter 3 - The calcineurin-B like protein 1.....	81

Discussion	128
The importance of plant nutrient uptake and its biochemical analysis.....	128
Heterologous expression and purification of eukaryotic (membrane) proteins	129
The voltage gated K ⁺ channel AKT1.....	130
The protein kinase CIPK23.....	131
The Ca ²⁺ binding protein CBL1.....	132
AKT1 - The <i>Arabidopsis</i> K ⁺ transporter 1	134
Channel or transporter?	134
The role of the AKT1 N-terminus.....	134
The AKT1 pore and its opening	135
The impact cyclic nucleotides on AKT1	137
The CBL interacting protein kinase CIPK23	139
How can CIPK23 be so diverse in its interactions and yet so specific?	139
The Calcineurin-B like protein CBL1	141
CBL1 and 9 – similarities and differences.....	141
CBL-CIPK complexes are involved in plant programmed cell death.....	143
The role of Mn ²⁺ in <i>A. thaliana</i> and points of contact with the AKT1-CIPK23-CBL1/9 network .	145
References.....	147
Acknowledgements	160
Curriculum vitae	162
Declaration	163

List of Figures

Figure 1: Potassium ion uptake in plants.	4
Figure 2: General structure of voltage gated shaker-like channels.	6
Figure 3: Transmembrane domains of A) shaker/KvAP and B) CNBD superfamily channels.....	7
Figure 4: 3D structure of the homotetrameric voltage gated K ⁺ channel AKT1 in different conformational states.....	9
Figure 5: The AKT1 transmembrane domain and formation of the pore.....	10
Figure 6: 3D structures of AKT1 protomers in the inactive state of the channel.	11
Figure 7: 3D structures of the MloK1 cyclic nucleotide binding domains.....	13
Figure 8: Ankyrin repeat domains.	14
Figure 9: CBL interacting protein kinases as members of the serine/threonine kinase family.	18
Figure 10: Structure of CIPK proteins.	19
Figure 11: Schematic representation of CIPK23 activation mechanisms.	21
Figure 12: The EF hand Ca ²⁺ binding motif.....	23
Figure 13: The calcineurin-B like protein CBL4.....	25
Figure 14: The regulation mechanisms of K ⁺ uptake in <i>A. thaliana</i>	26
Figure 15: The voltage sensor domain of AKT1 aligned in the closed (green) and pre-open state (cyan).....	135
Figure 16: Cyclic nucleotide binding domains of CNG and HCN channels.	138
Figure 17: Comparison of CBL1 and CBL9.	142
Figure 18: Schematic representation of the Yellow Mangaleon FRET sensor	146

List of Tables

Table 1: Micro- and macronutrients in plants	1
Table 2: Features of <i>Arabidopsis thaliana</i> CBL proteins.	24

List of Abbreviations

μ	Micro
2YT	Double Yeast extract and tryptone medium
3D	Three dimensional
Å	Angström
A	anionic
<i>A. thaliana</i>	<i>Arabidopsis thaliana</i>
aa	Amino acid
ABC	ATP binding cassette
ABI2	Protein phosphatase 2C 77
ADP	Adenosine diphosphate
AIP1	Protein phosphatase 2C 3
AKT	Arabidopsis K ⁺ transporter
AL	Activation Loop
AMT	Ammonium transporter
AP2C1	Protein phosphatase 2C 25
AR	Ankyrin repeat
ARD	Ankyrin repeat domain
AS	After solubilization
AtKC1	<i>Arabidopsis thaliana</i> K ⁺ channel 1
ATP	Adenosine-triphosphate
CAi	Center of advanced imaging
cal	calories
CaM	Calmodulin
cAMP	Cyclic adenosine monophosphate
CBL	Calcineurin-B like
CD	Cell debris
CECF	Continuous exchange continuous flow
CFP	Cyan fluorescent protein
cGMP	Cyclic guanosine monophosphate
CHAPS	3 [(3 Cholamidopropyl)dimethylammonio] 1 propanesulfonate
CIPK	CBL-interacting protein kinase
CMC	Critical micellar concentration
CNBD	Cyclic nucleotide binding domain
CNG	Cyclic nucleotide gated
cNMP	Cyclic nucleotide monophosphate
CTP	Cytidine triphosphate
CV	Column volume
DFG	Deutsche Forschungsgesellschaft
DNA	Desoxyribonucleic acid
DO	Drop out
DREAM	downstream regulatory element antagonist modulator
DTT	Dithiothreitol
<i>E. coli</i>	<i>Escherichia coli</i>
EAG	ether á go-go channel
EDTA	Ethylenediaminetetraacetic acid
EGTA	ethylene glycol-bis(β-aminoethyl ether)-N,N',N'-tetraacetic acid)
EM	Electron microscopy
ESI	Electrospray ionisation
<i>et al.</i>	Et alii
Fe-S	Iron-sulphur cluster
fw	Forward

g	Gram/ gravity
G	Gibbs free energy
Gdn	Guanidinium
GFP	Green fluorescent protein
GLP	Germin-like protein
GTP	Guanine triphosphate
h	Hour
H	Enthalpie
HAK	High affinity K ⁺ transporter
HATS	High affinity uptake system
HCN	Hyperpolarization activated cyclic nucleotide modulated
HEK	Human embryotic kidney
HF	High fidelity
HR	Hypersensitive response
HRP	Horse raddish peroxidase
IB	Inclusion body
IgG	Immune globuline G
IMAC	Imobilized metal affinity chromatography
IPTG	Isopropyl β-D-thiogalactoside
IRT	Iron transport protein
ITC	Isothermal titration calorimetry
KAT	K ⁺ channel in <i>Arabidopsis thaliana</i>
KChIP	Kv channel-interacting protein
K _D	Dissociation constant
kDa	Kilo Dalton
KHA	plant K ⁺ channel domain rich in hydrophobic and acidic residues
KJ	Kilo Joule
KT	K ⁺ transporter
KUP	K ⁺ uptake permease
KvAP	K ⁺ voltage gated channel from <i>Aeropyrum pernix</i>
l	liter
LATS	Low affinity uptake system
LB	Luria bethani medium
LiAc	Lithium acetate
M	Molar
m	Mili
m/z	Mass to charge ratio
MALS	Multi angle light scattering
MaM	Mn ²⁺ binding modified Calmodulin
MAPK	Mitogen-activated protein kinase
MGT	Magnesiumtransporter
min	minute(s)
MloK	<i>Mesorhizobium loti</i> K ⁺ channel
MnSOD	Mn ²⁺ dependent superoxide dismutase
MS	Mass spectrometry
MWCO	Molecular weight cut off
n	Nano
N	non ionic
NADPH	Nicotinamide adenine dinucleotide phosphate (reduced)
NRAMP	Natural resistance-associated macrophage protein
NRT	Nitrate transporter
NRT	Nicotinamide riboside transporter
NTA	Nitrilotriacetic acid
OD	Optical density at 600 nm

on	Over night
PAGE	Poly acrylamide electrophoresis
PBC	phosphate binding cassette
PCD	Programmed cell death
PCR	Polymerase chain reaction
PDB	Protein data bank
PDR	Pleiotropic drug resistance
PEG	Poly ethylene glycol
PHT	Phosphate-transporter
Pma1	Plasma membrane ATPase 1
PP2C	Proteinphosphatase 2C
PP2CA	Protein phosphatase 2C 37
PPI	Protein phosphatase interacting domain
PSII	Photosystem II
PTM	Post translational modification
Rboh	Respiratory burst oxidase homolog
rev	Reverse
RMSD	Root mean square deviation
RNA	Ribonucleic acid
RNS	Reactive nitrogen species
ROS	Reactive oxygen species
rpm	Rounds per minute
<i>S. cerevisiae</i>	<i>Sacheromyces cerevisiae</i>
SDS	Sodium dodecyl sulfate
SEC	Size exclusion chromatography
Sf9	Spodoptera frugiperda 9
SI	Supplemental information
siRNA	Small interfering ribonucleic acid
SOS	Salt overly sensitive
SULTR	Sulfate-transporter
TCA	Trichloroacetic acid
TCEP	Tris(2-chlorethyl)phosphat
TEV	Tobacco etch virus
TM	Transmembran
TMD	Transmembrane domain
TTP	Thymidine triphosphate
UTP	Uracil triphosphate
V	Volt/voltage
w/v	Weight to volume
wt	Wild type
YC	Yellow camaleon
YFP	Yellow fluorescent protein
YM	Yellow mangaleon
YPD	Yeast peptone dextrose medium
Z	zwitter ionic

<u>Amino acid</u>	<u>Tree letter code</u>	<u>One letter code</u>
Alanine	Ala	A
Arginine	Arg	R
Asparagine	Asn	N
Aspartic acid	Asp	D
Cysteine	Cys	C
Glutamic acid	Glu	E
Glutamine	Gln	Q
Glycine	Gly	G
Histidine	His	H
Isoleucine	Ile	I
Leucine	Leu	L
Lysine	Lys	K
Methionine	Met	M
Phenylalanine	Phe	F
Proline	Pro	P
Serine	Ser	S
Threonine	Thr	T
Tryptophan	Trp	W
Tyrosine	Tyr	Y
Valine	Val	V

Introduction

Minerals in Plants - Micro- and Macronutrients

Plants comprise a large kingdom within eukaryotes and play an indispensable role for all living matter on earth by the conversion of CO₂ to O₂ [1]. Plant viability and growth depends on a variety of factors. Here, the nutrient availability in the soil plays an essential role, aside of further abiotic factors like temperature, water availability and many more [2]. The uptake of these nutrients is mainly facilitated by the plant roots. Hereby a distinction between micro- and macronutrients regarding the plants requirement is made [3-5].

Table 1: Micro- and macronutrients in plants, form of uptake, concentration in plant dry weight and their functions in plants.
Adapted from [2-5]

Element	Form of uptake	Concentration in plant [µg/g dry weight]	function in the plant
Micronutrients			
Chlorine (Cl)	Cl ⁻	3	photosynthesis, osmotic balance
Boron (B)	H ₃ BO ₃	2	cell wall stability
Iron (Fe)	Fe ²⁺ , Fe ³⁺	2	chlorophyll synthesis, energy transfer
Manganese (Mn)	Mn ²⁺	1	photosynthesis (PSII), enzyme cofactor
Zinc (Zn)	Zn ²⁺	0.3	enzyme cofactor
Copper (Cu)	Cu ²⁺	0.1	photosynthesis, respiration, oxido-reduction
Nickel (Ni)	Ni ⁺	0.001	enzyme cofactor
Molybdenum (Mo)	MoO ₄ ²⁻	0.001	enzyme cofactor
Macronutrients			
Nitrogen (N)	NH ₄ ⁺ , NO ₃ ⁻	1000	nucleic and amino acids, Chlorophyll
Potassium (P)	K ⁺	250	osmotic balance, enzyme activation
Calcium (Ca)	Ca ²⁺	125	Cell wall, signaling, enzyme
Magnesium (Mg)	Mg ²⁺	80	Chlorophyll
Phosphorus (P)	H ₂ PO ₄ ⁻ , HPO ₄ ²⁻	60	nucleic acids, energy (ATP)
Sulfur (S)	SO ₄ ²⁻	30	proteins (disulfide)

Minerals defined as micronutrients are required in small amounts by the plant cells. Typically they make up 0.05 % or less of the dry weight of a plant. [6]. Amongst these micronutrients are chlorine (Cl⁻), Boron (H₃BO₃), iron (Fe²⁺ and Fe³⁺), manganese (Mn²⁺), zinc (Zn²⁺), copper (Cu²⁺), nickel (Ni⁺), and molybdenum (MoO₄²⁻). These ions predominantly function as catalytic cofactors for example in enzymes.

Chlorine, in the form of chloride (Cl⁻), is mainly involved in the maintenance of the osmotic balance, the membrane potential and charge balance but also found to be essential for photosynthesis [7, 8]. The role of boron in plants is not fully elucidated, but it is known to be involved in the cell wall stability by crosslinking pectin-polymers [9]. Iron, as Fe²⁺ and Fe³⁺, is prominently known to be involved in the formation of Fe-S clusters, in proteins as ferredoxin and play a predominant role in electron transfer during photosynthesis [10]. Besides Fe-S clusters iron ions can be coordinated in heme groups as well. Iron ions are further involved in mitochondrial respiration, hormone biosynthesis and capturing of reactive oxygen species [11].

Manganese can occur in different oxidation states (II, III and IV) and amongst others functions as enzymatic cofactor in the oxygen-evolving complex in the H₂O splitting reaction in photosystem II and in the capturing of reactive oxygen species [12]. When present in higher concentrations, manganese can become toxic for the plant cell, as uptake and translocation of other mineral nutrients gets prevented [13]. Zinc mainly occurs as an enzymatic cofactor. It is coordinated via the Zinc finger motif in a variety of proteins that are involved in the transcription and translation machinery, metalloproteases and oxidoreductases [14, 15].

The involvement of copper in plants covers a variety of processes such as photosynthesis, mitochondrial respiration, carbon and nitrogen metabolism as well as oxidative stress protection. Noteworthy, copper ions can switch between Cu⁺ and Cu²⁺ and thereby are potentially toxic as they have the potential to form free radicals [14, 16]. About the role of nickel ions in plants only little is known, except for its toxicity by inducing oxidative stress and interfering with other divalent metal ions, but a role in urease activity is stated [17-19]. Molybdenum is complexed by a pterin compound to form the active molybdenum cofactor and thereby functions as enzymatic cofactor in nitrogen assimilation, sulfur metabolism, hormone synthesis and stress reactions [20, 21].

Compared to micronutrients, plants require macronutrients in significantly larger amounts. Macronutrients classically make up 0.1 % or more of the plants dry weight [6]. These macronutrients include nitrogen (NH₄⁺, NO₃⁻), potassium (K⁺), calcium (Ca²⁺), magnesium (Mg²⁺), phosphorus (H₂PO₄, HPO₄²⁻) and sulfur (SO₄²⁻) [3].

Nitrogen uptake has both high and low affinity components. Either way nitrogen can be taken up by *A. thaliana* roots in the form of NH₄⁺ by proteins of the AMT family or NO₃⁻ by NRT family transporters [22, 23]. The predominant occurrence of nitrogen in the cell is as amino groups in amino acids, as part of nucleic acids and in a variety of non protein compounds [22, 24]. Like nitrogen, the uptake of potassium can be divided into high affinity K⁺/H⁺ cotransport and low affinity uptake by channels. While the high affinity uptake is mainly facilitated by members of the HAK/KUP/KT family, the low affinity uptake is primarily facilitated by an inward rectifying channel of the voltage gated K⁺ channel family [23, 25]. The predominant function of K⁺ is being the main cationic osmolyte within the cell and thereby the preservation of the cell turgor. Besides K⁺ is involved in membrane polarization, enzyme activation and functionality [26-28].

Calcium is taken up in the form of Ca²⁺ through the plant roots by specific and non specific ion channels and stored in the vacuole [29]. The predominant function of Ca²⁺ within the plant cell is its function as a second messenger in a variety of signaling processes, like root hair elongation, physiological responses to biotic and abiotic stress or programmed cell death [30-34]. Magnesium, in the form of Mg²⁺, is taken up by the cell through MGT family transporters [35]. Predominantly Mg²⁺ is found in the chloroplasts where it is coordinated within the porphyrin ring of the chlorophyll molecule. It further functions as an enzymatic cofactor e. g. in phosphotransferases and ATPases and an essential role in gene transcription and translation by binding to nucleic acids is stated [36-38].

Phosphorus is utilized by plants in its inorganic form (P_i) as H₂PO₄⁻ or HPO₄²⁻ depending on the soil pH. The uptake is performed by Pht P_i transporters [23]. Most prominently phosphorus is involved in the energy household of the cell, by formation and disruption of the pyrophosphate bond in ATP. Further it is also found in other nucleotide triphosphates (CTP, GTP, UTP, TTP) and therefore an essential component of DNA and RNA. In the headgroups of phospholipids, phosphorus plays another essential role in lipid homeostasis and membrane integrity [39, 40]. Plants take up sulfur mainly in the form of

sulfate (SO_4^{2-}) via membrane transporters of the SULTR family. The main function of sulfur in the cell is as component of the amino acids cysteine and methionine and therefore the involvement in disulfide bonds and iron-sulfur clusters. Further sulfur is found in glutathione, hence the capturing of reactive oxygen species and in minor amounts in sulfolipids in chloroplast thylakoids [41, 42].

Ca^{2+} signaling in plants as initial response to nutrient deprivation

When the environmental conditions drastically change, adaption mechanisms are vital for plant survival. When one of the essential nutrients becomes scarce, this leads to abiotic stress in the plant [43]. The initialization of responses to such stress factors is facilitated by changes in the cytosolic Ca^{2+} concentration. Ca^{2+} is a prominent second messenger in eukaryotes and initiates the response to abiotic stresses in plants [34]. The cytosolic Ca^{2+} concentration is kept constant in a range of 100-200 nM when no stress reaction is induced, but can rise up to low micromolar levels ($\sim 1\text{-}1.5\text{ }\mu\text{M}$) [44, 45]. For such increasing cytosolic Ca^{2+} concentrations, Ca^{2+} gets released from the vacuole, ER or cell wall. In these compartments Ca^{2+} is stored in concentrations up to 1-10 mM [31, 46]. These Ca^{2+} releases thereby function as signals for the plant cell to induce a certain reaction. Since these signals do not consist of a simple increase in cytosolic Ca^{2+} , but are highly specific in respect to time and localization, reaching from a simple single release events to highly complex sparks and waves, these signals are also named Ca^{2+} signatures [45-48].

One stimulus that yields in such a stress reaction is K^+ deprivation or starvation. On the one hand, a direct hyperpolarization of the plasma membrane in the root cells can be observed [28, 49] and secondly an elevation of the cytosolic Ca^{2+} concentration occurs [50]. Two sequential and specific Ca^{2+} signatures are generated in root cells [51]. A first increase in the cytosolic Ca^{2+} concentration can be observed after 1 min of Ca^{2+} deprivation. The cytosolic Ca^{2+} returns back to the basal level within 7 min. This signal occurs specifically in the post meristematic elongation zone of the plant root and aligns with the expression pattern of the K^+ channel AKT1 and its activating proteins CIPK23 and CBL1/9 [51]. This first Ca^{2+} stimulus occurs within the same speed as the membrane hyperpolarization, but declines faster. Hence both processes go hand in hand to activate the K^+ uptake via the Ca^{2+} dependent voltage gated K^+ channel AKT1.

After 18 h a secondary Ca^{2+} signal is detected that persists for several hours in the root hair differentiation zone. This second Ca^{2+} signal is not observed when K^+ supply is restored after the first K^+ signal. Since the timing and duration of both Ca^{2+} signatures differs significantly, it is assumed that the first short and direct signal triggers an initial short term response to K^+ deprivation, while the second longer lasting Ca^{2+} signal triggers a long term adaption mechanism to maintain the plant's viability on low K^+ medium [51].

Potassium uptake in plants

Since K^+ comprises essential functions in plants, the constancy of the cytosolic K^+ concentration is of high importance for the plant viability [26]. The cytosolic K^+ concentration is in the range of 100 mM [52, 53], while the K^+ concentration in the soil can be highly fluctuating, but usually is between 0.1 and 1 mM [3, 54]. Since K^+ is essential but its availability from the soil is low, it is a limiting factor for plant growth and viability. Therefore plants have developed strategies to accomplish K^+ uptake against the concentration gradient under limiting K^+ conditions [55, 56].

For the uptake of potassium by plant roots a dual mechanism was stated by Epstein *et al.* (Figure 1.A) [57]. At extracellular K^+ concentrations below 100 μ M the high affinity transport systems (HATS) dominate in the uptake process. The uptake via HATS follows a Michaelis-Menten kinetic and therefore reaches a maximal velocity (v_{max}). This active transport is facilitated by K^+/H^+ symporters. At extracellular concentrations above 100 μ M, low affinity transport systems (LATS) predominantly facilitate the K^+ uptake in a linear, non saturable way. Thereby the K^+ ions pass the membrane passively through channels to the inside of the root cell [57-59].

The energetically unfavorable uptake of K^+ against its concentration gradient becomes favorable by the generation of a pH ($pH_{ext} = 5.5$; $pH_{int} = 7.3$) and electrical gradient (ΔV_M negative inside) over the plasma membrane. These gradients are created by a H^+ ATPase in the plasma membrane, that pumps H^+ ions out of the cell [60]. While the K^+/H^+ symporters directly use the H^+ gradient as driving force for the K^+ import, the electrical gradient over the plasma membrane allows the passive uptake of K^+ via channels. Upon K^+ deprivation further hyperpolarization of the cell membrane potential is induced and thereby the passive K^+ uptake via channels is further promoted [28, 61]. On the other side in situations of salt stress, meaning high Na^+ concentrations in the external medium a depolarization of the membrane can be observed [62, 63].

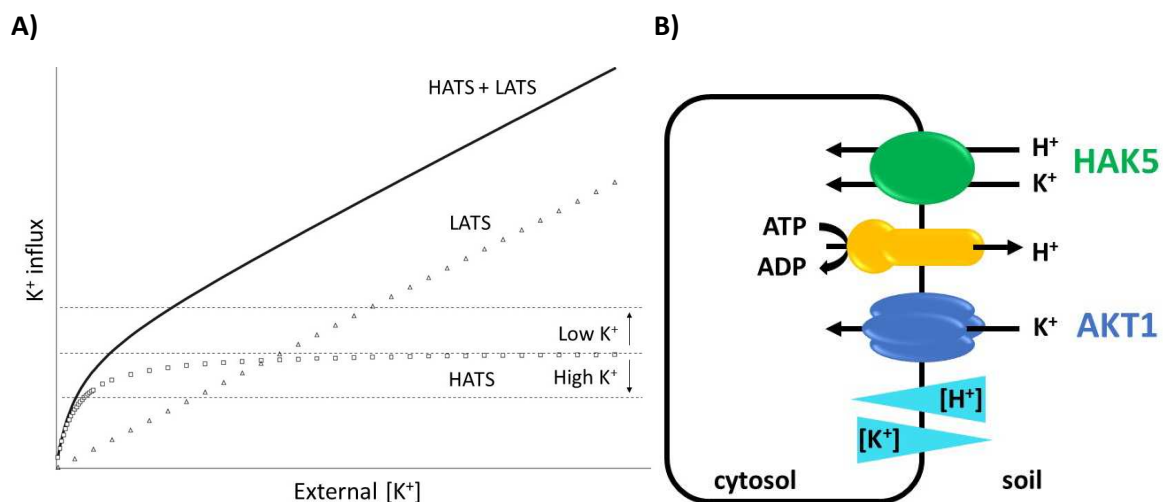


Figure 1: Potassium ion uptake in plants. A) High and low affinity transport systems (HATS/LATS) contribute differently to the K^+ uptake into the plant cell. While the uptake by HATS follows a Michaelis-Menten kinetic and a maximum velocity is reached (\circ), the LATS perform the uptake in a linear, non saturable way (Δ). B) In *A. thaliana* the main components of K^+ uptake from the soil are the K^+/H^+ symporter HAK5 (green) and the voltage gated shaker channel AKT1 (blue). A H^+ ATPase (yellow) is used to generate a proton gradient which is required to make the K^+ uptake energetically favorable for the cell directly by proton symport (HAK5) or indirectly through the electrical gradient (AKT1 channel). The H^+ and K^+ gradients over the membrane are depicted in cyan. Adapted from [58, 64].

Throughout the last decades various proteins involved in K⁺ uptake in plants were identified [65]. The main contributors to K⁺ uptake in *A. thaliana* belong to the HAK/KUP/KT and voltage gated K⁺ channel families (Figure 1.B). The predominant HATS in *Arabidopsis thaliana* is a member of the HAK/KUP/KT family, namely the K⁺/H⁺ symporter HAK5. Genes encoding for members of the HAK/KUP/KT family were found in all known plant genomes, but not in animals [66]. So far no 3D structures of HAK/KUP/KT have been resolved. But the transporters were predicted to have 10 -14 transmembrane segments and a cytosolic N-terminus [67]. The expression of the *athak5* gene was shown to be upregulated during K⁺ deprivation to increase K⁺ uptake capacity in the root cells [62, 68]. Triggers for the upregulation are the membrane hyperpolarization and the formation of reactive oxygen species such as H₂O₂, which accumulate in the root cells due to K⁺ deprivation [49, 69]. On the other side the *athak5* gene gets repressed after K⁺ supply [70]. Inhibition of HAK5 on transcriptional level is achieved by NH₄⁺ if present in millimolar concentrations [61].

Another, NH₄⁺ insensitive uptake system, is a member of the voltage gated K⁺ channel family. The inward rectifying channel AKT1 significantly contributes to K⁺ uptake even at concentrations as low as 10 μM. This is in controversy to the Epstein model, according to which AKT1 as a passive channel should be a low affinity uptake system (LATS) and only contribute to the K⁺ uptake at concentrations above 100 μM [27, 61]. None the less, it was found that at external K⁺ concentrations below 10 μM HAK5 alone facilitates the uptake, while in the range of 10-200 μM both HAK5 and AKT1 are active and at concentrations above 200 μM AKT1 preliminary contributes to the K⁺ uptake in *A. thaliana* [64, 71]. Hence AKT1 does not fulfill the classical prerequisites of a LATS and other, yet unidentified LATS operating in the millimolar K⁺ range are postulated [71-73]. Unlike HAK5, AKT1 is not regulated on a transcriptional level in dependence of the external K⁺ concentration [74], but its activation is triggered by the Ca²⁺ signatures. The precise structure and regulation of AKT1 as a member of the voltage gated K⁺ channel family will be described in the next chapters.

The shaker-like voltage gated K⁺ channel AKT1

Shaker channels vs. plant voltage gated K⁺ channels – structural features

Shaker channels were first identified from the *Drosophila melanogaster* shaker gene locus [75]. Upon electrophysiological studies, this gene locus was found to play an important role in the maintenance of the K⁺ homeostasis in the fly, as it encodes for a family of K⁺ channels [76]. Channels of this shaker like fold were also found in the plasma membrane of plants [77, 78] and amongst others act in K⁺ distribution within the plant and in the previously described K⁺ uptake from the soil. To this point in *A. thaliana* nine genes encoding for either inward or outward rectifying shaker-like channels are known [79].

In general shaker or shaker-like channels consist as tetramers within the plasma membrane and upon tetramerization form a central pore that is selective for K⁺ [55, 80]. Each monomer consists of a short cytosolic N-terminal sequence and the pore forming transmembrane domain (TMD), which harbors the voltage sensor as well as the pore domain. Plant shaker-like channels further comprise a large cytosolic C-terminal part. The TMD is connected via a C-linker domain to a cyclic nucleotide binding domain (CNBD), an ankyrin repeat domain (ARD) and a plant K⁺ channel motif rich in hydrophobic and acidic residues (KHA motif) [55, 79-81]. The overall structural features of a plant shaker-like channel and its tetrameric assembly are depicted in Figure 2 and will be described in more detail in the following sections.

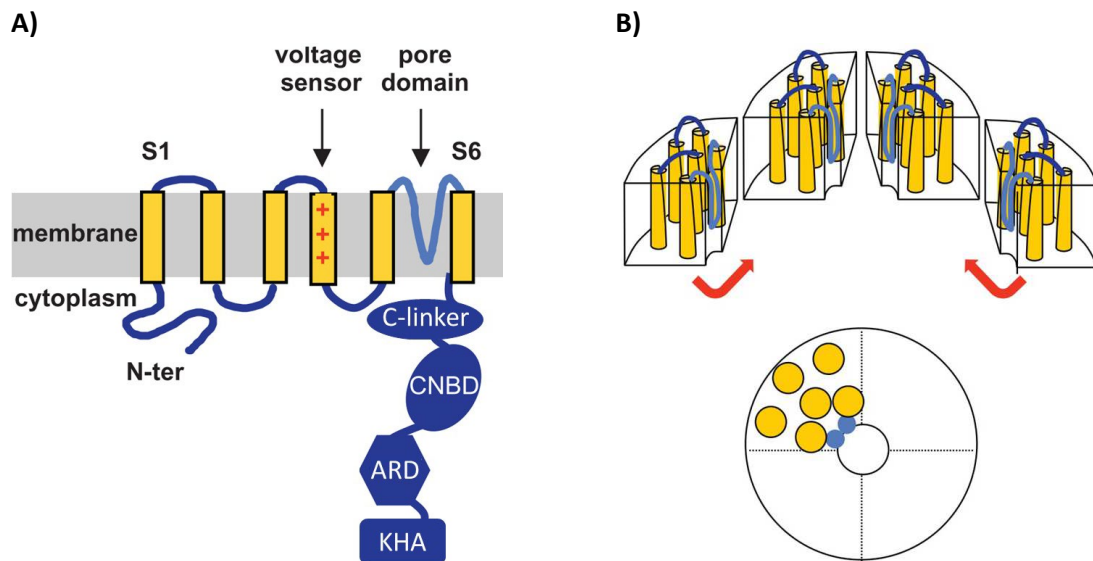


Figure 2: General structure of voltage gated shaker-like channels. A) Structural elements of a shaker-like channel protomer. N-terminally each protomer consists of a short cytosolic sequence and a transmembrane domain (TMD). The transmembrane segment four functions as the voltage sensor and between transmembrane segment 5 and 6 the pore domain is located. The C-linker connects the TMD with the cytosolic cyclic nucleotide binding domain (CNBD), ankyrin repeat domain (ARD) and KHA motif. B) Assembly of the tetrameric channel. Upon tetramerization the pore domains of the protomers form the pore of the K⁺ channel. Pictures are derived and modified from Chérel et al. 2014 [55].

In 2018 Jegla *et al.* made a reclassification of shaker channels. The previously named plant shaker or shaker-like K⁺ channels and shaker channels from metazoans were assigned to different superfamilies, namely the CNBD channel superfamily and shaker/KvAP superfamily respectively [25]. The main differences are the lacking C-terminal CNBD domains in the shaker/KvAP channels and the fact that shaker/KvAP channels are solely depolarization activated, while channels of the CNBD superfamily can be both hyper- or depolarization gated. Hence the family of plant shaker-like channels is renamed to plant voltage gated K⁺ channels and assigned to the CNBD superfamily [25]. Further structural and mechanistical differences between these two superfamilies will be described in the next section.

The transmembrane domain

The core piece of each shaker/KvAP or CNBD channel is its transmembrane domain. For channels from both superfamilies a protomer classically consists of 6 transmembrane segments (S1-S6). Each TMD can be divided into two subdomains. Thereby charged amino acids within the transmembrane segments 1 – 4 function as the voltage sensor domain with segment 4 as the sensor. The transmembrane segments S5 and S6 together with their intermediate loop build the pore domain [82, 83]. The arrangement of the transmembrane segments and models for pore opening follow a similar pattern for both superfamilies, but vary in some aspects (Figure 3).

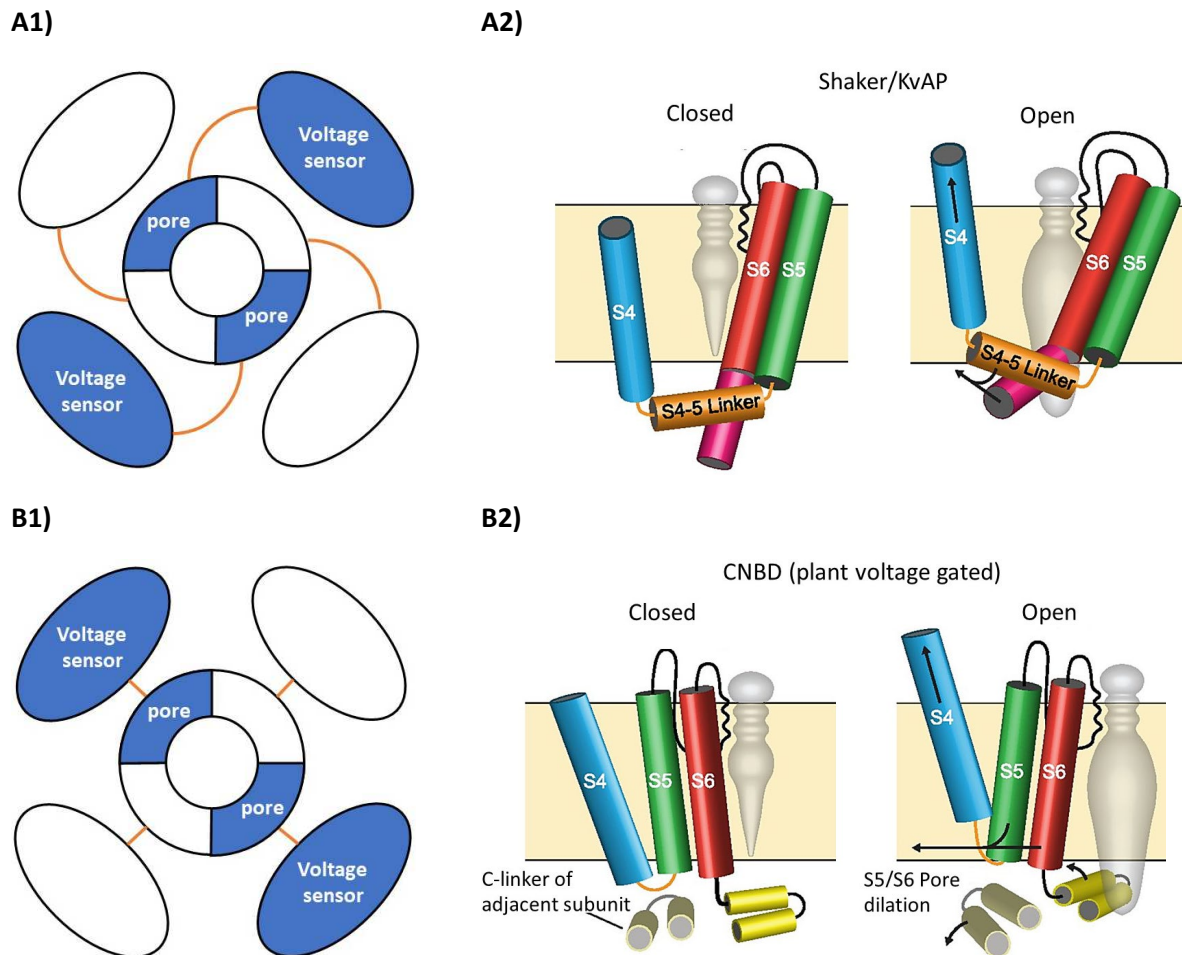


Figure 3: Transmembrane domains of A) shaker/KvAP and B) CNBD superfamily channels. 1) Domain orientation of the voltage sensors in respect to the pore domains. The linker between the pore domain and the voltage sensor is colored in orange. 2) Opening mechanism of the pore domains of A2) channels of the Shaker/KvAP superfamily and B2) channels of the CNBD superfamily including plant voltage gated K^+ channels. Only one pore domain of the tetrameric channel is shown. The membrane is colored in sand with the extracellular space on the top and the cytosol at the bottom. The pore is visualized as a gray cone. The voltage sensing transmembrane segment 4 (S4) is depicted in blue and the transmembrane segments of the pore domain (S5, S6) are depicted in green and red. The interconnecting loop between S5 and 6 which functions as the selectivity filter is depicted as a black line. The linker between transmembrane segment 4 and 5 is colored in orange. Specific for the shaker/KvAP channels this linker is extended (S4-5 linker). The prolonged transmembrane segment 6 of shaker/KvAP channels/ activation gate is colored in pink. The C-linker which is specific for CNBD channels and following transmembrane segment 6 is colored in yellow. The movements of the transmembrane segments upon changes in the membrane potential and accompanied channel opening are indicated by the black arrows. Pictures are derived from Jegla et al. 2018 [25].

The positioning of the voltage sensor domains in respect to the pore domains differs between the two superfamilies (Figure 3.A1 and B1). For the shaker/KvAP channels the voltage sensor domain is connected via a S4-5 linker helix to the pore domain and the voltage sensor domain of each protomer is situated to the pore domain of the neighboring protomer [84-86]. The voltage sensor domains of CNBD channels contain a comparably shorter, non-helical linker between S4 and S5. Hence, voltage sensor domains of CNBD superfamily channels are located to the pore domains of the same protomer [87, 88].

For both superfamilies the positive charges in S4 of the voltage sensor domain (predominantly arginine side chains) interact with negatively charged sidechains within the S1-S3 transmembrane segments. These charges in S4 can sense the electric field over the plasma membrane and move the S4 helix towards the extracellular space upon changes in membrane polarization [83, 85, 89]. For both depolarization and hyperpolarization activated channels an identical direction for the movement of the voltage sensor (S4) is stated (Figure 3.A2 and B2) [90, 91]. Upon the S4 movements, the conformational change within the voltage sensor domain is transduced to the pore domain (Figure 3.A2 and B2). The S5 transmembrane segment faces the voltage sensor domain, the intermediate loop comprises the selectivity filter and together with transmembrane segment 6 forms the pore in the tetrameric state of the channel [86, 92]. This selectivity filter comprises a TXXTXGYG motif which is conserved for shaker/KvAP and CNBD channels [25, 83, 93].

The conformational changes in the pore domain during channel opening differ for both superfamilies (Figure 3.A2 and B2). In shaker/KvAP channels the movements in the S4 voltage sensor forward the conformational change to S5 and S6 helices via a linking helix (S4-5 linker). This S4-5 linker shares a significant interaction surface with the C-terminal extracellular extension of S6. This so called activation gate blocks the pore in the resting state and upon movement of the voltage sensor S4 and the S4-5 linker is moved aside and opens the pore for K^+ [82]. CNBD channels neither comprise a helical S4-5 linker, nor an activation gate. A short, non helical loop brings the extracellular ends of S4 and S5 in close proximity and C-terminal to the transmembrane segment 6 the C-linker is found. It forms a flexible gating ring on the cytosolic site of the transmembrane domain [25]. This C-linker is found in all voltage gated K^+ channels of land plants [94, 95]. It is the interconnecting part between the TMD and the C-terminally following CNBD and forms a major interface between the two domains. The movement of the S4 upon channel activation is directly coupled to a reorientation of the C-linkers of the neighboring protomers. Hence, the C-linker plays an essential role in forwarding conformational changes in the TMD to the CNBD and visa versa [96]. The C-linker was found to have a central role even in channels with CNBDs that are incapable of cNMP binding [25, 97].

Voltage sensing and pore opening of hyperpolarization activated CNBD channels

Recently the 3D structures of two plant voltage gated K^+ channels were resolved by cryo EM, namely KAT1 and the object of this study AKT1 [93, 98]. For AKT1 the transmembrane domain with transmembrane segments 1-6 and the pore loop, the C-linker consisting of four helices (A-D) and the CNBD structure could be modeled from cryo EM data. The N-terminus, besides a short helix (amino acids 6-14), as well as the C-terminal part of the protein, which include the ARD and KHA domain, could not be resolved. The opposing protomers are named I/I' and II/II' respectively [93]. In Figure 4 two different conformations of the homotetrameric channel are depicted.

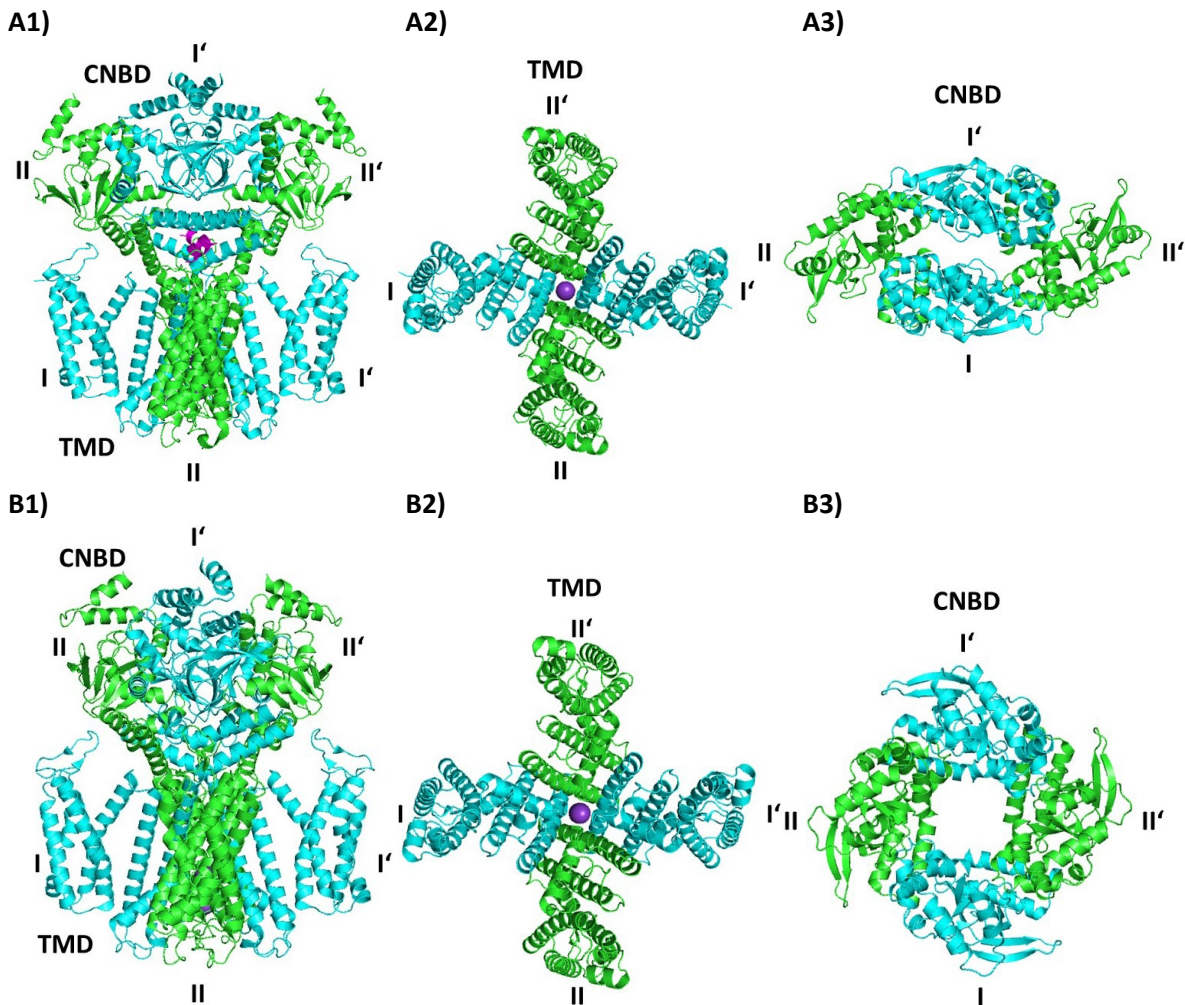


Figure 4: 3D structure of the homotetrameric voltage gated K^+ channel AKT1 in different conformational states. A) resembles the inactive state based on the wildtype protein. B) resembles the pre-open state, which was mimicked by a constitutively active AKT1 mutant (D379A). The protomers I/I' are colored in cyan and the protomers II/II' are colored in green. The short N-terminal sequence (aa 6-14) is shown in magenta (A1 only). Structures A1) and B1) resemble the structure of the whole channel (without ARD and KHA domain) in the inactive (A) and pre-open state (B) respectively. The extracellular space is on the bottom and the cytosolic space on top of the picture. Structures A2) and B2) show the TMDs in inactive (A) and pre-open state (B) of the channel viewed from the extracellular space. Structures A3) and B3) show the CNBDs in inactive (A) and pre-open state (B) of the channel viewed from the cytosolic space. K^+ ions located in the pore are colored in purple. The pictures are derived from the cryo EM structures of Lu et al. 2022 (PDB entries 7WSW and 7FCV) [93].

Cryo EM studies on homotetramers of the AKT1 wildtype show a 2 fold symmetry for their cytosolic part (Figure 4.A). A constitutively active mutant of AKT1 (D379A)¹ shows a 3D structure with a 4 fold symmetry for the cytoplasmic domain (Figure 4.B), while the transmembrane domain remains in a 4

¹ This mutant resembles the symmetry found for the phosphorylated, hence activated AKT1 channel. Regulation of AKT1 by phosphorylation will be discussed in a following chapter.

fold symmetry in both states of the channel. The TMDs show a non domain swapped arrangement of the voltage sensor and pore domains (Figure 4.A2 and B2), as it is stated for CNBD channels [25]. As stated by the authors, the cryo EM structure of wt AKT1 shows a depolarized state of the TMD and hence an inactive state of the channel (Figure 5). The structure for the mutant AKT1 is stated as the pre-open state. The pore is still in the closed state, but the cytoplasmatic domains have switched their conformation to a symmetry comparable to the 4-fold symmetry of the basally active KAT1, as well as the phosphorylated AKT1 channel [93, 98].

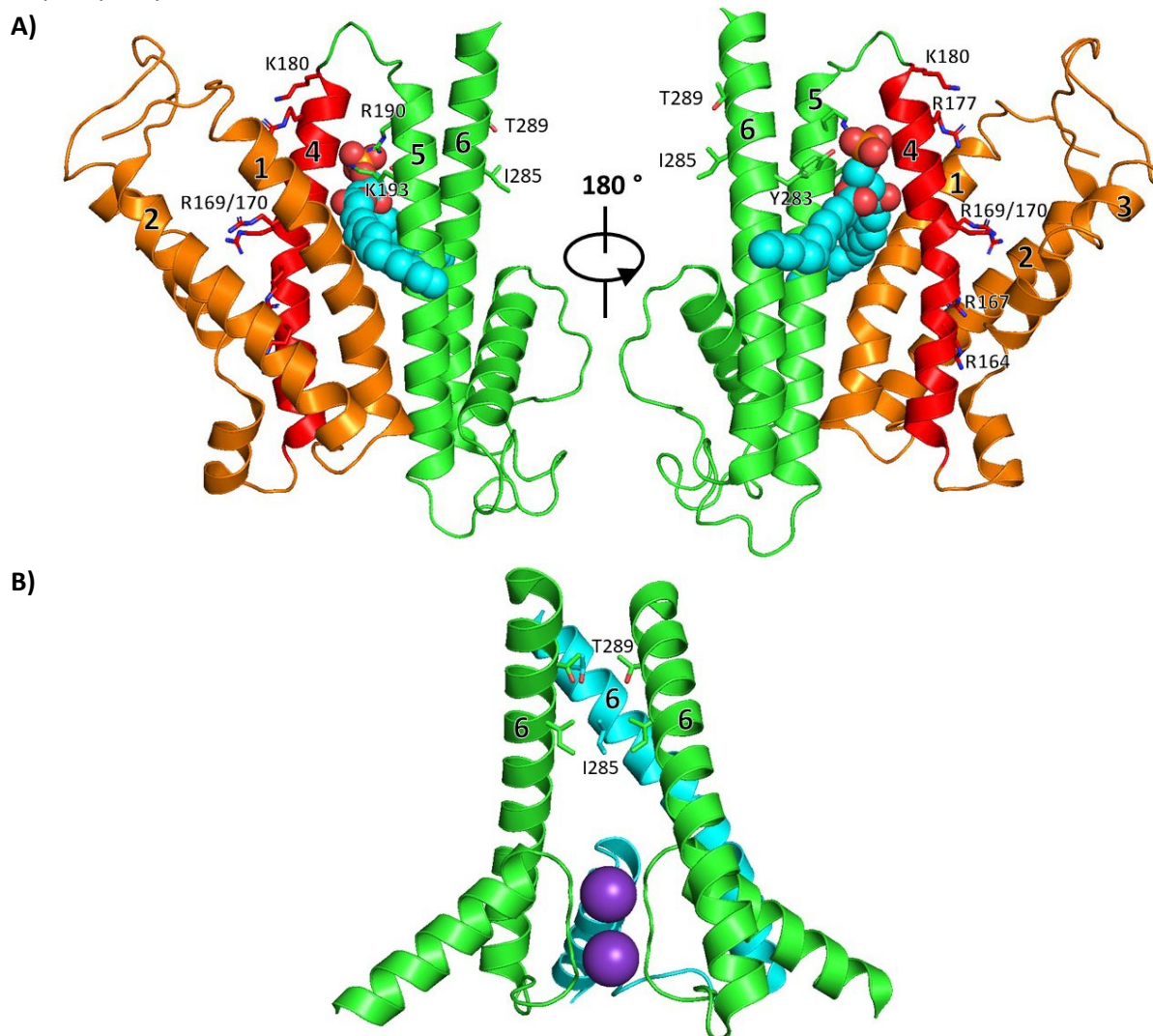


Figure 5: The AKT1 transmembrane domain and formation of the pore. A) The voltage sensor domain helices S1-3 (orange), the voltage sensor S4 (red) and the pore domain helices S5-6 (green) of a TMD are in the conformation corresponding to the inactive channel. A phospholipid is intercalated between the voltage sensor and pore domain (cyan spheres). B) The pore is formed by the helical segments S6 and S5-S6 the loop. The loop comprises the selectivity filter for K⁺ (purple spheres) and a short helical segment. Only 3 of 4 protomers are depicted. The relevant sidechains of positively charged S4 residues, residues involved in phospholipid coordination and pore closure and are depicted as sticks. The pictures are derived from the cryo EM structures of Lu et al. 2022 (PDB entry 7WSW) [93].

The voltage sensor domains of AKT1 are organized as a bundle of four-helices whereby S3 comprises a discontinuous α -helix. The S4 voltage sensor presents six positively charged amino acids, all facing towards S1-S3 (R164, R167, R169, R170, R177 and K180) [93]. In the structurally and functionally related KAT1 the arginine residues facing towards the extracellular space were found to be essential for voltage sensing [98]. In AKT1 this would correspond to R164 and R167 (Figure 5.A).

The interface between the voltage sensor domain and pore domain of AKT1 is formed by S1, S4 and S5. On the extracellular site, the end of the S1 helix is interposed between the start of the S4 voltage sensor helix and the end of the transmembrane segment S5 within the same protomer. This is also found for KAT1 where the importance for these interactions was verified by mutational studies [98]. Different from other hyperpolarization activated K⁺ channels, AKT1 and KAT1 show four phospholipids intercalated in the interface between voltage sensor and pore domains [93, 98]. In AKT1 the headgroups are coordinated by the three amino acid residues R190, K193 and Y283 within the S5 and S6 helices. Upon mutational studies these residues, and hence the coordination of phospholipids were found to be essential for AKT1 activity [93].

Lu *et al.* 2022 state a different conformation for the pore of the inactive and pre-open state of the channel. In the inactive state I285, which is located in the S6 helix, forms the narrowest point of the pore. For the structure of the constitutively active mutant the pore and is further narrowed by I285 and T289. Hence Lu *et al.* claim this conformation as the pre-open state [93].

Upon computational analysis the S4 voltage sensor of KAT1 was calculated to move 5-7 Å towards the extracellular space upon hyperpolarization, which is consistent with findings for depolarization activated channels [90, 91]. The movement of the voltage sensor (S4) is directly coupled to a lateral reorientation of the C-linker of the neighboring protomer which results in the opening of the S6 gate. Hence the interaction between S4 and the C-linker of the adjacent protomer functions as point of communication between the protomers. This interaction between the S4-S5 loop and the C-linker is as well found for AKT1 (Figure 6).

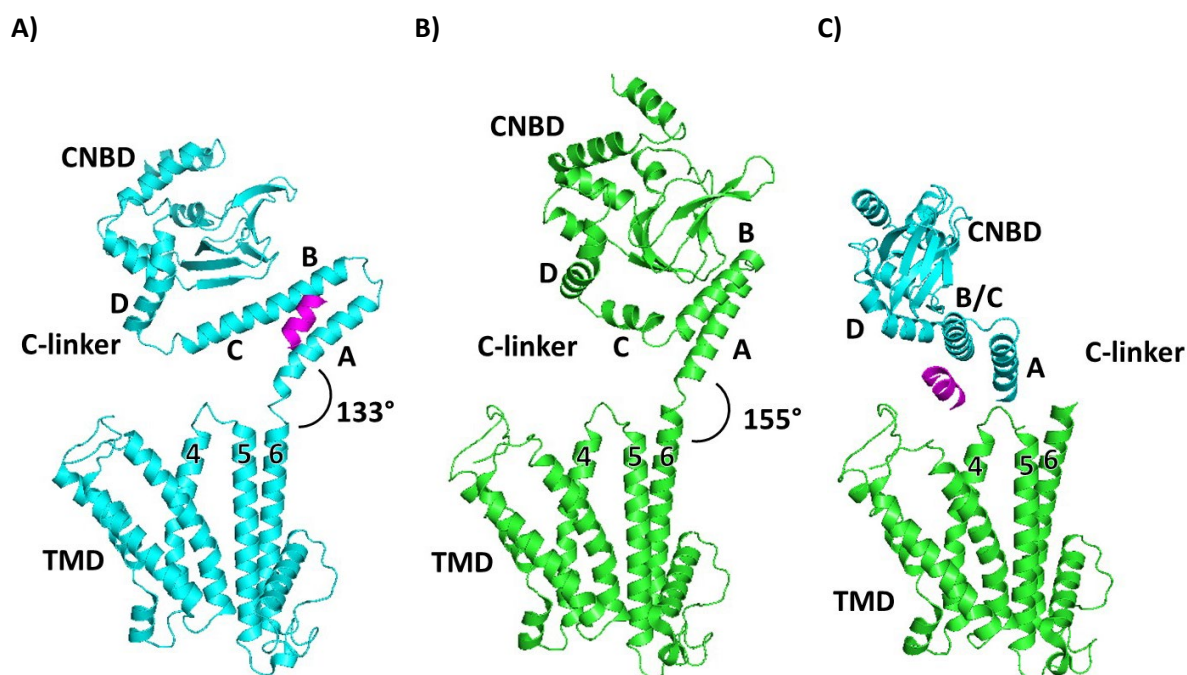


Figure 6: 3D structures of AKT1 protomers in the inactive state of the channel. The four helices of the C-linker are labeled from A-D and the relevant transmembrane segments of the pore domain are labeled 4, 5 and 6. A) In protomer I/I' (cyan) the C-linker helices B and C align to one straight helix. The short N-terminal sequence (aa 6-14) is shown in magenta and attaches to the A and B helix of the C-linker in its straight state. B) In protomer II/II' (green) the C-linker helices B and C form a kink. The different states of the C-linker result in different angulations of the C-linker/CNBD in respect to the transmembrane domain, with 133° when the C-linker is in the straight state and 155° when the C-linker is in the kinked state. C) The positioning of the short N-terminal sequence attached to protomer I/I' in respect to the TMD of protomer II/II'. The extracellular space is on the bottom and the cytosolic space on top of the pictures. The pictures are derived from the cryo EM structures of Lu *et al.* 2022 (PDB entry 7WSW).

The C-linkers of AKT1 were found to exist in two significantly different conformations in the closed state of the homotetrameric AKT1 wt channel (Figure 6). For two opposite subunits (I/I') the C-linker helices B and C arrange almost linearly to one long helix. The B and C segments of the other two protomers (II/II') form a kink which is in accordance to the C-linker consensus [93]. A cysteine at position 331 of the C-linker was found to form a disulfide bond with the cysteine at position 8 of the N-terminal sequence which precedes the TMD. This interaction was found for the straight C-linkers but not the kinked ones. The positioning of the N-terminus at the A and B helices of the straight C-linker (I/I') also brings the N-terminus in proximity to the voltage sensor (S4) of the neighboring TMD (II/II') (Figure 6.C). The presence of this N-terminal helix likely hinders the movement of the voltage sensor towards the cytosolic space upon hyperpolarization. Therefore the accompanying reorientation of the C-linker in the neighboring protomer and the channel opening will be hindered [93].

The different states of the C-linker result in different angulation of the CNBD in respect to the TMD, namely 133° for protomers I/I' and 155° for protomers II/II'. Since in the pre-open channel all four C-linkers comprise the kinked conformation, the interaction of protomers I/I' with the N-terminus is broken and the reorientation of the C-linkers is coupled to a rearrangement of the CNBDs. The CNBDs of protomer I/I' tilt towards the membrane away from the pore, while the CNBDs of protomers II/II' move closer to the axis of the pore [93]. Possibly the reorientation of the C-linkers and CNBDs will be followed by the reorientation of the TMDs, which will result in pore opening and K⁺ uptake. But in order to postulate a complete mechanism for the AKT1 channel opening, a 3D structure of the channel in the open conformation will be required.

The cyclic nucleotide binding domain

While plant voltage gated K⁺ channels share a familiar shaker-like transmembrane domain, they differ from metazoan shaker channels by their C-termini. It was found to be specific for plant voltage gated K⁺ channels to comprise a cyclic nucleotide binding domain (CNBD) within their C-terminal cytosolic domain [25, 81]. The CNBD is connected to the preceding transmembrane domain via a conserved C-linker, which was described in the previous section.

Cyclic nucleotide binding domains play an important role in the regulation of voltage gated K⁺ channels by binding cyclic nucleotides (cNMP) like cAMP or cGMP [84, 97]. Cyclic nucleotides are known to be involved in a variety of signaling processes in plants, for example in response to biotic or abiotic stresses [99]. In case of plant voltage gated K⁺ channels like AKT1, the cyclic nucleotide cGMP was shown to have an effect on K⁺ currents [100]. Moreover channels were found that do not to bind cyclic nucleotides to their CNBD but flavonoids [25]. Flavonoids were found to bind to the CNBD of members of the CNBD superfamily, namely mammalian EAG channels [101-103]. Flavonoids are polyphenolic secondary metabolic compounds and highly abundant in plants as well. They perform a variety of functions in the plant, most prominently the coloring and flavor of fruits and flowers [104, 105]. Hence it is likely that they can function as ligands to voltage gated K⁺ channels in plants as well [25].

It is known that upon binding of cyclic nucleotides like cAMP or cGMP, the CNBD undergoes a conformational change which promotes the opening of the pore [25, 84]. A CNBD forms a globular domain and consists of two structurally differing segments. On the basis of 3D structures of the prokaryotic MloK1 CNBD in presence and without cAMP [84] the cAMP binding and the accompanying structural rearrangements in the CNBD will be described (Figure 7 **Figure 1**).

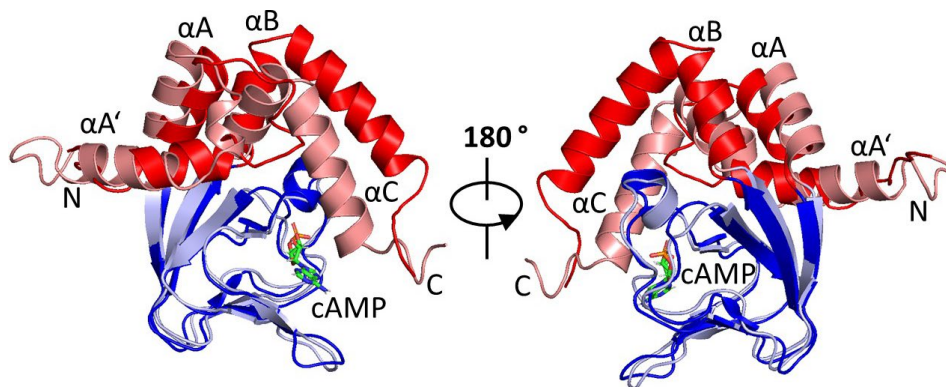


Figure 7: 3D structures of the MloK1 cyclic nucleotide binding domains. The CNBD in the cAMP-free and -bound states. The core domain of the CNBD is depicted in blue (blue = cNMP-free; light blue = cAMP-bound). The helical segment is depicted in red with the helices labeled accordingly (red = cNMP-free; light red = cAMP-bound). cAMP is depicted as sticks, with the C atoms in green, the N atoms in blue and the P atoms in orange. The structures of the MloK1 CNBD were adapted from Schünke *et al.* 2011 [84] based on the PDB structures 2KXL and 2KOG.

The core of the CNBD comprises an antiparallel β -roll, consisting of 8 β -sheets (β 1-8), with a short interior α -helix. The short α -helix is known as the phosphate binding cassette (PBC) and is conserved in a variety of CNBDs from other voltage gated channels [106-108]. The core domain forms the binding site for the cNMP by interactions with the phosphate and ribose of the nucleotide. Here a highly conserved arginine is involved in interactions with negatively charged phosphate moiety of the cNMP [108, 109]. Second to this core domain is an α -helical segment, that consists of four helices (α A, α A', α B, α C) [84]. While the conformation of the core domain remains almost unchanged upon binding of cyclic nucleotides, the helical segment undergoes a significant conformational change in the CNBD (Figure 7) [84]. The α B and α C helices do not change their position relative to each other due to hydrophobic interactions, but upon cAMP binding they move as a unit together on top of the cAMP purine ring. Thereby they stabilize the cAMP bound complex and function as a “lid” to the binding pocket [108, 110].

Both AKT1 and the MloK1 channel belong to the CNBD channel superfamily stated by Jegla *et al.* 2018 [25], but differ in their activation. While MloK1 channel opening relies only on the cyclic nucleotide binding (cyclic nucleotide gating/CNG), for plant voltage gated K^+ channels like AKT1 activation by hyperpolarization as well as modulation of the activity by nucleotide binding is stated (hyperpolarization-activated cyclic nucleotide-gated/ HCN) [100]. The 3D structures of mammalian voltage gated (hyperpolarization activated) channels or their CNBDs in their apo and cNMP bound state show the most differences in the conformation of the CNBD as well. In accordance to the movements in MloK1, the α B and α C-helices are moved towards the β -roll in the cNMP bound state [111, 112]. For AKT1 only the structure of the cNMP free CNBD is known [93]. Therefore it still needs to be proven to which point the cyclic nucleotide binding mechanism is applicable for plant AKT1.

The Ankyrin Repeat Domain

Ankyrin repeats are highly abundant and conserved in all three domains of life [113] including plant voltage gated K⁺ channels like AKT1 [25, 81]. Upon concatenation of multiple ankyrin repeats they form ankyrin repeat domains (ARDs). These domains function as platforms for protein-protein interactions in a variety of cellular processes, amongst others in signaling events [114]. Classically ARDs consist of 4-7 ankyrin repeats [115]. Degeneration in the amino acid composition of the canonical repeat and variation in the number of repeats assures the specificity for the respective interaction and explains the versatility of occurrence of this domain [116-119]. Still there are conserved residues to maintain the structure of the individual repeat (Figure 8) [113, 120, 121].

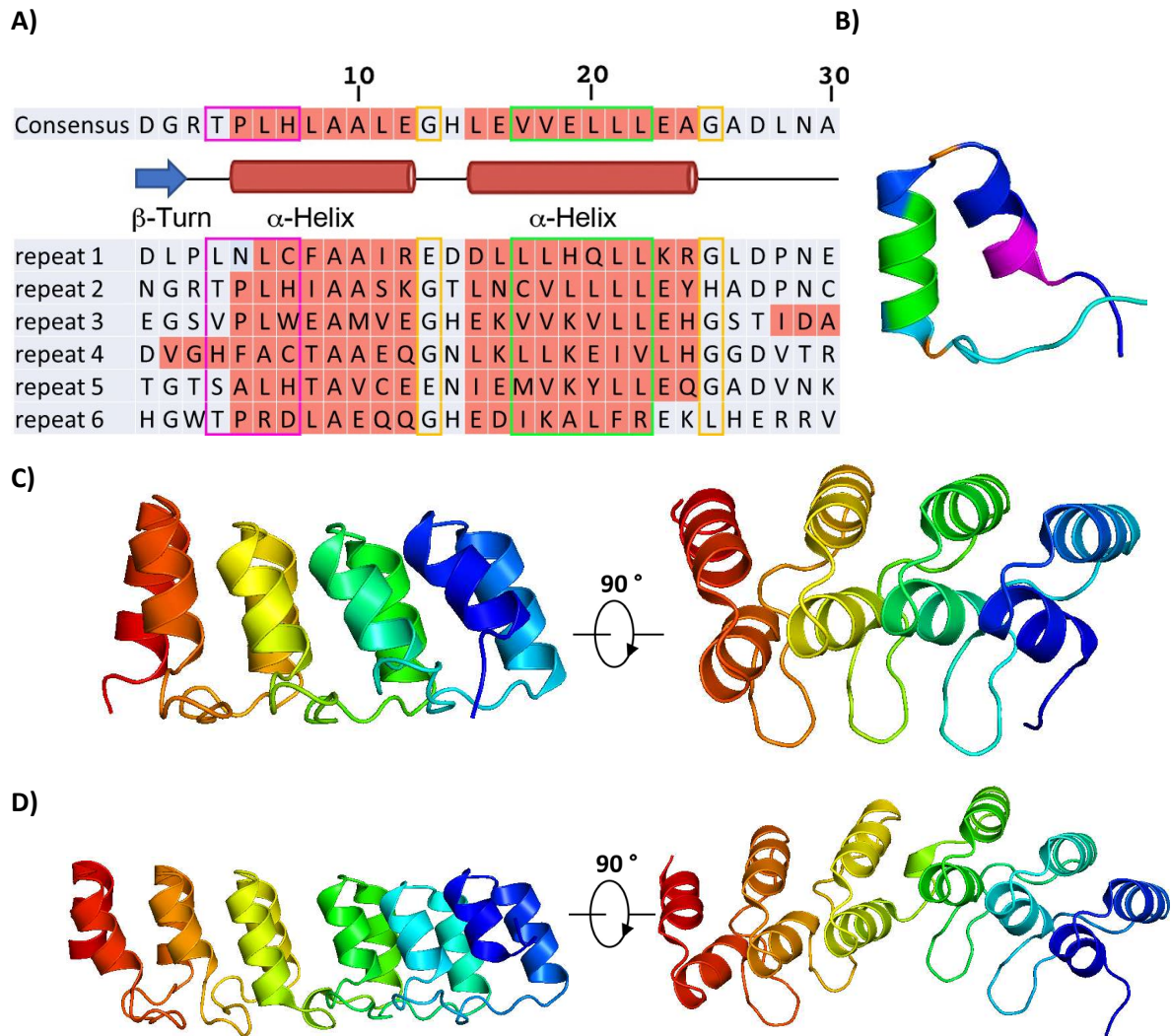


Figure 8: Ankyrin repeat domains. A) Sequence alignment of the eukaryotic ankyrin repeat consensus sequence and the AKT1 ankyrin repeats. The helical regions of the aligned sequences are colored in red. The corresponding secondary structure elements are depicted: blue arrow = β -turn; red cylinders = α -helices, black lines = unstructured loops. The conserved TPLH and VVXLLL motifs are framed in magenta and green respectively. The helix ending glycine residues at positions 13 and 25 are framed in orange. Derived from Jernigan et al. 2014 and Sanchez-Barrena et al. 2020 [113, 119]. B) 3D structure of a consensus sequence based ankyrin repeat. The conserved TPLH and VVXLLL motifs and the helix ending glycine residues at positions 13 and 25 comprise the same coloration as in A). The color gradient from blue to cyan corresponds to the amino acid sequence from N- to C-terminal. C) Designed ankyrin repeat protein consisting of four identical consensus repeats. D) Ankyrin repeat domain of the voltage gated K⁺ channel AKT1 from *A. thaliana*. The color gradient in C) and D) from blue to red corresponds to the amino acid sequence from N- to C-terminal. The structures in B) and C) are derived from Mosavi et al. 2002 (PDB entry 1NOR) [121]. The structure of the ARD from AKT1 is derived from Sanchez-Barrena et al. 2020 (PDB entry 5AAR) [119].

The canonical ankyrin repeat consists of 30 amino acids (Figure 8.A) which comprise a β -turn, two anti parallel α -helices and a loop for the connection with the next repeat [122]. Thereby each ankyrin repeat comprises an L-like shape where the helices form the vertical arm and the loop forms the basis [122]. The tetrapeptide TPLH at position 6-9 (magenta in Figure 8.A and B) of the consensus sequence is highly conserved [113]. It forms the beginning of the first α -helix of the ankyrin motif and contributes to its stability by hydrogen bonding between the threonine OH- group and the histidine imidazole ring [123]. At positions 17-22 the VVXLLL motif, where X* resembles any hydrophilic residue, (green in Figure 8.A and B) forms the main part of the second α -helix. It stabilizes the structure of the ankyrin repeat itself by hydrophobic interactions as well as the global structure of the ARD by interactions with the neighboring repeats [114, 122]. Further two glycine residues are conserved at positions 13 and 25 (orange in Figure 8.A and B), which mark the end of the two helices [122].

The ankyrin repeats assemble in a nearly linear behavior with $\sim 13^\circ$ of curvature [114]. Hence, the more repeats the more concave the overall domain structure becomes (Figure 8.C and D). The non helical part of the ankyrin repeats forms hairpin like structures with a β -turn connecting two neighboring repeats. Thereby the last amino acids of the preceding ankyrin repeat and the first amino acids of the next AR comprise the β -turn and form a β -sheet like structure [116, 122]. The interaction surface of the ARD with other proteins is predominantly formed by this β -turn hairpins, but in some cases the surface of the inner helices can be used for the interaction as well [120].

The 3D structure of the ankyrin repeat domain of AKT1 was resolved as a separate domain [119, 124]. It consists of 6 ankyrin repeats (Figure 8.D). Repeats 1, 2, 4 and 5 follow the canonical structure, while repeats 3 and 6 lack the β -turn and hairpin. For C-terminal ankyrin repeats the lacking loop is common [121], whilst the amino acids that are supposed to form the loop of ankyrin repeat 3 form an additional turn in the first helix of ankyrin repeat 4. Therefore the β -sheet like structure is only formed by 4 instead of 5 hairpins and its surface is more concave compared to the canonical ankyrin repeat domain. Nonetheless the ankyrin repeats can be aligned to the consensus sequence with significant similarities in the conserved regions (Figure 8.A). In contrary to the symmetric architecture of the ARDs in general an asymmetric distribution of charges can be found on the surface of the ARD from AKT1. In detail the basic residues R528, R552 and K561 are found within the first two ankyrin repeats, while the acidic residues D581, E594, E624, E658, E659 and E690 within the third loop and the subsequent repeats contribute to the effect. This structural feature assures the basis for the specificity of the AKT1 channel interaction with its upstream interaction partner CIPK23 [119, 125].

Within the tetrameric AKT1 channel the ankyrin repeat domains neither show interactions with themselves nor with the other cytoplasmic domains of the K^+ channel [80]. In the recently resolved cryo EM structure of the channel the positioning of the ARD in respect to the tetrameric channel remains elusive, but hints were given that they are positioned concentrated on top of the CNBDs when the channel is inactive and move apart to “octopus shaped” tails in the preactivated state [93].

At their very C-terminus plant inward rectifying voltage gated K^+ channels harbor a KHA domain (plant K^+ channel motif rich in hydrophobic and acidic residues) [80, 126]. This amino acid sequence contains two high homology regions where hydrophobic and acidic amino acids are accumulated respectively [127]. These KHA domains function in the assembly and stabilization of the tetrameric K^+ channel by interacting with the CNBD from a neighboring subunit [80, 128]. Upon findings by Daram *et al.* both the area of the C-linker and the CNBD itself was stated to be involved in interactions with the KHA domain [80].

The regulation of AKT1 uptake via the silent shaker subunit AtKC1

For AKT1 two main mechanisms of regulation are known. One way for modulation of the AKT1 activity is its assembly as heterotetramer with the silent shaker subunit AtKC1 [129-131]. AKT1 and AtKC1 share 42,95 % identity within their amino acid sequence (CLUSTAL O (1.2.4) [132] uniprot entry P92960 and Q38998). For AtKC1 a similar domain structure like for AKT1 was proposed. AtKC1 comprises a TMD, a C-linker, a putative CNBD and an KHA motif, but lacks an ARD [93, 133].

AtKC1 is called silent because it is not permeable for K^+ when expressed alone [134]. Upon formation of AKT1:AtKC1 heterotetramers the efficiency of K^+ uptake is diminished compared to the homotetrameric AKT1 channel [134]. In other words, the interaction of AtKC1 with AKT1 results in a shift of the activation potential of the channel to more negative values compared to the homotetramer [79, 135]. For the wildtype channel the half maximal activation potential was determined to -101.7 ± 2.0 mV in *Xenopus* oocytes by voltage clamp experiments. Comparably this value was shifted to -178.2 ± 3.2 mV in the presence of AtKC1 [93]. Regulation of AKT1 by AtKC1 was found to function mainly under low K^+ conditions, meaning 100 μ M or less K^+ in the external medium [135]. AKT1 homotetramers activated by the downstream events of a Ca^{2+} signature show K^+ leakage at low external K^+ concentrations [131]. Hence, the formation of AKT1:AtKC1 heterotetramers may reduce the loss of K^+ under K^+ limiting conditions [129, 131].

The decreased activity of AKT1:AtKC1 channels is in correspondence with the cryo EM structure of the AKT1:AtKC1 heterotetramer. The 3D structure comprises a 2 fold symmetry with high structural similarity compared to the inactive AKT1 wildtype channel (RMDS 2.78 Å over 1753 C α atoms) [93]. The gate of the channel is closed and the C-linkers of the AKT1 protomer comprise the kinked conformation while the AtKC1 protomers exhibit the straight conformation (see Figure 6). Noteworthy the C-linkers of AtKC1 exhibit the straight conformation without the stabilization by the N-terminus, as it was shown for the AKT1 homotetramer (Figure 6.C).

Regulation of AKT1 by phosphorylation via CIPK23

Both AKT1 homo and AKT1:AtKC1 heterotetramers are under the control of a further regulation mechanism, namely of the phosphorylation of AKT1 by CIPK23 [129, 136]. CIPK23 (CBL interacting protein kinase 23) is a member of a protein kinase family that comprises 26 proteins in *A. thaliana* [137]. Together with their upstream activators the CBLs, the CBL interacting protein kinases form a complex phosphorylation network within the plant [137]. Under low K^+ conditions, as a response to a Ca^{2+} signature, CIPK23 itself gets activated by interactions with the Ca^{2+} sensors CBL1 or 9. Thereby CIPK23 can activate its downstream target AKT1, as well as HAK5 for K^+ uptake in the plant roots [70, 71]. AKT1 can be activated by the CIPK23 kinase domain alone, while HAK5 activation by CIPK23 requires the full sized kinase protein [138, 139]. For AKT1 its ankyrin repeat domain (ARD) was found to be the interaction platform for CIPK23 [119], while HAK5 lacks an ARD and gets phosphorylated at its N-terminus [139]. Hence the interaction sites of CIPK23 differ between its targets and no specific CIPK interaction domain is known [140].

The crosstalk between the ARD and CIPK23 was found to be essential for the AKT1 channel activation [138, 141]. Thereby the ARD functions as a docking platform for CIPK23 to bring the kinase in the right position for the phosphorylation of the AKT1 channel. The importance of AKT1 phosphorylation by CIPK23 for channel activity was shown in a variety of two electrode voltage clamp experiments in *Xenopus* oocytes. If the AKT1 channel is expressed in absence of CIPK23 no currents were measured [141]. Phosphorylation at the serine residues S26 (cytosolic N-terminus) and S338 (kink between C-linker helices B and C) were found to be the essential for AKT1 function. Mutations to alanine, hence the abolishment of the potential phosphorylation site, significantly impair K^+ currents while the creation of phosphomimetic mutants resulted in a constitutively active channel. The phosphorylation of the homotetrameric AKT1 is accompanied by a symmetry rearrangement from a 2 fold symmetry towards a 4 fold symmetry [93]. Further phosphorylation sites within the ARD at S714 and S716 (KHA domain) were found to be essential for full activation of the AKT1 channel (Kudla unpublished).

Besides the activation of AKT1, a negative impact on the channel activity was found to be comprised by CBL10. Not only does the Ca^{2+} binding protein reduce AKT1 mediated currents in *Xenopus* oocytes experiments, but it was also found to compete directly with CIPK23 for AKT1 binding. Thereby CBL10 can impair AKT1 K^+ uptake and act as negative regulator independently of a CIPK protein kinase [142].

The CBL interacting protein kinase CIPK23

CIPK23 is a serine/threonine protein kinase

The catalytic domains of CIPKs follow the canonical serine/threonine kinase fold [125, 143]. Serine/threonine kinases comprise a large family of protein kinases and are present in all three domains of life [144]. In their catalytic center they transfer a phosphate group from ATP to the oxygen of a serine or threonine sidechain (Figure 9.A) [143, 145]. This phosphorylation process is known to be essential for a broad variety of signaling processes in cells, from cell proliferation, programmed cell death to reactions to biotic and abiotic stress in plants [145-147].

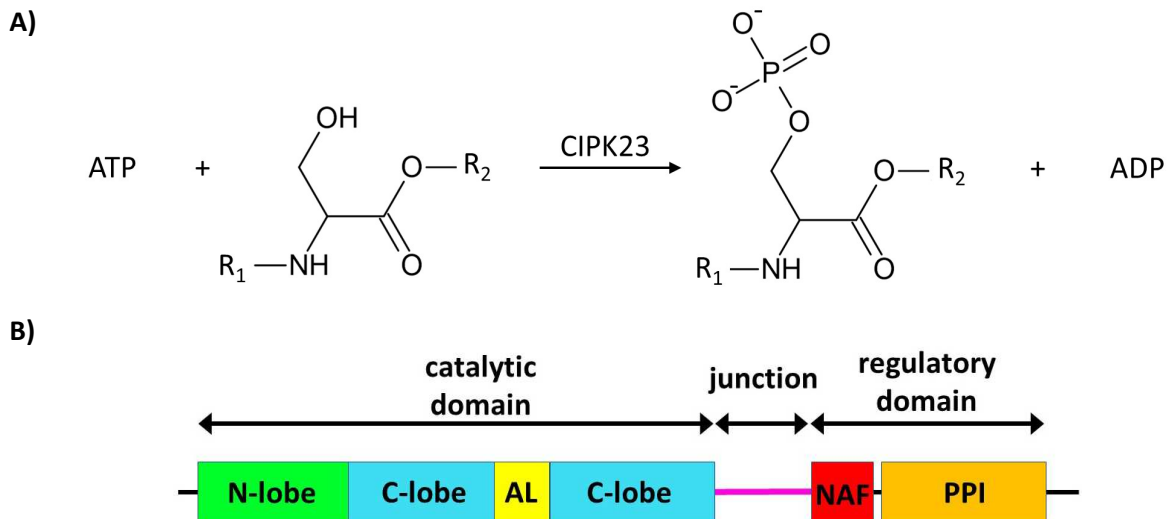


Figure 9: CBL interacting protein kinases as members of the serine/threonine kinase family. A) Phosphorylation reaction of a serine sidechain by the serine/threonine kinase CIPK23. A phosphate group is transferred from an ATP molecule to the oxygen of a serine sidechain. B) Schematic representation of the domain structure of a CIPK proteins. The catalytic domain comprises the classical structure of the serine/threonine proteases.

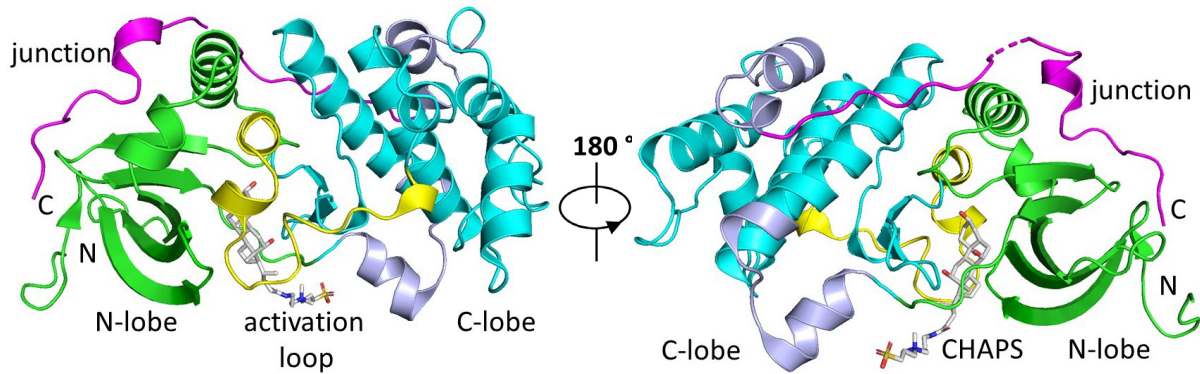
Both auto and trans-phosphorylation events can be comprised by this class of protein kinases. The trans-phosphorylation events are complex as both upstream and downstream interaction partners can be phosphorylated by CIPK proteins [140, 148]. Differing from other serine/threonine protein kinases [143, 145], CIPKs rather use Mn^{2+} than Mg^{2+} as cofactor for the coordination of phosphate groups of the ATP substrates [148].

CIPK proteins can be subdivided into two domains, the N-terminal catalytic domain and the C-terminal regulatory domain (Figure 9.B). The catalytic domain accomplishes the phosphorylation and consists of the N- and C-lobe (green and cyan respectively) as well as the activation loop (yellow). The C-terminal regulatory domain comprises the NAF domain (red), also known as FISL motif (named after the predominant amino acids N, A, F, I, S and L), and a PPI (protein phosphatase interaction) motif (orange) [149, 150]. While the catalytic domain contains the ATP and substrate binding site, the NAF domain is responsible for the interaction with CBL proteins and the PPI domain represents the interaction site for PP2C-type phosphatases [151]. The two domains are connected by a junction (magenta).

Structural insights into CBL interacting protein kinases

In order to understand the interactions between CIPK23 and its phosphorylation target AKT1, as well as its own activation by CBL 1 or 9, insights into CIPK protein structures are necessary. So far no 3D structure of a full length CIPK protein has been resolved, but the partial structures of the CIPK23 catalytic domain and the CIPK24 regulatory domain are known (Figure 10) [125, 152].

A)



B)

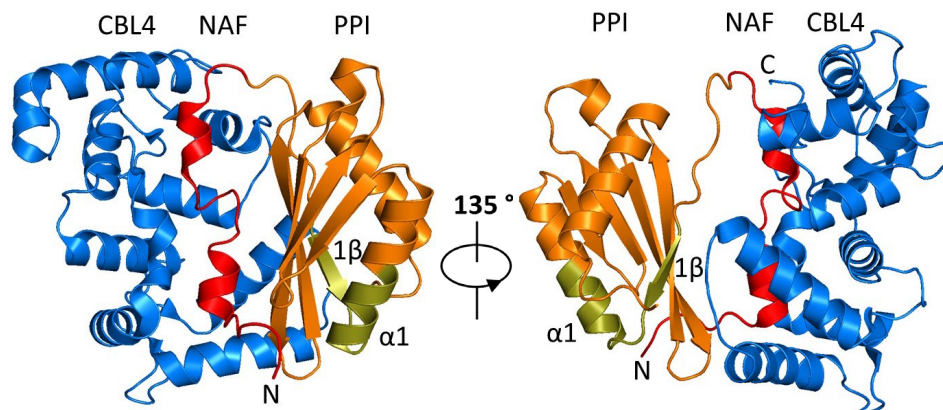


Figure 10: Structure of CIPK proteins. A) Crystal structure of the CIPK23 kinase domain (PDB 4CZT [125]). B) Crystal structure of the CIPK24 regulatory domain in complex with CBL1 (PDB 2EH8 [152]). The color coding of the 3D structures resembles the coloration scheme in Figure 9.B. N-lobe = green, C-lobe = cyan, activation loop = yellow, junction = magenta, AKT1 interaction site = grey, NAF domain = red, PPI domain = orange, CBL4 blue, phosphatase interaction site = olive. In A) the co-crystallized CHAPS molecule in the active site is depicted as white sticks and the ARD interaction surface is colored in grey. In B) the phosphatase interaction site is colored in olive and CBL4 is depicted in marine.

The resolved structure of the CIPK23 catalytic domain resembles the open/ inactive state of the kinase and can be divided into two lobes (Figure 10.A) [148]. The N-lobe comprises a β -sheet consisting of 6 β -strands and two α -helices, while the C-lobe is a predominantly α -helical coil. This C-lobe was determined as the interaction surface for the ankyrin repeat domain of AKT1 by molecular dynamics simulation experiments. Surface residues of the C-lobe, facing away from the active site, comprise electrostatic interactions (Figure 10.A grey) together with the concave site of the ARD. Acidic residues within the ARD (E624 E658, E659; see section “The Ankyrin Repeat Domain”) were found to be essential for AKT1 activation by CIPK23 [119]. The cavity between the N- and C-lobe comprises the ATP, metal ion and substrate binding site and the activation loop connects the N- and C-lobe. In the crystal structure the cavity is partially occupied by a CHAPS molecule and a short helical turn of the activation loop [125]. Hence the N- and C-lobes are moved away from each other to prevent ATP and substrate binding (Figure 10.B).

The junction that connects the catalytic and regulatory domain was found to be essential for the kinase activity as well [149, 153]. It comprises an extended non structured polypeptide chain with a short α -helical turn. This peptide attaches to the surface of the catalytic domain and reaches from the C to the N-lobe where it interacts with the long helix and the β -sheet by conserved hydrophobic interactions [125]. This is not a crystallization artifact but a common feature for stabilization of the helical structure within the C-lobe [154, 155].

Based on the crystal structures of the regulatory domain of CIPK14 and 24, the NAF/ FISL motif was found to comprise two amphipathic helical segments with an interconnecting loop [152, 156]. In the inactive state of the kinase, the NAF motif has an autoinhibitory function by interacting with the kinase domain [150]. It was found that for CIPK23 the position of the co-crystallized CHAPS is naturally occupied by the NAF domain [125]. In the crystal structure of the CIPK24 regulatory domain, the NAF domain is bound by CBL4 (Figure 10.B). This hints towards a kinase activation by structural rearrangements of the NAF domain. The specificity of each CBL-CIPK interaction was found in amino acid variations within the NAF loop [157]. Generally the CBL-CIPK complex is preliminary stabilized by hydrophobic interactions between the CBL and the NAF domain, as well as between the CBL and the PPI domain [152].

The PPI domain comprises the interaction platform for PP2C phosphatases, in case of CIPK23 the phosphatase AIP1 [138]. The crystal structure of the CIPK24 regulatory domain shows the PPI domain as a β -sheet that consists of 5 β -strands and two α -helices [152]. The phosphatase binding is comprised by β -strand 1 and the α -helix 1 of the PPI domain (Figure 10.C olive). The amino acids within the β -strand 1 and the α -helix 1 are highly conserved and relevant for phosphatase binding, while the amino acids within the interconnecting loop are more variable. Hence these residues can be responsible for CIPK-phosphatase specificity [152]. Due to the proximity of the CBL and phosphatase interaction surfaces and hence possible steric hindrances the binding of a phosphatase to the PPI or the binding of a CBL to the NAF motif may exclude the binding of the other at the same time [137, 152].

Regulation of the CIPK kinase activity

CIPK23 was found to be intrinsically inactive and needs activation in order to confer phosphorylation towards its targets [125, 149]. Two modes of activation are known (Figure 11). In general, the relative positions of the two lobes in respect to each other change between the open/inactive to the closed/active state. The short helical turn of the activation loop and the NAF domain get released and thereby ATP and substrate binding is enabled [125].

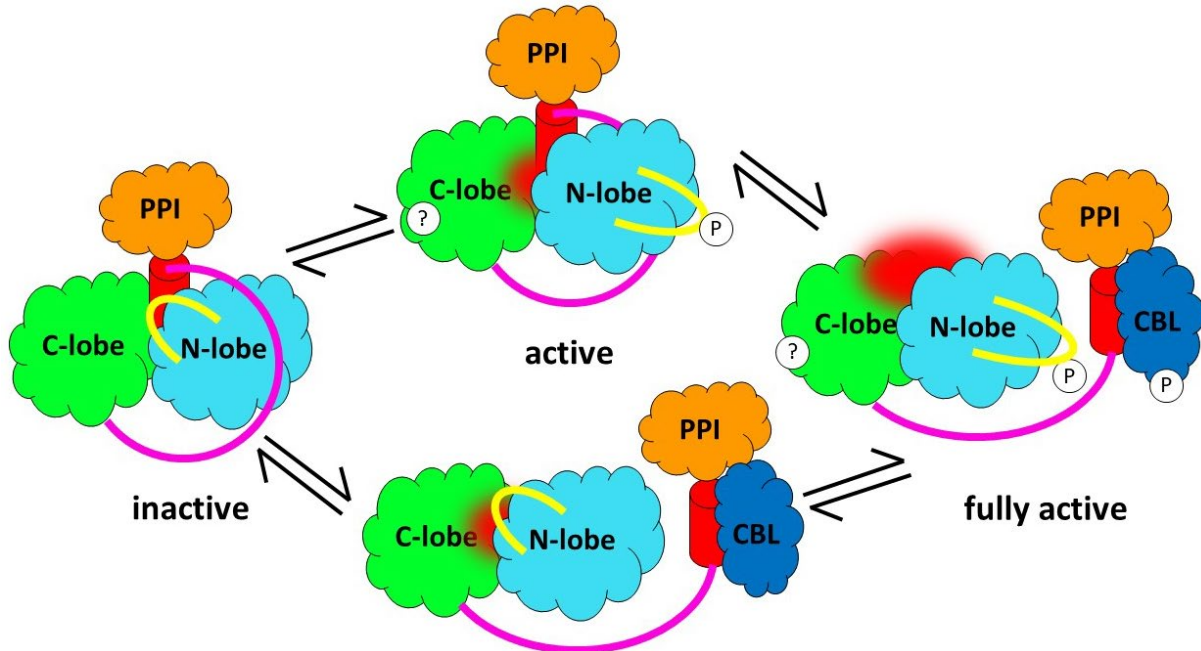


Figure 11: Schematic representation of CIPK23 activation mechanisms. In the inactive state both the activation loop (yellow) and the NAF domain (red) occupy the active site of the kinase. Both phosphorylation of the activation loop or CBL binding contribute to the activation of the kinase domain. Additive effects on the kinase activity can be achieved when both modes of activation come together for full activation of the kinase. For CIPK9 and 24 additional phosphorylation at the C-lobe was stated to further promote kinase activity [153, 158]. As well, the CBL can be phosphorylated by the CIPK to promote the stability and activity of the CBL-CIPK complex [125, 148]. The color coding resembles the coloration scheme in Figure 9.B. N-lobe = green, C-lobe = cyan, activation loop = yellow, junction = magenta, NAF domain = red, PPI domain = orange, CBL4 blue, phosphorylation sites (P) = white.

The first activation mechanism is the activation by phosphorylation [159, 160]. The residues S176, T190 and Y197 in the CIPK23 activation loop are conserved for CIPK activation loops in general [125]. Hence these amino acids comprise potential phosphorylation sites for CIPK23 [125]. In general phosphorylation of this loop results in conformational changes that open the active site of the kinase for substrate binding [161]. But so far the kinase that creates this phosphorylation has not been identified [149, 162]. Recently, hints were given towards a protein kinase named MPK6 [146], which is known to be involved in responses to abscisic acid release [163]. Besides the trans-phosphorylation, autophosphorylation within the C-lobe was found to be important for the activity of CIPK9 or 24 [153, 158], while for CIPK23 so far nothing is stated. The phosphorylation of the activation loop hints towards an alternative, CBL and Ca^{2+} signature independent activation mechanism for CIPKs [149, 159].

The NAF motif of the regulatory domain comprises the second point of regulation for CIPKs. Upon CBL4 binding to the CIPK24 NAF motif, it is no longer accessible for interactions and inhibition of the kinase domain (Figure 10.C) [149, 152]. Hence, the binding of a CBL to the NAF domain promotes the activation of the kinase. For the CIPK23-CBL1/9 complex it was found, that also CBL1 and 9 have conserved phosphorylation sites at their C-terminus [148]. While the phosphorylation does not affect the CBL protein itself, the stability of the CIPK-CBL complex is enhanced and the kinase activity promoted [164]. This phosphorylation was found to be essential for the AKT1 activation by the CBL-CIPK complex [148].

The opening of the active site for substrate binding and kinase activity can be both achieved by phosphorylation of the activation loop and by interaction with the CBL. Each mechanism alone has shown to promote the activity of CIPKs, but additive effects are stated when both mechanisms come together [125].

Phosphorylation is an essential but reversible process. The dephosphorylation is classically comprised by phosphatases [165]. The negative regulation of CIPKs by phosphatases can be comprised by different mechanisms. Here again a highly complex interaction network arises, since each phosphorylation site gets removed by a different phosphatase. For CIPK24 it is stated that upon binding of the phosphatase ABI2 to the PPI site, the kinase activity is inhibited [151], while CIPK6 is directly inhibited by interactions of the phosphatase PP2CA with the kinase domain [166]. For CIPK9 the autophosphorylation gets removed by yet another phosphatase (AP2C1) [158]. The PP2C phosphatase AIP1 is known as interaction partner for CIPK23. They interact via the PPI domain of CIPK23. AIP1 is also known to directly dephosphorylate the AKT1 channel. The phosphatase might use CIPK23 as a scaffold to come in contact with AKT1 and inhibit the channel activation via the CIPK-CBL pathway. [138].

The calcineurin B-like proteins CBL1 and 9

So far it has only been mentioned that CIPKs are activated by CBLs. Together with the CBL interacting protein kinases they form a highly complex but yet specific interaction network [47, 51, 137, 167]. In case of the AKT1 activating CIPK23, the interaction partners are CBL1 and 9 [50]. In different interaction studies it was shown that CBL1, 2, 3, 5 and 9 can interact with CIPK23 [50, 141], while only CBL1 or 9 in complex with CIPK23 can activate the K⁺ channel AKT1 [51, 141]. CBL1 and 9 share a sequence identity of 89.67 % (CLUSTAL O (1.2.4), uniprot entry O81445 and Q9LTB8 [132]).

CBLs are prominent Ca²⁺ sensors in plants, that are the initiation point in deciphering the Ca²⁺ signatures like the increasing Ca²⁺ concentrations in *A. thaliana* roots upon K⁺ deprivation [47] (see “Ca²⁺ signaling in plants as initial response to nutrient deprivation”). CBLs received their name from the significant structural similarity with the mammalian Ca²⁺ sensor calcineurin B [168, 169]. They comprise 10 members in *A. thaliana* [137].

The EF hand Ca^{2+} binding motif

With the discovery of Ca^{2+} signatures the question arises how these changing Ca^{2+} concentrations in the cytosol are translated into downstream events like the pore opening of the AKT1 channel. The recognition of changing Ca^{2+} concentrations by CBLs is accomplished by a Ca^{2+} binding motif [44]. The EF hand motif was first found in the crystal structure of parvalbumin. It comprises a helix-loop-helix motif, with the helices named E and F [170]. Classically, EF hands come in pairs and cluster together to form EF-lobes. Thereby the EF hands are separated by a conserved number of amino acids [171, 172]. The loop that connects the E and F helices comprises the binding site for one Ca^{2+} ion. Some EF hand proteins were found to bind Mg^{2+} or Mn^{2+} as well [173-176]. The binding motif comprises 12 amino acid residues of which 6 are involved in Ca^{2+} binding (Figure 12.A). The coordinates $\text{X}^*\text{Y}^*\text{ZG-YI-X}^{**}\text{-Z}$ are assigned to these 6 amino acids. The variable intermediate amino acids are labeled as *, while position 6 and 8 are occupied by conserved glycine (G) and isoleucine (I) residues respectively [177].

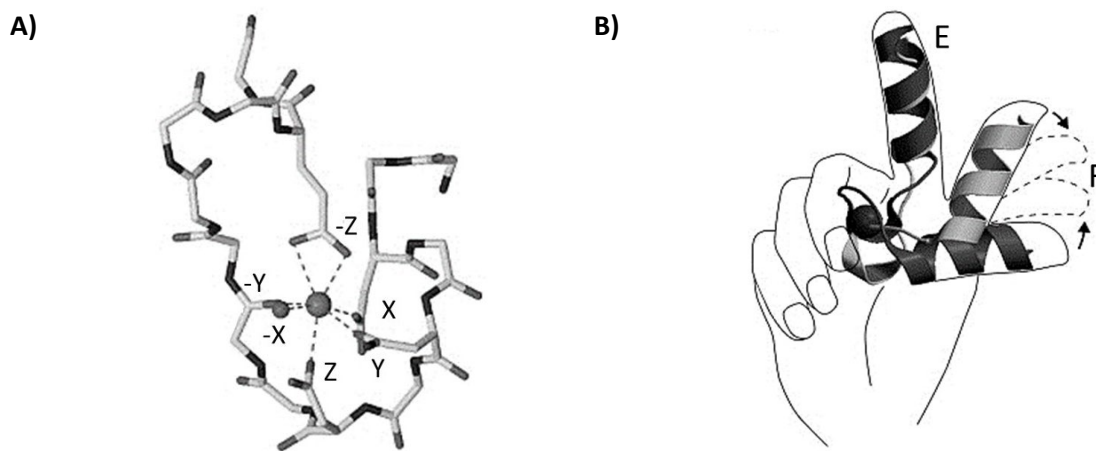


Figure 12: The EF hand Ca^{2+} binding motif. A) Stick representation of an EF hand Ca^{2+} binding loop. The coordinates X, Y, Z, -Y, -X and -Z are labeled accordingly. At the X, Y, Z and -Z the Ca^{2+} is coordinated by the amino acid sidechains, while at the -X a water molecule (small grey sphere) comprises the interaction. At the -Y coordinate the carbonyl oxygen of the peptide backbone further stabilizes the Ca^{2+} . B) Cartoon representation of an EF hand. Upon Ca^{2+} binding the EF hand conformation changes from the closed (grey) to the open (dark grey) state. Extracted from Lewit-Bentley et al. 2000 [177]

Ca^{2+} is coordinated in a classical bipyramidal pentagonal geometry [177]. In the consensus sequence the X and Y positions are occupied by aspartate (D) or asparagine (N), while at the Z position an aspartate (D) asparagine (N) or serine (S) is located. At the -Y position, not the sidechain, but the carbonyl oxygen of the peptide backbone is involved in the coordination of Ca^{2+} and at the -X position a water molecule is provided [178]. The -Z coordinate is essential for Ca^{2+} binding and occupied by a glutamate (E). Alterations in this amino acid position are known to impair Ca^{2+} binding [179, 180]. Upon Ca^{2+} binding, helix F moves away from the E-helix and the EF hand switches between the closed (Ca^{2+} free) and the open (Ca^{2+} bound) hand (Figure 12.B) [177].

Calcineurin-B like proteins

CBLs comprise a conserved core domain of four EF hands with an invariant number of amino acids in the spacing regions that separate the EF hands. The ratio between canonical and non canonical EF hands differs for the 10 CBL proteins from 2 to 0 (Table 2) [171]. Noteworthy EF hand 1 deviates from the canonical sequence in all known CBLs, but still was found to bind Ca^{2+} . It comprises 14 amino acids instead of 12 ($\text{X}^{***}\text{Y}^*\text{ZG-YI-X}^{**}\text{-Z}$) [176, 181]. Differing from the consensus sequence of a canonical EF hand the consensus sequence for EF hand 1 in CBLs comprises a serine (S) at position X, two additional amino acids inserted between the X and Y position, an isoleucine (I) at position Y and an aspartate (E) at position Z. Meanwhile the -Y, -X and -Z positions are in correspondence with the canonical sequence, as well as the glycine residue that is conserved between the Z and -Y coordinate and the isoleucine between the -Y and -X coordinate [137].

Table 2: Features of *Arabidopsis thaliana* CBL proteins. Their N-terminal domains, the number of canonical EF hands and their subcellular localization are listed [137, 182].

	N-terminal domain	canonical EF hands	Localization
CBL1	short	2	plasma membrane
CBL2	long	0	tonoplast
CBL3	long	0	tonoplast
CBL4	short	0	plasma membrane
CBL5	short	0	plasma membrane
CBL6	long	1	tonoplast
CBL7	long	1	cytosol/nucleus
CBL8	short (lipidation site degenerated)	0	cytosol/nucleus
CBL9	short	2	plasma membrane
CBL10	long (1 putative TM segment)	1	tonoplast plasma membrane

CBLs can be divided into two subgroups. The first subgroup comprises a rather short N-terminal domain (43-48 amino acids). This N-terminus harbors lipid modification sites (MGCXXS/T motif) for membrane association of the CBLs [137, 140]. CBL1, CBL4, CBL5, CBL8 and CBL9 can be assigned to this group [137]. All members of this subgroup were found to be located to the plasma membrane, except for CBL8. CBL8 is localized in the cytosol and the nucleus, since its lipid modifications site is degenerated [137, 183]. These lipid modifications consist of a myristoylation at the N-terminal methionine and S-acylation of cysteine at position 3 [184]. For other N-myristoylated Ca^{2+} binding proteins a calcium-myristoyl switch mechanism is stated [179], but this is not the case for CBLs [137]. Still the myristoylation was found to be necessary for the CIPK24 kinase activation by CBL4, but not for membrane association of CBL4 [185]. For CBL1 these lipid modifications were found to be essential for its localization the plasma membrane and hence its function to activate AKT1 *in vivo* [184].

The second subgroup does not comprise myristoylations, but an extended N-terminal domain similar to K^+ channel interacting proteins (KCHIP) [137]. CBL2, CBL3, CBL6, CBL7 and CBL10 can be assigned to this subgroup. Thereby CBL2, 3, 6 and 10 are tonoplast associated, while CBL7 is located to the cytosol and nucleus [137, 183]. CBL10 comprises a special role in this group, since it does not only contain a large N-terminal domain, but a putative single transmembrane segment as a membrane anchor [183]. While one study stated a tonoplast association for CBL10 [137], another study showed CBL10 to be located to the plasma membrane [182]. All together the different N-termini, the varying compositions of the EF hands and the accompanying different Ca^{2+} affinities as well as the different subcellular localizations result in unique characteristics for each CBL protein and hence specific signal transduction in response to a Ca^{2+} signature [137].

Insights into the 3D structure of calcineurin-B like proteins

In the structures of CBL2 and 4 the EF hand domains were both found as globular domains with their four EF hands arranged in two EF lobes that are located to the surface on one site of the protein (Figure 13.A) [176, 181]. The EF-lobes are stabilized by hydrophobic interactions. In detail the adjacent Ca^{2+} binding loops form short antiparallel β -sheets between the sidechain of the -Y coordinate (isoleucine) and the conserved isoleucine that is located between the -Y and -X coordinate of the adjacent EF loop [176]. This interaction between the two EF-loops hints towards a cooperativity for their Ca^{2+} binding. Experimental prove is still pending but cooperativity has already been proved for other EF hand proteins [186-188].

On the opposing site a large hydrophobic crevice can be found where the C-terminus of the CBL protein is located. Upon CIPK binding the NAF motif binds to the hydrophobic crevice (Figure 13.B). While the structures align with an RMSD of 1.122 Å over 140 C_α atoms, CBL4 still undergoes significant structural rearrangements. The loop between the F1 and E2 helices as well as the helices F3 and E4 together with their interconnecting loop are moved to make place for the NAF domain [152].

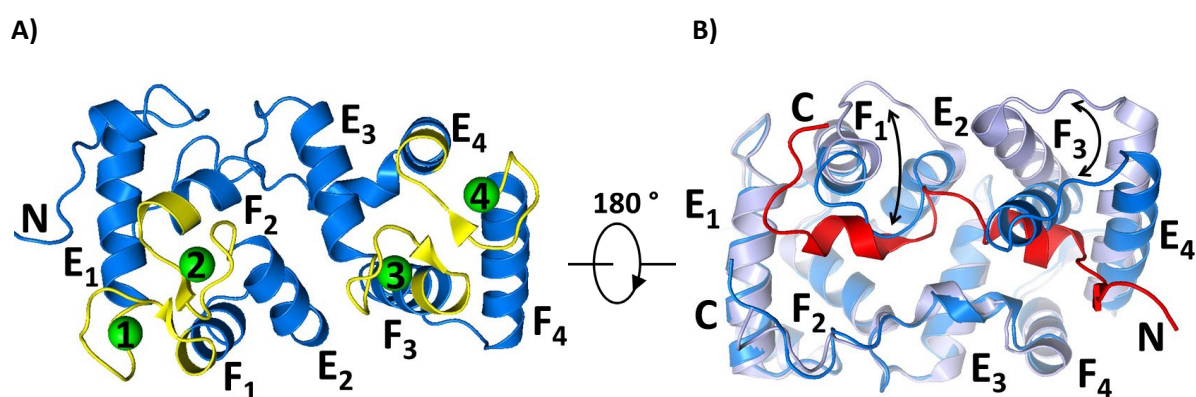


Figure 13: The calcineurin-B like protein CBL4. A) Representation of CBL4 in the free state (marine). All four EF hands 1-4 (yellow) are occupied with Ca^{2+} (green spheres). The yellow triangles within the EF loops represent the short stabilizing β -sheets. B) Representation of the NAF binding crevice on the opposite site of the EF hands in the free (marine) and CIPK24 bound state (light blue). In the CIPK24 bound state the NAF motif is bound to the crevice and the structural rearrangements are marked by black arrows. The structures are derived from Sanchez-Barrena et al. 2005 [176] and 2007 [152] (PDB entry 1V1G and 2EHB).

So far Ca^{2+} binding data for CBLs is only available for CBL2 and 4. The number of bound Ca^{2+} can differ for the CIPK associated and free states. The crystal structure of CBL2 comprises two Ca^{2+} ions in the EF hands 1 and 4, while in the CBL2-CIPK14 complex Ca^{2+} can be found in all four EF hands [156, 181]. The other way around, CBL4 was found to crystallize with Ca^{2+} ions bound to all four EF hands in the free state. When the protein was exposed to a 1:1 mix of CaCl_2 and MnCl_2 EF hand 4 was occupied by a Mn^{2+} in the crystal structure, coordinated in the same bipyramidal pentagonal way as Ca^{2+} . The Mn^{2+} binding was not a crystallization artifact since Mn^{2+} binding to CBL4 could be further confirmed by thermal melting experiments. Either way the CBL4 ion binding capability is reduced to the binding of two Ca^{2+} ions to EF hand 1 and 4 in the complex with its interacting kinase CIPK24 [152, 176]. Further CBL4 dimerization upon increasing Ca^{2+} concentrations was proposed, while Mn^{2+} or Mg^{2+} did not have an influence on the CBL4 oligomeric state [176].

The regulation of the voltage gated K⁺ channel AKT1

Both CBL 1 and 9 are located to the plasma membrane where they sense increasing Ca²⁺ concentrations and there upon recruit CIPK23 to the plasma membrane as well. This brings the kinase in proximity to both the high and low affinity K⁺ uptake system HAK5 and AKT1 [139, 141, 189]. Upon phosphorylation of the channels, CIPK23 itself as well as the C-terminus of the CBL1 or 9 the K⁺ uptake is activated [60, 73, 139, 148].

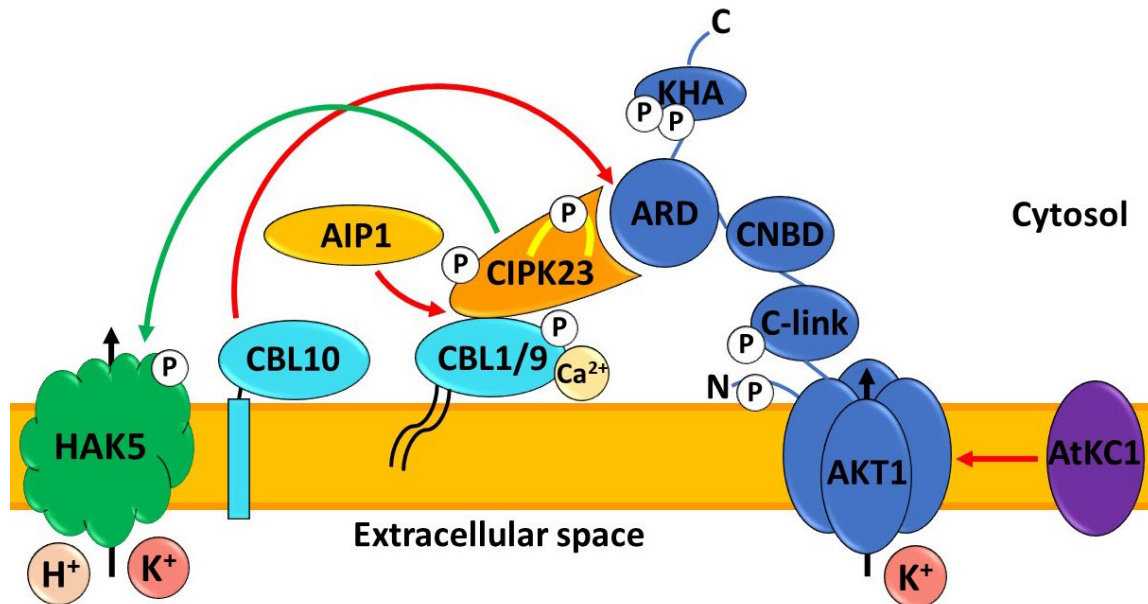


Figure 14: The regulation mechanisms of K⁺ uptake in *A. thaliana*. Upon Ca²⁺ signatures CBL1 and 9 (cyan) are activated by Ca²⁺ binding. Thereby they bind to CIPK23 (orange) and activate its kinase activity towards the CBL1/9 C-terminus, presumably itself, as well as its downstream targets AKT1 (blue) and HAK5 (green). The known phosphorylation sites are marked by white circles. The kinase that mediates phosphorylation of the CIPK23 activation loop (yellow) is not known. Upon phosphorylation the K⁺ uptake gets induced. The AKT1-CIPK23-CBL1/9 complex can be negatively regulated by different mechanisms. Heterotetramer formation with AtKC1 (purple) reduces K⁺ uptake. CBL10 (cyan) directly competes for the AKT1 interaction with CIPK23. For dephosphorylation the PP2C phosphatase AIP1 (honey) binds to CIPK23, thereby impairs CBL1/9 binding and can dephosphorylate both CIPK23 as well as AKT1.

Other factors lead to reduced or impaired AKT1 channel activity. On the one hand the formation of heterotetramers with AtKC1 shifts the activation potential significantly to more negative values [129]. The other point of negative regulation is CIPK23. CBL10 can directly compete with CIPK23 for the interaction with AKT1 and prevent binding and activation of AKT1 by the CBL1/9-CIPK23 complex. Thereby CBL10 does not require the interaction with a CIPK [142]. Further the PP2C phosphatase AIP1 can bind to CIPK23 and thereby impair CBL binding and dephosphorylate both the kinase and the AKT1 channel [136].

Aim of Studies

Potassium ions (K^+) are an essential macronutrient in plants and hence the understanding of its uptake mechanisms into the plant, is a topic of high interest. One of the components involved in K^+ uptake from the soil is the voltage gated K^+ channel AKT1 from *A. thaliana*. In 2018 the precise mechanisms for the activation and regulation AKT1 were not fully understood. Therefore this study aimed for the structural and functional analysis of the components involved in K^+ uptake, namely the channel AKT1 itself as well as its activating kinase CIPK23 and the Ca^{2+} sensor proteins CBL1 and CBL9. In a variety of *in planta* and *Xenopus* oocyte experiments these components were already shown to be essential for AKT1 mediated K^+ uptake [138, 141, 148].

The functional expression of the AKT1 channel had already been postulated in *S. cerevisiae* [81]. As well the expression host *E. coli* had been established for the overexpression of the AKT1 ankyrin repeat domain (ARD) [124], the catalytic domain of CIPK23 [125] and the full sized CBLs (CBL2 and 4) [190, 191]. Additionally, wheat germ cell free expression approaches were found to yield in functional full sized CIPK23 [148]. On the basis of these findings, the first aim of this thesis was the optimization of the expression conditions and the establishment of subsequent purification procedures for all four proteins. While the isolation of the full sized proteins was preferred, as well the expression and purification of the cytosolic domains of AKT1 was attempted.

After the successful isolation of the proteins, the second aim of this thesis was the determination of the 3D structures of the full sized AKT1 channel as well as full sized CIPK23 and CBL1/9. Initial success for the resolution of the 3D structures of the AKT1 ARD [119, 124], the catalytic domain of CIPK23 [125] and CBL proteins 2 and 4 [125, 181] by crystallization served as a basis for further attempts. Since the crystallization of membrane proteins can be challenging, additional trials by cryo EM should be attempted, as this was shown to be successful for the AKT1 related channel Eag1 [87]. Besides the resolution of the single components, cryo EM is a popular method for the structural determination of protein complexes as well [192]. Hence, the analysis of the AKT1-CIPK23-CBL1/9 activation complex was of interest as well.

The third aim of this thesis was to analyze interactions of the isolated AKT1, CIPK23 and CBL1/9 by biophysical methods like isothermal titration calorimetry (ITC) and surface plasmon resonance (SPR). Thereby the thermodynamic and kinetic parameters of interactions of the AKT1 channel with CIPK23, CBL1/9 and the CIPK23-CBL1 and CIPK23-CBL9 complexes should be determined. Additionally the determination of the Ca^{2+} affinities for CBL1 and CBL9 are of high interest to improve the understanding how the Ca^{2+} signatures are translated into downstream activation of the AKT1 channel.

Chapters

- Chapter 1 The voltage gated K⁺ channel AKT1 from *Arabidopsis thaliana*
Heterologous expression and purification of the voltage gated K⁺ channel AKT1 from *A. thaliana*
- Chapter 2 The CBL interacting protein kinase CIPK23
Expression and Purification trials of CIPK23 from *A. thaliana*
- Chapter 3 The calcineurin-B like protein 1
Calcium binding of AtCBL1: first structural and functional insights
To be submitted

Chapter 1 – The voltage gated K⁺ channel AKT1 from *Arabidopsis thaliana*

Title: Heterologous expression and purification of the voltage gated K⁺ channel AKT1 from *A. thaliana*

Authors: Alexandra Bork and Lutz Schmitt

Own proportion of this work: 90 %

Cloning

Expression of full size AKT1 in *E. coli*

Expression, membrane preparation and test solubilization from
S. cerevisiae

Expression and purification of AKT1 single domains

Cell free expression and purification

Preparation of figures

Writing of the manuscript

Heterologous expression and purification of the voltage gated K⁺ channel AKT1 from *A. thaliana*

Abstract

Potassium (K⁺) is an essential nutrient in plants. As the K⁺ concentration in the soil is comparably lower than in the plant cell cytosol, the uptake has to be performed against the concentration gradient. One of the proteins involved in the K⁺ uptake in *A. thaliana* is the voltage gated shaker channel AKT1. In this study different expression and purification attempts to isolate the functional channel were made. At first the expression of the full length channel in both *E. coli* and *S. cerevisiae* was attempted. Here only in *S. cerevisiae* protein could be produced. By expression as GFP-fusion protein, AKT1 was shown to be located in the plasma membrane, but could not be solubilized from the membranes. Attempts to express and purify the cytosolic domains of AKT1 in *E. coli* resulted in the formation of inclusion bodies. In this study no suitable refolding conditions could be found. Lastly by wheat germ lysate based cell free expression the isolation of full length AKT1 could be archived. Altogether it was shown that AKT1 needed an eucaryotic expression host for successful expression and could only be purified from a cell free environment.

Introduction

Mineral nutrients are essential for plant viability and growth. Amongst others the mineral potassium (K⁺) is one of the most abundant cations within a cell's cytosol and vacuole [1, 2]. Thereby it serves as a main player in the regulation of the osmotic pressure, the membrane potential and is involved in charge compensation as well as enzymatic activation [3-5]. While in the soil the K⁺ concentration is in the range 0.1 to 1 mM, the cytosolic concentration is with 100 – 200 mM a hundred to a thousand times higher [6]. Hence, to keep the cytosolic K⁺ concentration stable, the ion uptake has to be performed against its concentration gradient.

In *Arabidopsis thaliana* (*A. thaliana*) several membrane channels and transporters are known to be involved in the K⁺ uptake in root cells under low K⁺ conditions. Amongst them are the members of the HAK/KUP/KT and voltage gated Shaker-like channel family [7]. The high affinity uptake is mainly facilitated by the K⁺/H⁺ symporter HAK5 at external K⁺ concentrations below 10 μM [8, 9], while at higher concentrations the low affinity inward rectifying K⁺ channel AKT1 starts to contribute to K⁺ uptake and becomes the main player at concentrations above 500 μM [5, 10].

The functional AKT1 channel exists as a tetramer [11]. Each AKT1 monomer consists of a transmembrane domain (TMD), as well as the cytosolic cyclic nucleotide binding domain (CNBD) and a C-terminal ankyrin repeat domain (ARD) and KHA (plant K⁺ channel motif rich in hydrophobic and acidic residues) domain [6]. While the transmembrane domain classically consists of 6 transmembrane segments, the pore of the channel is formed by the loop between segment 5 and 6 upon tetramerization. The transmembrane segment 6 is linked via a C-linker to the CNBD. Upon cyclic nucleotide binding the CNBD modulates its conformation. This movement is transmitted via the C-linker to the TMD, hence the opening of the pore [12]. For AKT1 cGMP was found to modulate the channel activity [13]. The CNBD is connected to the ARD, which consists of 6 ankyrin repeats, a conserved motif for protein-protein interaction. In case of AKT1, the ARD confers specificity to its interaction partner CIPK23 [14], but has no influence on the channel function itself [15]. Lastly the C terminal KHA domain, which mainly harbors hydrophobic and acidic amino acids, can be found in AKT1 [16]. It is thought to contribute to interactions between the protomers and the stabilization of the tetramer [17, 18].

The activation of AKT1 is facilitated by a complex signal transduction pathway. Upon K⁺ deprivation the activity of AKT1 gets upregulated by phosphorylation. Therefore Ca²⁺ functions as second messenger, as it is recognized by the calcineurin-B like Ca²⁺ sensor proteins CBL1 and CBL9. These lipid anchored CBLs activate their downstream target, the CBL interacting protein kinase CIPK23. CIPK23 is a serine/threonine protein kinase, which upon CBL binding gets activated and recruited to the plasma membrane. There the kinase binds the ARD of AKT1 and upon phosphorylation at the N-terminus (S26 [11]), the C-linker (S338 [11]) and within the KHA domain (S714, S716 Kudla unpublished) promotes AKT1 activity [6]. The PP2C type phosphatase AIP1 was identified as a counterplayer of CIPK23. Upon dephosphorylation AIP1 reverses the effect of CIPK23, but the precise interaction so far remains elusive [15]. Further downregulation or inactivation of AKT1 is facilitated by formation of heterotetramers with the silent shaker α -subunit AtKC1 [19, 20], while a complete inhibition is achieved by Ba²⁺ ions [21].

In this study the main aim was to express and purify the full length AKT1 channel for structural and functional analysis. Therefore expression and purification attempts of full length AKT1 in *E. coli*, *S. cerevisiae* as well as in a cell free environment were performed. Additional trials to isolate the cytosolic CNBD and ARD+KHA domain from *E. coli* inclusion bodies were attempted. Whilst at the starting point of this project only the 3D structure of the ARD was solved [14, 22], recently the cryo EM structure of the TMD and CNBD of AKT1 was published by Lu *et al* 2022 [11].

Material and Methods

Cloning

In this study the expression of AKT1 full length and the single domains (CNBD: aa 287 – 500, ARD: aa 518 – 857*¹) was attempted in different expression hosts (*E. coli*, *S. cerevisiae* and cell free expression). All sizes for the resulting proteins were calculated with the ProParam online tool [23].

FX cloning

The expression from plasmid was attempted for the full length AKT1 and the AKT1 cytosolic domains in *E. coli* and additionally for the full length protein in *S. cerevisiae*. The respective expression plasmids were generated by FX cloning [24]. The *S. cerevisiae* codon optimized *akt1* gene (GenScript) from *A. thaliana* was fully or partially amplified by PCR with the respective primer pairs (for AKT1_{full length}: AKT1-FX fw and rev; for CNBD: AKT1-CNBD-FX fw and rev; for ARD: AKT1-ARD-FX fw, AKT1-FX rev) listed in Table S1. The primers were designed via the FX-cloning webpage [25]. For the amplification the Q5[®] HF Polymerase (NEB) was used according to the manufacturer's instructions. The FX plasmid backbones used in this study and their features are described in Table S2. The resulting plasmids were verified by sequencing (Microsynth). The plasmids with the p7XC3H, p7XNH3 and pBXC3H, pBXNH3 backbones were used for transformation of *E. coli* C41 (DE3) and *E. coli* Rosetta (DE3) pLysS according to standard protocol, while the plasmids with the pYEXNH3, pYEXNHG3, pYEXC3H, pYEXC3GH backbones were used for transformation of *S. cerevisiae* Δ PP.

¹ This construct will further be named ARD, but contains the sequence of the ARD and the C-terminal KHA domain as well.

pRE5 cloning

For the expression of full length AKT1 from *S. cerevisiae* genome the *S. cerevisiae* codon optimized *akt1* gene from *A. thaliana* was cloned into pRE5 backbone (GenScript). The pRE5 plasmid was originally created by Robert Ernst, encoding for a his5+ auxothrophy marker, the PDR5 promoter, an N-terminal 14xHis-tag and about 40 bp long 5' and 3' sequences for homologous recombination into the *pdr5* locus of the *S. cerevisiae* Δ PDR5prom Δ PDR5 strain (further named Δ PP) [26]. As the 3' region for homologous recombination was missing in this construct (pRE5-AKT1), it was inserted via Q5® Site-Directed Mutagenesis following the manufacturer's instructions (NEB) and using the primers AKT1_Cterm_homReg_fw and rev. In addition, a TEV cleavage site was inserted using primers TEV-AKT1 fw and rev listed in Table S1. The resulting plasmid pRE5-14His-TEV-AKT1 was verified by sequencing (Microsynth).

Transformation and homologous recombination into Δ PP genome

For homologous recombination of the AKT1 expression cassette into the *S. cerevisiae* Δ PP genome the pRE5-14His-TEV-AKT1 plasmid was cleaved with the restriction enzymes *Apal* and *SbfI* (both NEB) according to the manufacturer's instructions and the cleavage was controlled on a 1 % (w/v) agarose gel.

For *S. cerevisiae* Δ PP transformation, initially 50 ml YP medium (20 g/L Tryptone/Peptone from Casein, 10 g/L yeast extract) supplemented with 2 % (w/v) glucose was inoculated to an OD₆₀₀ of 0.2 from an overnight 5 ml preculture. When an OD₆₀₀ of 0.5-0.7 was reached the cells were harvested at 4000 g for 15 min at 4 °C, washed with 10 ml sterile ddH₂O, again centrifuged at 4000 g for 5 min at 4 °C and resuspended in 2 ml sterile ddH₂O. 100 μ l of those cells were transferred to a sterile Eppendorf tube and supplemented with 300 μ l transformation master mix. This sterile master mix consisted of 240 μ l PEG 4000 (50 % w/v), 36 μ l 1M LiAc, 5 μ l carrier ssDNA (Sigma) and 20 μ l ddH₂O. 50 μ l of the 14His-TEV-AKT1 expression cassette or 2.5 μ g plasmid DNA were added and the transformation mix was incubated for 40 min at 42 °C. The cells were then harvested for 5 min at 700 g, resuspended in 100 μ l sterile ddH₂O and plated on -His drop out agar plates (homologous recombination; -His for selection of *S. cerevisiae* Δ PP with genomically integrated *akt1*) or -Ura-Trp drop out agar plates (plasmid transformation; -Ura for plasmid selection, -Trp for *S. cerevisiae* Δ PP selection). The plates were incubated at 30 °C for at least 2 days until colonies were visible. The precise composition of the *S. cerevisiae* drop out media were derived from the doctoral thesis of Robert Ernst [26].

Colony PCR

For verification of the correct insertion of the AKT1 expression cassette into the *S. cerevisiae* Δ PP genome a colony PCR was performed. To do so, a colony was picked from the transformation plate and used to inoculate 5 ml YPD overnight culture. The cells were harvested the next day and the genomic DNA was isolated using the Quick DNA fungal/bacterial miniprep kit (Zymo Research). The PCR was performed with the Q5® HF Polymerase (NEB) using the genomic DNA or the pRE5-14His-TEV-AKT1 plasmid (positive control) as template according to the manufacturer's instructions. The primers: 5' homologous region fw, 3' homologous region rev (Table S1) were used and the presence of PCR products was visualized on a 1 % (w/v) agarose gel with MIDORIGreen Xtra DNA stain (NIPPON Genetics).

pIVEX cloning

To create a suitable vector for cell free expression of full length AKT1, at first the *akt1* gene was amplified from the pRE5-AKT1 vector using the pIVEX1.4 and pIVEX1.3 AKT1 fw and rev primers mentioned in Table S1. Thereby *Sma*I and *Nco*I cleavage sites were introduced at the 5' and 3' end respectively and the gene was then cloned into the pIVEX1.4 or pIVEX1.3 vector (Biotech Rabbit) coding for a N-terminal 6xHis tag and a factor Xa cleavage site or a C-terminal 6xHis tag respectively. The plasmids were verified by sequencing (Microsynth).

Small scale Expression

Test expression in *E. coli*

Full length AKT1 as well as the CNBD and ARD domain were expressed under control of the T7 and araBAD promoter in *E. coli* Rosetta (DE3) pLysS. The full length AKT1 was as well tested in *E. coli* C41 (DE3). A clone was picked to inoculate 50 ml of LB medium supplemented with 50 µg/ml kanamycin (p7XC3H and p7XNH3 plasmids) or 100 µg/ml ampicillin (pBXC3H and pBXNH3 plasmids) and 36 µg/ml chloramphenicol (pLysS) to an OD₆₀₀ of 0.05. The cells were cultivated in a baffled flask and grown at 37 °C with 180 rpm shaking until an OD₆₀₀ of 0.5. For the induction of the expression either 0.5 mM IPTG (p7XC3H and p7XNH3 plasmids) or 0.01 % (w/v) L-arabinose (pBXC3H and pBXNH3 plasmids) was used. Cell samples corresponding to 1 OD equivalent were taken directly before induction and at 1 h, 2 h, 3 h and 16 h (on = over night) after induction. The expression was analyzed by SDS-PAGE (10 % gels) and subsequent Coomassie staining (50 % (v/v) Methanol, 10 % (v/v) acetic acid, 1 g/L Coomassie® G250 Brilliant blue (Serva)). Additionally Western blotting for protein detection via its 10xHis tag was performed using pentaHis monoclonal primary antibody (mouse) (Qiagen) and α-mouse-HRP coupled secondary antibody (Jackson Immuno Research) according to standard protocols.

Inclusion body test

After the test expression in *E. coli* Rosetta (DE3) pLysS, the cytosolic domains (CNBD and ARD) of AKT1 were tested for the formation of inclusion bodies. To do so, a cell pellet of a 50 ml overnight expression was harvested and resuspended in 10 ml buffer (50 mM Tris pH 8.0, 150 mM NaCl) supplemented with cOmplete® EDTA free protease inhibitor tablet (Roche). The cells were lysed by three rounds of 1 minute sonication at 50 % power with 2 min intermediate cooling on ice. The soluble fraction was separated from the cell debris, membranes and potentially present inclusion bodies by ultracentrifugation at 122000 g, 4 °C for 30 min. Samples for SDS-PAGE were taken from the supernatant (AS) and the cell debris pellet (CD) and analyzed as described above.

Small scale expression in *S. cerevisiae* ΔPP

The expression of full size AKT1 in *S. cerevisiae* ΔPP was tested from pYEXNHG3, pYEXNH3 and pYEXC3GH and pYEXC3H plasmids (Table S2) as well as after homologous recombination into *S. cerevisiae* ΔPP genome (N-terminally 14xHis-tagged). 50 ml -Ura -Trp DO medium [26] for plasmid expression or YPD for expression from genome was inoculated to an OD₆₀₀ of 0.2 and incubated in a baffled flask at 30 °C. In case of the plasmid transformed cells, the expression was induced at an OD₆₀₀ of 0.5 with sterile 2 % (w/v) galactose solution and the cells were harvested after incubation for further 16 h under the previous conditions. For subcellular localization of AKT1, cells expressing the N- or C-terminally 10xHis-GFP-tagged proteins were analyzed by fluorescence microscopy subsequent to the test expression (CAi). The expression from the *S. cerevisiae* ΔPP genome took place under the constitutive Pdr5 promoter. Hence no induction was necessary and the cells were harvested when an OD of 1.0 was reached.

Before analysis on a SDS PAGE 2 OD equivalents of *S. cerevisiae* ΔPP cells (after plasmid and genomic expression) were harvested, washed with sterile ddH₂O and resuspended in 1 ml ddH₂O. For breakage of the cells, 150 µl yeast extraction buffer (1.85 M NaOH, 7.5 % (v/v) β-Mercaptoethanol) was added and incubated for 10 min on ice. The precipitation of the proteome was performed by adding 150 µl 50 % (w/v) TCA. The samples were again incubated on ice, before centrifugation at 14000 g for 10 min at 4 °C. The pellet was washed twice in 50 µl 1 M Tris pH 8.0. The final pellet was resuspended in 60 µl 2.5x SDS loading dye and 10 µl of this were loaded on the SDS gels. The SDS-PAGE and subsequent blotting was performed as described before. The yeGFP fusion constructs were additionally analyzed for the detection of the GFP fluorescence using the blue fluorescence channel of the Amersham Imager 680.

Large scale expression:

... in *E. coli*/Rosetta (DE3) pLysS

For large scale expression of the CNBD and ARD domains, 2 l LB medium in a 5 l baffled flask was supplemented with 100 µg/ml ampicillin (pBXNH3 plasmids) and 36 µg/ml chloramphenicol (pLysS) and inoculated from an overnight culture to a starting OD₆₀₀ of 0.1. The cells were grown at 37 °C shaking at 180 rpm until an OD₆₀₀ of 0.5 - 0.8 was reached. The expression was then induced with 0.1 % (v/v) L-arabinose and shaken at 180 rpm and 37 °C or 25 °C for further 3 h. In an alternative expression approach of the ARD from p7XNH3 plasmid, the culture was grown in 2YT medium (16 g/l Tryptone/Peptone, 10 g/l yeast extract, 5 g/l NaCl) at 37 °C supplemented with 50 µg/ml kanamycin and 36 µg/ml chloramphenicol (pLysS) and cooled down in the incubator to 16 °C before induction with 0.5 mM IPTG. The expression was performed for 16 h over night at 16 °C.

Either way the cells were harvested by centrifugation at 6500 g for 30 min at 4 °C. The cell pellets were washed with resuspension buffer (50 mM Tris pH 8.0, 150 mM NaCl) and centrifuged again for 10 min at 4000 g at 4 °C. The resulting cell pellets were frozen in liquid nitrogen and stored at -80 °C until further use.

... in *S. cerevisiae* ΔPP from plasmid

For large scale expression of full length AKT1 from pYEXNHG3 and pYEXC3GH plasmids (N- or C-terminally 10xHis-yeGFP-3C tagged) 50 mL -Ura -Trp DO [26] precultures were inoculated in baffled flasks and incubated at 30 °C and 180 rpm overnight. For the expression cultures 1 L -Ura -Trp DO medium in a 5 L baffled flask was inoculated to an OD₆₀₀ of 0.1. The cells were cultivated at 30 °C and 180 rpm until an OD₆₀₀ of 0.4 was reached. For the induction of the expression 2 % (w/v) sterile galactose solution was added and the temperature was lowered to 25 °C. After 16 h the cells were harvested at 5500 g at 4 °C for 30 min. The pellet was washed with ddH₂O and again centrifuged at 5500 g at 4 °C for 15 min. Afterwards the pellet was frozen in liquid nitrogen and stored at -80 °C until further use.

... in *S. cerevisiae* ΔPP from genome

In case of the large scale expression of AKT1 from genome with N-terminal 14xHis-TEV tag, the cells were grown in YPD medium. 100 ml preculture were inoculated and grown overnight at 30 °C at 180 rpm and used to inoculate 1 l medium to an OD₆₀₀ of 0.05. The cells were grown at 25 °C for 18 h at 200 rpm. When an OD₆₀₀ of 1.5 was reached 100 ml boost medium (50 g/l yeast extract, 100 g/l tryptone peptone from casein) were added and the cells were harvested as described above when an OD₆₀₀ of 3.5 was reached.

Purification from *E. coli*

Purification of the ARD from soluble fraction via IMAC

A cell pellet from a 2 l 2YT culture was resuspended in 50 ml buffer (50 mM Tris pH 7.5, 150 mM NaCl) supplemented with 1 cOmplete Protease-Inhibitor tablet (Roche), 1 mg DNase and 1 mM MgCl₂ before lysis by three rounds of sonication at 50 % power for 1 minute with 2 minutes cooling on ice in between. 30 mM Imidazole was added to the lysed cells and the lysate was clarified by ultracentrifugation at 160000 g at 4 °C for 1 h. The cleared lysate was applied onto a Ni²⁺ loaded and buffer equilibrated HiTrap 5 ml Chelating HP column. The column was washed with 50 ml buffer (50 mM Tris pH 7.5, 150 mM NaCl, 30 mM Imidazole) and bound protein was eluted in 2 ml fractions by applying an imidazole gradient from 30 – 400 mM over 50 ml. Washing with 400 mM Imidazole was continued for further 25 ml before 50 mM EDTA were added to strip Ni²⁺ ions and remaining protein off the column. The protein concentration was determined with a NanoDrop One (Thermo Scientific).

Inclusion body preparation

For the preparation of ARD or CNBD inclusion bodies the previously produced *E. coli* Rosetta (DE3) pLysS cell pellet was resuspended in buffer (50 mM Tris pH 7.5, 150 mM NaCl, 1 mM DTT) supplemented with 1 cOmplete Protease-Inhibitor tablet (Roche), 1 mg DNase and 40 mM MgCl₂ and 5 μM Pepstatin-A. Cell lysis was performed by three rounds of 1 min sonication at 50 % power with 2 min cooling on ice in between. The lysate was centrifuged for 30 minutes at 26000 g. The supernatant was discarded and the pellet was washed in 40 ml of wash buffer (50 mM Tris pH 7.5, 150 mM NaCl, 50 mM EDTA, 1 % (v/v) Triton-X-100, 1 mM DTT), centrifuged for 30 min at 26000 g, washed in 40 ml wash buffer (without Triton-X-100) and centrifuged again for 30 min at 26000 g.

To solubilize the protein from the inclusion bodies, the pellet was resuspended and incubated under stirring at 4 °C for 18 hours in buffer (50 mM Tris pH 7.5, 150 mM NaCl, 1 mM DTT) containing 6 M guanidine hydrochloride or urea [27]. The solvate was centrifuged for 30 minutes at 160000 g and 4 °C (45Ti rotor) to clarify the protein solution. The supernatant was either frozen in liquid nitrogen or submitted to dialysis directly to remove the chaotropic agent from the protein solution and to enable refolding of the target protein. 10 ml of the unfolded protein, adjusted to 2-3 mg/ml, were filled into a dialysis pipe (Spectra/Por® 1 Dialysis Membrane Standard RC Tubing MWCO: 6-8 kDa) and dialyzed against 1 L buffer (50 mM Tris pH 7.5, 150 mM NaCl) for 18 hours at 4 °C. The dialysate was centrifuged for 30 minutes at 20000 g and 4 °C to remove aggregated protein.

SEC Purification of AKT1 domains

The dialyzed and centrifuged protein solution was loaded onto a SEC column (Superdex200 10/300 or HiLoad Superdex75 26/600 pg (Cytiva)) preequilibrated with buffer (50 mM Tris pH 7.5, 150 mM NaCl) at a flow rate of 0.4 ml/min or 2 ml/min respectively at 10 °C. The eluted protein fractions were collected and concentration was determined using a NanoDrop One. Throughout the whole purification procedure SDS samples were taken and analyzed on 10 % SDS gels as described before.

S. cerevisiae ΔPP membrane preparation

The preparation of *S. cerevisiae* ΔPP membranes was performed after the same procedure for both cells that have expressed AKT1 from plasmid or after genomic integration. The thawed cell pellet was resuspended in 80 ml buffer (50 mM Tris pH 8.0, 300 mM KCl) supplemented with 5 mM EDTA, 5 μM Pepstatin-A and cOmplete EDTA free protease inhibitor tablet (Roche). The *S. cerevisiae* ΔPP cells were mixed with 300 g glass beads and disrupted in a bead mill by 6 runs of 1 min each with 1 min break in between. The beads were washed twice with buffer and the suspension was transferred to

centrifugation. The low spin was performed two times at 1500 g for 15 min at 4 °C followed by 2 times centrifugation at 5000 g for 15 min at 4 °C (Beckmann JA10 rotor). The supernatant was then submitted to high spin centrifugation at 20000 g for 1 h at 4 °C (Beckmann JA25-50 rotor). The membrane pellet was resuspended and homogenized in a potter tube with buffer (50 mM Tris pH 8.0, 300 mM KCl, 20 % (v/v) glycerol). The membrane samples were adjusted to a concentration of 10 mg/ml total protein and flash frozen in liquid nitrogen until further use. Throughout the whole membrane preparation procedure samples were taken and analyzed by SDS PAGE and Western blotting as described before. For the eGFP fusion constructs the gels were additionally analyzed for the detection of the GFP fluorescence using the blue fluorescence channel of the Amersham Imager 680.

Test solubilization

In order to find a detergent suitable for solubilization of AKT1 from the *S. cerevisiae* ΔPP membranes, different detergents were screened (Table S3 and S4). 160 µl thawed membranes were mixed with either 40 µl detergent stock (CMC 2 %) or 20 µl detergent stock and 20 µl buffer (CMC 1%). The samples were incubated for 1 h at 8 °C and 650 rpm and subsequently centrifuged at 88.000 g for 25 min at 4 °C. 80 µl of the supernatant were mixed with 20 µl SDS loading dye and analyzed by dot blot on a nitrocellulose membrane. 3 µl sample were applied to the membrane. After drying the membrane over night, the treatment was the same as for a standard Western blot. The presence of AKT1 was detected via a pentaHis primary antibody (Qiagen). The most promising samples were additionally submitted to SDS-PAGE analysis and subsequent Western blotting for verification of the integrity of full length AKT1.

Cell free expression and Purification of AKT1

Cell free Expression

In order to express the *akt1* gene in a continuous exchange cell free (CECF) environment the RTS 100 wheat germ kit (biotech rabbit) was chosen. The cell free gene expression was performed according to the manual at 24 °C for 16 h with 900 rpm shaking. 2.5 µg plasmid DNA (pIVEX1.4 AKT1 or pIVEX1.3 AKT1) were used and both reaction and feeding solution were supplemented with either 1 % (w/v) Brij35, Triton-X-100 or Sucrose Monododecanoate.

Purification of AKT1 from Cell free expression

After the expression in the presence of 1 % (w/v) Brij35, the 50 µl reaction solution was centrifuged at 138000 g for 30 min at 4 °C to remove potentially aggregated protein. The supernatant of the ultracentrifugation step was then submitted to IMAC purification using 10 µl preequilibrated (50 mM Tris pH 8.0, 150 mM NaCl, 0.05 % (w/v) Brij35) magnetic beads (Qiagen). For binding, the suspension was incubated for 30 min in an overhead rotor. Afterwards the beads were washed with 3 times 100 µl buffer. For elution of the protein, 50 µl buffer supplemented with 150 mM Imidazole was added to the beads and incubated for 30 min in an overhead rotor. This was repeated 4 times and the protein concentrations of the elution fractions were determined using a NanoDrop One. Protein containing fractions were pooled and concentrated to 50 µl using an Amicon Ultra-0.5 centrifugal filter concentrator with a 30 kDa cutoff membrane (Millipore) and centrifuged at 138000 g for 20 min at 4 °C for the removal of potential aggregates.

The concentrated protein solution (50 µl) was further purified using SEC. The sample was applied at a flow rate of 0.04 ml/min to a Superdex200 increase 3.2/100 column (GE), which was pre-equilibrated with SEC buffer (50 mM Tris pH 8.0, 150 mM NaCl and 0.05 % (w/v) Brij35). The eluted protein fractions were collected in a microtiter plate and the concentration was determined using a NanoDrop One as described above. Throughout the whole purification procedure SDS samples were taken and analyzed on 10 % SDS gels as described above.

Results

AKT1 expression in *E. coli*

A first step towards the structural and functional analysis of a protein is the determination of a suitable host organism for its expression. Initially for the *A. thaliana* potassium channel AKT1, *E. coli* as one of the most common expression hosts, was chosen. AKT1 expression was attempted under two different promoter systems (T7 and araBAD) as well as two different *E. coli* strains. *E. coli* C41 (DE3) is specified for over expression of toxic proteins[28]. *E. coli* Rosetta (DE3) pLysS is specified for the expression of eukaryotic proteins containing codons rarely used in *E. coli* [29] and the pLysS plasmid encodes for the T7 lysozyme, hence ensures suppression of T7 basal expression. Despite the different tags, promoters, strains tested and the fact that the test expression was conducted twice from freshly transformed cells, AKT1 could not be expressed in detectable amounts in *E. coli* (Figure S1). Hence an eucaryotic expression host was tested next.

AKT1 expression and membrane preparation in *S. cerevisiae* ΔPP

The FX cloning technique allows fast cloning of a gene into a variety of expression vectors for different expression hosts. Besides the *E. coli* plasmids that did not result in expression of AKT1, expression vectors for *S. cerevisiae* were created and used for transformation of *S. cerevisiae* ΔPP. Here AKT1 expression with a N- or C-terminal 10xHis-tag alone (99.4 kDa), or in combination with yeGFP (126 kDa) was tested under Gal1 promoter (Figure 1.A-C) and the *in vivo* GFP fluorescence was visualized by microscopy (Figure 1.D and E).

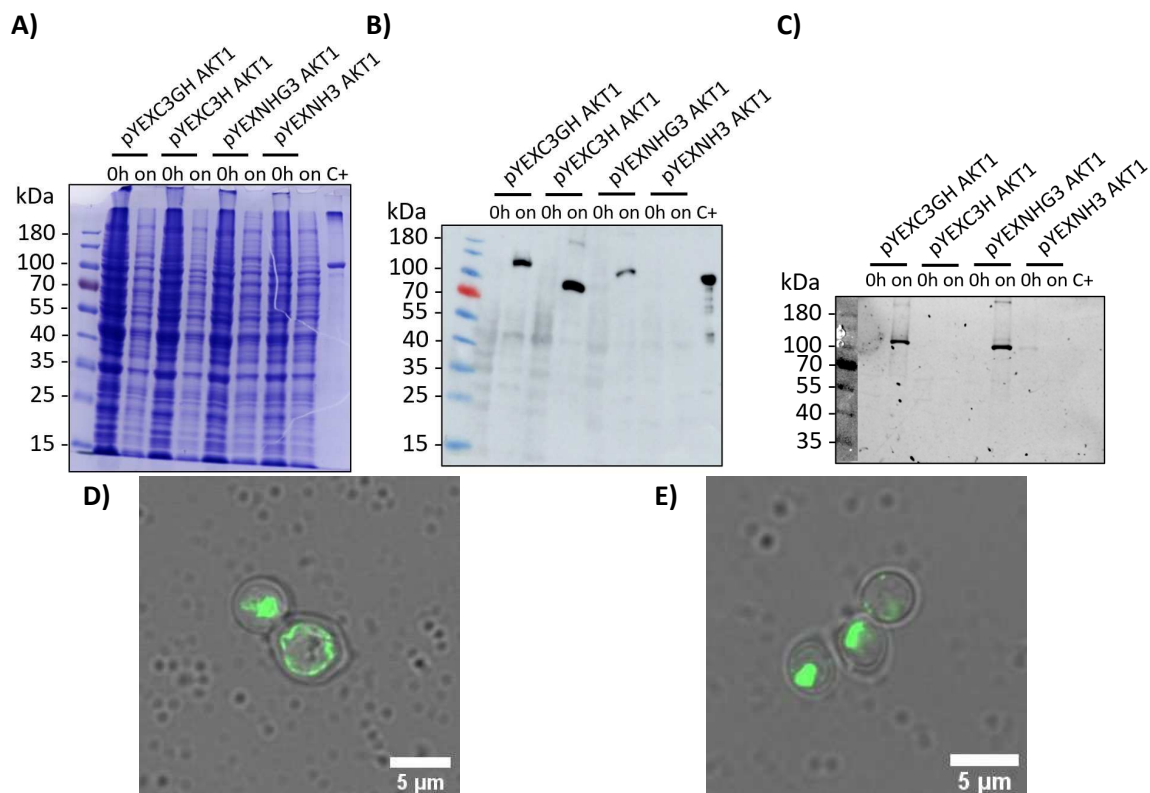


Figure 1: Test expression of AKT1 in *S. cerevisiae* ΔPP. The whole cell samples before induction (0h) and after 16 h overnight expression (on) were loaded onto 10 % SDS gels and analyzed by Coomassie staining (A), Western blot using pentaHis primary antibody, α-mouse-IgG-HRPO-coupled secondary antibody and detection by luminescence with an exposure time of 80 sec (B) as well as in case of the GFP fusion constructs in-gel GFP measurement (C). The expression was tested under Gal1 promoter with N- (pYEXNH3) or C-terminal 10xHis tag (pYEXC3H) or N- (pYEXNHG3) or C-terminal 10His-yeGFP-tag (pYEXC3GH). The expression was induced with 2 % (w/v) galactose. The expression took place in -Ura -Trp DO medium at 30 °C. As positive control (C+) for the Western blotting purified and His tagged NisB protein was used. Additionally, the GFP fusion constructs were analyzed towards their subcellular localization by confocal fluorescence microscopy N-terminal 10xHis-yeGFP tagged (D) or C-terminal 10xHis-GFP tagged AKT1-GFP fusion construct (E).

The expression of AKT1 in *S. cerevisiae* was shown to be successful for the C-terminally 10xHis and 10xHis-yeGFP tagged as well as the N-terminally 10xHis-yeGFP tagged AKT1. Only the N-terminally 10xHis tagged AKT1 construct showed no expression in the two test expression experiments (Figure 1.A-C). With the help of confocal fluorescence microscopy, it could be further shown that both the N- and C-terminally 10xHis-yeGFP tagged versions of AKT1 were expressed with a functionally folded GFP in *S. cerevisiae* Δ PP membranes. While the N-terminally tagged protein was visualized in the plasma membrane, the C-terminally tagged AKT1 resided mainly in the inner compartments, most likely ER or vacuole (Figure 1.D and E).

In a next step the preparation of AKT1 membranes was attempted. Membranes of *S. cerevisiae* Δ PP cells expressing either the N- or the C-terminally 10xHis-yeGFP tagged AKT1 were prepared (Figure S2 and S3), despite the fact that the C-terminally tagged AKT1 was mainly located in inner compartments. In case of the membrane preparation from cells expressing the N-terminally tagged 10xHis-yeGFP-AKT1 (126 kDa) no signals at the respective size could be detected in the Western blot at all (Figure S2.1), not even for whole cells. Whilst for the membrane preparation of cells expressing the C-terminally tagged AKT1-yeGFP-10xHis, the full length protein could only be detected in whole cells (Figure S2.2). The in gel GFP measurements showed signals at 126 kDa for the final membrane pellets for both constructs, but as these signals were not His-positive on the Western blot, they were not assigned to AKT1-GFP fusion proteins.

At this point it was assumed that AKT1 was degraded as soon as the cells were disrupted, despite the fact that protease inhibitors were added throughout the membrane preparation procedure. Noteworthy, KCl was used in all buffers of the membrane preparations. K^+ ions are known to form the highly insoluble potassium dodecylsulfate in presence of sodium dodecylsulfate (SDS). SDS was present in the loading dye of the KCl containing SDS-PAGE samples. Therefore, the SDS detergent, that was supposed to keep the proteins in an unfolded but soluble form, was precipitated. In an additional membrane preparation of the N-terminally 10xHis-yeGFP tagged AKT1, KCl was exchanged for NaCl to prevent this effect and exclude that the missing signals were caused by the lack of functional detergent in the SDS samples. This did not lead to the desired result. Neither the Western blot (empty; not shown) nor the Coomassie gel or in-gel GFP showed a signal for the full length AKT1 fusion construct at 126 kDa (Figure S3).

Despite the fact that the preparation of AKT1-GFP membranes did not succeed, still the N-terminally His-GFP tagged protein was shown to be located in the plasma membrane (Figure 1D and 1E). GFP is a rather bulky tag that, no matter if N- or C-terminal, might have an influence on the proteins functionality. Hence, constitutive expression of N-terminally 14xHis-tagged AKT1 under the Pdr5 promoter after chromosomal integration [30] was attempted next. This method allows expression under more stable conditions, as full YPD medium instead of minimal DO medium could be used and faster growth of the cell cultures could be achieved. The insertion of the AKT1 expression cassette into *S. cerevisiae* Δ PP genome was verified by colony PCR (Figure S4.A). The test expression showed signals at 100 kDa (theoretical size 99.98 kDa) for two tested colonies, as well as signals at higher molecular weights (above 180 kDa) likely caused by aggregated protein (Figure S4.C). Additionally, non transformed *S. cerevisiae* Δ PP cells were tested, which did not show these signals. Hence the signals at 100 kDa and above could be assigned to AKT1. Since the constitutive expression of AKT1 was shown to work, next a large scale expression was attempted and the cells were submitted to membrane preparation as done before for the expression from plasmid (Figure 2).

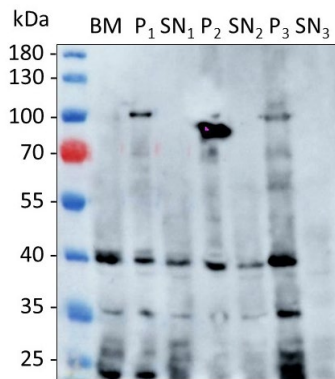


Figure 2: Membrane preparation from *S. cerevisiae* Δ PP expressing 14His-TEV-AKT1 after homologous recombination into the *Prd5* locus. The proteins were separated on a 10 % SDS gel and the Western blot was developed using pentaHis primary antibody, α -mouse-IgG-HRPO-coupled secondary antibody and detected by luminescence with an exposure time of 90 sec. BM = disrupted cells after bead mill; P_1 = pellet after first centrifugation at 1500 g; SN_1 = supernatant of first centrifugation step at 1500 g; P_2 = pellet after second centrifugation at 5000 g; SN_2 = supernatant of second centrifugation step at 5000 g; P_3 = pellet after third centrifugation at 20000 g (membrane pellet); SN_3 = supernatant of third centrifugation step at 20000 g.

A Western blot signal at 100 kDa could be visualized for the final membranes (P_3), hinting towards full length AKT1, despite the loss of protein during the two low spin centrifugation steps (P_1 and P_2), since here signals at 100 kDa were visible for the pellets. The additional signals of lower molecular weight that were visible during the whole preparation procedure were either caused by degradation or unspecific binding of the primary antibody to Δ PP endogenous histidine rich proteins. None the less, membranes containing full length AKT1 could be prepared.

In the next step these membranes were submitted to a detergent screening, in order to find a detergent suitable for the solubilization of AKT1 (Figure S5). In total 94 detergents with different characteristics were tested. The supernatants of these test solubilizations were analyzed for the presence of His-positive protein by dot blot. Significant signals could only be detected for harsh detergents such as several members of the Fos-Choline family (D11, E1-7, E9-11), Cyclo-Fos (D7-D10, E1) and further detergents as members of the Anzergent family (D1-3), n-Decyl-N, N-Dimethylglycin (C2), Sodium-Dodecanoly Sarcosine (G7) or Sucrose Monododecanoate (G8) (Figure S5.A; Table S3 and S4). Noteworthy none of these detergents was able to solubilize the full length AKT1 as the subsequent Coomassie and Western blot analysis revealed no signals above 40 kDa (Figure S5.B-E).

AKT1 single domains expression and purification from inclusion bodies

Since full length AKT1 could be expressed, but was not stable nor could be solubilized from *S. cerevisiae* Δ PP membranes, in a next step the expression and purification of the cytosolic CNBD and ARD domains of AKT1 was attempted. At that time point the structure of AKT1 was not resolved. Hence, for the determination of the protein sections different approaches had to be attempted. According to uniprot entry Q38998 the 6th transmembrane segment was calculated to end after amino acid 286. Hence the construct for the CNBD was chosen to start at amino acid 287. The end point was chosen at amino acid 500 as the calculated end point of the CNBD according to uniprot (entry Q38998; 3rd of October 2019). For the ARD, the sequence start was chosen at amino acid 518, which was the same starting point as for the crystal structure resolved by Chaves-Sanjuan [22]. Whilst the crystal structure of the ARD was resolved until amino acid 702, this construct reached until the C-terminal end of the AKT1 sequence at amino acid 857, hence included the C-terminal KHA domain as well. In the following a sum up will be given, while the detailed results can be derived from the bachelor theses of Christian Mammen [31] and Isabelle Mohnen [32].

While for the full length multi domain membrane protein, *E. coli* was shown not to be a suitable expression host, for the cytosolic CNBD and ARD alone another attempt for expression in *E. coli* Rosetta (DE3) pLysS was made (Figure S6 and S7). For the test expression a N- or C-terminal 10xHis tag was tested under the control of the T7 or araBAD promoter. For both constructs the expression with N-terminal 10xHis tag under the araBAD promoter showed the best results. Here, besides the signals at 30 kDa for the CNBD (theoretical size 28.77 kDa) and 40 kDa for the ARD (theoretical size 39.80 kDa) no degradation was visible. As the over night expression did not lead to increased yields, 3 h expression time was chosen for further expression experiments of the CNBD and ARD.

Both constructs were submitted to another test expression under control of the araBAD promoter at different temperatures with subsequent cell disruption and ultracentrifugation. At this point it was tested whether the AKT1 single domains were functionally folded and hence in the soluble fraction/supernatant after ultracentrifugation, or whether they formed insoluble aggregates such as inclusion bodies and therefore would be found in the pellet (Figure S8). The ARD could be expressed at all three temperatures in comparable amounts, but after the ultracentrifugation all protein was found in the cell debris pellet. Hence inclusion bodies were formed despite lowering the temperature to 16 °C (Figure S8.A and S8.B). The same result was found for the CNBD as it formed insoluble aggregates at 37, 25 and 16 °C and showed a significantly lower expression at 16 °C (Figure S8.C and S8.D).

The purification from inclusion bodies is a well established procedure and if successful yields in protein of high purity. At first the solubilization of the ARD with Gdn-HCl was attempted (Figure S9). While the protein could be solubilized successfully from the inclusion bodies, subsequent dialysis resulted in high amounts of aggregated protein. This was directly visible as white precipitates in the dialysis tube. High amounts of ARD protein were detected in the ultracentrifugation pellet. While 1 mg protein (in 500 µl) were loaded onto the Superdex200 10/300 column, size exclusion chromatography resulted in peaks of very low intensity and only 125 µg ARD protein (in 500 µl) could be found in the elution fraction E₁. Hence the protein could not be refolded from the Gdn-HCl solubilized inclusion bodies in sufficient amounts and a different solubilization agent was tested.

Next solubilization of ARD inclusion bodies with urea and subsequent refolding was tested. For the urea solubilized ARD inclusion bodies, significantly more protein (39.3 mg in 5 ml) compared to the previous attempt with GdnHCl could be submitted to SEC (Figure S10). But all protein eluted in the void volume of the column, hence was still not properly refolded. The same procedure was performed for the CNBD (Figure S11). Detectable amounts of protein remained in the pellet of the solubilization. During dialysis nearly all protein aggregated, since white precipitates were formed in the dialysis tube. Compared to the ARD, only low amounts of protein remained soluble (6 mg in 5 ml) and did not lead to detectable signals in the SEC chromatogram.

Although the inclusion body test had shown that the ARD (amino acid 518 - 857) was present in inclusion bodies an attempt for the purification from the soluble fraction was made, as the ARD (amino acid 516-730) could successfully be purified this way by Chaves-Sanjuan *et al.*[22]. The expression conditions were chosen accordingly (16 °C for 16 h in YPD under T7 promoter with N-terminal His-tag) and an IMAC purification was attempted (Figure S12). This resulted in strong signals on the western blot at 40 kDa for the cell debris pellet, while no signal could be detected in the IMAC load (SN). Still besides high impurities, 40 µg ARD could be isolated (E₄).

Cell free expression of AKT1

So far all attempts failed to isolate the full length AKT1, or its single domains in functional fold. Hence, the expression in a cell free environment was attempted. Here the wheat germ lysate based CECF (continuous exchange cell free) approach was chosen, as this attempt has been shown to work for the AKT1 activating kinase CIPK23 [33] as well as for other membrane proteins[34]. For the expression AKT1 was cloned into pIVEX vectors and submitted to test expressions with N- or C- terminal 6xHis tag (99.8 and 98.2 kDa respectively) in presence of 1% (w/v) Brij35, Triton-X-100 or Sucrose Monododecanoate (Figure 3.A and B). Detectable signals at ~100 kDa and therefore expression of AKT1 could only be shown for the C-terminally 6xHis tagged AKT1 in presence of Brij35 or Sucrose-Monododecanoate.

Since Brij35 was used for the purification of AKT1 activating proteins CIPK23 and CBL1 as well, a further cell free expression attempt of AKT1 in presence of Brij35 was performed with subsequent purification (Figure 3.C-E). In the purification procedure high amounts of protein were lost due to aggregation or non functionally folded AKT1. This could be concluded as Western blot signals at 100 kDa were detected for the ultracentrifugation pellet of the expression mix and in the supernatant of the IMAC magnetic beads. Despite, 40.5 µg AKT1 (in 50 µl) could be eluted from the IMAC beads and were submitted to SEC. The SEC chromatogram (Figure 3.E) showed three non separable peaks. The last peak (E₂) at an elution volume of 1.5 ml (2.15 µg protein in 50 µl) showed a His positive signal at 100 kDa on the Western blot, which could be assigned to full length AKT1.

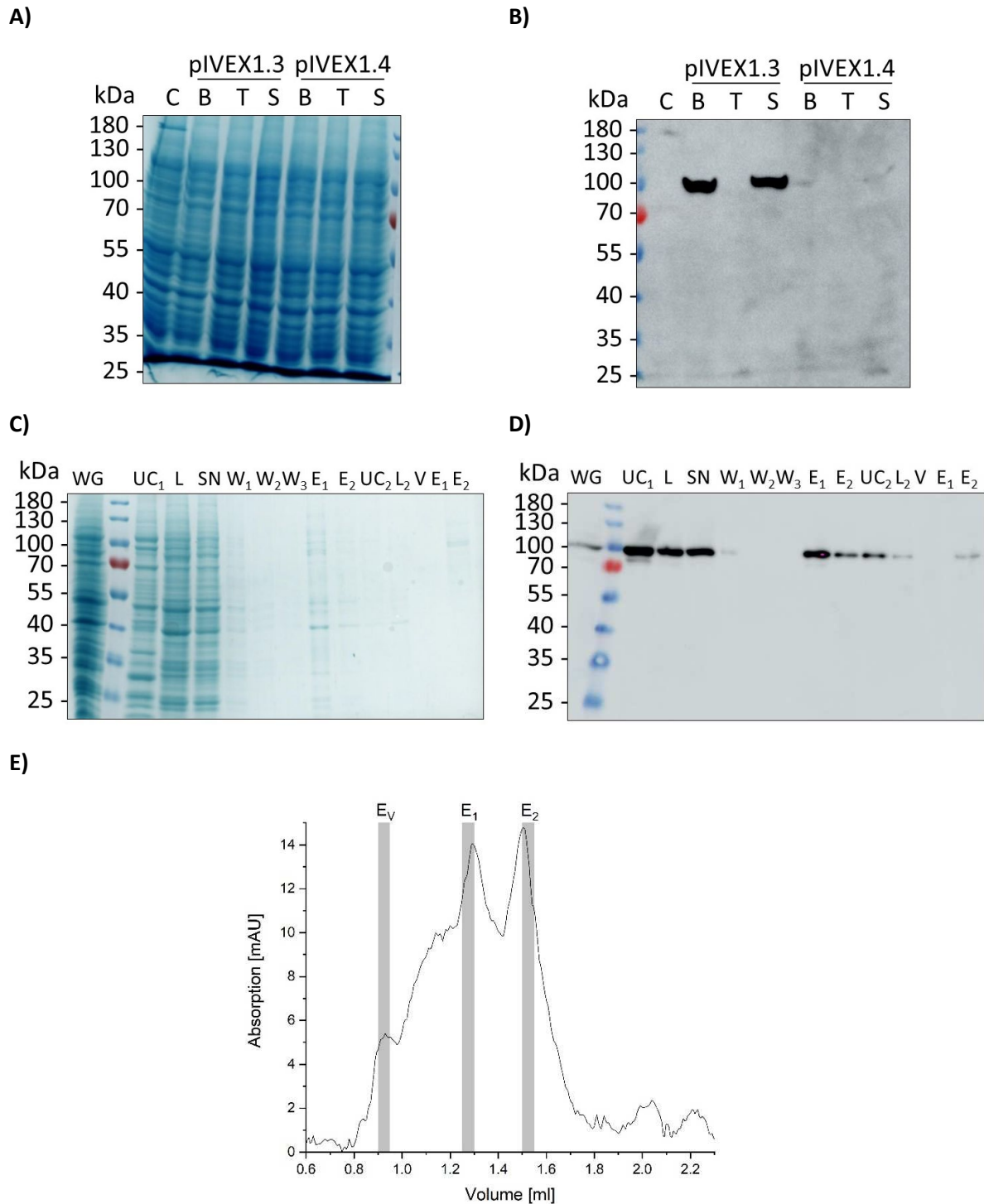


Figure 3: Cell free expression of AKT1. Test expression (A and B) from pIVEX 1.3 (C-terminal 6xHis-tag) and 1.4 (N-terminal 6xHis-Xa-tag) and subsequent purification of C-terminally 6xHis-tagged AKT1 (C-E). Coomassie-stained 10 % SDS gels (A and C) and corresponding western blot analysis (B and D) representing the various steps/ samples from the expression and purification of AKT1. C = control expression, B = expression in presence of 1 % (w/v) Brij35; T = expression in presence of 1 % (v/v) Triton-X-100; S = expression in presence of 1 % (w/v) Sucrose Monododecanoate; WG = wheat germ expression; UC1 = pellet after ultra centrifugation of reaction mix; L = IMAC load; SN = supernatant of IMAC magnetic beads; W₁₋₃ = IMAC wash; E₁₋₂ = IMAC elution; UC₂ = pellet after ultracentrifugation of SEC load; L₂ = SEC load; V = void; E₁ = SEC Elution peak 1; E₂ = SEC Elution peak 2. The blot was developed using pentaHis primary antibody and α -mouse-IgG-HRPO-coupled secondary antibody. (E) SEC of AKT1-6xHis. X-axis represents the elution volume in ml while the Y-axis represents the UV absorption at 280 nm in mAU units. The SEC was performed on a Superdex200 increase 3.2/100. The grey bars in (E) represent the fractions shown on the SDS gel and western blot.

Discussion

At the time of this study, only the 3D structure of the AKT1 ankyrin repeat domain had been determined [22]. Hence the main focus of this study was to express, and purify full length AKT1 for structural and functional studies. The first step towards elucidating a proteins structure and function is always its heterologous expression. The expression or more precisely overexpression of recombinant proteins is always connected with stress and potentially cytotoxic effects for the expression host [35]. Although AKT1 is an eukaryotic protein and its sequence was codon optimized for yeast expression, still expression in the procaryotic expression host *E. coli* was attempted. *E. coli* is one of the most common expression hosts for large scale expression and protein production and has been shown to work for the expression of the AKT1 ankyrin repeat domain [22], the kinase domain of the AKT1 interacting CIPK23 [36] and CBL1 [Chapter 3] and 9 [37] as well as membrane proteins in general [38]. Here the two strains *E. coli* C41 (DE3) and *E. coli* Rosetta (DE3) pLysS were chosen. While *E. coli* C41 (DE3) is specified for the expression of potentially toxic proteins [28], *E. coli* Rosetta (DE3) pLysS is especially suitable for the expression of eukaryotic proteins, as it encodes for codons rarely used in *E. coli* [29]. This strain as well contains the pLysS plasmid to prevent cytotoxic effects, as it encodes for the T7 lysozyme for suppression of T7 basal expression.

In this study none of the used *E. coli* strains could express the full length AKT1, despite the different promoters and tag positions tested (Figure S1). In *E. coli* protein biosynthesis takes place rather fast and the mRNA can be translated by several ribosomes at the same time (Polysomes) [39]. Eucaryotes contain a more complex, modified mRNA (5' cap and poly-A tail), the translation is spatially separated from the preceding transcription and takes place at the rough ER [40]. Additionally, pro- and eucaryotes differ in their subset of chaperones and co- and posttranslational modification enzymes [41]. Hence, as AKT1 is a eukaryotic and with 100 kDa rather large multi domain membrane protein, which further needs to assemble to a tetramer to become functional, a prokaryotic expression host organism was found not to be suitable.

The expression of full length AKT1 in the eukaryotic expression host *S. cerevisiae* Δ PP was shown to work both for the expression from a plasmid as well as after homologous recombination of the AKT1 expression cassette into the Pdr5 locus of the *S. cerevisiae* Δ PP chromosome (Figure 1 and S4). Noteworthy N-terminally tagged AKT1 was located in the plasma membrane, while C-terminally tagged AKT1 remained in inner compartments, such as ER or vacuole (Figure 1.D and E). An improper folding of the C-terminally tagged AKT1 proteins is unlikely. If the protein itself was not properly folded the C-terminal GFP would not be folded and therefore fluorescent as well [42]. Hence the position of the tag seems to influence the localization of the protein.

Despite this finding, *S. cerevisiae* Δ PP membranes were prepared from cells expressing N- or C-terminally His-GFP tagged AKT1 (Figure S2 and S3). As none of both resulted in membranes that contained full length AKT1, further expression attempts were performed after insertion of the *akt1* expression cassette into the *S. cerevisiae* Δ PP genome. Whilst this attempt resulted in a faint signal for the full length AKT1 in the prepared membranes, subsequently no detergent could be found that was able to solubilize AKT1 from those membranes. Throughout the membrane preparations of the His-GFP fusion proteins as well for all samples of the detergent screen of the 14xHis-AKT1 no protein bands above 70 kDa could be visualized on the Coomassie stained gels. Proper *S. cerevisiae* membranes should at least result in a SDS PAGE band at 100 kDa that can be assigned to the plasma membrane P2-type-H⁺-ATPase Pma1. This membrane protein is constitutively present in detectable amounts in healthy *S. cerevisiae* cells [43]. The lack of Pma1 or any other signals above 70 kDa at first was assigned

to the fact that KCl was used in the membrane preparation buffers. The presence of K⁺ ions was supposed to stabilize the K⁺ channel AKT1, but on the other hand resulted in the formation of insoluble potassium dodecylsulfate upon the addition of SDS, that was contained in the SDS PAGE loading dye. Due to this precipitation no detergent was present in the SDS samples to keep the unfolded proteins in a soluble state. Changing KCl to NaCl solved the precipitation of SDS but not the lack of AKT1 signals in the gels and Western blots (Figure S3). Noteworthy throughout all membrane preparations the samples were constantly cooled and protease inhibitors against serine and threonine proteases (cOmplete Protease tablets (Roche)), metallo-proteases (EDTA) as well as asparagine proteases (Pepstatin-A) were used. Hence, degradation due to proteases can be excluded.

Since the preparation of AKT1 membranes did not succeed, the expression and purification of the cytosolic domains of AKT1 was attempted. While the transmembrane domain alone might not be stable, the expression and purification of the CNBD (aa 287 – 500) and ARD (aa 518 – 857) was tested. Compared to the full length AKT1, the partial sequences could be expressed successfully in *E. coli* but in this study both the CNBD and the ARD construct were shown to form inclusion bodies independent of the expression temperature (Figure S8). As mentioned before, the sequence of the *akt1* gene was codon optimized for expression in *S. cerevisiae*. Likely the different codon usage between *E. coli* and *S. cerevisiae* may have caused the misfolding or still that the procaryotic expression machinery is not suitable for the domains of eukaryotic AKT1. Another reason for the instability of the CNBD construct can be found by comparing the chosen sequence with the recently determined single particle cryo EM structure of full length AKT1 [11]. The N terminus of the CNBD construct (aa 287), which was assumed to be at the end of the 6th helical transmembrane segment (uniport entry Q38998 [44]), turned out to be in the middle of a longer helical segment. The same problem turned out to be the case for the C-terminal end (aa 500) of the CNBD construct as well. It is commonly known that cleavage of a protein sequence within a helix has negative effects on its stability. Hence the chosen sequence section turns out as not suitable for the expression and purification of the CNBD as single domain.

For the ARD construct the formation of inclusion bodies may have other reasons. While the sequence starting point (aa 518) was not traceable in the cryo EM structure, position 518 resembles the first amino acid resolved in the crystal structure of the ARD (PDB entry 5AAR). Noteworthy the construct chosen for the crystallization of the ARD by Chaves-Sanjuan *et al.* started two amino acids earlier (aa 516) and ended after aa 706 [22]. Hence the KHA domain (aa 790-857 according to uniport entry Q38998 [44]) was not included. The aa 718-857 sequence used in this study included both ARD and KHA domain. Submission of this sequence to the XtalPred online prediction tool [45], calculated the resulting protein as stable and suitable for crystallization. On the other hand, this was shown not to be true. It can be assumed that the KHA domain is the reason for the instability of the construct. The KHA domain of AKT1 so far remains the only domain for which no structural information is present. While the full length AKT1 was submitted to cryo EM, the structure of this C-terminal part remained elusive [11]. It is likely that this domain is unstructured and has a high intrinsic flexibility. According to uniport entry Q38998 [44] after aa 701 no secondary structure element, such as α -helix or β strand are indicated. Despite extensive screening of suitable expression conditions by Christian Mammen [31] and inclusion body refolding conditions by Isabelle Mohnen [32] no suitable expression and purification condition for the AKT1 single domains could be found.

In this study all attempts to isolate AKT1 or its domains after cellular expression failed, hence cell free expression was performed. Since the prokaryotic translation machinery was shown not to work for AKT1, the wheat germ lysate based continuous exchange cell-free expression (CECF) was chosen. The

translation machinery is originated from wheat germ embryos, hence an eukaryotic plant source and therefore was thought to be suitable for the production of a multidomain plant membrane protein [46]. Lastly, only with the cell free expression attempt in presence of Brij35 detergent, AKT1 could be expressed and purified in its full length, but not in suitable homogeneity and quantity for subsequent structural studies. All together the findings of this study showed that the eukaryotic 100 kDa multi domain protein AKT1 needed the presence of an eukaryotic translation machinery and could not be produced in *E. coli*. Before improvements towards the purification procedure could be attempted, the cryo EM structure of AKT1 was published by Lu *et al.* [11]. This group used Sf9 insect cells for AKT1 protein production. Compared to the wheat germ based cell free expression, Sf9 insect cells allow the introduction of post translational modifications and more importantly easier upscaling in the expression volume [47]. But this approach is not established in the biochemistry I institute.

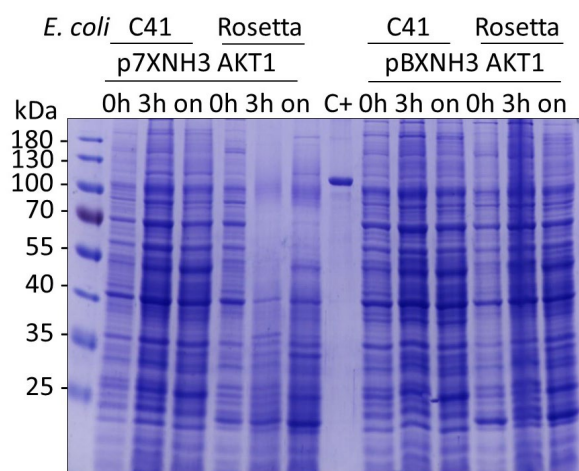
References

1. Maathuis, F.J., *Physiological functions of mineral macronutrients*. Curr Opin Plant Biol, 2009. **12**(3): p. 250-8.
2. Walker, D.J., R.A. Leigh, and A.J. Miller, *Potassium homeostasis in vacuolate plant cells*. Proc Natl Acad Sci U S A, 1996. **93**(19): p. 10510-4.
3. Wang, Y. and W.H. Wu, *Plant sensing and signaling in response to K⁺-deficiency*. Mol Plant, 2010. **3**(2): p. 280-7.
4. Szczerba, M.W., D.T. Britto, and H.J. Kronzucker, *K⁺ transport in plants: physiology and molecular biology*. J Plant Physiol, 2009. **166**(5): p. 447-66.
5. Alemán, F., et al., *Root K(+) acquisition in plants: the Arabidopsis thaliana model*. Plant Cell Physiol, 2011. **52**(9): p. 1603-12.
6. Chérel, I., et al., *Molecular mechanisms involved in plant adaptation to low K(+) availability*. J Exp Bot, 2014. **65**(3): p. 833-48.
7. Grabov, A., *Plant KT/KUP/HAK potassium transporters: single family - multiple functions*. Ann Bot, 2007. **99**(6): p. 1035-41.
8. Nieves-Cordones, M., et al., *The Arabidopsis thaliana HAK5 K⁺ transporter is required for plant growth and K⁺ acquisition from low K⁺ solutions under saline conditions*. Mol Plant, 2010. **3**(2): p. 326-33.
9. Ragel, P., et al., *The CBL-Interacting Protein Kinase CIPK23 Regulates HAK5-Mediated High-Affinity K⁺ Uptake in Arabidopsis Roots*. Plant Physiol, 2015. **169**(4): p. 2863-73.
10. Hirsch, R.E., et al., *A role for the AKT1 potassium channel in plant nutrition*. Science, 1998. **280**(5365): p. 918-21.
11. Lu, Y., et al., *Structural basis for the activity regulation of a potassium channel AKT1 from Arabidopsis*. Nat Commun, 2022. **13**(1): p. 5682.
12. Schünke, S., et al., *Structural insights into conformational changes of a cyclic nucleotide-binding domain in solution from Mesorhizobium loti K1 channel*. Proc Natl Acad Sci U S A, 2011. **108**(15): p. 6121-6.
13. Gaymard, F., et al., *The baculovirus/insect cell system as an alternative to Xenopus oocytes. First characterization of the AKT1 K⁺ channel from Arabidopsis thaliana*. J Biol Chem, 1996. **271**(37): p. 22863-70.
14. Sanchez-Barrena, M.J., et al., *Recognition and Activation of the Plant AKT1 Potassium Channel by the Kinase CIPK23*. Plant Physiol, 2020. **182**(4): p. 2143-2153.
15. Lee, S.C., et al., *A protein phosphorylation/dephosphorylation network regulates a plant potassium channel*. Proc Natl Acad Sci U S A, 2007. **104**(40): p. 15959-64.
16. Pilot, G., et al., *Five-group distribution of the Shaker-like K⁺ channel family in higher plants*. J Mol Evol, 2003. **56**(4): p. 418-34.
17. Daram, P., et al., *Tetramerization of the AKT1 plant potassium channel involves its C-terminal cytoplasmic domain*. EMBO J, 1997. **16**(12): p. 3455-63.
18. Ehrhardt, T., S. Zimmermann, and B. Müller-Rober, *Association of plant K⁺(in) channels is mediated by conserved C-termini and does not affect subunit assembly*. FEBS Lett, 1997. **409**(2): p. 166-70.
19. Geiger, D., et al., *Heteromeric AtKC1:AKT1 channels in Arabidopsis roots facilitate growth under K⁺-limiting conditions*. J Biol Chem, 2009. **284**(32): p. 21288-95.
20. Wang, Y., et al., *Potassium channel alpha-subunit AtKC1 negatively regulates AKT1-mediated K(+) uptake in Arabidopsis roots under low-K(+) stress*. Cell Res, 2010. **20**(7): p. 826-37.
21. Rubio, F., et al., *Systems involved in K⁺ uptake from diluted solutions in pepper plants as revealed by the use of specific inhibitors*. J Plant Physiol, 2010. **167**(17): p. 1494-9.
22. Chaves-Sanjuan, A., et al., *Preliminary crystallographic analysis of the ankyrin-repeat domain of Arabidopsis thaliana AKT1: identification of the domain boundaries for protein crystallization*. Acta Crystallogr F Struct Biol Commun, 2014. **70**(Pt 4): p. 509-12.
23. Gasteiger E., H.C., Gattiker A., Duvaud S., Wilkins M.R., Appel R.D., Bairoch A. *The Proteomics Protocols Handbook*. 2005; Available from: <https://web.expasy.org/protparam/>.

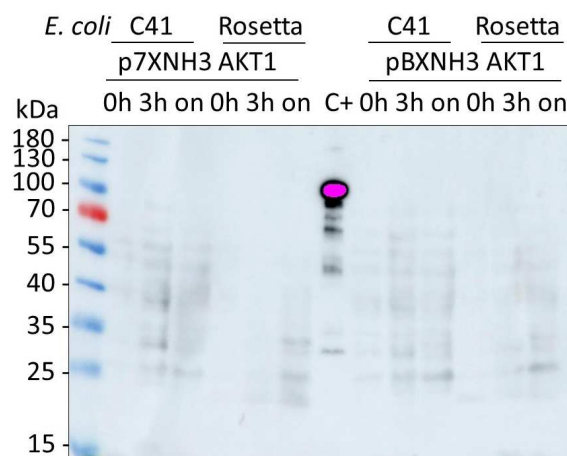
24. Geertsma, E.R. and R. Dutzler, *A versatile and efficient high-throughput cloning tool for structural biology*. *Biochemistry*, 2011. **50**(15): p. 3272-8.
25. Geertsma, E.R. *FX cloning primer design tool*. Available from: <https://www.fxcloning.org/>.
26. Ernst, R., *Molekulare Analyse von ABC-Transportern am Beispiel von Pdr5p aus S. cerevisiae und der isolierten NBD des humanen TAP1*, in *Mathematisch-Naturwissenschaftlichen Fakultät*. 2007, Heinrich-Heine Universität: Düsseldorf. p. 165.
27. Singh, A., et al., *Protein recovery from inclusion bodies of Escherichia coli using mild solubilization process*. *Microb Cell Fact*, 2015. **14**: p. 41.
28. Schlegel, S., P. Genevaux, and J.W. de Gier, *De-convoluting the Genetic Adaptations of E. coli C41(DE3) in Real Time Reveals How Alleviating Protein Production Stress Improves Yields*. *Cell Rep*, 2015. **10**(10): p. 1758-1766.
29. Tegel, H., et al., *Increased levels of recombinant human proteins with the Escherichia coli strain Rosetta(DE3)*. *Protein Expr Purif*, 2010. **69**(2): p. 159-67.
30. Gupta, R.P., et al., *Generating symmetry in the asymmetric ATP-binding cassette (ABC) transporter Pdr5 from Saccharomyces cerevisiae*. *J Biol Chem*, 2014. **289**(22): p. 15272-9.
31. Mammen, C., *Domains of the Ca²⁺ dependent K⁺ channel AKT1 from A. thaliana*, in *Biochemistry I*. 2020, Heinrich-Heine-Universität. p. 79.
32. Mohnen, I., *Soluble domains of the Shaker-like K⁺ channel AKT1 from A. thaliana*, in *Biochemistry I*. 2020, Heinrich-Heine-Universität: Düsseldorf. p. 90.
33. Hashimoto, K., et al., *Phosphorylation of calcineurin B-like (CBL) calcium sensor proteins by their CBL-interacting protein kinases (CIPKs) is required for full activity of CBL-CIPK complexes toward their target proteins*. *J Biol Chem*, 2012. **287**(11): p. 7956-68.
34. Focke, P.J., et al., *Combining in Vitro Folding with Cell Free Protein Synthesis for Membrane Protein Expression*. *Biochemistry*, 2016. **55**(30): p. 4212-9.
35. Bolognesi, B. and B. Lehner, *Protein Overexpression: Reaching the limit*. *Elife*, 2018.
36. Chaves-Sanjuan, A., et al., *Structural basis of the regulatory mechanism of the plant CIPK family of protein kinases controlling ion homeostasis and abiotic stress*. *Proc Natl Acad Sci U S A*, 2014. **111**(42): p. E4532-41.
37. Günes, C., *Investigation of the Calcineurin B-like Calcium Sensor CBL9*, in *Biochemie I*. 2022, Heinrich-Heine-Universität: Düsseldorf. p. 97.
38. Drew, D., et al., *Assembly and overexpression of membrane proteins in Escherichia coli*. *Biochim Biophys Acta*, 2003. **1610**(1): p. 3-10.
39. Berg, J.M., J.L. Tymoczko, and L. Stryer, *Stryer Biochemie*. 7 ed. 2013: Springer-Verlag Berlin Heidelberg 2013. XLII, 1198.
40. Netzer, W.J. and F.U. Hartl, *Recombination of protein domains facilitated by co-translational folding in eukaryotes*. *Nature*, 1997. **388**(6640): p. 343-9.
41. Hartl, F.U. and M. Hayer-Hartl, *Molecular chaperones in the cytosol: from nascent chain to folded protein*. *Science*, 2002. **295**(5561): p. 1852-8.
42. Geertsma, E.R., et al., *Quality control of overexpressed membrane proteins*. *Proc Natl Acad Sci U S A*, 2008. **105**(15): p. 5722-7.
43. Serrano, R., M.C. Kielland-Brandt, and G.R. Fink, *Yeast plasma membrane ATPase is essential for growth and has homology with (Na⁺ + K⁺), K⁺- and Ca²⁺-ATPases*. *Nature*, 1986. **319**(6055): p. 689-93.
44. Consortium, T.U., *UniProt: the Universal Protein Knowledgebase in 2023*. *Nucleic Acids Research*, 2022. **51**(D1): p. D523-D531.
45. Slabinski, L., et al., *XtalPred: a web server for prediction of protein crystallizability*. *Bioinformatics*, 2007. **23**(24): p. 3403-5.
46. Endo, Y. and T. Sawasaki, *Cell-free expression systems for eukaryotic protein production*. *Curr Opin Biotechnol*, 2006. **17**(4): p. 373-80.
47. Maiorella, B., et al., *Large-Scale Insect Cell-Culture for Recombinant Protein Production*. *Nature Biotechnology*, 1988. **6**(12): p. 1406-1410.

Supplemental Information

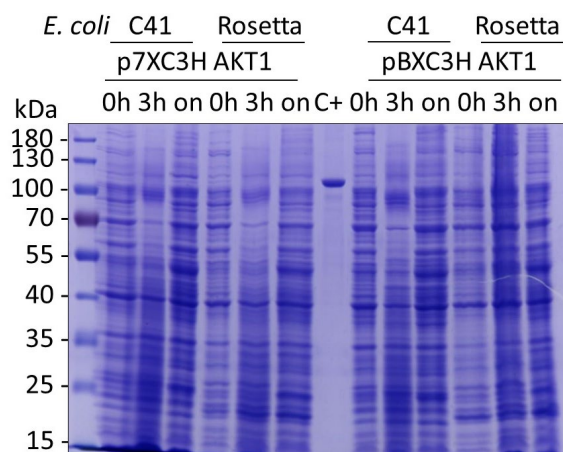
A)



B)



C)



D)

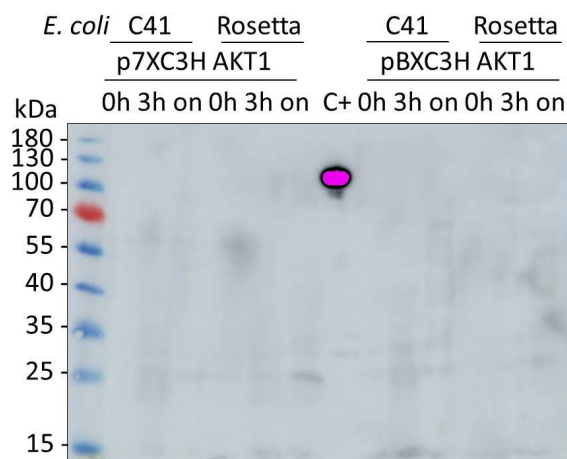


Figure S1: Test expression of AKT1 in *E. coli* C41 (DE3) and Rosetta (DE3) pLysS under T7 and araBAD promoter with N- (A and B) or C-terminal (C and D) 10xHis-tag. Coomassie stained gels (A and C) and Western Blots (B and D) of the AKT1 testexpression. The blot was developed using pentaHis primary antibody and α -mouse-IgG-HRPO-coupled secondary antibody and detected by luminescence with an exposure time of 40 s. As positive control (C+) for the Western blotting purified and His tagged NisB protein was used. The p7XNH3-AKT1 plasmid encoded for N-terminally His-tagged AKT1 expressed under T7 promoter, the pBXNH3-AKT1 plasmid encoded for N-terminally His-tagged AKT1 expressed under araBAD promoter, the p7XC3H-AKT1 plasmid encoded for C-terminally His-tagged AKT1 expressed under T7 promoter and the pBXC3H-AKT1 plasmid encoded for C-terminally His-tagged AKT1 expressed under araBAD promoter. The testexpression was conducted at 37 °C and whole cell samples were taken as 1 OD equivalent before induction with 0.5 mM IPTG or 0.01 % L-arabinose, 3h and 16h (on = overnight) after induction.

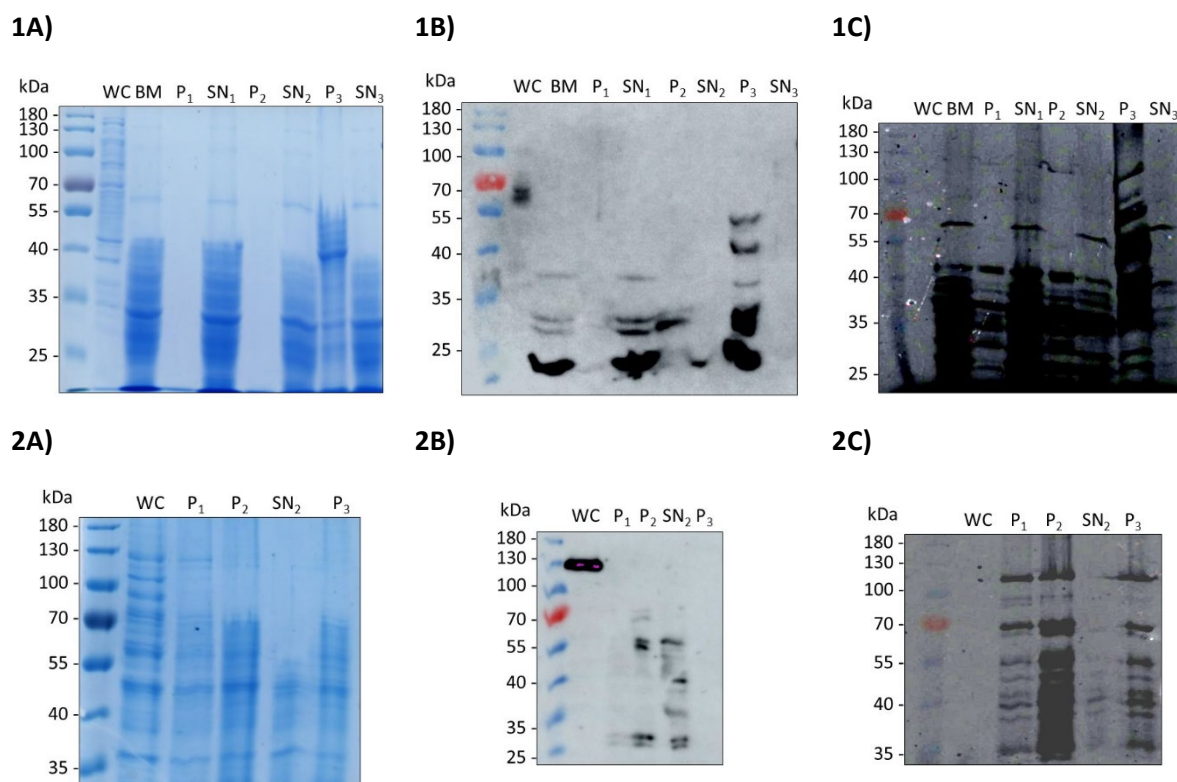


Figure S2: Membrane preparation of GFP AKT1 fusion constructs from *S. cerevisiae* Δ PP. Coomassie stained gels (A) Western Blots (B) and in-gel GFP fluorescence (C) of the N-terminally (1) and C-terminally (2) 10His-yeGFP tagged AKT1 membrane preparation. The blot was developed using pentaHis primary antibody and α -mouse-IgG-HRPO-coupled secondary antibody and detected by luminescence with an exposure time of 40 s. The in-gel GFP fluorescence was detected by exposure at 480 nm (blue channel/Cy2 filter). WC = whole cells; BM = broken cells after bead mill; P₁ = pellet after first centrifugation at 1500 g; SN₁ = supernatant of first centrifugation step at 1500 g; P₂ = pellet after second centrifugation at 5000 g; SN₂ = supernatant of second centrifugation step at 5000 g; P₃ = pellet after third centrifugation at 20000 g (membrane pellet); SN₃ = supernatant of third centrifugation step at 20000 g.

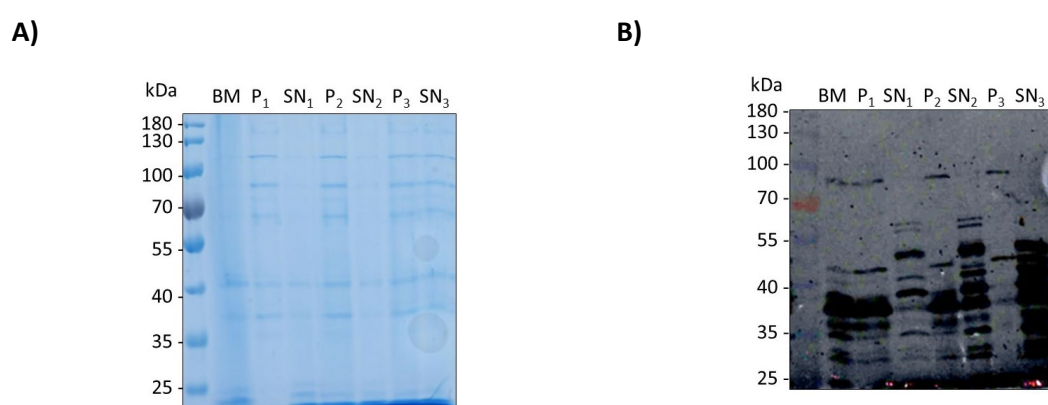


Figure S3: Membrane preparation of N-terminally 10xHis-yeGFP tagged AKT1 from *S. cerevisiae* Δ PP in presence of 150 mM NaCl. Coomassie stained gels (A) and in-gel GFP fluorescence (B) The blot was developed using pentaHis primary antibody and α -mouse-IgG-HRPO-coupled secondary antibody and detected by luminescence with an exposure time of 40 s but showed no signals at all (not depicted). The in-gel GFP fluorescence was detected by exposure at 480 nm (blue channel/Cy2 filter). WC = whole cells; BM = broken cells after bead mill ; P₁ = pellet after first centrifugation at 1500 g; SN₁ = supernatant of first centrifugation step at 1500 g; P₂ = pellet after second centrifugation at 5000 g; SN₂ = supernatant of second centrifugation step at 5000 g; P₃ = pellet after third centrifugation at 20000 g (membrane pellet); SN₃ = supernatant of third centrifugation step at 20000 g

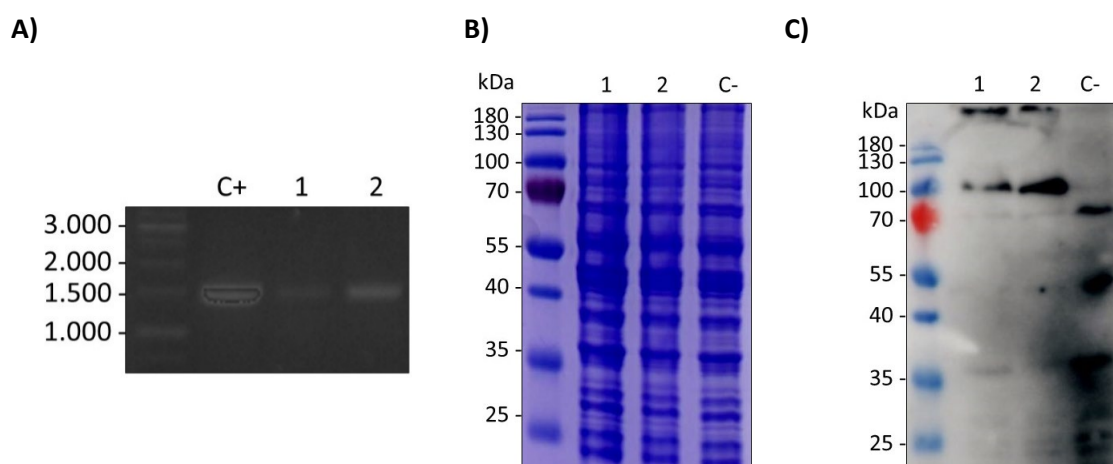
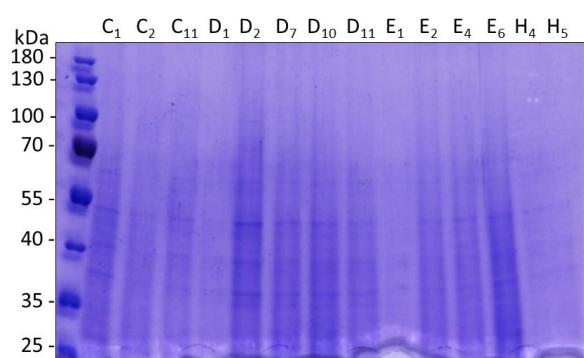


Figure S4: Colony PCR and test expression of AKT1 in *S. cerevisiae* Δ PP after homologous recombination at the *Pdr5* locus. A) The colony PCR was performed with Q5 polymerase and primers binding in the 5' and 3' homologous region of the AKT1 expression cassette. Isolated genomic *S. cerevisiae* Δ PP DNA of colonies 1 and 2 was used as template. A PCR from pRE5-14His-TEV-AKT1 plasmid was used as positive control. The samples were analyzed on a 1 % (w/v) agarose gel. B) and C) The AKT1 expression was tested under the constitutive *Pdr5* promoter with N-terminal 14xHis tag. The expression took place overnight YPD medium at 30 °C. 1 and 2 represent the two colonies that were tested for expression. As negative control (C-) for the expression, non transformed *S. cerevisiae* Δ PP cells were used. The whole cells samples were separated on 10 % SDS gels analyzed by B) Coomassie staining and C) Western blot; developed using pentaHis primary antibody and α -mouse-IgG-HRPO-coupled secondary antibody and detected by luminescence with an exposure time of 100 s.

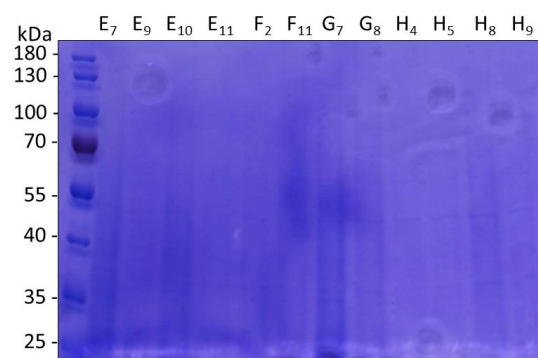
A)

	1	2	3	4	5	6	7	8	9	10	11	12
A												
B												
C												
D												
E												
F												
G												
H												

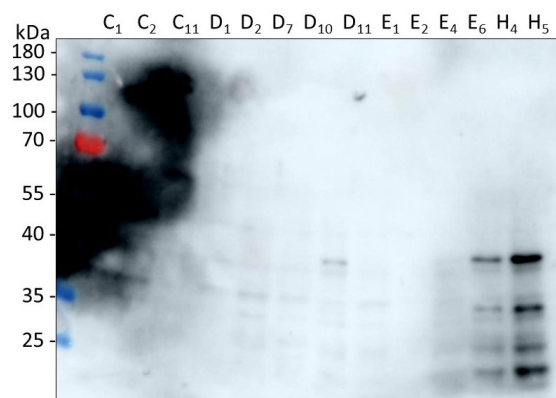
B)



C)



D)



E)

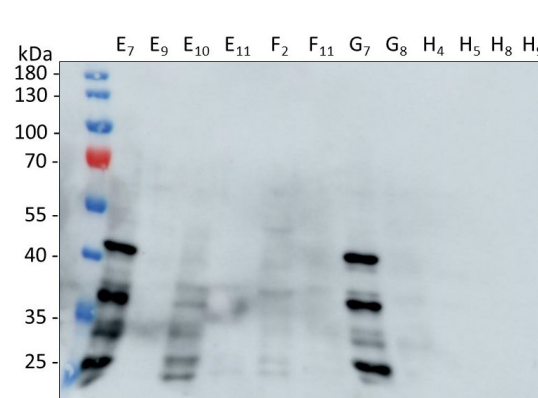


Figure S5: Test solubilization of *S. cerevisiae* ΔPP 14xHis-TEV-AKT1 membranes. A) Dot blot of the solubilized fraction after ultracentrifugation. B), C) Coomassie stained gels and D), E) Western blot of the most promising dot blot samples. The blots were developed using pentaHis primary antibody and α-mouse-IgG-HRPO-coupled secondary antibody and detected by luminescence with an exposure time of 100 s. The tested detergents are listed in table S2 and S3.

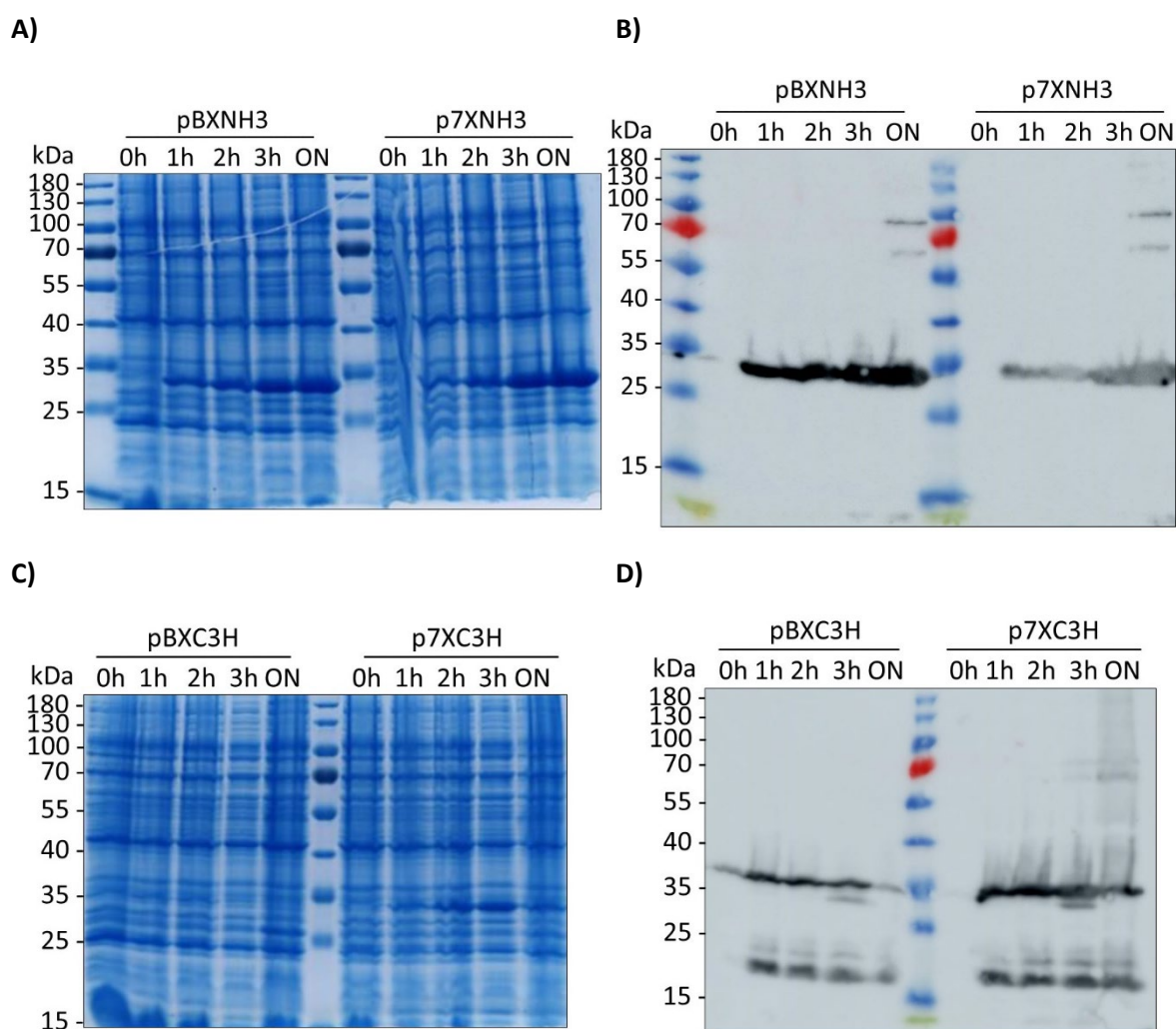


Figure S6: Test expression of the CNBD in *E. coli* Rosetta (DE3) pLysS under T7 and araBAD promoter with N- (A and B) or C-terminal (C and D) 10xHis-tag. A), C) Coomassie stained gels and B), D) Western blots of the CNBD test expression. The blot was developed using pentaHis primary antibody and α -mouse-IgG-HRPO-coupled secondary antibody and detected by luminescence with an exposure time of 60 s. The p7XNH3-CNBD plasmid encoded for N-terminally His-tagged CNBD expressed under T7 promoter, the pBXNH3-CNBD plasmid encoded for N-terminally His-tagged CNBD expressed under araBAD promoter, the p7XC3H-CNBD plasmid encoded for C-terminally His-tagged CNBD expressed under T7 promoter and the pBXC3H-CNBD plasmid encoded for C-terminally His-tagged CNBD expressed under araBAD promoter. The testexpression was conducted at 37 °C and whole cell samples were taken as 1 OD equivalent before induction with 0.5 mM IPTG or 0.01 % L-arabinose, 1h, 2, 3h and 16h (on = overnight) after induction.

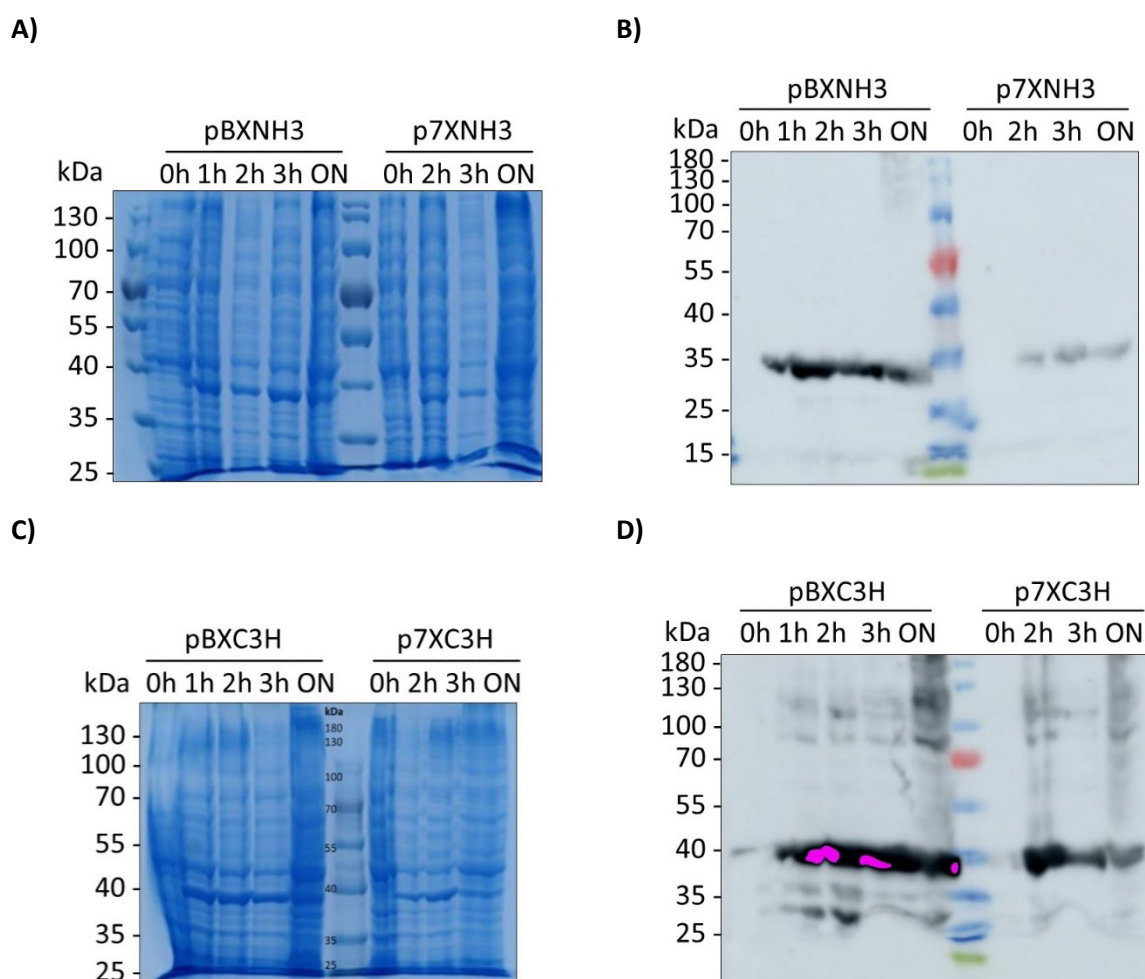


Figure S7: Test expression of the ARD in *E. coli* Rosetta (DE3) pLysS under T7 and araBAD promoter with N- (A and B) or C-terminal (C and D) 10xHis-tag. A), C) Coomassie stained gels and B), D) Western blots of the ARD test expression. The blot was developed using pentaHis primary antibody and α -mouse-IgG-HRPO-coupled secondary antibody and detected by luminescence with an exposure time of 60 s. The p7XNH3-ARD plasmid encoded for N-terminally His-tagged ARD expressed under T7 promoter, the pBXNH3-ARD plasmid encoded for N-terminally His-tagged ARD expressed under araBAD promoter, the p7XC3H-ARD plasmid encoded for C-terminally His-tagged ARD expressed under T7 promoter and the pBXC3H-ARD plasmid encoded for C-terminally His-tagged ARD expressed under araBAD promoter. The testexpression was conducted at 37 °C and whole cell samples were taken as 1 OD equivalent before induction with 0.5 mM IPTG or 0.01 % L-arabinose, 1h, 2, 3h and 16h (on = overnight) after induction.

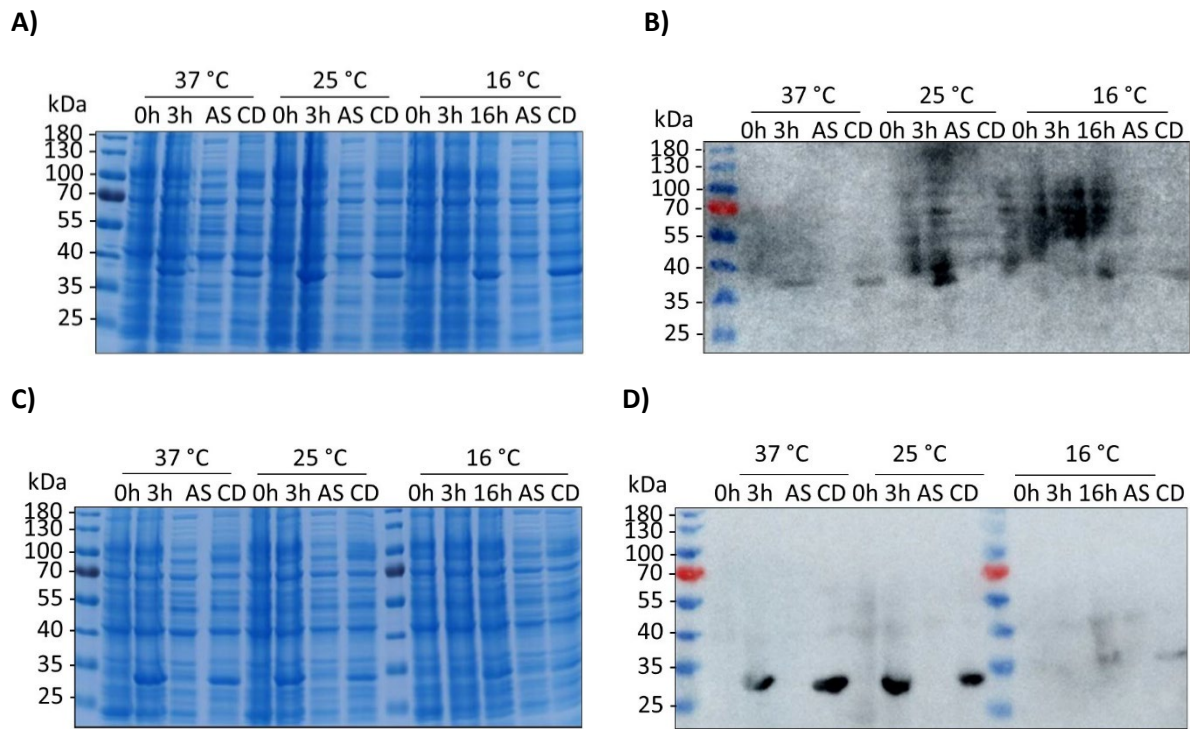


Figure S8: Test expression of AKT1 single domains in *E. coli* Rosetta (DE3) pLysS with subsequent test for inclusion bodies. The expression of the ARD (A - B) and CNBD (C - D) was tested at 37 and 25 °C for 3 h and 16 °C for 3 and 16 h under araBAD promoter with N-terminal 10xHis-tag. A), C) Coomassie stained gels and B), D) Western blots of the expression and inclusion body test. The blot was developed using pentaHis primary antibody and α -mouse-IgG-HRPO-coupled secondary antibody and detected by luminescence with an exposure time of 60 s. Whole cell samples were taken as 1 OD equivalent before induction with 0.01 % L-arabinose, 3h and 16h after induction. AS resembles the supernatant and CD the cell debris pellet after sonification and ultracentrifugation.

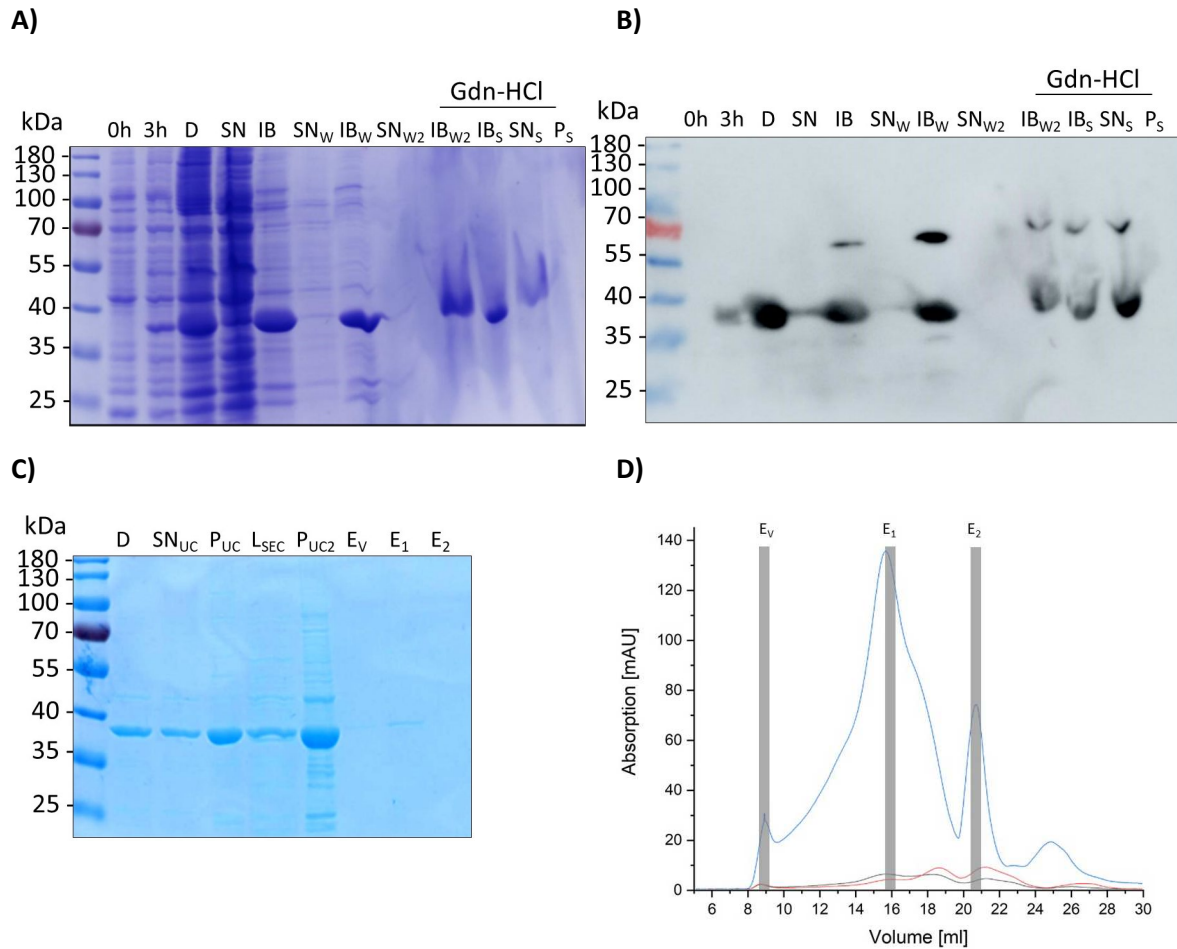


Figure S9: Purification of the ARD from inclusion bodies. A), B) Expression of the N-terminally 10xHis-tagged ARD in *E. coli* Rosetta (DE3) pLysS with subsequent inclusion body preparation and solubilization with guanidinium hydrochloride (GdnHCl) and C), D) subsequent refolding by dialysis and size exclusion chromatography on a Superdex200 10/300 column. 0h = cells before induction, 3h = cells after 3h of expression, D = disrupted cells, SN = supernatant after ultracentrifugation, IB = pellet after ultracentrifugation/ inclusion bodies, SN_W = supernatant of the first wash step with 1 % (v/v) Triton-X-100, IB_W = pellet/ inclusion bodies after first wash step with 1% (v/v) Triton-X-100, SN_{W2} = supernatant of the second wash step, IB_{W2} = pellet/ inclusion bodies after second washing step IB_S = solubilized inclusion bodies, SN_S = supernatant after ultracentrifugation of the solubilized inclusion bodies, P_S = pellet after ultracentrifugation of the solubilized inclusion bodies, D = dialyzed protein, SN_{UC} = supernatant after ultracentrifugation of dialysate, P_{UC} = pellet after ultracentrifugation of dialysate, L_{SEC} = SEC load/ concentrated dialysate, P_{UC2} = pellet after ultracentrifugation of the SEC load, E_V = SEC elution fraction of the void volume, E₁ = SEC elution fraction at 16 ml E₂ = SEC elution fraction at 20.5 ml. A), C) Coomassie stained gels and B) Western Blot of the expression and inclusion body preparation, solubilization, refolding and D) size exclusion chromatography. The blot was developed using pentaHis primary antibody and α -mouse-IgG-HRPO-coupled secondary antibody and detected by luminescence with an exposure time of 60 s. In D) the blue line of the SEC chromatogram resembles the absorption at 216 nm, the red line resembles the absorption at 260 nm and the black line resembles the absorption at 280 nm.

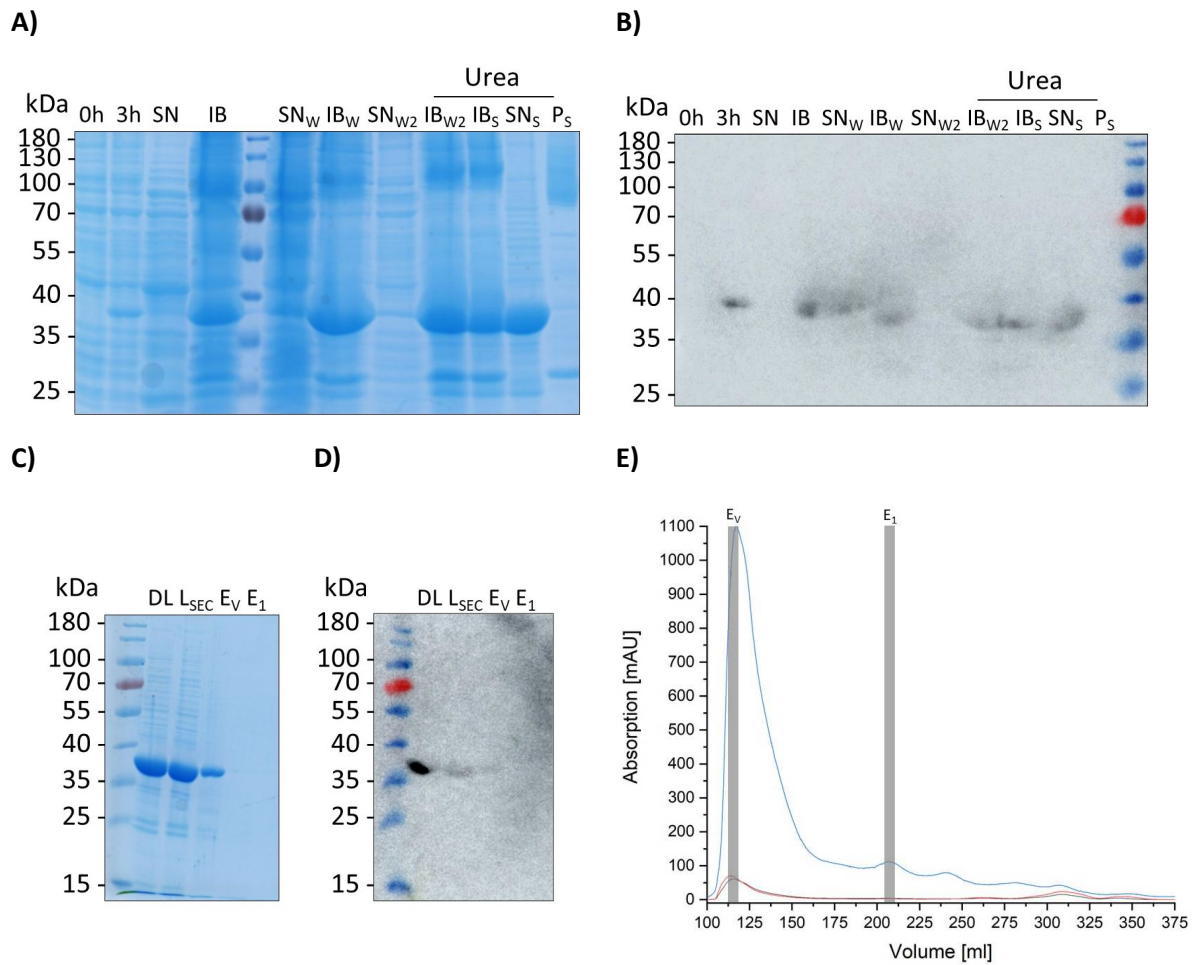


Figure S10: Purification of the ARD from inclusion bodies. A), B) Expression of the N-terminally 10xHis-tagged ARD in *E. coli* Rosetta (DE3) pLysS with subsequent inclusion body preparation and solubilization with urea and C), D) subsequent refolding by dialysis and size exclusion chromatography on a HiLoad Superdex200 26/600 column. 0h = cells before induction, 3h = cells after 3h of expression, D = disrupted cells, SN = supernatant after ultracentrifugation, IB = pellet after ultracentrifugation/ inclusion bodies, SN_W = supernatant of the first wash step with 1 % (v/v) Triton-X-100, IB_W = pellet/ inclusion bodies after first wash step with 1% (v/v) Triton-X-100, SN_{W2} = supernatant of the second wash step, IB_{W2} = pellet/ inclusion bodies after second washing step IB_S = solubilized inclusion bodies, SN_S = supernatant after ultra centrifugation of the solubilized inclusion bodies, P_S = pellet after ultracentrifugation of the solubilized inclusion bodies, DL = dialyzed protein, SN_{UC} = supernatant after ultracentrifugation of dialysate, P_{UC} = pellet after ultracentrifugation of dialysate, L_{SEC} = SEC load/ concentrated dialysate, P_{UC2} = pellet after ultracentrifugation of the SEC load, E_V = SEC elution fraction of the void volume, E₁ = SEC elution fraction at 210 ml. A), C) Coomassie stained gels and B) Western Blot of the expression and inclusion body preparation, solubilization, refolding and D) size exclusion chromatography. The blot was developed using pentaHis primary antibody and α -mouse-IgG-HRPO-coupled secondary antibody and detected by luminescence with an exposure time of 60 s. In D) the blue line of the SEC chromatogram resembles the absorption at 216 nm, the red line resembles the absorption at 260 nm and the black line resembles the absorption at 280 nm.

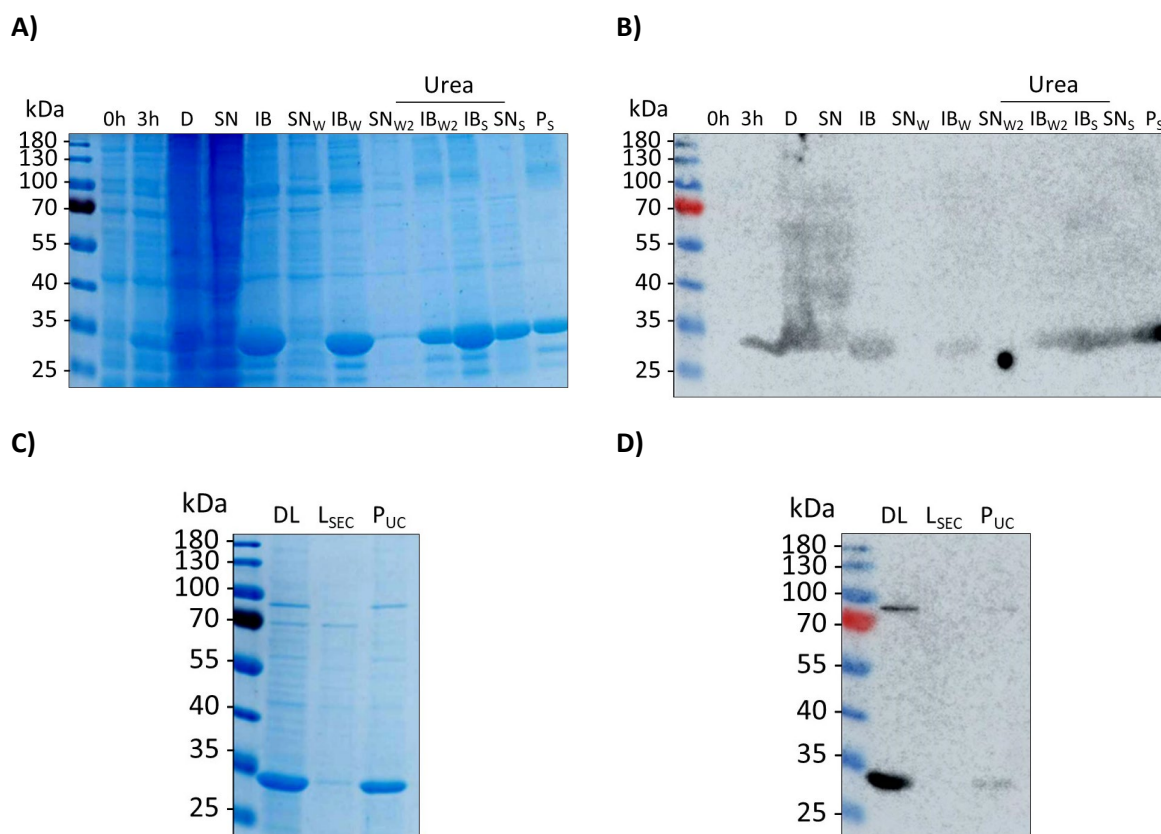


Figure S11: Purification of the CNBD from inclusion bodies. Expression of the N-terminally 10xHis-tagged CNBD in *E. coli* Rosetta (DE3) pLysS with subsequent inclusion body preparation and solubilization with urea (A and B) and subsequent refolding by dialysis (C). 0h = cells before induction, 3h = cells after 3h of expression, D = disrupted cells, SN = supernatant after ultracentrifugation, IB = pellet after ultracentrifugation/ inclusion bodies, SN_W = supernatant of the first wash step with 1 % (v/v) Triton-X-100, IB_W = pellet/ inclusion bodies after first wash step with 1% (v/v) Triton-X-100, SN_{W2} = supernatant of the second wash step, IB_{W2} = pellet/ inclusion bodies after second washing step IB_S = solubilized inclusion bodies, SN_S = supernatant after ultra centrifugation of the solubilized inclusion bodies, P_S = pellet after ultracentrifugation of the solubilized inclusion bodies, D = dialyzed protein, SN_{UC} = supernatant after ultracentrifugation of dialysate, P_{UC} = pellet after ultracentrifugation of dialysate, L_{SEC} = SEC load/ concentrated dialysate, P_{UC2} = pellet after ultracentrifugation of the SEC load. A), C) Coomassie stained gels and B) Western Blot of the expression and inclusion body preparation, solubilization, refolding. The blot was developed using pentaHis primary antibody and α -mouse-IgG-HRPO-coupled secondary antibody and detected by luminescence with an exposure time of 60 s.

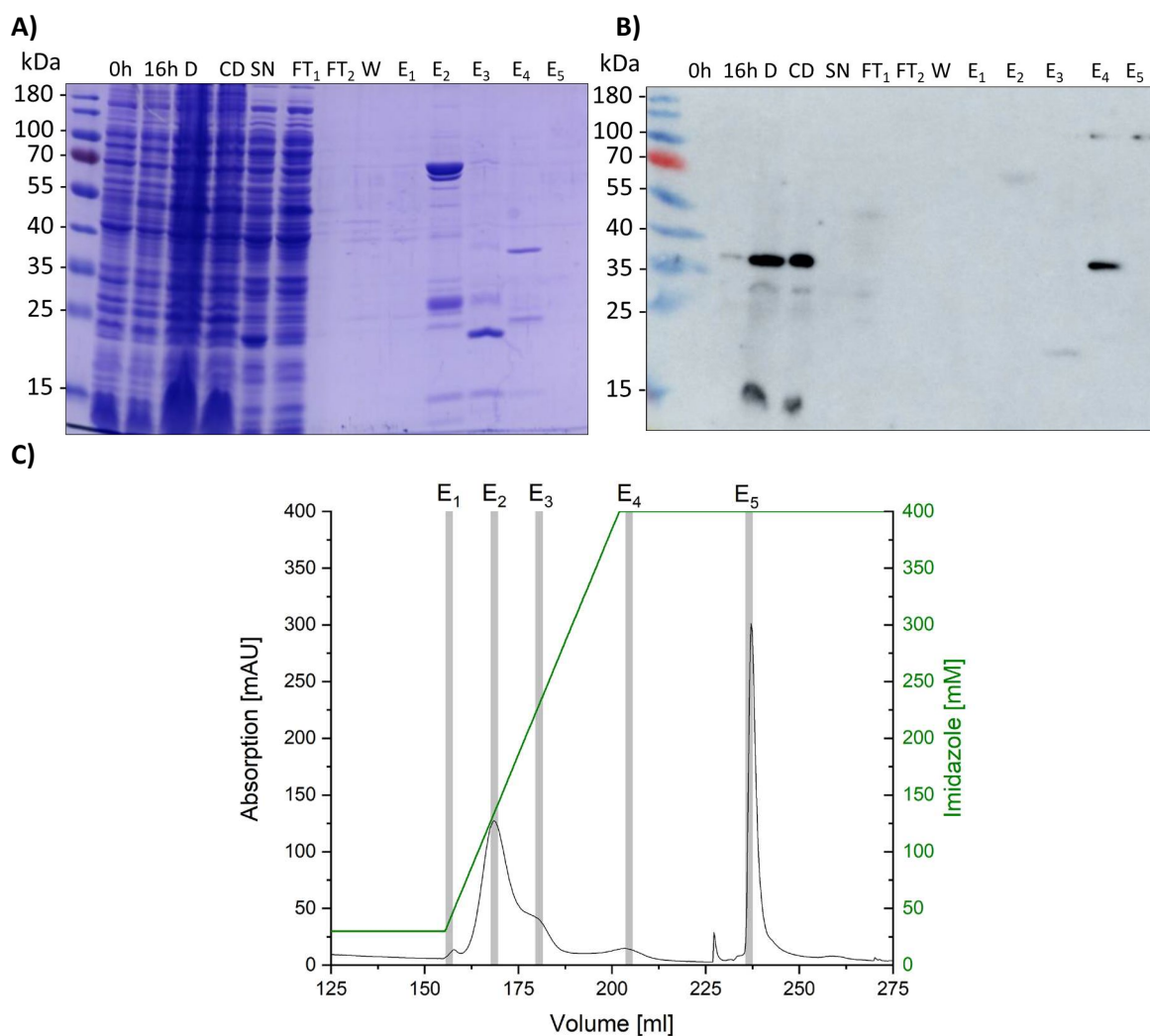


Figure S12: Purification of the ARD from soluble fraction after the protocol from Chaves-Sanjuan et al 2014 [1]. Expression of the N-terminally 10xHis-tagged ARD in *E. coli* Rosetta (DE3) pLysS with subsequent IMAC purification with a 5 ml HiTrap Chelating column. 0h = cells before induction with 0.5 mM IPTG, 16h = cells after 16h of expression at 16 °C, D = disrupted cells, CD = cell debris pellet, SN = supernatant after ultracentrifugation/ IMAC load, FT₁ = early IMAC flow through, FT₂ = late IMAC flowthrough, W = IMAC wash, E₁₋₅ = IMAC elution fractions. A) Coomassie stained gel and B) Western blot of the expression and IMAC purification and C) IMAC chromatogram. The black line of the chromatogram resembles the absorption at 280 nm and the green line resembles the Imidazole concentration, the grey bars resemble the fractions analyzed on the Coomassie gel and Western blot. The blot was developed using pentaHis primary antibody and α -mouse-IgG-HRPO-coupled secondary antibody and detected by luminescence with an exposure time of 60 s.

Table S1: List of primers used in this study.

Name	Sequence 5' → 3'	Length [bp]	GC [%]	Tm [°C]
AKT1-FX fw	ATATATGCTCTTCTAGTAGAGGTGGTGCCTTATTATGCGGTCAA	44	41	71
AKT1-FX rev	TATATAGCTCTTCATGCGGAGTCTGTAGCAAAGATT AAGTGGTC	44	41	71
AKT1 TMD FX rev	TATATAGCTCTTCCTGCATTTGTCATGTTACCGATCAAGTAAGC	44	39	70
AKT1 CNBD FX fw	ATATATGCTCTTCTAGTAACATGACAAATTTGGTT GTTCAT	41	29	65
AKT1 CNBD FX rev	TATATAGCTCTTCATGCATCCATTTTACCTCTTGCCAACATGTT	44	36	69
AKT1 ARD FX fw	ATATATGCTCTTCTAGTCCATTGAATTTGTGTTTTGCTGCAATT	44	32	68
TEV_AKT1_fw	TATTTTCAGTCCATGAGAGGTGGTGCC	27	48	67
TEV_AKT1_rev	CAGGTTTTCTCCATGGTGTATGGTGTATGG	28	50	64
AKT1_Cterm_homReg_fw	GAATTCACACCACCATCCGGTATGAGGCCGCCTGCAGGTTCGAC	43	60	>75
AKT1_Cterm_homReg_rev	TAGCAATTCGTAATCAGCGCATTTGGCTTAGGAGTCTGTAGCAAAGATTAAAGTGGTC	57	42	>75
AKT1-fw	GATTCGTTGTTTCTCCATAC	20	40	53
AKT1-rev	GGTGTCTACCGTTGTTATCTG	22	45	58
pIVEX 1.4 AKT1 fw	GCGGCATCGAAGGCCGCGGCCGCTTAATTAACATATGACCATGAGAGGTGGTGCCTTATTATGC	65	52,3	>75
pIVEX 1.4 AKT1 rev	AACCAGAAGAGCTGGGTACCTTAGTTAGTTACCGGATCCCTTAGGAGTCTGTAGCAAAGATTAAAGTGGT	69	44,9	>75
pIVEX 1.3 AKT1 fw	ACACAGCTTACAAATACTCCCCACAACAGCTTGTCGAACCCATGAGAGGTGGTGCCT	58	51,7	>75
pIVEX 1.3 AKT1 rev	TACCTTATTAATGATGATGATGATGATGAGAACCCC CCCCTGAGGAGTCTGTAGCAAAGATTAAAGTGGT	69	42	>75
5' homologous region fw	GGCCCCTATTACAATAAACA	20	40	51
3' homologous region rev	TGGTGTGAATTCTAGCAATT	20	35	52

Table S2: FX plasmids used in this study

Name	Encoded tag	Promoter	Expression host	Marker
pINItcat	-	-	<i>E. coli</i>	Chloramphenicol
p7XC3H	C-terminal 10His-3C-	T7	<i>E. coli</i>	Kanamycin
p7XNH3	N-terminal 10His-3C-	T7	<i>E. coli</i>	Kanamycin
pBXC3H	C-terminal 10His-3C-	araBAD	<i>E. coli</i>	Ampicillin
pBXNH3	N-terminal 10His-3C-	araBAD	<i>E. coli</i>	Ampicillin
pYEXC3H	C-terminal 10His-3C-	Gal1	<i>S. cerevisiae</i>	-Ura auxotrophy/ Ampicillin
pYEXC3GH	C-terminal 10His-GFP-3C-	Gal1	<i>S. cerevisiae</i>	-Ura auxotrophy/ Ampicillin
pYEXNH3	N-terminal 10His-3C-	Gal1	<i>S. cerevisiae</i>	-Ura auxotrophy/ Ampicillin
pYEXNHG3	N-terminal 10His-GFP-3C-	Gal1	<i>S. cerevisiae</i>	-Ura auxotrophy/ Ampicillin

Table S3: List of detergents used for detergent screen part I. N = non ionic, Z = zwitter ionic A = anionic

Nr.	Position	Detergent	(w/v)	Property
1	A1	Anameg R-7	1%	N
2	A2	Anapoe R-20	1%	N
3	A3	Anapoe R-35	1%	N
4	A4	Anapoe R-58	1%	N
5	A5	Anapoe R-80	1%	N
6	A6	Anapoe R-C10E6	1%	N
7	A7	Anapoe R-C10E9	1%	N
8	A8	Anapoe R-C12E8	1%	N
9	A9	Anapoe R-C12E9	1%	N
10	A10	Anapoe R-C12E10	1%	N
11	A11	Anapoe R-C13E8	1%	N
12	A12	Anapoe R-X-100	1%	N
13	B1	Anapoe R-X-114	1%	N
14	B2	Anapoe R-X-305	1%	N
15	B3	Anapoe R-X-405	1%	N
16	B4	Big CHAP	1%	N
17	B5	Big CHAP deoxy	1%	N
18	B6	CYGLU R-3	2%	N
19	B7	CYMAL R-1	2%	N
20	B8	CYMAL R-2	2%	N
21	B9	CYMAL R-3	1%	N
22	B10	2,6-Dimethyl-4-heptyl- α -D-maltopyranoside	2%	N
23	B11	n-Decyl- α -D-maltopyranoside	2%	N
24	B12	n-Decyl- β -D-maltopyranoside	2%	N
25	C1	n-Decyl- β -D-thiomaltopyranosid	2%	N
26	C2	n-Decyl-N,N-Dimethylglycin	2%	N
27	C3	n-Dodecyl- α -D-maltopyranoside	1%	N
28	C4	n-Dodecyl- β -D-maltopyranoside (DDM)	1%	N
29	C5	n-Heptyl- β -D-thioglucopyranoside	2%	N
30	C6	n-Heptyl- β -D-Glucopyranoside	2%	N
31	C7	n-Nonyl- β -D-thiomaltopyranoside	1%	N
32	C8	n-Dodecyl- β -D-thiomaltopyranoside	1%	N
33	C9	CYMAL 4	2%	N
34	C10	CYMAL R-5	2%	N
35	C11	CYMAL 6	1%	N
36	C12	CYMAL 7	1%	N
37	D1	Anzergent 3-8	2%	Z
38	D2	Anzergent R3-10	2%	Z
39	D3	Anzergent R3-12	1%	Z
40	D4	Anzergent R3-14	1%	Z
41	D5	CHAPS	2%	Z
42	D6	CHAPSO	2%	Z
43	D7	CyclofosTM-4	2%	Z
44	D8	CyclofosTM-5	1%	Z
45	D9	CyclofosTM-6	1%	Z
46	D10	CyclofosTM-7	1%	Z
47	D11	Fos-Choline R-9	2%	Z
48	D12	Fos-Choline-10	2%	Z
49	E1	CyclofosTM-3	2%	Z
50	E2	Fos-Choline R-11	1%	Z
51	E3	Fos-Choline R-12	1%	Z
52	E4	Fos-Choline R-13	1%	Z
53	E5	Fos-Choline R-14	1%	Z

Table S4: List of detergents used for detergent screen part II. N = non ionic, Z = zwitter ionic A = anionic

54	E6	Fos-Choline R-15	1%	Z
55	E7	Fos-Choline R-16	1%	Z
56	E8	Fos-Choline R-Iso-9	2%	Z
57	E9	Fos-Choline R-Iso-11	2%	Z
58	E10	Fos-Choline R-Unisat-11-10	1%	Z
59	E11	Fos-Choline R-8	2%	Z
60	E12	n-Dodecyl-N,N-dimethylglycine	1%	Z
61	F1	n-Dodecyl-N,N-dimethylamine-N-oxide (DDAO)	1%	Z
62	F2	Cholic acid, sodium salt	1%	A
63	F3	Deoxycholic acid, sodium salt	1%	A
64	F4	Fosmea-8	1%	A
65	F5	Fosmea R-10	1%	A
66	F6	Hexaethylene Glycol Monoethyl Ether (C8E6)	1%	N
67	F7	n-Hexyl- β -D-Glucopyranoside	2%	N
68	F8	n-Hexyl- β -D-Maltopyranoside	2%	N
69	F9	n-Nonyl- β -D- Glucopyranoside	1%	N
70	F10	n-Nonyl- β -D-Maltopyranoside	1%	N
71	F11	MEGA-8	2%	N
72	F12	Octaethylene Glycol Monodecyl Ether (C12E8)	1%	N
74	G1	n-Octyl- β -D-Thiomaltopyranoside	1%	N
75	G2	n-Octyl- β -D-Maltopyranoside	2%	N
76	G3	Pentaethylene Glycol Monodecyl Ether (C10E5)	1%	N
77	G4	PMAL-C8	1%	N
78	G5	propyl(bi)cyclohexyl- β -maltoside (PCC- β -M)	1%	N
79	G6	2-Propyl-1-Pentyl Maltopyranoside	2%	N
80	G7	Sodium Dodecanoyl Sarcosine	1%	A
81	G8	Sucrose Monododecanoate	1%	N
82	G9	n-Tetradecyl- β -D-Maltopyranoside	1%	N
83	G10	n-Tetradecyl-N,N-Dimethylamine-N-Oxide (TDAO)	1%	Z
84	G11	Tetraethylene Glycol Monoethyl Ether (C8E4)	1%	N
85	G12	n-Tridecyl- β -D-Maltopyranoside	1%	N
86	H1	n-Undecyl- α -D-Maltopyranoside	1%	N
87	H2	n-Undecyl- β -D-Maltopyranoside	1%	N
88	H3	n-Undecyl- β -D-Thiomaltopyranoside	1%	N
89	H4	sodium dodecyl sulfate (SDS) (C+)	1%	A
90	H5	Puffer (C-)	0%	-
91	H6	n-Octyl- β -D-glucopyranoside (OG)	2%	N
92	H7	glyco-diosgenin (GDN)	2%	N
93	H8	Lauryl-Maltose-Neopentyl-Glycol (LMNG)	2%	N
94	H9	PCC	2%	?
95	H10	Fos-Choline-16 (FC16)	2%	Z

References SI

1. Chaves-Sanjuan, A., et al., *Preliminary crystallographic analysis of the ankyrin-repeat domain of Arabidopsis thaliana AKT1: identification of the domain boundaries for protein crystallization*. Acta Crystallogr F Struct Biol Commun, 2014. **70**(Pt 4): p. 509-12.

Chapter 2 - The CBL interacting protein kinase CIPK23

Title: Expression and Purification trials of CIPK23 from *A. thaliana*

Authors: Alexandra Bork and Lutz Schmitt

Own proportion of this work: 90 %

Cloning

Expression and Purification of CIPK23

In silico analyses (modeling)

Cell free expression of 6xHis-X_a-CIPK23

Data analysis

Preparation of figures

Writing of the manuscript

Expression and Purification trials of CIPK23 from *A. thaliana*

Abstract

CIPK proteins resemble a large group of serine/threonine protein kinases in *A. thaliana*. Amongst these, CIPK23 plays a crucial role in the Ca^{2+} induced activation of the K^+ channel AKT1 by phosphorylation of the channel. As so far only the structure of the CIPK23 kinase domain has been resolved, the expression and purification of full length CIPK23 was attempted in this study. Since purification trials in *E. coli* resulted in the formation of 40 kDa N-terminal degradation products, an AlphaFold2 model was created. This structure revealed a junction between the N-terminal kinase domain and the C-terminal regulatory domain that remains rather flexible and extended without any secondary structure. This part was identified as the putative point of degradation during expression. Further attempts in wheat germ CECF could prevented this degradation but resulted in high amounts of aggregation of the full length protein. Hence the purification of the full length CIPK23 could not be established in this study and will remain problematic in the future due to the highly flexible unstructured junction domain.

Introduction

Plants are sessile organisms. Therefore the adaption to changes in their environment is indispensable to their survival. In these adaption processes the divalent cation Ca^{2+} plays a crucial role, as it is known to function as a second messenger in plants [1-3]. Changes in cytosolic Ca^{2+} concentrations, also known as Ca^{2+} signatures [4, 5], get deciphered and downstream translated by a complex network of proteins. Amongst these are the Ca^{2+} sensing calcineurin-B-like proteins (CBLs), which upon Ca^{2+} binding activate a group of serine/threonine kinases, called CBL interacting protein kinases (CIPKs) [6, 7]. These kinases then, upon a variety of phosphorylation events, activate their downstream targets.

One of the 26 CIPK proteins known in *A. thaliana* is CIPK23. CIPK23 activates the inward-rectifying K^+ channel AKT1 upon K^+ deprivation, which resides in the plasma membrane, and itself gets activated by binding of CBL1 or 9 [8-10]. This kinase is not only involved in the K^+ uptake by AKT1 but plays a major role in K^+ uptake in general as it also targets other K^+ uptake proteins such as HAK5 [11] and KUP4 [12]. Besides K^+ uptake CIPK23 is involved in the uptake of a variety of other ionic substances (e.g. NO_3^- [13]) as well as the inhibition of NH_4^+ import [14], all in complex with either CBL1 or CBL9. How the CIPK23 protein is able to interact with such a variety of targets so far is not fully understood, but it can be stated that the interaction is not accomplished by a specific domain [10].

CIPK kinases in general are divided into a N-terminal kinase domain connected by a junction domain with a C-terminal regulatory domain [6]. The kinase domain harbors the ATP binding site and the so called activation loop. The regulatory domain contains the protein phosphatase interaction site (PPI), for the interaction with PP2C-type phosphatases and the NAF domain, also known as FISL motif [15], which is involved in CBL binding and functions as an autoinhibitory domain in absence of CBLs [6, 10]. Upon CBL binding conformational changes lead to the release of autoinhibitory domain from the kinase domain and the NAF domain gets placed in a cleft of the CBL protein at the opposite site of the Ca^{2+} binding sites [16]. This enables the autophosphorylation of the kinase and hence its activation [15].

The CBLs and PP2C type phosphatases are stated to be competitive counterplayers in activation and inactivation of the CIPK, as their interaction sites, the PPI and NAF domain, are in close proximity and only one of the interacting proteins can bind at a time [16]. Without the activation by CBL binding or phosphorylation by other kinases, CIPK23 has been shown to be inactive [17]. CIPKs do not contain any membrane anchors and are located in the cyto- and nucleoplasm [18]. Hence the CIPK protein needs

to be recruited to the vacuolar or the plasma membrane and its downstream target. As CBL1 and 9 are known to be plasma membrane associated [19], CIPK23 upon CBL1 or 9 binding gets recruited to the plasma membrane to activate its target AKT1.

For CIPK proteins partial 3D structures have been determined so far, as there are the kinase domains of CIPK23 and CIPK24 [17] as well as the regulatory domains of CIPK24 [16] and CIPK14 [20] in complex with CBL4/SOS3 or CBL2 respectively. Additionally, the structure of the CIPK23 kinase domain in complex with the ankyrin repeat domain (ARD) of AKT1 was modelled via docking experiments [21]. Specifically the latter finding gave first information about the precise interaction site of CIPK23 with its downstream target AKT1. The specificity of AKT1 towards CIPK23 is provided by the concave site of the ARD via electrostatic interactions with the CIPK23 kinase domain. Further the kinase active site and regulatory activation loop remain accessible in the complex, hence the function of CIPK23 upon AKT1 binding would not be altered. The K_D of this interaction was determined in the high nanomolar range (980 nM)[21].

So far, no 3D structure of a full length CIPK protein exists and the kinase activity of CIPK23 has only been determined in presence of synthetic substrates [22]. Hence in this study different expression and purification attempts were made in order to obtain full-length CIPK23 for structure determination and functional analysis of both, the kinase activity as well as the interaction with AKT1 and CBL1/9.

Material and Methods

Expression and purification from *E. coli*/Rosetta (DE3) pLysS

Cloning

The *cipk23* gene from *A. thaliana* was amplified via PCR, introducing a 5' *SpeI* and 3' *XhoI* cleavage site using primers listed in Table S1 (CIPK23_Spe_For, CIPK23_Xho_RG) into a modified version of pET24b(+) vector that already encodes a N-terminal StrepII-tag (Kudla *et al.* unpublished; Figure S1). A TEV protease cleavage site was introduced into the pET24b(+)-StrepII-CIPK23 plasmid via Q5® Site-Directed Mutagenesis using the TEV-CIPK primers (Table S1) and following the manufacturer's instructions (NEB). The resulting plasmid pET24b(+)-StrepII-TEV-CBL1 was verified by sequencing and used for transformation of *E. coli* Rosetta (DE3) pLysS.

Gene Expression

Wild type CIPK23 protein was expressed from a IPTG inducible pET24b(+) vector using the following protocol. A single colony was used to inoculate 50 ml of LB medium supplemented with 50 µg/ml kanamycin (pET24b(+)) and 36 µg/ml chloramphenicol (pLysS) in a baffled flask and grown for 14 h at 37 °C with 180 rpm shaking. 2 l 2xYT medium in a 5 l baffled flask supplemented with 50 µg/ml kanamycin and 36 µg/ml chloramphenicol was inoculated with 50 ml of an overnight culture and grown at 37 °C shaking at 180 rpm until an OD₆₀₀ of 0.6 - 0.8 was reached. In the initial experiments the cells were cooled down to 25 °C and IPTG was added to a final concentration of 1 mM to induce the expression for 3 h. In later experiments the temperature was decreased to 16 °C before induction and the cells were grown for further 16 h. Either way the cells were harvested by centrifugation at 5000 g for 20 min at 4 °C. The cell pellets were washed with buffer (50 mM Tris pH 8.0, 150 mM NaCl) and centrifuged again for 10 min at 4000 g at 4 °C. The resulting cell pellets were frozen as 8 g aliquots (wet weight) in liquid nitrogen and stored at – 80 °C until further use.

Protein Purification from *E. coli* Rosetta (DE3) pLysS

Cell disruption and preparation of cleared lysates

A two-step purification approach was used for isolation of the StrepII-tagged CIPK23. The cell pellet (8 g) was resuspended in 50 ml resuspension buffer (50 mM Tris pH 8.0, 150 mM NaCl) supplemented with 1 mg DNaseI (Sigma), 1 mM MgCl₂ and 1 cOmplete™ EDTA free Protease inhibitor tablet (Roche) and stirred for 1 h at 10 °C. The cells were disrupted by passing three times through a high-pressure cell disrupter (Microfluidics M-110P) at 1.5 bar at 10 °C. The lysate was centrifuged at 130000 g for 45 min at 4 °C to remove cell debris. The cleared lysate was then submitted to affinity chromatography either with loose Strep Tactin beads (IBA) or prepacked StrepTrap™ HP (Cytiva) columns.

Loose Strep Tactin beads

In initial experiments 5 ml loose Strep Tactin beads were loaded onto a gravity flow column and equilibrated with wash buffer (50 mM Tris pH 8.0, 150 mM NaCl, 0.5 mM TCEP, 5 mM EDTA, 5 mM EGTA). The cleared lysate was applied and the flowthrough was collected. The beads were washed with 5x 10 ml wash buffer (EDTA and EGTA reduced to 0.2 mM each) and the protein was eluted by application of 6 times 2.5 ml wash buffer (without EDTA and EGTA) supplemented with 2.5 mM Desthiobiotin.

StrepTrap Column purification

For the column purification trials 0.25 % (w/v) Brij35 (Millipore) was added to the cleared lysate and incubated at 10 °C for 30 min under mild stirring. The cleared lysate was then applied to two 5 ml StrepTrap™ HP (Cytiva) columns pre-equilibrated with wash buffer (50 mM Tris pH 8.0, 150 mM NaCl, 0.05 % (w/v) Brij35) at a flow rate of 2 ml/min. The columns were subsequently washed with 50 ml of wash buffer, 50 ml wash buffer supplemented with 5 mM ATP and again 50 ml wash buffer without ATP. The StrepII-tagged CIPK23 protein was then eluted with 60 ml of wash buffer supplemented with 2.5 mM Desthiobiotin in 2 ml fractions. The protein concentration was determined with a NanoDrop One (Thermo Scientific).

Size Exclusion Chromatography of CIPK23

The protein containing elution fractions from the affinity chromatography were pooled and concentrated in an Amicon Ultra-15 centrifugal filter concentrator with a 30 kDa cutoff membrane (Millipore) to a final volume of 500 µl. The concentrated protein solution was centrifuged for 30 min at 4 °C and 138000 g to remove potential aggregates. The protein solution was then further purified using size exclusion chromatography (SEC). It was applied to a Superdex200 10/300 column (GE) at a flow rate of 0.3 ml/min pre-equilibrated with SEC buffer (50 mM Tris pH 8.0, 150 mM NaCl and 0.05 % (w/v) Brij35). The eluted protein fractions were collected and concentration was determined using NanoDrop One as described above.

The purity of the protein was analyzed by SDS-PAGE (10 %) and Coomassie staining (50 % (v/v) methanol, 10 % (v/v) acetic acid, 1 g/L Coomassie G250 Brilliant Blue (Serva)). Western blot analysis was further performed to detect CIPK23 via its StrepII-tag using Strep tag® II monoclonal primary antibody (mouse) (Millipore) and α-mouse-HRP coupled secondary antibodies (Jackson Immuno Research).

Cell free expression and Purification of CIPK23

Cloning

To create a suitable vector for cell free expression, the *cipk23* gene was amplified from the pET24b(+)_StrepII-CIPK23 vector using the pIVEX1.4 CIPK23 fw and rev primers listed in Table S1. Thereby SmaI and NcoI cleavage sites were introduced at the 5' and 3' end respectively and the gene was then cloned into the pIVEX 1.4 vector (Biotech Rabbit) coding for a N-terminal 6xHis tag and a factor Xa cleavage site. The plasmid was verified by sequencing (Microsynth).

Cell free Gene Expression

In order to express the *cipk23* gene in a cell free environment the RTS 100 wheat germ kit (biotech rabbit) was chosen. The cell free gene expression was performed according to the manual at 24 °C for 16 h with 900 rpm shaking. 2.5 µg plasmid DNA (pIVEX1.4 CIPK23 (6xHis-X_a tagged) or pIVEX1.4 StrepII-TEV-CIPK23) were used. Both reaction and feeding solution were supplemented with 0.05 % (w/v) Brij35 detergent.

Purification of CIPK23 from cell free expression

Ni-NTA magnetic beads

After expression, the 50 µl reaction solution was centrifuged at 138000 g for 30 min at 4 °C to remove potentially aggregated protein. The supernatant of the ultracentrifugation step was then submitted to IMAC purification using 5 µl equilibrated (50 mM Tris pH 8.0, 150 mM NaCl, 0.05 % (w/v) Brij35) magnetic beads (Qiagen). For binding, the suspension was incubated for 30 min in an overhead rotor. Afterwards the beads were washed with 3 times 100 µl buffer. For elution of the protein, 50 µl buffer supplemented with 150 mM Imidazole was added to the beads and incubated for 30 min in an overhead rotor. This was repeated 5 times and the protein concentrations of the elution fractions were determined using NanoDrop One. Protein containing fractions were pooled and concentrated to 50 µl using an Amicon Ultra-0.5 centrifugal filter concentrator with a 30 kDa cutoff membrane (Millipore).

Strep Tactin magnetic beads

The procedure for the purification of the StrepII-tagged protein from cell free expression was in accordance to the description for the 6xHis-tagged version. Here 5 µl Strep Tactin magnetic beads (Qiagen) were used and the protein was eluted with 2.5 mM Desthiobiotin.

Small scale Size Exclusion Chromatography of CIPK23

The concentrated protein solution (50 µl) was further purified using SEC. It was applied to a equilibrated (50 mM Tris pH 8.0, 150 mM NaCl and 0.05 % (w/v) Brij35) Superdex200 increase 3.2/100 column (GE) at a flow rate of 0.04 ml/min. The eluted protein fractions were collected in a microtiter plate and concentration was determined using NanoDrop One as described above.

The SDS-PAGE was performed as described for the purification from *E. coli*. For the Western blot analysis, the detection of CIPK23 via its 6xHis-tag was performed using penta His monoclonal primary antibody (mouse) (Qiagen) and α-mouse-HRP coupled secondary antibodies (Jackson Immuno Research).

Results

Expression and Purification trials in *E. coli* Rosetta (DE3) pLysS

So far only the structure of the kinase domain of CIPK23 has been resolved[17]. The next step towards elucidating the 3D structure and the function of CIPK23 itself and in complex with CBL1 or 9 and AKT1, is the purification of the full-length protein. To do so, expression in *E. coli* Rosetta (DE3) pLysS was attempted. With a theoretical size of 55.8 kDa (ProtParam, Expasy [23]) the protein could be produced after 3 h at 25 °C showing a clear signal at ~ 55 kDa in both, the Coomassie stained gel as well as the Western blot (Figure 1.A and B). Yet these expression conditions lead to high amounts of either aggregated protein or insoluble inclusion bodies as there was an intense band at 55 kDa for the sample of the cell debris pellet after the ultracentrifugation of the disrupted cells. Nonetheless, the cleared lysate was submitted to Strep Tactin purification. Whilst in the load of the Strep Tactin purification a 40 kDa C-terminal degradation product could be detected, this could completely be removed with the flow through and was not detected for the elution fractions. This purification approach resulted in 0.27 mg protein from 8 g cells (wet weight) after concentration of the elution fractions with still several impurities or degradation products present. As an example the additional band at 70 kDa might be caused by the chaperone DnaK, as an issue during the Bachelor thesis of Polina Kuznecov [24].

The Strep Tactin purified protein was submitted to size exclusion chromatography (Figure 1.C). This resulted in two elution peaks. The first peak eluted 8 ml after injection and resembled the void peak (E_v). The latter elution peak (E_1) eluted after 20 ml, hence almost 1 column volume and likely was caused by Desthiobiotin. Unfortunately, StrepII positive bands could only be detected for the void peak, indicating that the CIPK23 protein was present in soluble aggregates and not functionally folded.

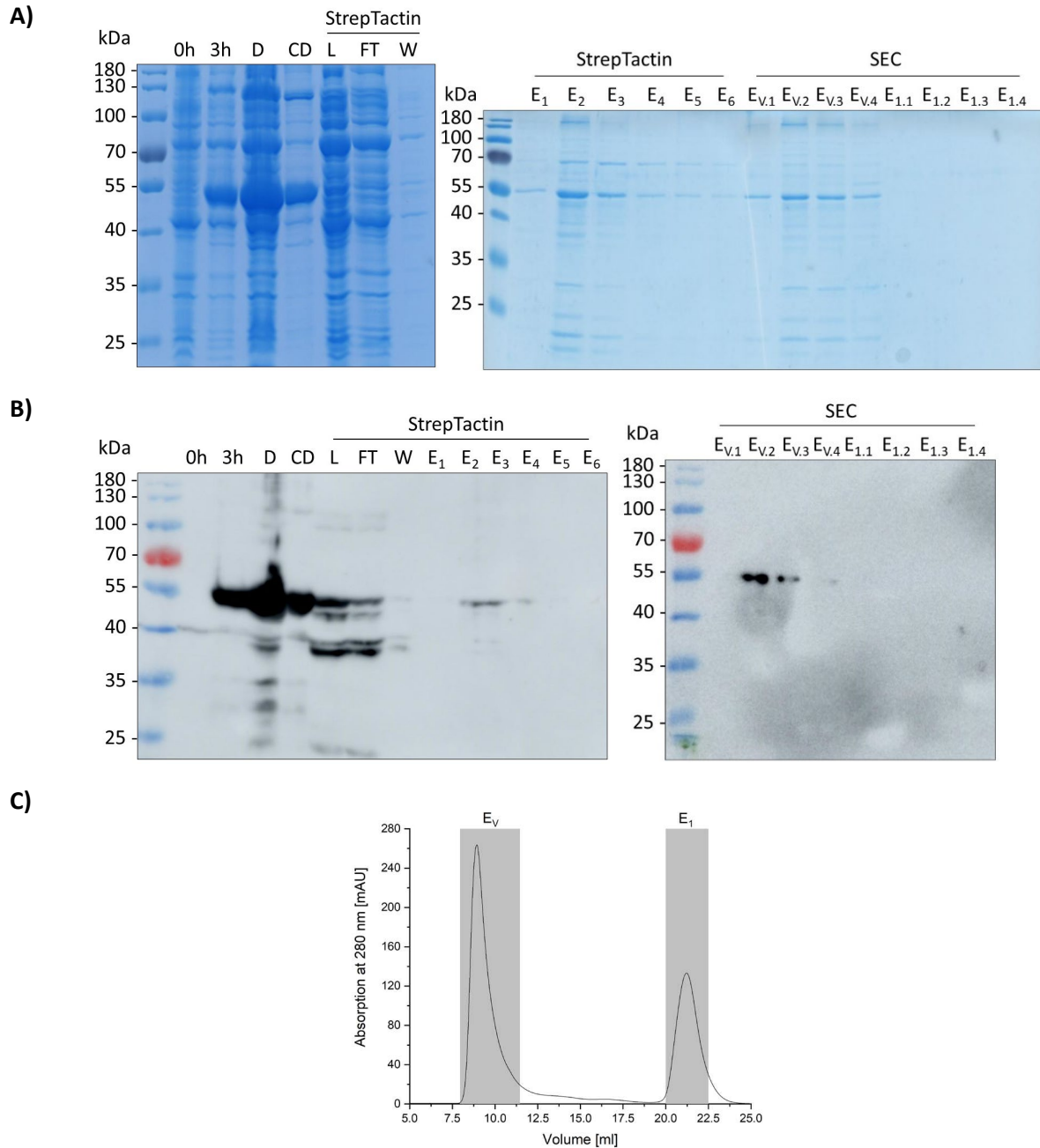


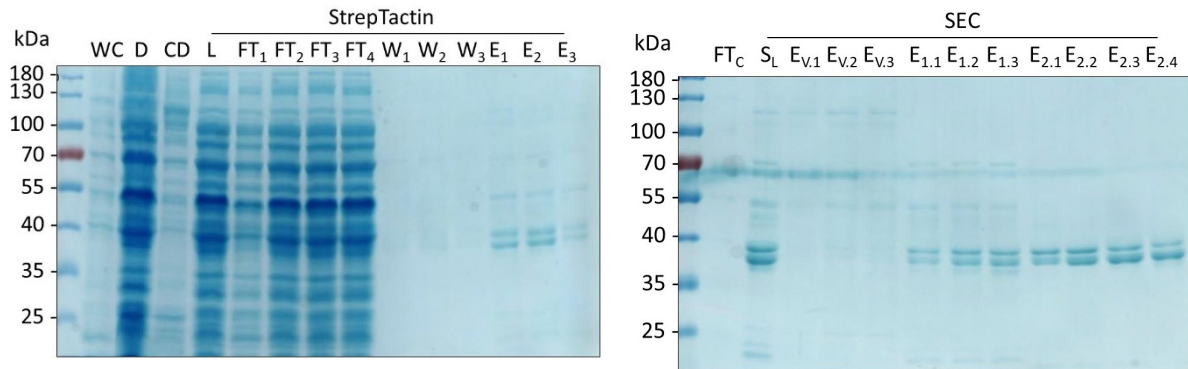
Figure 1: Purification of StrepII-TEV-CIPK23. (A) Coomassie-stained 10 % SDS gel and (B) Western blot analysis representing the various steps/ samples from the purification of CIPK23. 0h = cells before induction; 3h = cells after 3h of expression with 1 mM IPTG; D = disrupted cells; CD = cell debris pellet; L = load; FT = StrepTrap HP flow through; W = wash; E₁₋₆ = Strep Tactin elution fractions; E_{V.1-V.4} = void peak E_V; E_{1.1-1.4} = SEC Elution peak E₁. The blot was developed using α -StrepII primary antibody and α -mouse-IgG-HRPO-coupled secondary antibody. (C) Size exclusion chromatogram of the CIPK23. X-axis represents the elution volume in ml while the Y-axis represents the UV absorption at 280 nm in mAU units. The size exclusion chromatography was performed on a Superdex200 10/300. The grey bars represent the fractions shown on the SDS gel and Western blot.

To circumvent the formation of insoluble aggregates, inclusion bodies or the co-purification of chaperones such as DnaK, the expression conditions were changed to a lower temperature (16 °C) and therefore a longer expression time (16 h) as well [17]. To further improve the purification procedure for the affinity chromatography, the loose Strep Tactin beads were exchanged by prepacked StrepTrap™ HP columns, an additional ATP wash to remove potentially copurified DnaK was established and the detergent Brij35 was added to all buffers after cell disruption [25].

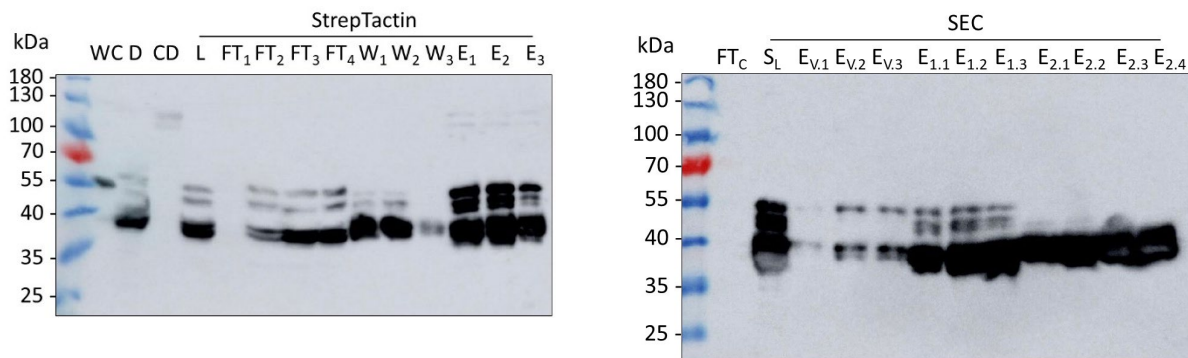
At first the changed expression conditions lead to the desired result as in the cell debris no StrepII positive band could be detected anymore, but on the other hand C-terminal degradation products were visible from the disruption of the cells on for all further purification steps (Figure 2.A and B). These degradation products were copurified with the full length protein during StrepTrap purification and resulted in about six times more protein purified after concentration (1.6 mg), compared to the purification without BriJ35.

The protein was then submitted to SEC (Figure 2.D). Compared to the previous SEC chromatogram instead of two peaks, three peaks were visible. The first peak (E_v) again eluted 8 ml after injection and was again caused by soluble aggregates. This peak contained protein species corresponding to both the full-length 55 kDa protein as well as the 40 kDa degradation product. Interestingly the middle peak (E_1), which eluted 11 ml after the injection contained these two protein species as well. This indicates that the addition of BriJ35 detergent not fully but at least partially could stabilize the full-length protein and keep it in a soluble non aggregated form. The last SEC peak (E_2) which eluted 15 ml after injection only contained the C-terminally degraded species of CIPK23.

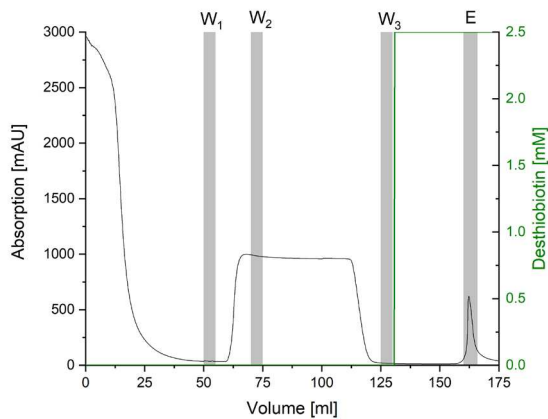
A)



B)



C)



D)

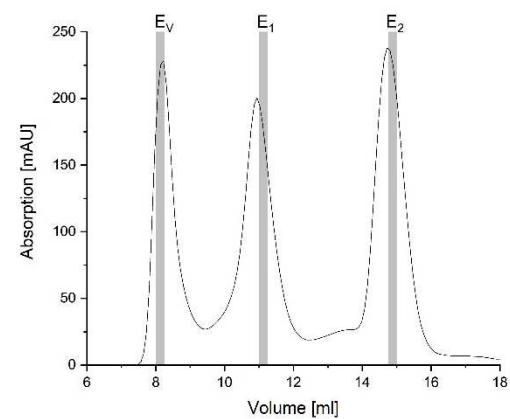


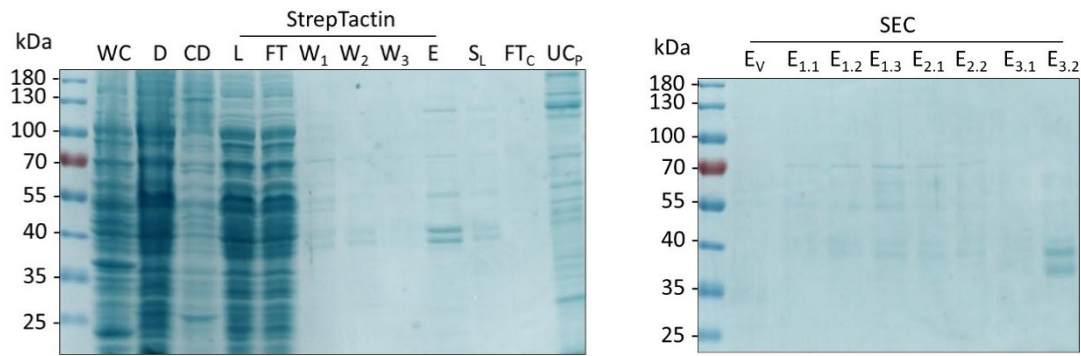
Figure 2: Purification of StrepII-TEV-CIPK23 in presence of 0.05 % BriJ35. (A) Coomassie-stained 10 % SDS gel and (B) Western blot analysis representing the various steps from the purification of CIPK23. WC = whole cells after 3h of expression with 1 mM IPTG; D = disrupted cells; CD = cell debris pellet; L = load; FT₁₋₄ = StrepTrap HP flow through fractions 1-4; W₁ = wash 1; W₂ = wash 2 (with 5 mM ATP) W₃ = wash 3 (without ATP); E₁₋₆ = Strep Tactin elution fractions; E_{V.1-3} = void peak E_V; E_{1.1-1.3} = SEC Elution peak E₁; E_{2.1-2.4} = SEC Elution peak E₂. The blot was developed using α -StrepII primary antibody and α -mouse-IgG-HRPO-coupled secondary antibody. (C) Strep Tactin affinity chromatogram of CIPK23. X-axis represents the elution volume in ml while the left Y-axis represents the UV absorption at 280 nm in mAU units and the right Y-axis represents the concentration of Desthiobiotin in mM (D) Size exclusion chromatogram of CIPK23. X-axis represents the elution volume in ml while the Y-axis represents the UV absorption at 280 nm in mAU units. The size exclusion chromatography was performed on a Superdex200 10/300. The grey bars in (C) and (D) represent the fractions shown on the SDS gel and Western blot. This figure was adapted from the Bachelor thesis of Carolin Sebastiany 2021 [26].

Since the last purification (Figure 2) suggested that Brij35 could improve but not fully ensure the stability of full length CIPK23, in the next trials, precautions to prevent degradation and improve stabilization were taken. Therefore 5 mM EDTA and 5 mM EGTA as well as 5 μ M Pepstatin-A were added to the resuspended cells for the inhibition of metallo- and aspartate-proteases respectively. Additionally 5 % glycerol was added to all purification buffers to further stabilize the protein [27].

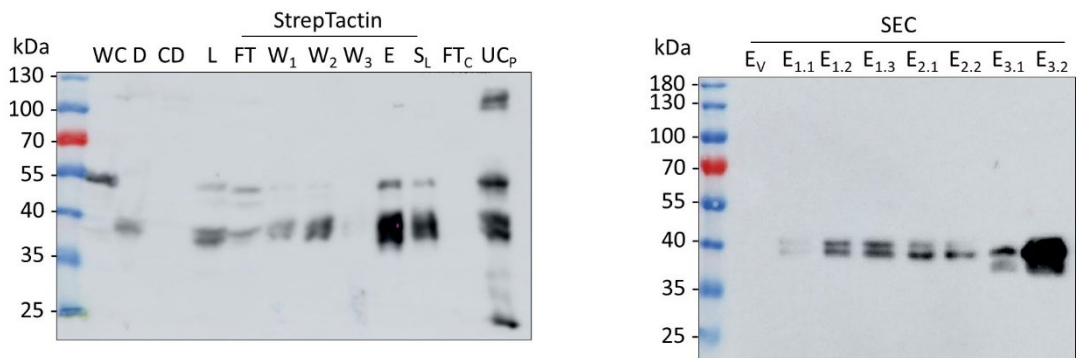
The Coomassie and Western blot (Figure 3.A and B) showed the same band pattern as for the purification with Brij35 before (Figure 2). Again, while in the whole cells the protein was expressed in its full length (55.9 kDa), as soon as the cells got disrupted a C-terminal degradation product of only 40 kDa appeared. Overall, only 0.62 mg protein from 8 g wet weight *E. coli* cells could be submitted to SEC as represented by a comparably small StrepTrap elution peak (Figure 2.C vs. Figure 3.C). Noteworthy high amounts of aggregates and degradation products were removed in the ultracentrifugation of the SEC load. The SEC chromatogram showed the same three peaks (Figure 3.D) as for the purification before (Figure 2.D), with elution volumes of 8 ml (E_V), 11 ml (E_1) and 15 ml (E_2).

Besides the overall lower intensities due to less protein that was loaded, the intensity of the E_1 peak, is almost diminished to the baseline. Taking a look at the bands in the Coomassie and Western blot, only the 40 kDa degradation fragments could be detected. With the use of EDTA, EGTA, Pepstatin-A and glycerol the CIPK23 protein could not be further stabilized, but no full length protein could be purified at all.

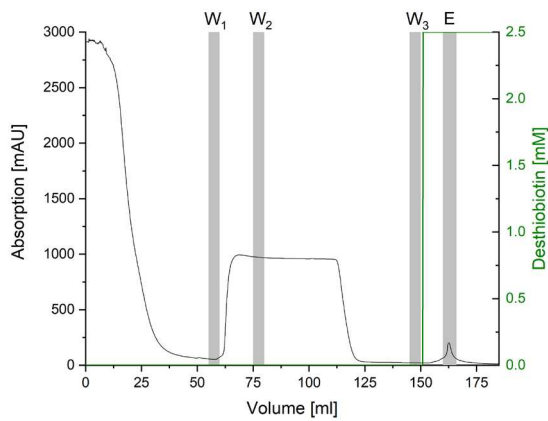
A)



B)



C)



D)

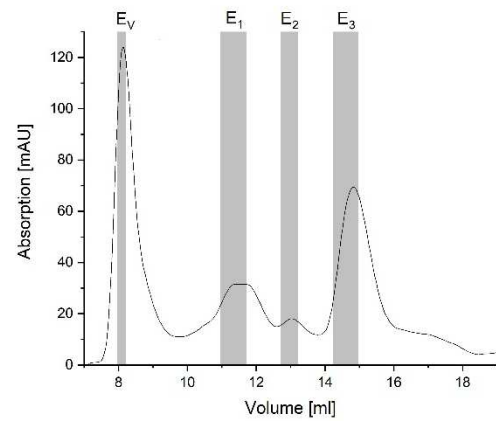


Figure 3: Purification of StrepII-TEV-CIPK23 in presence of 0.05 % Brij35, 5 mM EDTA, 5 mM EGTA, 5 μ M Pepstatin-A and 5 % glycerol. A) Coomassie-stained 10 % SDS gel and B) Western blot analysis representing the various steps from the purification of CIPK23. WC = whole cells after 3h of expression with 1 mM IPTG; D = disrupted cells; CD = cell debris pellet; L = load; FT = StrepTrap HP flow through; W₁ = wash 1; W₂ = wash 2 (with 5 mM ATP) W₃ = wash 3 (without ATP); E = Strep Tactin elution; S_L = SEC load; FT_C = flow through Amicon concentrator; UC_P = pellet after ultracentrifugation of SEC load; E_V = void peak E₁; E_{1.1-1.3} = SEC Elution peak E₁; E_{2.1-2.2} = SEC Elution peak E₂; E_{3.1-3.2} = SEC Elution peak E₃. The blot was developed using α -StrepII primary antibody and α -mouse-IgG-HRPO-coupled secondary antibody. C) Strep Tactin affinity chromatogram of CIPK23. X-axis represents the elution volume in ml while the left Y-axis represents the UV absorption at 280 nm in mAU units and the right Y-axis represents the concentration of Desthiobiotin in mM D) Size exclusion chromatogram of CIPK23. X-axis represents the elution volume in ml while the Y-axis represents the UV absorption at 280 nm in mAU units. The size exclusion chromatography was performed on a Superdex200 10/300. The grey bars in C) and D) represent the fractions shown on the SDS gel and Western blot. This figure was adapted from the Bachelor thesis of Carolin Sebastiany 2021[26].

Structural Modelling of full length CIPK23

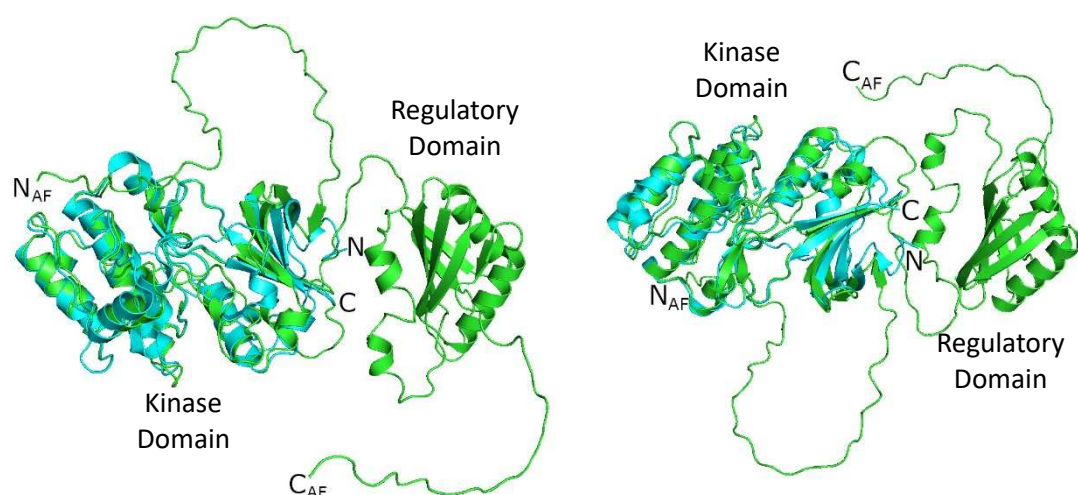
The purification of CIPK23 from *E. coli* did not result in the isolation of the full-length 55.9 kDa protein. Consistent over three purifications under different conditions always ~40 kDa degradation products were visible. To get insights into the structure and the potential reason for this finding, a structural model of the full-length StrepII-TEV-CIPK23 was created with AlphaFold 2.0 [28, 29]. This model was aligned to the resolved crystal structure of the CIPK23 kinase domain [17] and analyzed towards its surface hydrophobicity (Figure 4).

Besides the fact that the first 44 C α and the last 29 C α atoms could not be modeled with high reliability, the kinase domain could be aligned over 209 C α atoms with a RMSD of 0.84 Å (Figure 4.A). The structural model shows that the kinase domain is separated from the regulatory domain by a ~45 amino acid long, unstructured linker (junction domain) of which the first 25 aa are included in the crystal structure (amino acid 24-331 of the wildtype protein). Hence this the missing secondary structure in this area of the protein likely resembles the *in vivo* state.

Furthermore, the theoretical size of the StrepII-TEV tagged CIPK23 structure that was resolved so far (until amino acid 331) is 39.4 kDa [23]. This fits the size of the degradation products detected during the previous purifications. Hence, it can be assumed that this region in fact has no stabilizing secondary structure and is the major point of instability of the protein and is likely highly accessible for endogenous proteases.

The kinase is a cytosolic protein, which gets recruited to the plasma membrane by CBL1 or 9 [30]. It was stated by Kudla *et al.* (unpublished data) that the purification of CIPK23 requires the presence of Brij35 detergent. In order to get an insight into the background of this statement and to find an explanation, the surface of the structural model was colored according to Eisenberg hydrophobicity index [31] Figure 4.B. The coloring did not reveal a clear hydrophobic patch, which would explain the necessity of a detergent during the purification procedure. Only the NAF domain shows an increased amount of hydrophobic amino acids (Figure 4.B left). But in deviation from the AlphaFold model, this NAF domain should not be accessible, since it is bound to the active site of the kinase in the inactive state of CIPK23 [20, 32]. This correlates with the fact that the purification in presence of Brij35 did not yield in the purification of the full length protein.

A)



B)

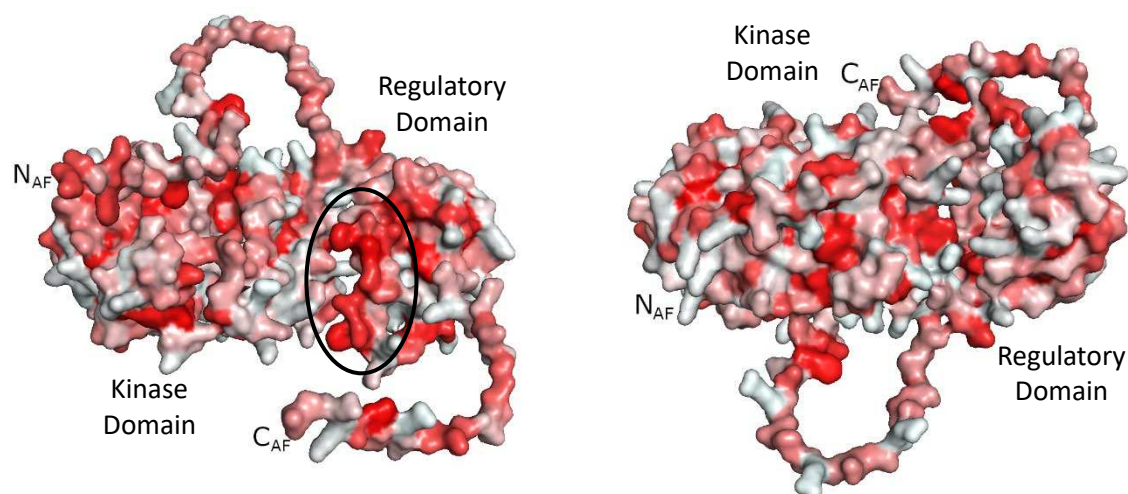


Figure 4: Structural modelling of CIPK23. A) AlphaFold model of full length StreptII-TEV-CIPK23 (green) and alignment with the resolved crystal structure of the N-terminal domain (cyan) (PDB entry 4CZU). The structures were aligned over 209 Ca atoms with a RMSD of 0.84 Å. B) Depiction of hydrophobicity of StreptII-TEV-CIPK23 AlphaFold model according to Eisenberg hydrophobicity scale (red = hydrophobic). The hydrophobic NAF domain is highlighted by a black oval. The right figures are rotated 180 degrees around the X-axis compared to left figures. The N- and C-termini are labeled as N and C for the crystal structure or N_{AF}C_{AF} for the AlphaFold model respectively.

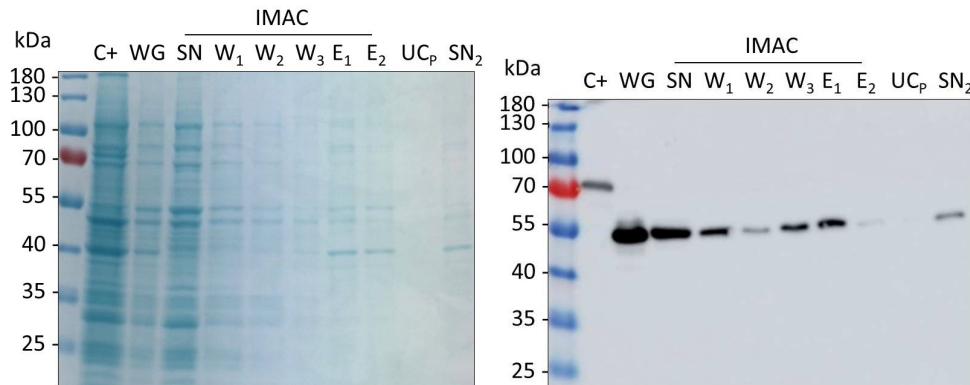
Expression and Purification trials from wheat germ lysate cell free expression

From the expression in *E. coli* and subsequent purification no stable full length CIPK23 could be obtained. Hence, the next attempt was to express CIPK23 in a cell free environment. Here a wheat germ lysate based CECF (continuous exchange cell free) approach was chosen, as it has been shown to be successful by Hashimoto *et al.* 2012 [22].

In first approaches the cell free expression of CIPK23 was tested with the pIVEX1.4_StreptII-TEV-CIPK23 (N-terminal StreptII-tagged CIPK23) compared to pIVEX1.4-CIPK23 (N-terminal 6xHis-Xa tag), resulting in successful expression for both constructs but overall high loss of protein during IMAC and Strep Tactin wash, respectively. The elution fractions were submitted to UV-Vis spectroscopic determination of the protein concentration. For the His-tagged version of CIPK23 53 µg and 39 µg for E₁ and E₂ while for the StreptII-tagged version 14.5 µg and 6.5 µg for E₁ and E₂ were eluted in 50 µl respectively. Since the yields from the His tag purification was significantly higher, the His-tagged version of CIPK23 was

chosen for further wheat germ expression attempts. An extensive screening for the optimization of the purification conditions, such as different chelating materials, was performed during the bachelor studies of Carolin Sebastiany, which showed best results for the purification of the His-tagged CIPK23 from magnetic Ni-NTA beads [26].

A)



B)

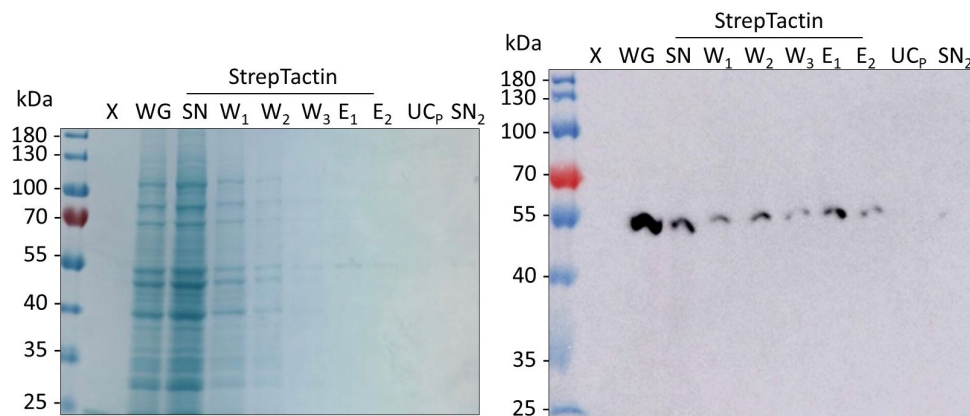


Figure 5: Purification of A) StrepII-TEV-CIPK23 and B) 6xHis-Xa-CIPK23 from wheat germ cell free expression. Coomassie-stained 10 % SDS gel and (B) Western blot analysis representing the various steps from the purification of CIPK23. C+ = positive control for the expression supplied by the wheat germ kit; WG = wheat germ reaction mix after 16 h of expression at 25 °C; SN = supernatant of IMAC/Strep Tactin magnetic beads; W₁₋₃ = wash; E₁₋₂ = elution; UC_p = pellet after ultracentrifugation; SN₂ = supernatant after ultracentrifugation; X = empty lane. The blot was developed using A) pentaHis or B) α -StrepII primary antibody respectively and α -mouse-IgG-HRPO-coupled secondary antibody. This figure was adapted from the Bachelor thesis of Carolin Sebastiany 2021 [26].

In the next attempt the 6xHis-Xa-CIPK23 was expressed under the same conditions as before. The reaction mix was submitted to ultracentrifugation after the 16 h expression, to remove potential aggregates. The resuspended pellet of this ultracentrifugation resulted in an intense band on the Western blot. Hence, the main percentage of the CIPK23 aggregated under the used expression conditions. This may explain why in the previous purification significant amounts of protein were lost during the purification steps.

Despite the loss of protein during ultracentrifugation, a minor amount remained in the supernatant and was submitted to IMAC magnetic beads purification. This resulted in a faint signal for the full length protein in the first two elution fractions which corresponded to 83 µg and 16 µg in 50 µl respectively. Although only signals at 55 kDa were visible in the blot, additional bands, probably degradation products, were visible on the Coomassie at 40 kDa. The protein solution was submitted to SEC purification. This resulted in a broad non homogeneous peak where none of the analyzed fractions resulted in a band on the Coomassie gel or the Western blot, likely due to too low concentrations.

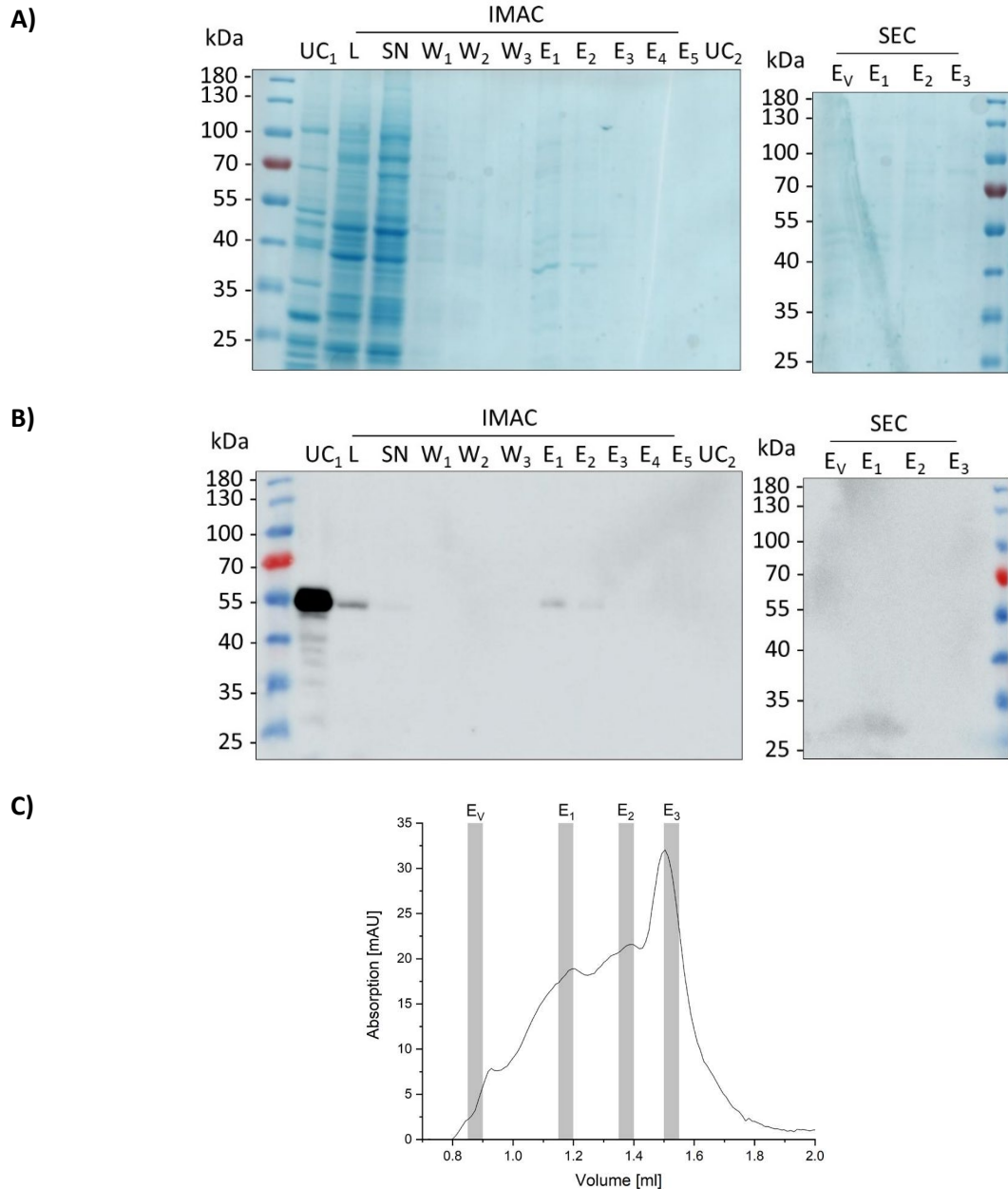


Figure 5: Purification of 6xHis-Xa-CIPK23 from wheat germ cell free expression. A) Coomassie-stained 10 % SDS gel and B) Western blot analysis representing the various steps from the purification of CIPK23. UC₁ = pellet after ultra centrifugation of reaction mix; L = IMAC load; SN = supernatant of IMAC magnetic beads; W₁₋₃ = IMAC wash; E₁₋₅ = IMAC elution; UC₂ = pellet after ultracentrifugation of SEC load; FT_C = flow through Amicon concentrator; UC_P = pellet after ultracentrifugation; E_V = void peak E_V; E₁ = SEC Elution peak E₁; E₂ = SEC Elution peak E₂; E₃ = SEC Elution peak E₃. The blot was developed using pentaHis primary antibody and α-mouse-IgG-HRPO-coupled secondary antibody. C) Size exclusion chromatogram of CIPK23. X-axis represents the elution volume in ml while the Y-axis represents the UV absorption at 280 nm in mAU units. The size exclusion chromatography was performed on a Superdex200 increase 3.2/100. The grey bars in C) represent the fractions shown on the SDS gel and Western blot.

Discussion

The main obstacle in this study was to express and purify CIPK23 in its full length. At first, the most common expression host for large scale expressions, *Escherichia coli* (*E. coli* Rosetta (DE3) pLysS), was chosen. This expression strain had been successfully used for the expression and purification of the kinase domain by Chaves-Sanjuan *et al.* 2014 [17] as well as for CBL1 and 9 (Chapter 3). Following their established expression protocol and adding Brij35 detergent to the purification buffers [25] resulted in detectable amounts of a soluble, but partially degraded protein. The C-terminal degradation could be detected as soon as the cells were disrupted. This may lead to the assumption that during cell disruption periplasmic proteases got in contact with the protein that was expressed in the cytosol. For the purifications shown in Figure 1 and 2 only cOmplete protease inhibitor tablets were used, which inhibit cysteine and serine proteases according to the manufacturer's manual [33]. Despite the attempt to prevent the C-terminal degradation of CIPK23 by further addition of Pepstatin-A for the inhibition of aspartate proteases as well as EDTA and EGTA for the inhibition of metallo-proteases, still degradation took place. Hence the observed degradation was not due to periplasmic proteases. On the other hand the addition of glycerol to further stabilize the protein by interacting with CIPK23 [27], did not lead to the desired result as well.

At this point it could be stated that full length CIPK23 is somehow intrinsically instable when expressed in *E. coli* and the complete stabilization and isolation of the full length CIPK23 from *E. coli* expression could not be established in this study. It needs to be taken into account that expression of eukaryotic proteins in a prokaryotic expression host like *E. coli* might lead to improper folding and posttranslational modification and hence negative influences on protein stability and functionality [34]. Neither disulfide bond formation or glycosylation motifs were reported for CIPK23 (UniProt entry Q93VD3 [35]), but only autophosphorylation events [22]. The introduction of a phosphate group is thought to rather have a regulatory effect than on the stability of the protein [36, 37]. The charged, hydrophilic phosphate group can result in structural rearrangements in the surroundings of the phosphorylated amino acid which can be essential for the regulation of the protein itself or its role in signal transduction. In order to comprise its function, the protein needs to be stable independent of its phosphorylation state [38].

In order to understand the formation of the degradation products and to identify the intrinsic region of breakage of the N-terminal 40 kDa CIPK23 fragments, an AlphaFold2 model of full-length CIPK23 was created. This structural model revealed an extended and unstructured junction domain which connects the N-terminal kinase domain with the C-terminal regulatory domain. Unstructured regions of a protein are often too flexible and not suitable for structure determination. On the other hand, the 3D structure of the CIPK23 kinase domain includes the first part of the junction and stabilizing hydrophobic interactions between the N-lobe and the junction are stated [17]. The structural model did not reveal a direct explanation for the use of Brij35 for the purification as no hydrophobic patches were visible. When the kinase domain of CIPK23 was crystalized, a CHAPS molecule was found at the active site [17]. Likely this is the origin for the idea to use detergent for the purification procedure. It was shown that the presence of Brij35 during the purification procedure could prevent the complete aggregation of CIPK23 but was not able to stabilize its full-length form. Possibly the protein was not properly folded from the beginning on and aggregates upon cell disruption. In this case Brij35 might play a similar role as SDS during electrophoresis and keep the unfolded protein soluble, prevent aggregation and therefore elution in the void peak of the SEC.

To fully exclude that the instability and degradation of CIPK23 was due to the procaryotic expression host, further expression and purification attempts were performed in wheat germ CECF approaches. This had already been shown to work for CIPK23 by Hashimoto *et al.* 2012 [22] and with the addition of Brij35 showed initial improvements in this study. The full-length protein could be expressed and no degradation was observed during the purification procedure. Only little amounts could be purified and high amounts of aggregation occurred during expression. While the used kit is not able to introduce posttranslational modifications, like glycosylation, disulfide bonding or signal sequence cleavage [33], this should not be relevant for CIPK23 and is not the reason for the aggregation. During the bachelor thesis of Carolin Sebastiany [26] several attempts were made to improve the purification yields by adjusting the purification conditions, which did not lead to satisfying results. The switch to an eucaryotic expression system could vanish the N-terminal degradation products but the functionality remains questionable. The high amounts of aggregation lead to the assumption that the minor amounts of soluble protein were not properly folded as well and only remained soluble due to the present detergent.

In this study the purification of the full length CIPK23 could not be established and will remain to be complicated in the future likely due to the highly flexible unstructured junction domain. On the other hand, this flexibility is crucial for the full functionality of the protein and will complicate the structural analysis of this protein alone and in complex with its up- and downstream interaction partners CBL1/9 and AKT1.

References

1. Thor, K., *Calcium-Nutrient and Messenger*. Front Plant Sci, 2019. **10**: p. 440.
2. Dong, Q., et al., *Ca(2+) signaling in plant responses to abiotic stresses*. J Integr Plant Biol, 2022. **64**(2): p. 287-300.
3. Knight, H., *Calcium signaling during abiotic stress in plants*. Int Rev Cytol, 2000. **195**: p. 269-324.
4. Batistic, O. and J. Kudla, *Analysis of calcium signaling pathways in plants*. Biochim Biophys Acta, 2012. **1820**(8): p. 1283-93.
5. Whalley, H.J. and M.R. Knight, *Calcium signatures are decoded by plants to give specific gene responses*. New Phytol, 2013. **197**(3): p. 690-693.
6. Batistic, O. and J. Kudla, *Plant calcineurin B-like proteins and their interacting protein kinases*. Biochim Biophys Acta, 2009. **1793**(6): p. 985-92.
7. Batistic, O. and J. Kudla, *Integration and channeling of calcium signaling through the CBL calcium sensor/CIPK protein kinase network*. Planta, 2004. **219**(6): p. 915-24.
8. Cheong, Y.H., et al., *Two calcineurin B-like calcium sensors, interacting with protein kinase CIPK23, regulate leaf transpiration and root potassium uptake in Arabidopsis*. Plant J, 2007. **52**(2): p. 223-39.
9. Behera, S., et al., *Two spatially and temporally distinct Ca(2+) signals convey Arabidopsis thaliana responses to K(+) deficiency*. New Phytol, 2017. **213**(2): p. 739-750.
10. Rodenas, R. and G. Vert, *Regulation of Root Nutrient Transporters by CIPK23: 'One Kinase to Rule Them All'*. Plant Cell Physiol, 2021. **62**(4): p. 553-563.
11. Ragel, P., et al., *The CBL-Interacting Protein Kinase CIPK23 Regulates HAK5-Mediated High-Affinity K+ Uptake in Arabidopsis Roots*. Plant Physiol, 2015. **169**(4): p. 2863-73.
12. Wang, P., et al., *Mapping proteome-wide targets of protein kinases in plant stress responses*. Proc Natl Acad Sci U S A, 2020. **117**(6): p. 3270-3280.
13. Ho, C.H., et al., *CHL1 functions as a nitrate sensor in plants*. Cell, 2009. **138**(6): p. 1184-94.
14. Straub, T., U. Ludewig, and B. Neuhauser, *The Kinase CIPK23 Inhibits Ammonium Transport in Arabidopsis thaliana*. Plant Cell, 2017. **29**(2): p. 409-422.

15. Guo, Y., et al., *Molecular characterization of functional domains in the protein kinase SOS2 that is required for plant salt tolerance*. Plant Cell, 2001. **13**(6): p. 1383-400.
16. Sanchez-Barrena, M.J., et al., *The structure of the C-terminal domain of the protein kinase AtSOS2 bound to the calcium sensor AtSOS3*. Mol Cell, 2007. **26**(3): p. 427-35.
17. Chaves-Sanjuan, A., et al., *Structural basis of the regulatory mechanism of the plant CIPK family of protein kinases controlling ion homeostasis and abiotic stress*. Proc Natl Acad Sci U S A, 2014. **111**(42): p. E4532-41.
18. Walter, M., et al., *Visualization of protein interactions in living plant cells using bimolecular fluorescence complementation*. Plant J, 2004. **40**(3): p. 428-38.
19. Batistic, O., et al., *Dual fatty acyl modification determines the localization and plasma membrane targeting of CBL/CIPK Ca²⁺ signaling complexes in Arabidopsis*. Plant Cell, 2008. **20**(5): p. 1346-62.
20. Akaboshi, M., et al., *The crystal structure of plant-specific calcium-binding protein AtCBL2 in complex with the regulatory domain of AtCIPK14*. J Mol Biol, 2008. **377**(1): p. 246-57.
21. Sanchez-Barrena, M.J., et al., *Recognition and Activation of the Plant AKT1 Potassium Channel by the Kinase CIPK23*. Plant Physiol, 2020. **182**(4): p. 2143-2153.
22. Hashimoto, K., et al., *Phosphorylation of calcineurin B-like (CBL) calcium sensor proteins by their CBL-interacting protein kinases (CIPKs) is required for full activity of CBL-CIPK complexes toward their target proteins*. J Biol Chem, 2012. **287**(11): p. 7956-68.
23. Gasteiger E., H.C., Gattiker A., Duvaud S., Wilkins M.R., Appel R.D., Bairoch A. *The Proteomics Protocols Handbook*. 2005; Available from: <https://web.expasy.org/protparam/>.
24. Kuznecov, P., *Interaction Partners of Ca²⁺ dependent K⁺ channel AKT1 from Arabidopsis thaliana* in Biochemie I. 2019, Heinrich-Heine-Universität: Düsseldorf. p. 101.
25. Ma, Y., et al., *Preparative scale cell-free production and quality optimization of MraY homologues in different expression modes*. J Biol Chem, 2011. **286**(45): p. 38844-53.
26. Sebastiany, C., *Studies on the CBL-interacting serine/ threonine-protein kinase CIPK23 from Arabidopsis thaliana*, in Biochemistry I. 2021, Heinrich-Heine-Universität Düsseldorf. p. 85.
27. Vagenende, V., M.G. Yap, and B.L. Trout, *Mechanisms of protein stabilization and prevention of protein aggregation by glycerol*. Biochemistry, 2009. **48**(46): p. 11084-96.
28. Jumper, J., et al., *Highly accurate protein structure prediction with AlphaFold*. Nature, 2021. **596**(7873): p. 583-589.
29. Mirdita, M., et al., *ColabFold: making protein folding accessible to all*. Nat Methods, 2022. **19**(6): p. 679-682.
30. Xu, J., et al., *A protein kinase, interacting with two calcineurin B-like proteins, regulates K⁺ transporter AKT1 in Arabidopsis*. Cell, 2006. **125**(7): p. 1347-60.
31. Eisenberg, D., et al., *Analysis of membrane and surface protein sequences with the hydrophobic moment plot*. J Mol Biol, 1984. **179**(1): p. 125-42.
32. Albrecht, V., et al., *The NAF domain defines a novel protein-protein interaction module conserved in Ca²⁺-regulated kinases*. EMBO J, 2001. **20**(5): p. 1051-63.
33. biotechrabbit, *RTS 100 Wheat Germ CECF Kit Manual*. 2015: p. 28.
34. Netzer, W.J. and F.U. Hartl, *Recombination of protein domains facilitated by co-translational folding in eukaryotes*. Nature, 1997. **388**(6640): p. 343-9.
35. Consortium, T.U., *UniProt: the Universal Protein Knowledgebase in 2023*. Nucleic Acids Research, 2022. **51**(D1): p. D523-D531.
36. Rubin, C.S. and O.M. Rosen, *Protein phosphorylation*. Annu Rev Biochem, 1975. **44**: p. 831-87.
37. Cohen, P., *The origins of protein phosphorylation*. Nat Cell Biol, 2002. **4**(5): p. E127-30.
38. Johnson, L.N. and D. Barford, *The effects of phosphorylation on the structure and function of proteins*. Annu Rev Biophys Biomol Struct, 1993. **22**: p. 199-232.

Supplemental Information

Table S1: List of primers used for cloning and site directed mutagenesis.

Name	Sequence 5' → 3'	Length [bp]	GC [%]	Tm [°C]
CIPK23_Spe_For	TTTACTAGTGCTTCTCGAACAACGCCTTC	29	45	70
CIPK23_Xho_RG	TTTCTCGAGTTATGTCGACTGTTTTGCAATTGTC	34	38	70
TEV_CIPK23_fw	TACTTCCAGGCTTCTCGAACAACGCCT	27	52	65
TEV_CIPK23_rev	CAGGTTTTCACTAGTTTTTTCGAACTGCG	29	41	60
pIVEX 1.4 CIPK23 fw	GCGGCATCGAAGGCCGCGGCCGCTTAATTAACATATGAC CGCTTCTCGAACAACGC	57	56,1	>75
pIVEX 1.4 CIPK23 rev	AACCAGAAGAGCTGGGTACCTTAGTTAGTTACCGGATCCCT TATGTCGACTGTTTTGC	58	46,6	>75



Figure S1: Plasmid map of pET24b(+)-StreptII-MCS. The sequence for the N-terminal StreptII tag was cloned into the original pET24b(+) vector (Novagene) by Kudla et al. (unpublished). The restriction sites for *SpeI* and *XhoI* are depicted, which were used for the insertion of the *cipk23* gene.

Chapter 3 - The calcineurin-B like protein 1

Title: Calcium binding of AtCBL1: first structural and functional insights

Authors: Alexandra Bork, Sander H. J. Smits, Lutz Schmitt

Published in: To be submitted

Own proportion of this work: 80 %

Cloning of expression plasmids

Expression and Purification of CBL1 wildtype and mutants

ITC analysis of CBL1 wildtype and mutants

In silico analyses (alignments, modeling)

Data analysis

Preparation of figures

Writing of the manuscript

Calcium binding of AtCBL1: first structural and functional insights

Alexandra Bork¹, Sander H J Smits^{1,2}, Lutz Schmitt^{1,*}

¹Institute of Biochemistry, Heinrich Heine University Düsseldorf, Düsseldorf, Germany.

²Center for Structural Studies, Heinrich Heine University Düsseldorf, Düsseldorf, Germany.

* To whom correspondence should be addressed:

Lutz Schmitt
Institute of Biochemistry
Heinrich Heine University Düsseldorf
Universitätsstr. 1
40225 Düsseldorf, Germany
Phone: +49(0)211-81-10773
Fax: +49(0)211-81-15310
E-mail: lutz.schmitt@hhu.de

Keywords: *A. thaliana*, EF-hand, Ca²⁺ binding, Calcineurin-B-like protein 1, ITC

Abstract

CBL1 is an EF hand Ca²⁺ binding protein from *A. thaliana* that is involved in the detection of cellular Ca²⁺ signals and the downstream signal transmission by interaction with the protein kinase CIPK23. So far, the structure and calcium ion binding affinities of CBL1 remain elusive. In this study it was observed that CBL1 has a tendency to form higher oligomeric states due to an intrinsic hydrophobicity and the presence of the detergent Brij35 was required for the purification of monomeric and functional protein. Functional insights into the *in vitro* Ca²⁺ binding capabilities of CBL1 were obtained by isothermal titration calorimetry (ITC) of the wildtype protein as well as single site EF hand mutants. Based on our results, a binding model of CBL1 for Ca²⁺ *in vivo* is proposed. Additionally, upon both, ITC measurements and the analysis of an AlphaFold2 model of CBL1, we could gain first insights into the formation of the dimer interface. We could identify an area around EF hand 4 to be relevant for the structural and functional integrity of monomeric CBL1 and likely EF hand 1 to be involved in the dimer interface.

Introduction

Mineral household is one of the main aspects of plant nutrition. These minerals can be divided into macro (e. g. Ca²⁺, Mg²⁺) and micro (e. g. Mn²⁺) nutrients based on their amounts required [1, 2]. Amongst the macronutrients, Ca²⁺ plays an essential role in plants as a second messenger. It is for example involved in the control of a variety of cellular processes [3, 4]. While the cytosolic Ca²⁺ concentration is in a range of 100-200 nM at resting level; the cell wall, vacuole, ER and mitochondria contain Ca²⁺ in concentrations up to 1-10 mM. Upon a variety of extracellular stimuli, the cytosolic Ca²⁺ concentration can rise up to low micromolar levels (~1- 1.5 µM) [5-8]. These fluctuations in cytosolic Ca²⁺ concentrations can be caused by changes in biotic or abiotic environmental factors such as salt stress, drought, heat or cold [9]. The complex changes in the cytosolic Ca²⁺ concentration of plants are also known as Ca²⁺ signatures [10, 11].

These signatures can be detected and further translated by a variety of calcium-binding proteins. Amongst these proteins is a class called calcineurin-B-like proteins (CBL), which upon Ca²⁺ binding show increased affinities towards their interacting calcium sensor/CBL-interacting protein kinases (CIPK) and form a complex network in plant cell signaling events [12]. The interaction between CBLs and CIPKs is

mediated by the NAF domain of the kinase. The NAF motif has an autoinhibitory function in the absence of the CBL protein, since it blocks the kinase active site [13]. Upon interactions with a certain CBL the NAF domain is released from the kinase active site, attaches to the CBL protein [14] and leaves the active site open for substrate binding and phosphorylation [15].

CBL binding to the CIPK protein triggers a complex network of phosphorylation events [10, 16]. One example for such a signaling cascade is the activation of the *A. thaliana* K⁺ channel AKT1 at the plasma membrane of root cells upon low K⁺ stress. The channel gets activated through phosphorylation by the kinase CIPK23 which itself gets activated by the binding of CBL1 or CBL9 upon Ca²⁺ signals [17, 18]. CBLs were found to be phosphorylated by CIPKs as well [17]. At a conserved C-terminal FPSF motif, the serine sidechain was found to be phosphorylated upon CIPK-CBL complex formation. This phosphorylation did not have effect on the CBL1 stability or localization. Neither does it have an impact on the CIPK23-CBL1 interaction but it is essential for the activation of AKT1. If the CBL1 phosphorylation site is impaired, no AKT1 mediated K⁺ currents can be detected in *Xenopus* oocytes [17]. On the other hand, CBL10 has been found to have an inhibitory effect on the AKT1 channel activity by directly competing with the CIPK23-CBL1/9 complex for the interaction [19].

All CBL proteins consist of a conserved core and are divided into two subgroups, one with a short N-terminal domain with lipidation sites and the other with an extended N-terminal domain without lipid modifications similar to the K⁺ channel interacting proteins (KChIP) [20]. While the latter primarily are located to the vacuolar membrane (e.g. CBL2, and CBL10), the CBLs of the subgroup with short N-terminus locate to the plasma membrane [20-22]. CBL1, which will be the object of this study, harbors a short N-terminus with a N-terminal myristoylation and S-acylation site at Cys3 [20, 21]. Since CBL1 belongs to the subgroup of CBLs that locate to the plasma membrane, CIPK23 gets recruited to the plasma membrane upon interaction with CBL1 as well. Thereby CIPK23 comes in proximity to its downstream phosphorylation target AKT1 [16, 23]. The myristoylation was necessary for kinase activation but not for membrane association as observed for the related CBL4 [24]. Further Batistic *et al.* state that lipid groups might introduce cooperativity to the Ca²⁺ binding of CBL proteins, but do not comprise a calcium-myristoyl switch mechanism like it was stated for other N-myristoylated Ca²⁺ binding proteins [20, 25].

The core domain of each CBL includes four potential Ca²⁺ binding sites. These so called EF-hand motifs consist of a helix (helix E) - loop – helix (helix F) motif [26]. They come in pairs, also known as EF-lobes and are separated by a conserved number of amino acid residues [12, 27]. The binding loop classically consists of 12 amino acids with 6 residues involved in the coordination of the Ca²⁺ ion; termed X, Y, Z, X, -Y, -Z. Thereby Ca²⁺ is coordinated in a classical bipyramidal pentagonal geometry [28]. The sidechains of Asp or Asn are commonly involved in Ca²⁺ complexation at positions X and Y, and the sidechains of Asp, Asn or Ser at the Z position. At the Y position, the carbonyl oxygen of the peptide bond of the backbone further stabilizes Ca²⁺ binding and at the X position, a water molecule is involved. The Z coordinate is filled by a conserved Glu [20, 29].

The first EF hand in CBL1 contains a binding loop sequence, which is uncommon for EF hands, but conserved in CBL proteins. This loop consists of 14 amino acids instead of the usual 12, but is still capable of binding Ca²⁺. Here, differing from the canonical sequence, the X and Y are occupied by Ser and Ile, respectively, while at -Y, the main chain carbonyl group of Leu is involved in Ca²⁺ binding [20, 29]. EF hand 2 has an amino acid substitution from Glu to Asp at the -Z coordinate, which should impair Ca²⁺ binding. The last two EF hands of CBL1, namely EF hand 3 and 4, correspond to the canonical EF

hand motif [12, 20, 30]. The number and arrangement of canonical to non canonical EF hands varies for all CBL proteins. Thereby these proteins exhibit different affinities to Ca^{2+} and allow a differential activation of the respective CBL-CIPK complexes and subsequent targets [20]. Crystallization studies of CBL2 alone and in complex with the regulatory domain of CIPK14 gave rise that the Ca^{2+} binding affinity and capability of the CBL protein might vary between the free and kinase bound state. Namely, free CBL2 had two Ca^{2+} ions bound while in complex with CIPK14 regulatory domain Ca^{2+} was found in all four EF hands [29, 31].

First *in vitro* insights into Ca^{2+} binding to CBL proteins was provided by the crystal structures of CBL2 and CBL4. Whilst CBL2 was crystalized with Ca^{2+} bound to EF hands 1 and 4; CBL4 was crystalized with either Ca^{2+} bound to all 4 EF hands or Ca^{2+} bound to EF hands 1-3 and Mn^{2+} to EF hand 4 when preincubated with CaCl_2 or a 1:1 mixture of CaCl_2 and MnCl_2 respectively [29, 32]. Whether the Mn^{2+} binding has an impact *in vivo*, or is just a crystallization artifact has not been conclusively clarified yet. Furthermore, the CBL4 structure was shown as a crystallographic dimer with the dimer interface formed by the C-terminal end of helix F3, the subsequent loop and the N-terminal end of helix E4. In detail a hydrogen bond is formed by Ser144 and its symmetry related residue. Sedimentation equilibrium experiments verified the presence of both a monomeric and dimeric CBL4 species, with an increase of the dimeric fraction correlating with increasing Ca^{2+} concentrations [32].

In this study, we heterologously expressed CBL1 from *A. thaliana* in *E. coli* and purified it to homogeneity. The oligomeric state was subsequently analyzed by multi-angle-light scattering (MALS) and its *in vitro* binding behavior towards Ca^{2+} , Mn^{2+} and Mg^{2+} experimentally by isothermal titration calorimetry (ITC). Based on these findings, we postulate a Ca^{2+} binding model and a potentially relevant binding of Mn^{2+} .

Material and Methods

Cloning

The *cbl1* gene from *A. thaliana* was amplified via PCR, introducing a 5' NheI cleavage site and a 3' SalI cleavage site using NheI-CBL1 fw and CBL1-SalI rev primers listed in Table S1 into pET24b(+) vector (Novagen). The N-terminal StrepII tag and the a TEV protease cleavage site were introduced into the pET24b(+)-CBL1 plasmid via Q5® Site-Directed Mutagenesis using StrepII-CBL1 fw and rev, TEV-CBL1 fw and rev primers respectively and following the manufacturer's instructions (NEB). The resulting plasmid pET24b(+)-StrepII-TEV-CBL1 was verified by sequencing. All mutations or deletions were introduced into the plasmid by site-directed mutagenesis. The respective primers were designed using NEBaseChanger™ and are listed in Table S1. All generated plasmids were verified by sequencing (Microsynth) and used for transformation of *E. coli* Rosetta (DE3) pLysS. The nomenclature E56, D91, E128, E172 etc. of the mutants is based on the sequence of the non-tagged CBL1 protein.

Gene Expression

StrepII-TEV-CBL1 protein (further referred to as wild type) as well as all the mutants were expressed from an IPTG inducible pET24b(+) vector using the following protocol. A single transformed *E. coli* Rosetta (DE3) pLysS colony was used to inoculate 50 ml of LB medium supplemented with 50 µg/ml kanamycin (pET24b(+)) and 36 µg/ml chloramphenicol (pLysS) in a baffled flask and grown for 14 h at 37 °C with 180 rpm shaking. 2 l 2xYT medium in a 5 l baffled flask were supplemented with 50 µg/ml kanamycin and 36 µg/ml chloramphenicol and inoculated with 50 ml of overnight culture. The cells were grown at 37 °C shaking at 180 rpm until an OD_{600} of 0.6 - 0.8 was reached. Prior to induction, the cells were cooled down to 25 °C for 30 min and IPTG was added to a final concentration of 1 mM to

induce the expression. The cells were grown for further 3 h and subsequently harvested by centrifugation at 5000 g for 20 min at 4 °C. The cell pellets were washed with resuspension buffer (50 mM Tris pH 8.0, 150 mM NaCl) and centrifuged again for 10 min at 4000 g at 4 °C. The resulting cell pellets were frozen as 8 g aliquots in liquid nitrogen and stored at – 80 °C until further use.

Protein Purification

A two-step purification approach was used for the isolation of StrepII-tagged CBL1 wildtype and variant proteins. Each cell pellet (8 g) was resuspended in 50 ml resuspension buffer containing 1 mg DNase I (Sigma), 1 mM MgCl₂ and 1 complete™ EDTA free Protease inhibitor tablet (Roche) and stirred for 1 h at 10 °C. The cells were disrupted by passing twice through a high-pressure cell disrupter (Constant Systems) at 1.5 bar at 10 °C. The lysate was centrifuged at 130000 g for 45 min at 4 °C to remove cell debris. 0.25 % (w/v) Brij35 was added to the supernatant and incubated at 10 °C for 30 min under mild stirring.

The cleared lysate was then applied to two 5 ml StrepTrap™ HP (Cytiva) columns (1 column volume (CV) = 10 ml) pre-equilibrated with wash buffer (50 mM Tris pH 8.0, 150 mM NaCl, 0.05 % (w/v) Brij35) at a flow rate of 2 ml/min. The column was washed with 8 CV of wash buffer. CBL1 protein was eluted with 3 CV of wash buffer supplemented with 2.5 mM Desthiobiotin. The elution fractions containing the protein were pooled and concentrated in an Amicon Ultra-15 centrifugal filter concentrator with a 10 kDa cutoff membrane (Millipore) to a final volume of 5 ml. The protein concentration was determined with a NanoDrop One (Thermo Scientific). 5 mM EDTA and 5 mM EGTA were added to the concentrated protein and the solution was further centrifuged for 30 min at 4 °C and 162500 g to remove potential aggregates. The concentrated protein solution was further purified using size exclusion chromatography (SEC). It was applied to a HiLoad Superdex75 pg 16/600 column (GE) equilibrated with SEC buffer (50 mM Tris pH 8.0, 150 mM NaCl and 0.05 % (w/v) Brij35) at a flow rate of 1 ml/min. The eluted protein fractions were collected, pooled and the concentration was determined using NanoDrop One as described above.

The purity of the protein was analyzed by SDS-PAGE (15 % gels) and Coomassie stain (1 g/L Coomassie® Brilliant Blue G250 (SERVA), 50 % (v/v) methanol, 10 % (v/v) glacial acetic acid). Western blot analysis was further performed to detect CBL1 via its StrepII-tag using Strep tag® II monoclonal primary antibody (mouse) (Millipore) and α-mouse-HRP coupled secondary antibody (Jackson Immuno Research) following standard protocols.

Mass Spectrometry

Protein containing bands were processed as described by Poschmann *et al.* 2015 [33]. Briefly, bands were destained, washed, reduced with dithiothreitol, alkylated with iodoacetamide and digested with trypsin (Serva, Heidelberg, Germany) in 50 mM NH₄HCO₃ overnight at 37 °C. Tryptic peptides were extracted with 0.1% trifluoroacetic acid and subjected to MS-coupled liquid chromatography. For peptide separation over a 120 minute LC-gradient with 300 nL/min an Ultimate 3000 Rapid Separation liquid chromatography system (Thermo Scientific, Bremen, Germany) equipped with an Acclaim PepMap 100 C18 column (75 µm inner diameter, 25 cm length, 2 µm particle size from Thermo Scientific, Bremen, Germany) was used. MS analysis was carried out on a Q-Exactive plus mass spectrometer (Thermo Scientific) operating in positive mode and equipped with a nano electrospray ionization source. Capillary temperature was set to 250 °C and source voltage to 1.5 kV. Survey scans were carried out over a mass range from 200-2,000 m/z at a resolution of 70,000 (at 200 m/z). The target value for the automatic gain control was 3,000,000 and the maximum fill time 50 ms. The 20 most intense peptide ions (excluding singly charged ions) were selected for fragmentation. Peptide

fragments were analyzed using a maximal fill time of 50 ms and automatic gain control target value of 100,000 and a resolution of 17,500 (at 200 m/z). Already fragmented ions were excluded for fragmentation for 10 s.

Acquired spectra were searched using Peaks Studio version 10.6 against the SwissProt dataset (release 2021_07, 219740215 entries) using for the main search a precursor mass tolerance of 20 ppm and a mass tolerance of 0.2 Da for fragment spectra. Carbamidomethyl at cysteines was set as fixed modification and 311 variable modifications were considered within the Peaks PTM node. Predefined values were used for other parameters including a maximum of three PTM per peptide.

SEC-MALS

For SEC-MALS analysis, a Superdex75 increase 10/300 column (GE) was equilibrated with SEC buffer (50 mM Tris pH 8.0, 150 mM NaCl, 0.05 % (w/v) Brij35) at a flow rate of 1 ml/min (Agilent Technologies 1200 series) and connected to a miniDAWN TREOS II light scattering device and Optilab-TrEX R-detector (Wyatt Technology Corp.). Typically, 200 µg protein sample was loaded onto the column and the obtained data were analyzed with ASTRA 7.3.2 software (Wyatt Technology Corp.). All proteins were analyzed as Brij35 detergent conjugates (dn/dc = 0.1850 ml/g).

ITC

All ITC experiments were performed with freshly purified protein. Chelex 100 resin (Biorad) was used to remove potential traces of Ca^{2+} , Mn^{2+} or any other divalent ions. The SEC buffer was incubated with Chelex for 30 min under mild agitation. Consequently, CaCl_2 , MnCl_2 and MgCl_2 titrant solutions were prepared to a final concentration of 1.125 mM using the Chelex treated SEC buffer. The concentration of the purified protein was adjusted to 1.5 mg/ml (56 µM) either by an additional concentration step (Amicon Ultra-15, 10 kDa, Millipore) or dilution with Chelex treated ITC buffer. Chelex was added to the protein solution 10 min prior to the measurements and the sample was incubated at room temperature under mild agitation.

The MicroCal200 (Malvern Panalytical) MicroCalorimeter was washed with water and methanol between each measurement. Both, sample and reference cells, were rinsed with Chelex treated ITC buffer before loading the protein and buffer solutions to the sample and reference cells, respectively. The measurements were performed at 25 °C under stirring at 750 rpm by adding 39.4 µl titrant solution (first titration 0.4 µl and subsequently 1 µl each). The reference power was set to 7 µcal/sec and after an initial delay of 60 sec, a spacing of 150 sec was used in between the injections.

MicroCal PEAQ-ITC analysis software (Malvern Panalytical) was used for data analysis. The possible fitting models “One Set of Sites”, “Two Sets of Sites” and the “sequential fitting model (2-4 sites)” were tested and the model resulting in the lowest reduced Chi-Square was chosen for the respective data set. For each series of measurements, one measurement titrating the protein with buffer and one measurement titrating the buffer with the used CaCl_2 , MnCl_2 or MgCl_2 solutions were performed as controls. As these controls did not lead to detectable signals, the data was corrected according to the offset calculated by the PEAQ software.

Figure preparation

For the preparation of the figures, the following programs were used: OriginPro 2019 (Origin Lab) Version 9.6.0.172, PEAQ analysis software (Malvern Panalytical) Version 1.41, PowerPoint (Microsoft Office) Version 2302. The structural model of CBL1 was created with AlphaFold2 [34, 35] and the figures of CBL1 and CBL4 (PDB entry 1v1f) were prepared using PyMol™ software version 2.5.3 Schrödinger, LLC (www.pymol.org).

Results

Structural model of CBL1

CBL1 is known to be a calcium ion sensor in *A. thaliana*, which is involved (via CIPK23 activation) in activating the uptake of potassium ions by AKT1. As this process is only poorly understood so far, we analyzed the function of CBL1 *in vitro*. The 3D structure of CBL1 has not been determined so far by crystallography or any other technique. Therefore and to gain insights into the 3D structure, a structural model of StreptII-TEV-CBL1 (further called CBL1 wildtype) was calculated using AlphaFold2 [34, 35] (Figure 1).

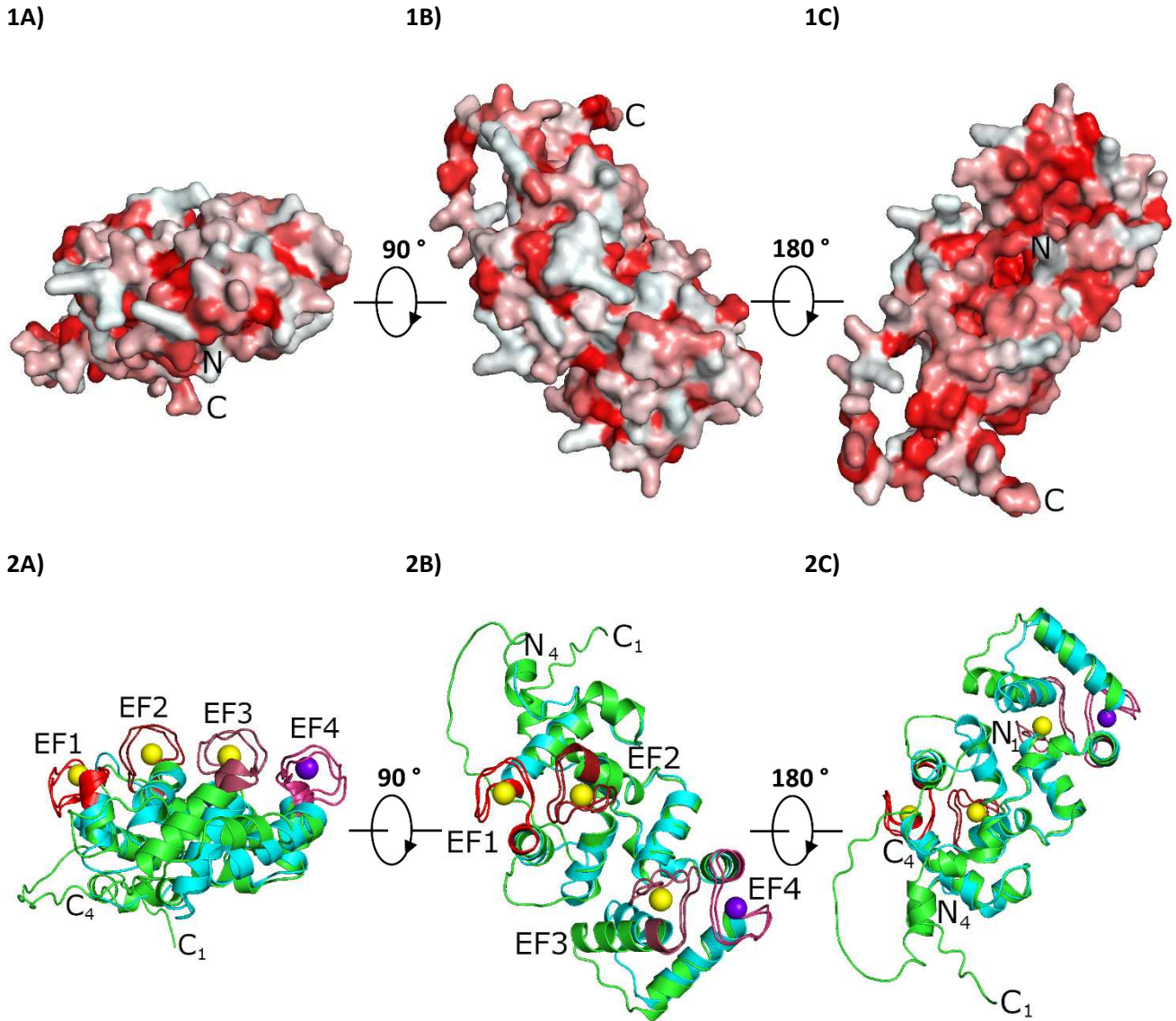


Figure 1: Structural model of CBL1. 1) Depiction of the hydrophobicity of StreptII-TEV-CBL1 AlphaFold model according to Eisenberg hydrophobicity scale (red = hydrophobic) Figure 1.B is rotated 90 degrees around the X-axis compared to figure 1.A, and 1.C is rotated 180° degrees compared to figure 1.B) Structural alignment of the AlphaFold2 generated StreptII-TEV-CBL1 structure (green) and the CBL4 structure (cyan) (PDB Entry 1v1f) with RMSD 1.29 Å over 185 Ca atoms. Ca^{2+} and Mn^{2+} ions from the CBL4 structure are depicted as yellow and purple spheres, respectively. EF hand 1 of both proteins is coloured in red, EF hand 2 in firebrick, EF hand 3 in raspberry and EF hand 4 in magenta.

CBL1 *in vivo* is stated to have two N-terminal lipid modifications [21]. Therefore, it is likely associated to a membrane. Thus, the structural model of CBL1 wildtype was analyzed towards its hydrophobicity by color-coding the protein according to Eisenberg hydrophobicity scale [36] (Figure 1.1). Here, red resembles hydrophobicity. One immediately can identify an accumulation of hydrophobic residues at one side of the protein (Figure.1C). As the N-terminus is exposed to this side and even though it is prolonged by the StrepII tag in this structure, it is possible that the protein is associated to the membrane from this particular end. However, in complex with CIPK23 this hydrophobic crevice is stated to bind the NAF domain of the kinase [31]. Hence a membrane association of this part would be contradictory.

In order to gain further insights, the CBL1 model was aligned to another member of CBL family, specifically to the crystal structure of CBL4 (PDB entry 1v1f) [32] (Figure 1.2). CBL4 is a member of the same subgroup of CBL proteins as CBL1 (short N-terminus) and was crystalized with Ca^{2+} bound to EF1-3 and Mn^{2+} bound to EF4, respectively. With a RMSD of 1.29 Å over 185 Cα atoms, the structures showed a high similarity. Comparing now the finding of the hydrophobic side of CBL1 (Figure 1.1C) with the structural alignment, this statement is further reinforced as this hydrophobic side seems to be opposite of the EF hands and therefore, if this side really is attached to the membrane, leaving the EF hands exposed to the cytosol.

Purification of CBL1 needs Brij35

A first step towards elucidating the function of CBL1 is the purification of functional and monomeric CBL1 protein. The CBL1 protein was produced by gene expression under a T7 promoter with a N-terminal StrepII tag and TEV cleavage site in *E. coli* Rosetta (DE3) pLysS and purified by StrepTactin affinity chromatography and size exclusion chromatography.

Purified CBL1 protein (without any detergent) eluted as a single peak (Figure S1) and exhibited a particle size of 225.6 ± 0.90 kDa as determined by SEC-MALS analysis. The calculated molecular weight of StrepII-TEV-CBL1 is 26.55 kDa (ProtParam, ExPASy [37]). Therefore, 225.6 ± 0.90 kDa would suggest a nonameric species. Since literature suggests N-terminal lipid modifications in the protein *in vivo* [21] and the analysis of the structural model also suggested a hydrophobic surface, the effect of detergent was tested on CBL1. The addition of 0.05 % (w/v) Brij35 to the SEC buffer shifted the elution profile to higher elution volumes and split the previously broad peak into three separated peaks (Figure S1), representing particles of 154.1 ± 0.97 kDa, 69.7 ± 0.67 kDa and 39.6 ± 0.47 kDa sizes, assuming that the protein was not interacting with the detergent micelles. As these sizes were still too high compared to the theoretical value, the results were analyzed as detergent conjugates, resulting in sizes of 54.4 ± 0.37 kDa and 25.1 ± 0.29 kDa for the second and third peak. This fits well to the theoretical size of 26.55 kDa for the monomer and 53.1 kDa for dimeric protein. Altogether, this implies that CBL1 interacts with a Brij35 micelle and needs the presence of detergent to be purified in its monomeric form. Hence, 0.05 % (w/v) Brij35 was incorporated in the buffers for all further purifications (Figure S2).

Since it was shown that CBL4 dimerizes upon Ca^{2+} binding [32], the effect of Ca^{2+} was also tested on CBL1 wildtype protein, which was purified as monomer. However, SEC-MALS confirmed the size of CBL1 in presence of 5 mM Ca^{2+} in the MALS buffer as monomeric (25.4 kDa). In an additional test, wildtype CBL1 was submitted to a SEC-MALS analysis after the incubation with 260 μM CaCl_2 resulting in particle sizes of 24.2 ± 0.37 kDa, hence CBL1 clearly did not dimerize in the presence of Ca^{2+} (Figure S5)

Interaction of CBL1 wildtype protein with different ions

CBL1, as an EF hand protein, is predestined to bind Ca^{2+} , but Mn^{2+} and Mg^{2+} were of further interest in this study as well. The EF hand 4 of CBL4 was shown to be crystalized in a Mn^{2+} bound state [32] and Mg^{2+} , besides its important role as macronutrient in plants [2], was shown to bind to other members of the EF hand protein family (CaM [38] and DREAM [39]). Hence, we analyzed the binding behavior of purified CBL1 wildtype (Figure S1) in its monomeric and dimeric form in respect to Ca^{2+} , Mn^{2+} and Mg^{2+} by isothermal titration calorimetry (ITC) (Figure 2 and Table 1, 2, 3).

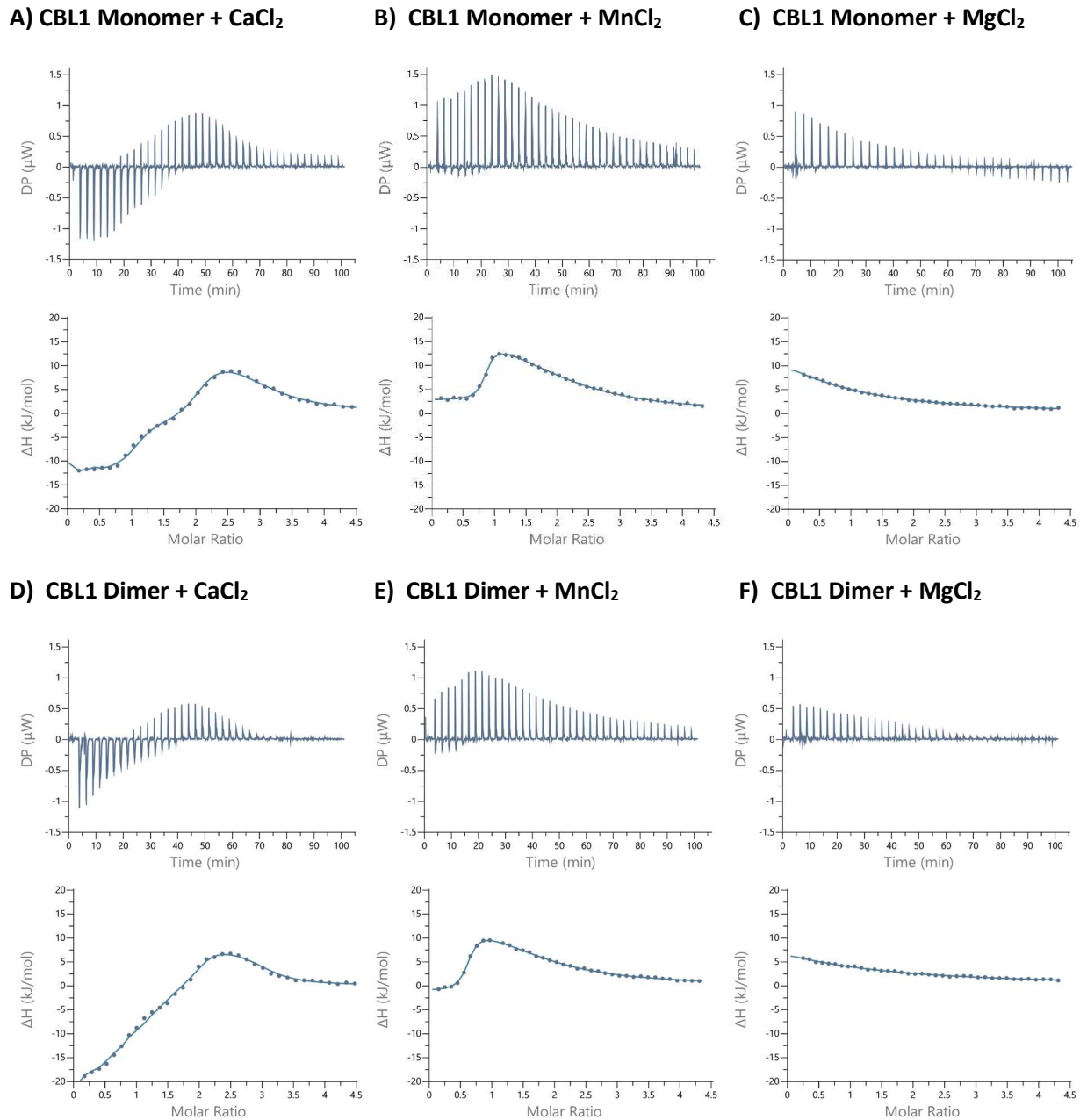


Figure 2: Interaction of CBL1 wildtype protein with different ions. ITC raw data and binding isotherms of 56 μM StrepII_{TEV}-CBL1 titrated with 1.13 mM CaCl_2 (A), MnCl_2 (B) or MgCl_2 (C) respectively. The protein was analyzed at 25 °C in its monomeric (1) and dimeric (2) form. In the upper panels the raw data is depicted. The Y-axis represents the change in heat capacity (μW) while the X-axis represents the time (min). The lower panel represents the integrated spikes with respect to time. Here the X-axis represents the molar ratio (ion: protein) while the Y-axis represents the change in heat capacity (ΔH). The data points were fitted with the fitting model resulting in the lowest reduced Chi-Square. For the CaCl_2 binding isotherm, this was the sequential fitting model with 3 sites. The MnCl_2 binding isotherm was fitted with the two sets of sites model. The MgCl_2 binding isotherm was fitted with the 'one set of sites model'.

The binding isotherm of the CBL1 wildtype titration with Ca^{2+} exhibited three phases for both, the monomeric (Figure 2.1A) and dimeric protein (Figure 2.2A), which can be assigned to three stoichiometrically, different binding events. Thus, Ca^{2+} binds to three EF hands of the monomeric as well as the dimeric protein. In case of the monomeric protein, two EF hands bound in an exothermic manner with K_D values of 8.18 ± 1.85 nM and ΔH of -12.5 ± 0.45 kJ/mol for one and 373 ± 75 nM and -3.14 ± 0.88 kJ/mol for the second. The third EF hand bound endothermically with a K_D of 8.60 ± 2.15 μM and ΔH of 15.3 ± 1.58 kJ/mol. In comparison, two EF hands of the dimeric protein showed values in the same order of magnitude, while for the third EF hand, the binding affinity was significantly increased from 373 ± 75 nM in case of monomeric protein to 52.1 ± 23.5 nM for the dimeric protein. Furthermore, the binding enthalpy was also changed from exo- to endothermically from -3.14 ± 0.88 kJ/mol to 3.64 ± 1.02 kJ/mol (Table 1).

On the contrary, the binding isotherm of the CBL1 wildtype titration with Mn^{2+} showed only two phases for both oligomeric states. Mn^{2+} was bound stoichiometrically by one EF hand and with lower affinity by two additional EF hands for both monomeric and dimeric CBL1. While the monomer CBL1 bound Mn^{2+} with a K_D of 186 ± 61.2 nM and ΔH of 2.44 ± 0.21 kJ/mol to one EF hand and a K_D of 36.3 ± 3.51 μM and ΔH of 14.7 ± 0.68 kJ/mol for two non-discriminable EF hands, dimeric CBL1 bound with comparable K_D values. For the two non-discriminable EF hands, the enthalpy with 11.9 ± 0.34 kJ/mol was comparable to the monomer, while for the high affinity EF hand, it was switched from endothermic to exothermic with -1.72 ± 0.43 kJ/mol.

The interaction of CBL1 with Mg^{2+} ions seemed to be different than for the other two ions, as the binding isotherm exhibited only monophasic binding. Mg^{2+} could bind to one EF hand of both monomeric and dimeric protein with an overall lowest K_D of 59.5 ± 11.3 μM and 67.7 ± 12.5 μM respectively. With enthalpies of 19.2 ± 3.28 kJ/mol and 6.81 ± 1.52 kJ/mol, the binding of Mg^{2+} to both oligomeric states remained endothermic but the value was decreased to less than half in the dimer.

Overall, it can be stated that *in vitro* all three ions, Ca^{2+} , Mn^{2+} and Mg^{2+} , were capable of binding to CBL1 in different manners. Between the binding to monomeric and dimeric protein only minor differences were detected for each ion tested. At this point the determined K_D values and enthalpies could not be assigned to the four EF hands.

Potential influence of the N-terminus of CBL1

As mentioned above, the N-terminus of CBL1 harbors two lipid modifications *in vivo* and these lipid modifications are stated to introduce cooperativity into Ca^{2+} binding [20, 21]. The mass spectrometric analysis could not provide any conclusive information whether such posttranslational modifications exist. To exclude an impact of the N-terminus itself or non identified modifications on both the oligomeric state of CBL1 as well as the ion binding, the N-terminally shortened CBL1 $\Delta 2$ -11 mutant was created.

No differences could be observed in the SEC elution profile, oligomeric state or the SEC-MALS analysis of CBL1 $\Delta 2$ -11 compared to wildtype CBL1 (Figure S6.B and S7.B and C). To exclude any functional impact, the mutant was analyzed towards its capability of binding Ca^{2+} and Mn^{2+} respectively (Figure S8, Table 1,2 and S1, S2, S3). For Ca^{2+} binding to the dimeric $\Delta 2$ -11 mutant as well as the Mn^{2+} binding to both monomeric and dimeric protein, no differences compared to the wildtype could be determined. Only the affinity towards Ca^{2+} of one EF hand of the monomeric $\Delta 2$ -11 mutant was slightly increased with a K_D of 150 ± 51.1 μM and ΔH -1.03 ± 2.32 kJ/mol compared to wildtype CBL1 with 373 ± 75 μM

and -3.14 ± 0.88 kJ/mol, respectively, but still in the same order of magnitude. Together, these results clearly show that the N-terminus does not have an impact on Ca^{2+} or Mn^{2+} binding by CBL1.

Comparison of the EF hands of CBL1 and CBL4

In order to gain insights into the composition of the binding motifs of the EF hands of CBL1 and its binding capability, the four EF-hands of CBL1 and CBL4 were aligned with respect to structure and sequence (Figure 3).

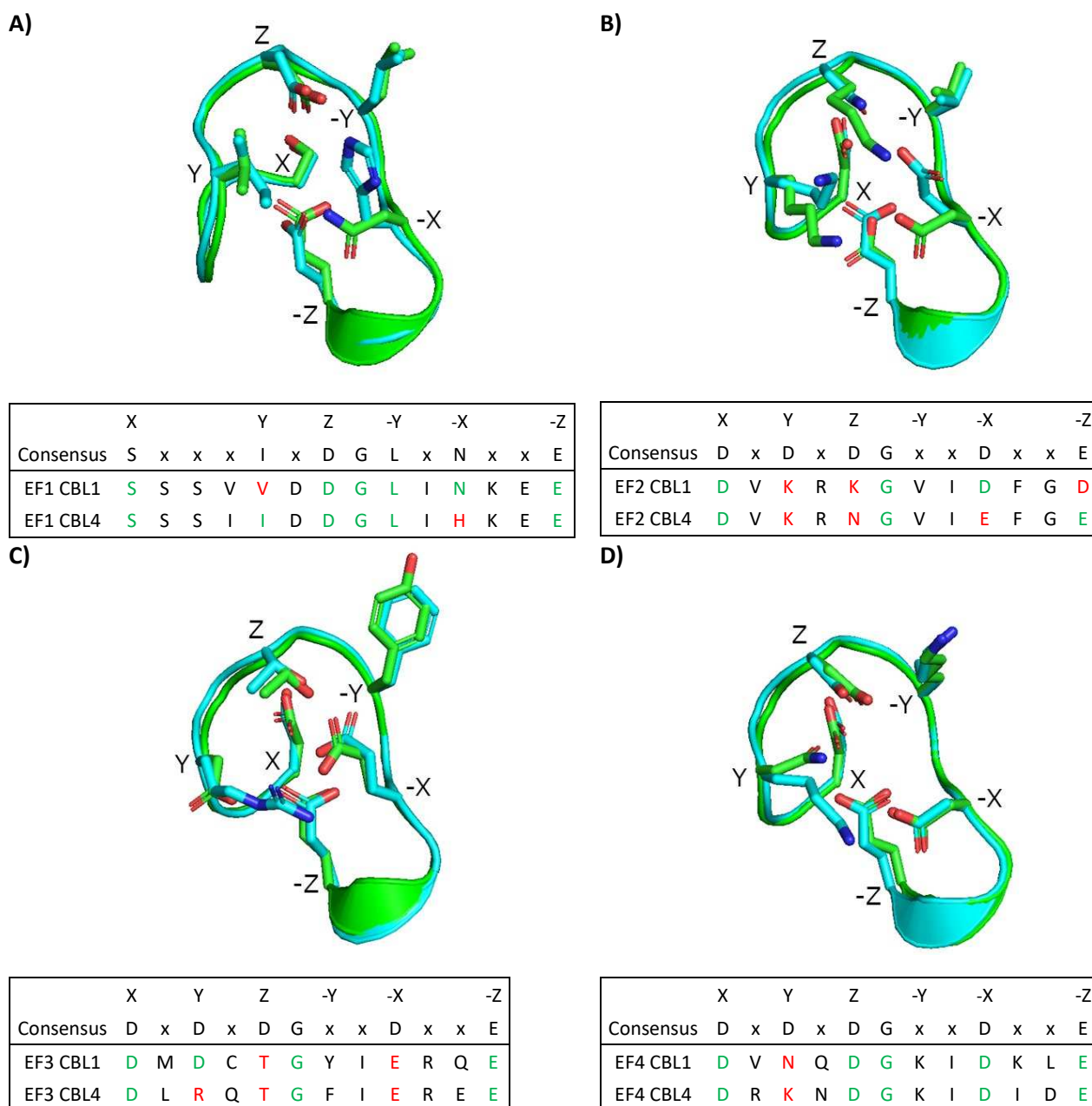


Figure 3: Structural alignments of the EF hands of the AlphaFold2 generated Streptococcus TEV-CBL1 structure (green) and CBL4 structure (cyan) (PDB entry 1v1f). A) RMSD 0.40 Å for EF hand 1 over 14 Ca atoms, B) RMSD 0.36 Å for EF hand 2 over 12 Ca atoms, C) RMSD 0.42 Å for EF hand 3 over 12 Ca atoms and D) RMSD 0.42 Å for EF hand 4 over 9 Ca atoms. The sequence alignments are based on the consensus sequences stated by Batistic et al. 2009 [20]. Amino acids identical to the consensus are marked in green, while similar amino acids are in orange and amino acids deviating from the consensus are marked in red.

All four EF hands in the crystal structure of CBL4 contained a bound divalent ion. EF hands 1, 2 and 3 were co-crystallized with Ca^{2+} , while EF hand 4 had Mn^{2+} bound. This was the case despite the fact that at least one coordinating residue differed from the consensus sequence [20]. Whether this binding pattern resembles the *in vivo* behavior of CBL4 or was a consequence of the crystallization condition cannot be stated.

When comparing the sequences of the CBL1 EF hands to both, the consensus and the CBL4 sequence, the salient deviation was the glutamate to aspartate mutation in the -Z position of CBL1 EF hand 2 (Figure 3.B). As it is known that the -Z position is critical for Ca^{2+} binding, this amino acid is commonly used for mutations from glutamate to glutamine in order to impair the binding capability of the EF-hands [40, 41]. Through the exchange of glutamate residue to aspartate, the side chain was shortened by one CH_2 group which questions the capability of Ca^{2+} binding by EF hand 2 and is coherent with the finding that CBL1 can only bind three Ca^{2+} ions.

Purification of CBL1 EF hand mutants

In order to investigate a potential cooperativity between the four EF hands of CBL1, mutations were created by substituting E to Q or D to N at the -Z positions. In result in either one EF hand at a point was impaired or a quadruple mutant, impairing all four EF hands. With the mutant E56Q the first EF hand was impaired, while in the D91N mutant the second EF hand, in the E128Q mutant the third and in the E172Q the fourth EF hand was impaired respectively [40, 41]. The quadruple mutant combined all four mutations.

All mutants were purified using the same protocol as established for the wildtype. While for E56Q, D91N and E128Q mutants, the amount of the monomeric protein species varied, the monomeric species was consistently absent for the E172Q and the E56Q D91N E128Q E172Q (quadruple) mutant (Figure S6.A). SEC-MALS analysis verified that the E172Q mutant could only be purified in its dimeric state, while the quadruple mutant, although showing the same elution profile, seemed to exist as a mix of monomeric and dimeric protein (Figure S7.A and D).

Interaction of CBL1 EF hand mutants with different ions

The purified EF hand mutants were analyzed accordingly via ITC (Figures 4, 5, S9, S10, S11, S12 and Tables 1-3, S3-S6). At first, to ensure that the binding was caused by specific ion-binding to the EF hands, the quadruple mutant was analyzed for its affinity towards Ca^{2+} (Figure 4.F), Mn^{2+} (Figure 5.F) and Mg^{2+} (Figure S11.F). Since a binding event could not be detected for all the tested ions, this clearly indicates that the detected signals of the wildtype protein and all mutants could be assigned to the ion binding event of the active EF hands.

EF hand mutants: Ca^{2+} binding

Comparing the binding isotherm of the CBL1 E56Q (EF1) mutant to the wildtype with respect to their Ca^{2+} affinity, the curve progression had changed from a three phasic to a two phasic binding curve for both monomeric and dimeric protein forms (Figure 4.B and S9.B). The affinities of the two active EF hands fit with two affinities determined for the wildtype protein. As the E56Q mutant lacked a K_D in the high nanomolar range, it can be concluded that EF hand 1 binds Ca^{2+} with a K_D of 373 ± 75.0 nM and ΔH of -3.14 ± 0.88 kJ/mol in the monomer and a K_D of 52.1 ± 23.5 nM and ΔH of 3.64 ± 1.02 kJ/mol in the dimer (previously determined in the wildtype measurement).

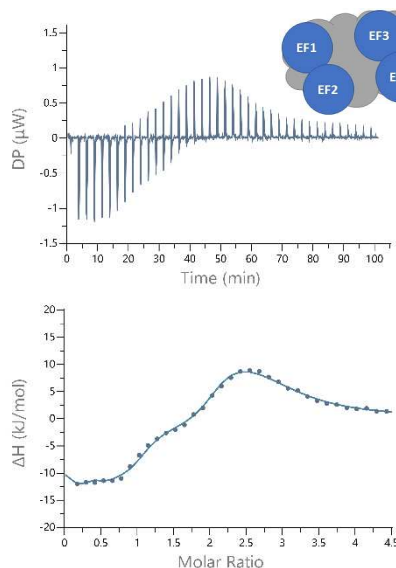
The D91N (EF2) mutation resulted in a Ca^{2+} binding isotherm with the same three phasic curve progression as the wildtype protein (Figure 4.C and S9.C). The K_D as well as the ΔH values were also highly similar to the wildtype (Table 1). Hence, EF hand 2 of CBL1 is not capable of binding Ca^{2+} .

The E128Q (EF3) mutant also displayed a two-phasic binding (Figure 4.D and S9.D) like the EF1 mutant. However, the endothermic peak, previously detected for wildtype and E56Q mutant, could no longer be detected. One EF hand bound in the lower nanomolar range and while the other in the higher nanomolar range, again comparable to the wildtype (Table 1). As EF hand 3 obviously binds in an endothermic manner, the K_D of $8.60 \pm 2.15 \mu\text{M}$ and ΔH $15.3 \pm 1.58 \text{ kJ/mol}$ (dimer $4.69 \pm 1.48 \mu\text{M}$ and $6.83 \pm 1.06 \text{ kJ/mol}$), determined for the wildtype, was assigned to this EF hand.

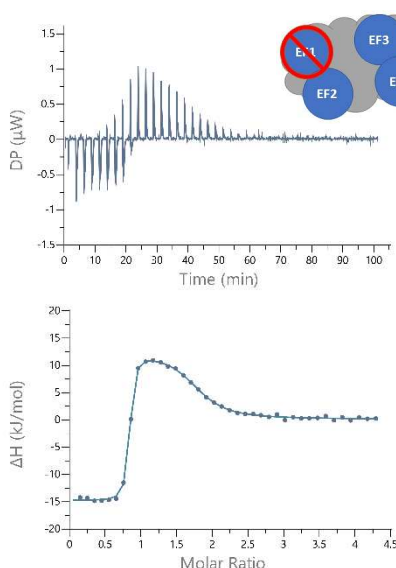
The E172Q (EF4) mutant also showed a two-phasic binding isotherm (Figure 4.E and S9.E). Noteworthy this mutant could only be purified in its dimeric form and no K_D in the low nanomolar range was detected. Hence by comparing with the wildtype results, the K_D of $8.18 \pm 1.85 \text{ nM}$ and ΔH of $-12.5 \pm 0.45 \text{ kJ/mol}$ for the monomer and the K_D of $13.4 \pm 7.20 \text{ nM}$ and ΔH of $-19.5 \pm 1.35 \text{ kJ/mol}$ for the dimer could be assigned to EF hand 4.

In general, impairing one EF hand of CBL1 did not have an influence on the Ca^{2+} binding affinities of the other EF hands. When comparing the monomer and dimer of CBL1, significant differences could only be detected for the wildtype and the D91N (EF2) mutant. For this mutant the affinity of EF hand 1 was significantly increased in the dimer and the reaction was shifted from exo- to endothermic, while the affinity of EF hand 4 was slightly decreased in the dimer (Table 1).

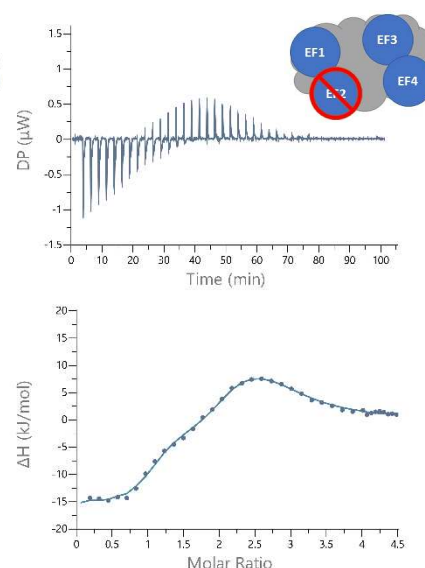
A) wildtype



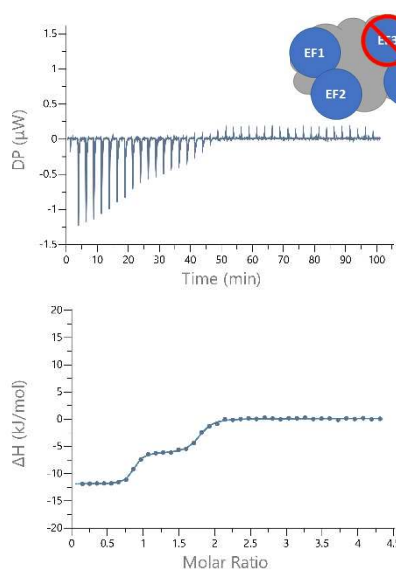
B) E56Q



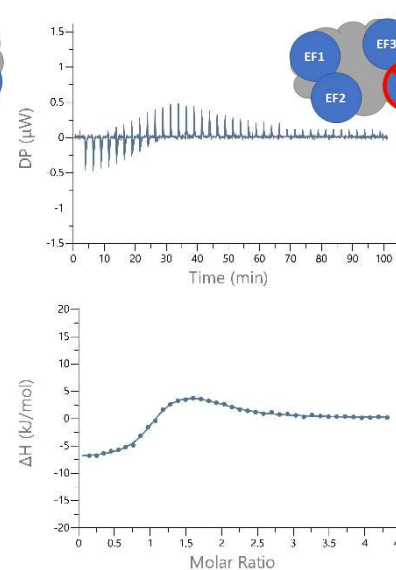
C) D91N



D) E128Q



E) E172Q



F) E56Q D91N E128Q E172Q

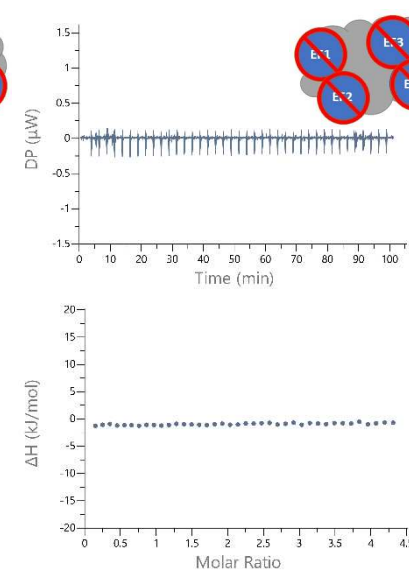


Figure 4: CBL1 EF hand mutants Ca^{2+} binding. ITC raw data and binding isotherms of 56 μM StrepII-TEV-CBL1 wt and the EF-hand mutants titrated with 1.13 mM CaCl_2 . In the upper panels the raw data is depicted. The Y-axis represents the change in heat capacity (μW) while the X-axis represents the time (min). The lower panel represents the integrated spikes in respect to time. Here the X-axis represents the molar ratio (ion: protein) while the Y-axis represents the change in heat capacity (ΔH). The wt, E56Q, D91N, and E172Q mutant were analyzed at 25 °C in their monomeric form by adding 1 μl per titration. For the E172Q and quadruple mutant no monomeric protein could be purified, hence the dimeric protein had to be used for the ITC measurements. The data points were fitted with the fitting model resulting in the lowest reduced Chi-Square. For the binding isotherms of the wt protein and the D91N mutant this was the sequential fitting model with 3 sites. The binding isotherms of the E56Q, E128Q and E172Q mutant were fitted with the two sets of sites model. The quadruple mutant showed no binding and therefore the data points could not be fitted with any fitting model.

Mn²⁺ binding of EF hand mutants

It was shown above (Figure 2) that Mn²⁺ can bind to three EF hands. In order to identify the high and low affinity sites, the CBL1 EF hand single site mutants were analyzed towards their Mn²⁺ affinity as well (Figure 5, S10 and Table 2, S5).

The binding isotherm of the CBL1 E56Q and CBL1 D91N mutants showed a highly similar curve progression compared to the wildtype in both oligomeric states (Figure 5.B, C and S10.B and C). The binding parameters for both the mutants, with one nanomolar and two micromolar binding sites, fit the wildtype data (Table 2). Hence, mutation of the -Z coordinate of EF hand 1 and 2 does not have an impact on the Mn²⁺ binding.

The E127Q mutant showed the most severe effect as the changes in heating capacity, which was almost diminished to baseline (Figure 5.D). The data could be fitted with the PEAQ software, but it resulted in high standard deviations as the changes in heat capacity were about the same intensity as for the quadrupole mutant. Thus, the E128Q mutant abolishes binding of CBL1 to Mn²⁺ entirely.

In comparison, the E172Q mutant showed signals of similar intensity as the wildtype, but only one phase was evident (Figure 5.E and S10.E). Here, two Mn²⁺ ions could bind with a K_D fitting the two non-discriminable low affinity EF hands of the wildtype. Hence, only the high affinity nanomolar binding site was impaired in the E172Q mutant.

With these results no clear assignment of the K_D values to the EF hands of CBL1 could be made. Likely EF hand 4 is the high affinity site with a K_D of 186 ± 61.2 nM and ΔH of 2.44 ± 0.21 kJ/mol for the monomer and a comparable K_D but differing ΔH of -1.72 ± 0.43 kJ/mol for the dimer and is strongly dependent on the functionality of EF hand 3.

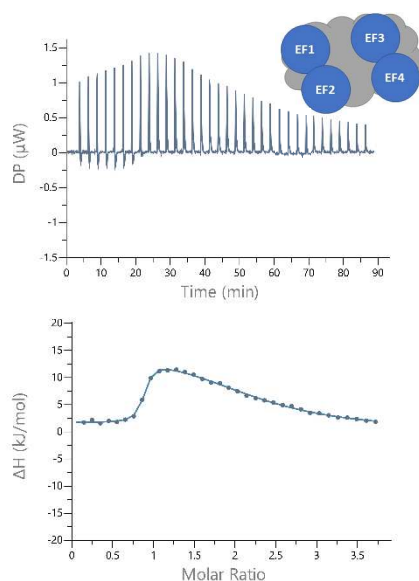
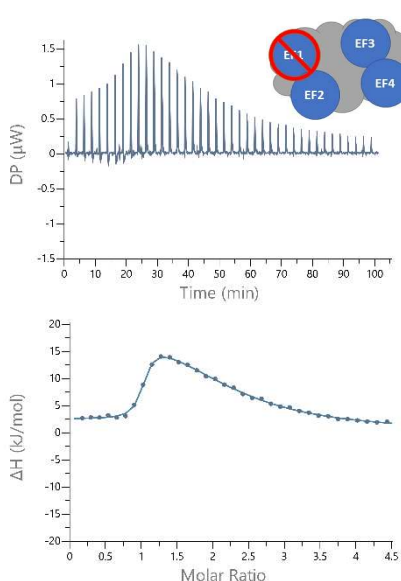
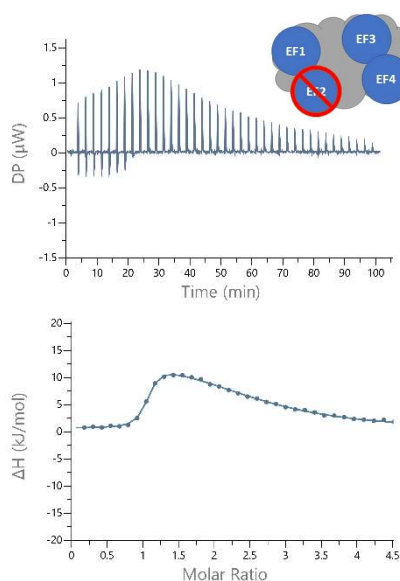
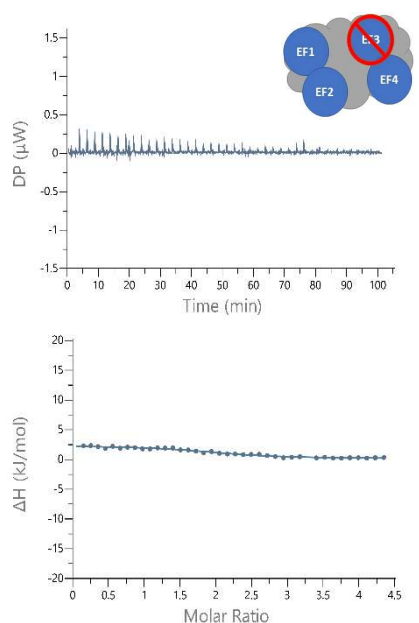
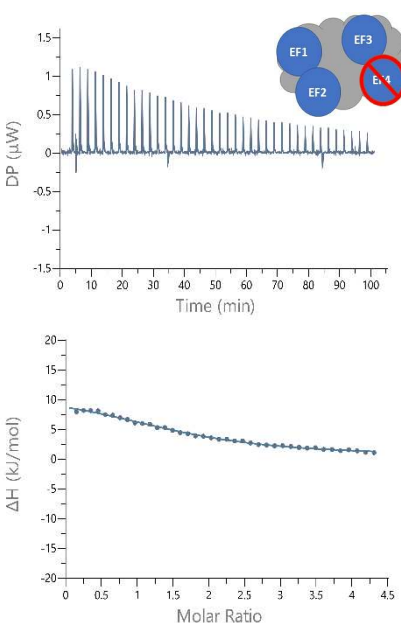
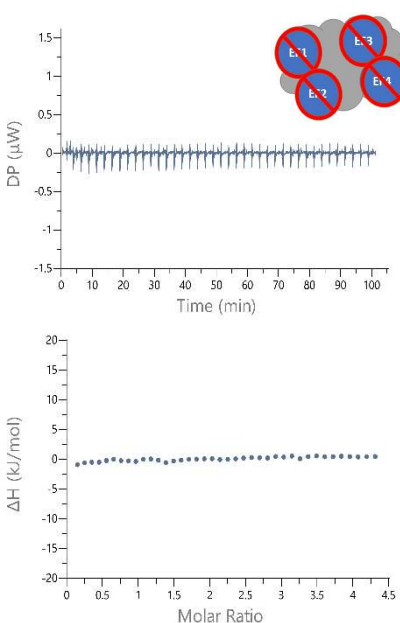
A) wildtype**B) E56Q****C) D91N****D) E128Q****E) E172Q****F) E56Q D91N E128Q E172Q**

Figure 5: CBL1 EF hand mutants Mn^{2+} binding. ITC raw data and binding isotherms of 56 μM StreptII-TEV-CBL1 wt and the EF-hand mutants titrated with 1.13 mM $MnCl_2$. In the upper panels the raw data is depicted. The Y-axis represents the change in heat capacity (μW) while the X-axis represents the time (min). The lower panel represents the integrated spikes in respect to time. Here the X-axis represents the molar ratio (ion: protein) while the Y-axis represents the change in heat capacity (ΔH). The wt, E56Q, D91N, and E128Q mutant were analyzed at 25 °C in their monomeric form by adding 1 μl per titration. For the E172Q and quadruple mutant no monomeric protein could be purified, hence the dimeric protein had to be used for the ITC measurements. The data points were fitted with the fitting model resulting in the lowest reduced Chi-Square. For the binding isotherms of the wt protein, the E56Q and the D91N mutant this was the two sets of sites fitting model. The binding isotherms of the E128Q and E172Q mutant were fitted with the one set of sites model. The quadruple mutant showed no binding and therefore the data points could not be fitted with any fitting model.

Mg²⁺ binding of EF mutants

As mentioned above, Mg²⁺ binds only to one EF hand. The E56Q, D91N and E128Q mutant showed the same affinities towards Mg²⁺ as the wildtype, while the E172Q mutant showed no binding at all (Figure S11.E, S12.E and Table 3, S6). Hence, the Mg²⁺ binding with a K_D of 59.5 ± 11.3 μM and a ΔH of 19.2 ± 3.28 kJ/mol in the monomer and K_D of 67.7 ± 12.5 μM and a ΔH of 6.81 ± 1.52 kJ/mol in the dimer was clearly assigned to EF hand 4 of CBL1.

Breaking the Dimer

Throughout all purifications, high amounts of dimeric CBL1 were eluted from the SEC. Hence, the potential dimeric interface was analyzed through a predicted dimeric model of CBL1 from AlphaFold2 for potential interactions (Figure 6.A). As seen in Figure 6.B, three interactions were found involving the four residues E141, E147, K155 and S182. The glutamate at position 141 was seen to interact with the serine at position 182 of other protomer. The other interactions were found between the glutamate at position 147 that shared an electrostatic interaction with a lysine at position 155 of the other protomer respectively. While E141 is located in the loop prior to the E-helix of EF hand 4, E147 and K155 are located in the E-helix of EF hand 4. By exchanging these three residues for alanine (further named NoDimer mutant) the three interactions should be impaired while the structure of the α-helix remains intact [42, 43].

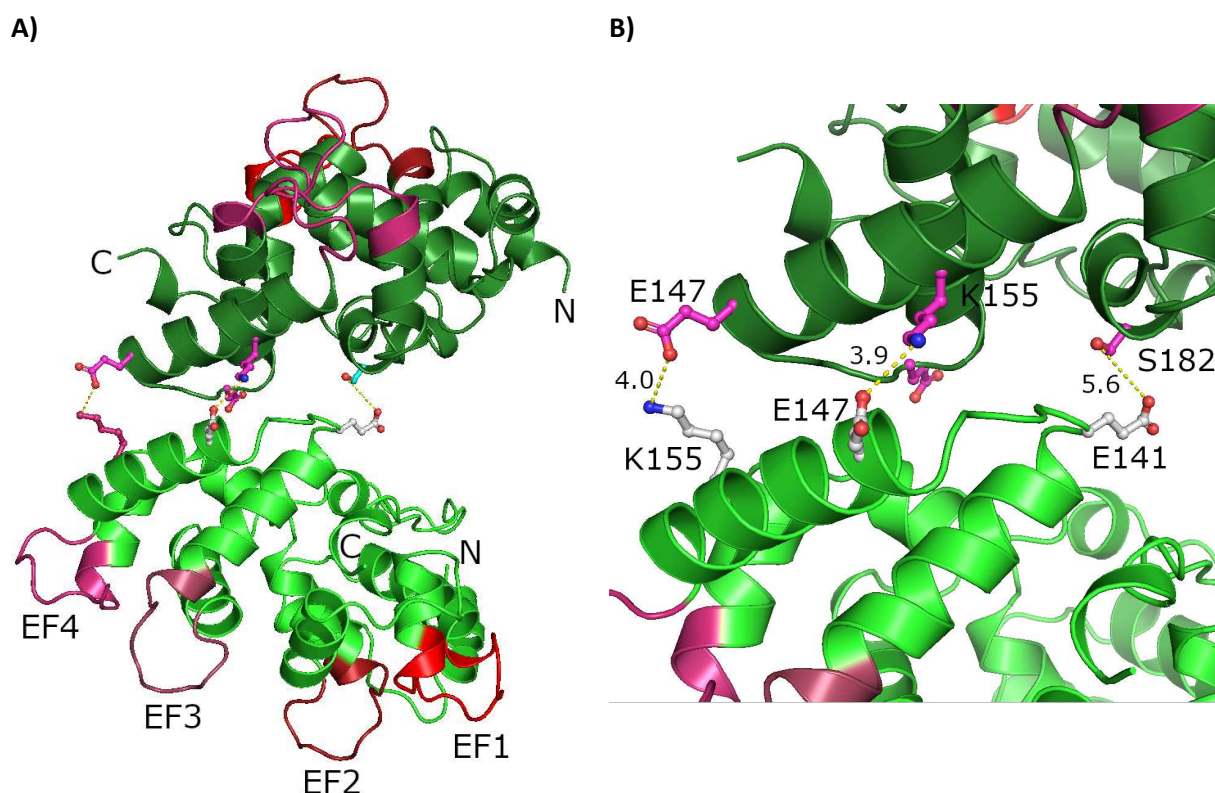


Figure 15: Alpha Fold model of the CBL1 dimer (A) and the potential CBL1 dimer interface (B). The model was generated by AlphaFold 2.0 using the non tagged CBL1 wt sequence. One monomer is colored in green and the other in dark green. The EF hand of both monomers 1 is coloured in red, EF hand 2 in firebrick, EF hand 3 in raspberry and EF hand 4 in warm pink. The amino acids involved in the dimerization and mutated in the NoDimer mutant (E141, E147 and K155) are depicted as sticks in white and magenta. The potential dimer interactions are depicted by the yellow dashed lines and the distances between the respective residues is given in Å.

Compared to the wildtype CBL1, the NoDimer mutant showed only one SEC elution peak, similar to the E172Q and quadrupole mutant (Figure S6). Most importantly, the exchange of amino acid residues E141, E147 and K155 to alanine changed the double band at 25 kDa on the SDS PAGE into one single

band (Figure S13). In the SEC-MALS analysis, the SEC peak split into two peaks of 114 ± 1.74 kDa and 44.5 ± 0.77 kDa. This was due to better resolution of the Superdex75 increase column (Figure S7.B), compared to the HiLoad Superdex75 column which was used for the preceding purification. While the 114 kDa peak was most likely caused by soluble aggregates, the 44.5 kDa at first fit neither the monomer nor the dimer properly. When looking at the Western blot (fraction E₁ was used for both MALS and ITC) besides the signal at 25 kDa an additional faint signal above 40 kDa was visible as well. For the wildtype a similar band pattern (25 kDa and 50 kDa) was visible for SDS samples of the dimeric protein as well. Hence the size of 44.5 kDa was assigned to the dimeric protein. This means that the AlphaFold2 prediction does not correspond to the real dimer interface. The Ca²⁺ binding of this mutant was also determined using ITC (Figure S14 and Table 1, S1, S2). It was observed that the affinity of EF hand 4 was decreased compared to the wildtype dimer from 13.4 ± 7.20 nM to 69.6 ± 57.9 nM while the binding enthalpy was reduced from -19.5 ± 1.35 kJ/mol to -25.5 ± 3.14 kJ/mol.

Table 3: Ca^{2+} binding parameters for CBL1 wildtype, E56Q (EF1), D91N (EF2), E128Q (EF3), E172Q (EF4), E56Q_D91N_E128Q_E172Q (quadruple), $\Delta 2-11$ (N11) and E141A_E147A_E155A (NoDimer). All values are calculated as means of at least 3 measurements. The errors were calculated from the standard deviation of the respective values. The ΔG , $-\Delta S$ and reduced Chi-Square values can be derived from Table S2 and 3.

Mutant	Oligomeric state	n1	K _D EF1	ΔH EF1	n3	K _D EF3	ΔH EF3	n4	K _D EF4	ΔH EF4
wildtype	Monomer	-	373 \pm 75 nM	-3.14 \pm 0.88 kJ/mol	-	8.60 \pm 2.15 μ M	15.3 \pm 1.58 kJ/mol	-	8.18 \pm 1.85 nM	-12.5 \pm 0.45 kJ/mol
	Dimer	-	52.1 \pm 23.5 nM	3.64 \pm 1.02 kJ/mol	-	4.69 \pm 1.48 μ M	6.83 \pm 1.06 kJ/mol	-	13.4 \pm 7.20 nM	-19.5 \pm 1.35 kJ/mol
E56Q	Monomer	-	-	-	0.94 \pm 0.06	3.39 \pm 0.88 μ M	12.5 \pm 1.18 kJ/mol	0.72 \pm 0.07	8.65 \pm 6.89 nM	-16.0 \pm 0.67 kJ/mol
	Dimer	-	-	-	0.92 \pm 0.06	3.61 \pm 0.14 μ M	11.9 \pm 0.13 kJ/mol	0.68 \pm 0.04	14.4 \pm 7.18 nM	-19.3 \pm 0.34 kJ/mol
D91N	Monomer	-	207 \pm 80.5 nM	-1.79 \pm 0.60 kJ/mol	-	5.74 \pm 1.36 μ M	10.6 \pm 2.01 kJ/mol	1	10.2 \pm 2.11 nM	-15.7 \pm 0.81 kJ/mol
	Dimer	-	81.2 \pm 37.0 nM	1.77 \pm 1.63 kJ/mol	-	5.11 \pm 0.85 μ M	5.55 \pm 0.92 kJ/mol	1	19.4 \pm 8.11 nM	-21.4 \pm 0.49 kJ/mol
E128Q	Monomer	1.24 \pm 0.33	353 \pm 93.0 nM	-6.62 \pm 0.26 kJ/mol	-	-	-	0.90 \pm 0.20	2.98 \pm 1.16 nM	-12.7 \pm 0.73 kJ/mol
	Dimer	1.34 \pm 0.36	281 \pm 73.1 nM	-8.12 \pm 0.49 kJ/mol	-	-	-	0.84 \pm 0.18	6.81 \pm 2.44 nM	-18.8 \pm 1.85 kJ/mol
E172Q	Dimer	0.85 \pm 0.16	279 \pm 104 nM	-7.33 \pm 0.22 kJ/mol	0.97 \pm 0.13	7.01 \pm 1.2 μ M	5.48 \pm 0.97 kJ/mol	-	-	-
$\Delta 2-11$	Monomer	-	150 \pm 51.1 nM	-1.03 \pm 2.32 kJ/mol	-	5.00 \pm 1.17 μ M	10.4 \pm 2.84 kJ/mol	-	18.4 \pm 6.77 nM	-12.9 \pm 1.04 kJ/mol
	Dimer	-	59.9 \pm 33.7 nM	0.99 \pm 1.77 kJ/mol	-	5.04 \pm 2.51 μ M	7.58 \pm 3.04 kJ/mol	-	11.9 \pm 7.85 nM	-17.8 \pm 1.56 kJ/mol
NoDimer	Dimer	-	55.5 \pm 38.9 nM	8.88 \pm 3.13 kJ/mol	-	4.43 \pm 2.55 μ M	4.92 \pm 1.50 kJ/mol	-	69.6 \pm 57.9 nM	-25.5 \pm 3.14 kJ/mol
Quadruple	Dimer	-	-	-	-	-	-	-	-	-

Table 4: Mn^{2+} binding parameters for CBL1 wildtype, E56Q (EF1), D91N (EF2), E128Q (EF3), E172Q (EF4), E56Q_D91N_E128Q_E172Q (quadruple) and $\Delta 2-11$ (N11). All values are calculated as means of at least 2 measurements. The errors were calculated from the standard deviation of the respective values. The ΔG , $-T\Delta S$ and reduced Chi-Square values can be derived from Table S4. As the parameters could not be assigned to the EF hands explicitly, here they are named low and high affinity sites.

Mutant	Oligomeric states	n low	K_D low	ΔH low	n high	K_D high	ΔH high
wildtype	Monomer	1.99 ± 0.09	$36.3 \pm 3.51 \mu M$	$14.7 \pm 0.68 \text{ kJ/mol}$	0.81 ± 0.11	$186 \pm 61.2 \text{ nM}$	$2.44 \pm 0.21 \text{ kJ/mol}$
	Dimer	1.76 ± 0.03	$21.5 \pm 4.67 \mu M$	$11.9 \pm 0.34 \text{ kJ/mol}$	0.62 ± 0.03	$169 \pm 15.5 \text{ nM}$	$-1.72 \pm 0.43 \text{ kJ/mol}$
E56Q	Monomer	1.46 ± 0.06	$21.6 \pm 2.74 \mu M$	$15.6 \pm 0.85 \text{ kJ/mol}$	0.76 ± 0.07	$67.3 \pm 25.7 \text{ nM}$	$1.89 \pm 0.48 \text{ kJ/mol}$
	Dimer	1.43 ± 0.04	$21.2 \pm 0.70 \mu M$	$14.2 \pm 0.50 \text{ kJ/mol}$	0.57 ± 0.03	$108 \pm 43.7 \text{ nM}$	$-0.75 \pm 0.70 \text{ kJ/mol}$
D91N	Monomer	2.06 ± 0.12	$24.3 \pm 4.34 \mu M$	$12.8 \pm 1.06 \text{ kJ/mol}$	0.88 ± 0.09	$83.4 \pm 16.0 \text{ nM}$	$0.42 \pm 0.11 \text{ kJ/mol}$
	Dimer	1.76 ± 0.24	$21.8 \pm 5.19 \mu M$	$12.2 \pm 0.95 \text{ kJ/mol}$	0.67 ± 0.28	$374 \pm 217 \text{ nM}$	$-4.14 \pm 0.06 \text{ kJ/mol}$
E128Q	Monomer	1.83 ± 0.17	$18.5 \pm 19.3 \mu M$	$2.96 \pm 1.15 \text{ kJ/mol}$	-	-	-
	Dimer	2.21 ± 0.10	$148 \pm 5.00 \mu M$	$2.96 \pm 0.18 \text{ kJ/mol}$	0.56 ± 0.03	$2.29 \pm 0.59 \mu M$	$-3.12 \pm 0.48 \text{ kJ/mol}$
E172Q	Dimer	1.55 ± 0.22	$36.1 \pm 5.58 \mu M$	$10.7 \pm 0.67 \text{ kJ/mol}$	-	-	-
$\Delta 2-11$	Monomer	1.97 ± 0.08	$26.6 \pm 3.41 \mu M$	$13.1 \pm 1.17 \text{ kJ/mol}$	0.70 ± 0.12	$151 \pm 33.1 \text{ nM}$	$2.11 \pm 1.25 \text{ kJ/mol}$
	Dimer	1.81 ± 0.20	$22.9 \pm 3.77 \mu M$	$11.8 \pm 0.66 \text{ kJ/mol}$	0.67 ± 0.07	$197 \pm 58.8 \text{ nM}$	$-1.51 \pm 0.72 \text{ kJ/mol}$
Quadruple	Dimer	-	-	-	-	-	-

Table 5: Mg^{2+} binding parameters for CBL1 wildtype, E56Q (EF1), D91N (EF2), E128Q (EF3), E172Q (EF4) and E56Q D91N E128Q E172Q (quadruple). All values are calculated as means of at least 2 measurements. The errors were calculated from the standard deviation of the respective values. The ΔH and reduced Chi-Square values can be derived from Table S5.

Mutant	Oligomeric state	n4	K_D EF4	ΔH EF4
wildtype	Monomer	0.88 ± 0.05	$59.5 \pm 11.3 \mu M$	$19.2 \pm 3.28 \text{ kJ/mol}$
	Dimer	0.85 ± 0.03	$67.7 \pm 12.5 \mu M$	$6.81 \pm 1.52 \text{ kJ/mol}$
EF1	Monomer	0.96 ± 0.14	$94.2 \pm 6.08 \mu M$	$20.2 \pm 3.68 \text{ kJ/mol}$
	Dimer	0.86 ± 0.08	$95.9 \pm 7.5 \mu M$	$16.2 \pm 0.30 \text{ kJ/mol}$
EF2	Monomer	1.02 ± 0.07	$55.7 \pm 9.35 \mu M$	$14.6 \pm 1.45 \text{ kJ/mol}$
	Dimer	0.87 ± 0.11	$92.6 \pm 9.45 \mu M$	$11.3 \pm 1.96 \text{ kJ/mol}$
EF3	Monomer	0.88 ± 0.01	$55.9 \pm 2.35 \mu M$	$13.8 \pm 0.20 \text{ kJ/mol}$
	Dimer	1.04 ± 0.03	$126 \pm 43.6 \mu M$	$15.1 \pm 4.37 \text{ kJ/mol}$
EF4	Dimer	-	-	-
Quadruple	Dimer	-	-	-

Discussion

The aim of this study was to purify and analyze the EF hand protein CBL1 from *A. thaliana* with respect to its *in vitro* binding affinity towards Ca^{2+} , Mn^{2+} and Mg^{2+} . Recombinant, functional and monomeric CBL1 protein required the addition of Brij35 detergent during the purification procedure (Figure S3). This is in contrast to the purifications of other CBL proteins such as CBL2 and CBL4 [32, 44], which did not require any detergent. Whilst CBL2 belongs to the subclass of CBL proteins with extended N-terminus, both CBL1 and 4 belong to the CBL subgroup with short N-terminus, which was shown to be lipid anchored at the N-terminus *in vivo* [20, 21]. This already suggests a membrane proximity and a certain degree of hydrophobicity in CBL1. A hydrophobic surface could be visualized in the predicted structural model of CBL1 (Figure 1). This hydrophobic crevice is stated to be present in all CBLs, since it represents the binding site for the NAF domains of the interacting protein kinase CIPK [31]. In the native state of the protein this hydrophobic crevice is covered by the proteins C-terminus, a conformational state that could not be modelled by AlphaFold2.0 [34, 35]. Hence, it is unlikely that this hydrophobic crevice is the reason for the requirement of Brij35 during CBL1 purification. Although it is known that myristoylation is essential for the correct positioning of CBL4 at the membrane [32] and the lipid modifications are essential for the *in vivo* functionality of CBL1 [21], these modifications do not occur in *E. coli* [20]. However, CBL1 was found to have an intrinsic hydrophobicity, too weak to keep the protein attached to the membrane during the purification, but strong enough to force the protein into higher oligomeric states without the presence of detergent micelles (Figure S1 and 3). This was further substantiated by the fact that the $\Delta 2-11$ mutant with the shortened N-terminus showed no difference compared to wildtype CBL1. Hence, the N-terminus itself and the StrepII tag are neither responsible for dimerization, the double band on the SDS PAGE or have an influence on the ion binding properties of CBL1, which is in contrast to Batistic *et al.* [21], who stated that the lipidation of CBL1 was required for its function and membrane attachment *in vivo*.

Putting the *in vitro* data of the monomeric CBL1 in an *in vivo* context, EF hand 4 with a K_D of 8.18 nM possesses a Ca^{2+} affinity that is significantly below the resting cytosolic Ca^{2+} concentration of 100 – 200 nM [5, 6]. Therefore, EF hand 4 is constitutively occupied by Ca^{2+} . EF hand 1 with a K_D of 373 nM shows an affinity slightly above the resting cytosolic Ca^{2+} concentration. Hence, EF hand 1 can function as the initial Ca^{2+} sensor, as it will recognize rising Ca^{2+} concentrations in the cytosol. EF hand 3 with a K_D of 8.60 μM has the lowest Ca^{2+} affinity. This EF hand can either function as a second sensor when cytosolic Ca^{2+} gets elevated up to μM levels or even a shut-down sensor, which shuts down the signal transduction and subsequent K^+ uptake by AKT1 when the Ca^{2+} concentration gets too high. As stated, exothermic binding, which is true for EF hands 1 and 4, but not for EF hand 3, hints towards a conformational change coupled to the Ca^{2+} binding event [45]. Similarly, EF hand 3 does not undergo a conformational change upon Ca^{2+} binding. Signal transduction usually is accompanied by conformational changes of the sensor protein [46]. Although this is not the case for CBL1 EF hand 3, upon Ca^{2+} binding, still a new platform for interaction can be created. Calcium signatures are known to be induced by biotic and abiotic stress [7, 9, 10]. These increased Ca^{2+} levels, if lasting too long can thereby induce programmed cell death (PCD) [47, 48]. For the sensing of the increasing Ca^{2+} and subsequent induction of PCD other members of the CBL family, namely CBL10 and CIPK6 are known to be involved in tomatoes [49]. In difference to CBL1, CBL10 belongs to the other subclass of CBL1 proteins, is located to the vacuolar membrane, lacks myristoylation [22] and harbors an extended N-terminal domain [12]. On the other hand interactions of CBL10 with the K^+ channel AKT1 at the plasma membrane, which is a downstream target of CBL1 in complex with CIPK23, have been stated [19]. For

CBL1, which is associated to the plasma membrane and harbors a short N-terminus with lipid modifications [20], so far no role in PCD is stated, but might represent a new avenue of research.

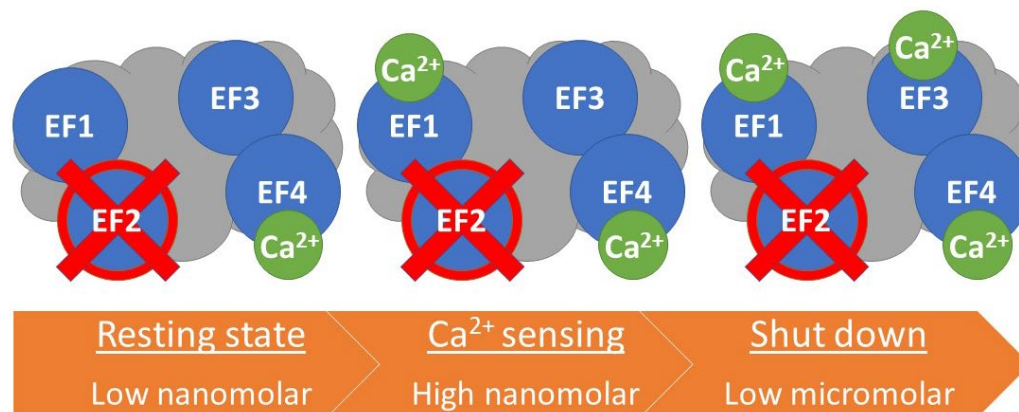


Figure 7: Ca^{2+} binding model for CBL1. EF hand 2 is not capable of binding Ca^{2+} . In the resting state and low nanomolar Ca^{2+} levels in the cytosol, Ca^{2+} is constitutively bound to EF hand 4. Increasing cytosolic Ca^{2+} levels to the high nanomolar range are recognized by CBL1 via Ca^{2+} binding to EF hand 1. If micromolar Ca^{2+} levels are reached, EF hand 3 can bind Ca^{2+} and potentially function as a switch off sensor for the signalling process.

The results for the Mn^{2+} binding are not as distinct. For Mn^{2+} binding, one can only conclude that there is one nanomolar high affinity and two micromolar low affinity sites. While the low affinity binding might be independent of the -Z coordination, the high affinity site can either be assigned to EF hand 3 or 4. If the latter is true, Mn^{2+} does not have an impact on CBL1 *in vivo*. The Ca^{2+} affinity for EF hand 4 (8.18 nM) is significantly higher than the affinity of the Mn^{2+} high affinity site (186 nM). The fact that in the E172Q mutant, where EF hand 4 is impaired, only the high affinity site vanished, points towards this statement. The assumption that EF hand 4 is a high affinity Mn^{2+} binding site is further substantiated by the fact that in the crystal structure of CBL4, Mn^{2+} was also found in EF hand 4 [32]. On the other hand, the impairment of EF hand 3 has the most severe effect on the CBL1 Mn^{2+} binding. The E128Q mutation vanishes all Mn^{2+} binding, which implies that there is cooperativity in the binding of Mn^{2+} . If EF hand 3 will emerge as the high affinity Mn^{2+} binding site, an impact of Mn^{2+} on CBL1 *in vivo* cannot be excluded. The cytosolic Mn^{2+} concentration in plants is stated to be in sub micromolar range [50] and therefore in the same order of magnitude as the high affinity site (186 nM). Thereby the Ca^{2+} affinity for EF hand 3 is, with 8.60 μM , significantly lower for EF hand 3 and would play a subordinated role *in vivo*. In order to indubitable identification of the CBL1 Mn^{2+} high affinity binding site will certainly need further investigation.

Mg^{2+} can only bind to EF hand 4 with a K_D of $59.5 \pm 11.3 \mu\text{M}$. The concentration of free Mg^{2+} in plant cells was found to be in the range of 0.4 – 0.5 mM [51] and therefore 10 fold higher. But the Mg^{2+} binding to CBL1 does not have an impact *in vivo* since the affinity of EF hand 4 is significantly higher for Ca^{2+} . Noteworthy all binding affinities were determined for the free and non phosphorylated CBL1. For CBL2 and 4 differences between the free and CIPK bound state are already postulated [29, 31]. Phosphorylation of the CBL C-terminus is known to have an influence on the CBL/CIPK complex as well and is essential for AKT1 activation *in vivo* [17]. If the phosphorylation of CBL1 has an influence on the Ca^{2+} binding features is not stated. Hence, the observed ion binding behavior of CBL1 may change upon CIPK23 binding and phosphorylation.

During all purifications high amounts of CBL1 and its variants were purified as dimer. Hence the dimeric structure was modeled by AlphaFold2 [34, 35]. This dimeric interface as seen from the modelled CBL1 dimeric structure is asymmetric and formed by the loop prior to the E4-helix of and the E4-helix. In

contrast, the crystallographic CBL4 dimer is symmetric and the dimer interface is formed by the C-terminus of helix F3, the connecting loop and the N-terminal part of helix E4 [32]. Initially, the dimeric structure was modelled in order to create a mutant (E141A E147A K155A/ NoDimer), to break the dimeric interface and to increase the yields of monomeric CBL1 protein. Instead, the NoDimer mutant resulted in further destabilization of the monomeric form and CBL1 protein could only be purified in higher oligomeric states. The same phenomenon was obtained for SEC elution profiles of the E172Q (EF4) mutant and the quadrupole mutant. Hence, the -Z component of EF hand 4 (E172) as well as the E4 helix (E147 and K155) and the preceding loop (E141) play an essential role in the stability of the monomer. Furthermore, the typical migration behavior of CBL1 wildtype and EF hand mutants on SDS PAGE changed for the NoDimer mutant from a double band at 25 kDa towards a single band. This was not expected and further confirms the importance of this area for the structural integrity of CBL1. Taking a look at the mass spectrometry data of this area of the protein, no differences could be detected which would explain the formation of the double signal in the wildtype and EF mutant proteins. The reduced binding affinity of EF hand 4 of the NoDimer mutant, from 13.4 ± 7.20 nM in the wildtype dimer to 69.6 ± 57.9 nM, further hints towards an influence of the residues E141, E147 and K155 on the structure and stability of CBL1, but likely this area of the protein does not represent the real dimer interface of CBL1.

When comparing the CBL1 affinities for divalent ions of both monomer and dimer, it is striking that the most severe differences can be detected for EF hand 1. The Ca^{2+} affinity of EF hand 1 is significantly increased in the dimer and the binding enthalpy changes from exo- to endothermic. According to Yamniuk *et al.*, exothermic metal binding to proteins hints towards ongoing conformational changes, while binding without structural changes in the protein is supposed to be endothermic [45]. This suggests that EF hand 1 does not undergo a conformational change in the dimeric protein, or is not capable of doing so as it is involved into the real dimeric interface of CBL1. However, structural information is necessary for further validation of this hypothesis.

The findings of this work present a first insight into the *in vitro* ion binding behavior of a CBL protein. Upon the findings we could suggest a binding model for the Ca^{2+} binding of CBL1 *in vivo*. We further could identify amino acids around EF4 to be essential for the structural and functional integrity of the protein.

Acknowledgments:

We thank the laboratory of Jörg Kudla (Institut für Biologie und Biotechnologie der Pflanzen, Universität Münster, Germany) for the helpful discussions and for providing the pET24-CBL1 plasmid which served as the starting point of this study. Special thanks goes to Eymen Hachani from the Biochemistry I laboratory at HHU for performing the MALS analysis and Dr. Anja Stefanski (MPL at HHU Düsseldorf) for performing the mass spectrometric analysis of CBL1. Further thanks go to the whole BC1 Institute at HHU Düsseldorf for the helpful discussions and support. This work was supported by the DFG (Schm1279/14-1).

Author contribution

L.S. and S.S. designed the research; A.B. performed the research; A.B., S.S. and L.S. analyzed the data; A.B. and L.S. wrote the paper.

Data availability

The data is available per e-mail upon request (lutz.schmitt@hhu.de). The supporting information can be found in the online version of this article.

References

1. Hänsch, R. and R.R. Mendel, *Physiological functions of mineral micronutrients (Cu, Zn, Mn, Fe, Ni, Mo, B, Cl)*. Current Opinion in Plant Biology, 2009. **12**(3): p. 259-266.
2. Maathuis, F.J., *Physiological functions of mineral macronutrients*. Curr Opin Plant Biol, 2009. **12**(3): p. 250-8.
3. Thor, K., *Calcium-Nutrient and Messenger*. Front Plant Sci, 2019. **10**: p. 440.
4. Reddy A.S.N, R.V.S., *Calcium as a messenger in stress signal transduction*. Handbook of Plant and Crop Physiology, 2001. **Second Edition**: p. 719-756.
5. Knight, H., *Calcium signaling during abiotic stress in plants*. Int Rev Cytol, 2000. **195**: p. 269-324.
6. Rudd, J.J. and V.E. Franklin-Tong, *Unravelling response-specificity in Ca(2+) signalling pathways in plant cells*. New Phytol, 2001. **151**(1): p. 7-33.
7. Dodd, A.N., J. Kudla, and D. Sanders, *The language of calcium signaling*. Annu Rev Plant Biol, 2010. **61**: p. 593-620.
8. Berridge, M.J., P. Lipp, and M.D. Bootman, *The versatility and universality of calcium signalling*. Nat Rev Mol Cell Biol, 2000. **1**(1): p. 11-21.
9. Dong, Q., et al., *Ca(2+) signaling in plant responses to abiotic stresses*. J Integr Plant Biol, 2022. **64**(2): p. 287-300.
10. Batistic, O. and J. Kudla, *Analysis of calcium signaling pathways in plants*. Biochim Biophys Acta, 2012. **1820**(8): p. 1283-93.
11. Whalley, H.J. and M.R. Knight, *Calcium signatures are decoded by plants to give specific gene responses*. New Phytol, 2013. **197**(3): p. 690-693.
12. Batistic, O. and J. Kudla, *Integration and channeling of calcium signaling through the CBL calcium sensor/CIPK protein kinase network*. Planta, 2004. **219**(6): p. 915-24.
13. Albrecht, V., et al., *The NAF domain defines a novel protein-protein interaction module conserved in Ca2+-regulated kinases*. EMBO J, 2001. **20**(5): p. 1051-63.
14. Sanchez-Barrena, M.J., et al., *The structure of the C-terminal domain of the protein kinase AtSOS2 bound to the calcium sensor AtSOS3*. Mol Cell, 2007. **26**(3): p. 427-35.
15. Chaves-Sanjuan, A., et al., *Structural basis of the regulatory mechanism of the plant CIPK family of protein kinases controlling ion homeostasis and abiotic stress*. Proc Natl Acad Sci U S A, 2014. **111**(42): p. E4532-41.
16. Lee, S.C., et al., *A protein phosphorylation/dephosphorylation network regulates a plant potassium channel*. Proc Natl Acad Sci U S A, 2007. **104**(40): p. 15959-64.
17. Hashimoto, K., et al., *Phosphorylation of calcineurin B-like (CBL) calcium sensor proteins by their CBL-interacting protein kinases (CIPKs) is required for full activity of CBL-CIPK complexes toward their target proteins*. J Biol Chem, 2012. **287**(11): p. 7956-68.
18. Hedrich, R., *Ion channels in plants*. Physiol Rev, 2012. **92**(4): p. 1777-811.
19. Ren, X.L., et al., *Calcineurin B-like protein CBL10 directly interacts with AKT1 and modulates K+ homeostasis in Arabidopsis*. Plant J, 2013. **74**(2): p. 258-66.
20. Batistic, O. and J. Kudla, *Plant calcineurin B-like proteins and their interacting protein kinases*. Biochim Biophys Acta, 2009. **1793**(6): p. 985-92.
21. Batistic, O., et al., *Dual fatty acyl modification determines the localization and plasma membrane targeting of CBL/CIPK Ca2+ signaling complexes in Arabidopsis*. Plant Cell, 2008. **20**(5): p. 1346-62.
22. Kim, B.G., et al., *The calcium sensor CBL10 mediates salt tolerance by regulating ion homeostasis in Arabidopsis*. Plant J, 2007. **52**(3): p. 473-84.
23. Rodenas, R. and G. Vert, *Regulation of Root Nutrient Transporters by CIPK23: 'One Kinase to Rule Them All'*. Plant Cell Physiol, 2021. **62**(4): p. 553-563.
24. Ishitani, M., et al., *SOS3 function in plant salt tolerance requires N-myristoylation and calcium binding*. Plant Cell, 2000. **12**(9): p. 1667-78.

25. Ames, J.B., et al., *Molecular mechanics of calcium-myristoyl switches*. Nature, 1997. **389**(6647): p. 198-202.
26. Kretsinger, R.H. and C.E. Nockolds, *Carp Muscle Calcium-binding Protein*. Journal of Biological Chemistry, 1973. **248**(9): p. 3313-3326.
27. Kawasaki, H. and R.H. Kretsinger, *Structural and functional diversity of EF-hand proteins: Evolutionary perspectives*. Protein Sci, 2017. **26**(10): p. 1898-1920.
28. Lewit-Bentley, A. and S. Rety, *EF-hand calcium-binding proteins*. Curr Opin Struct Biol, 2000. **10**(6): p. 637-43.
29. Nagae, M., et al., *The crystal structure of the novel calcium-binding protein AtCBL2 from Arabidopsis thaliana*. J Biol Chem, 2003. **278**(43): p. 42240-6.
30. Kudla, J., et al., *Genes for calcineurin B-like proteins in Arabidopsis are differentially regulated by stress signals*. Proc Natl Acad Sci U S A, 1999. **96**(8): p. 4718-23.
31. Akaboshi, M., et al., *The crystal structure of plant-specific calcium-binding protein AtCBL2 in complex with the regulatory domain of AtCIPK14*. J Mol Biol, 2008. **377**(1): p. 246-57.
32. Sanchez-Barrena, M.J., et al., *The structure of the Arabidopsis thaliana SOS3: molecular mechanism of sensing calcium for salt stress response*. J Mol Biol, 2005. **345**(5): p. 1253-64.
33. Poschmann, G., et al., *Redox proteomics reveal stress responsive proteins linking peroxiredoxin-1 status in glioma to chemosensitivity and oxidative stress*. Biochim Biophys Acta, 2015. **1854**(6): p. 624-31.
34. Jumper, J., et al., *Highly accurate protein structure prediction with AlphaFold*. Nature, 2021. **596**(7873): p. 583-589.
35. Mirdita, M., et al., *ColabFold: making protein folding accessible to all*. Nat Methods, 2022. **19**(6): p. 679-682.
36. Eisenberg, D., et al., *Analysis of membrane and surface protein sequences with the hydrophobic moment plot*. J Mol Biol, 1984. **179**(1): p. 125-42.
37. Gasteiger E., H.C., Gattiker A., Duvaud S., Wilkins M.R., Appel R.D., Bairoch A. *The Proteomics Protocols Handbook*. 2005; Available from: <https://web.expasy.org/protparam/>.
38. Ohki, S., M. Ikura, and M. Zhang, *Identification of Mg²⁺-binding sites and the role of Mg²⁺ on target recognition by calmodulin*. Biochemistry, 1997. **36**(14): p. 4309-16.
39. Osawa, M., et al., *Mg²⁺ and Ca²⁺ differentially regulate DNA binding and dimerization of DREAM*. J Biol Chem, 2005. **280**(18): p. 18008-14.
40. Ames, J.B., N. Hamasaki, and T. Molchanova, *Structure and calcium-binding studies of a recoverin mutant (E85Q) in an allosteric intermediate state*. Biochemistry, 2002. **41**(18): p. 5776-87.
41. Maune, J.F., C.B. Klee, and K. Beckingham, *Ca²⁺ binding and conformational change in two series of point mutations to the individual Ca(2+)-binding sites of calmodulin*. Journal of Biological Chemistry, 1992. **267**(8): p. 5286-5295.
42. Serrano, L., et al., *Effect of alanine versus glycine in alpha-helices on protein stability*. Nature, 1992. **356**(6368): p. 453-5.
43. Serrano, L., et al., *Alpha-helix stability in proteins. I. Empirical correlations concerning substitution of side-chains at the N and C-caps and the replacement of alanine by glycine or serine at solvent-exposed surfaces*. J Mol Biol, 1992. **227**(2): p. 544-59.
44. Sanchez-Barrena, M.J., et al., *SOS3 (salt overly sensitive 3) from Arabidopsis thaliana: expression, purification, crystallization and preliminary X-ray analysis*. Acta Crystallogr D Biol Crystallogr, 2004. **60**(Pt 7): p. 1272-4.
45. Yamniuk, A.P., Nguyen, L. T., Hoang, T. T., Vogel, H. J., *Metal ion binding properties and conformational states of calcium- and integrin-binding protein*. Biochemistry, 2004. **43**(9): p. 2558-68.
46. Berg, J.M., J.L. Tymoczko, and L. Stryer, *Stryer Biochemie*. 7 ed. 2013: Springer-Verlag Berlin Heidelberg 2013. XLII, 1198.
47. Petrov, V., et al., *ROS-mediated abiotic stress-induced programmed cell death in plants*. Front Plant Sci, 2015. **6**: p. 69.

48. Ren, H., et al., *Calcium Signaling in Plant Programmed Cell Death*. Cells, 2021. **10**(5).
49. de la Torre, F., et al., *The tomato calcium sensor Cbl10 and its interacting protein kinase Cipk6 define a signaling pathway in plant immunity*. Plant Cell, 2013. **25**(7): p. 2748-64.
50. Quiquampoix, H., Loughman, B. C., Ratcliffe, R. G. , *A ³¹P-NMR Study of the Uptake and Compartmentation of Manganese by Maize Roots*. Journal of Experimental Botany, 1993. **44**(269): p. 1819-1827.
51. Karley, A.J. and P.J. White, *Moving cationic minerals to edible tissues: potassium, magnesium, calcium*. Curr Opin Plant Biol, 2009. **12**(3): p. 291-8.

Supplementary Information

Calcium binding of AtCBL1: first structural and functional insights

Alexandra Bork¹, Sander H J Smits^{1,2}, Lutz Schmitt^{1,*}

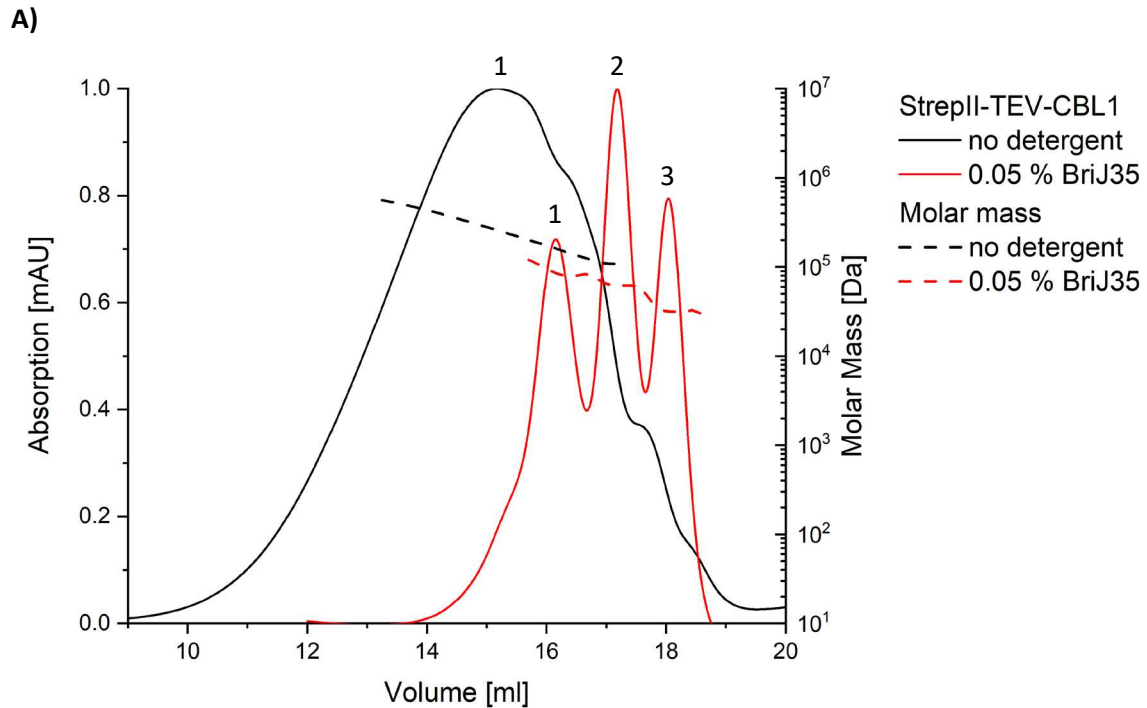
¹Institute of Biochemistry I, Heinrich Heine University Düsseldorf, Düsseldorf, Germany.

²Center for Structural Studies, Heinrich Heine University Düsseldorf, Düsseldorf, Germany.

* To whom correspondence should be addressed:

Lutz Schmitt
Institute of Biochemistry
Heinrich Heine University Düsseldorf
Universitätsstr. 1
40225 Düsseldorf, Germany
Phone: +49(0)211-81-10773
Fax: +49(0)211-81-15310
E-mail: lutz.schmitt@hhu.de

Keywords: *A. thaliana*, EF-hand, Ca²⁺ binding, Calcineurin-B-like protein 1, ITC

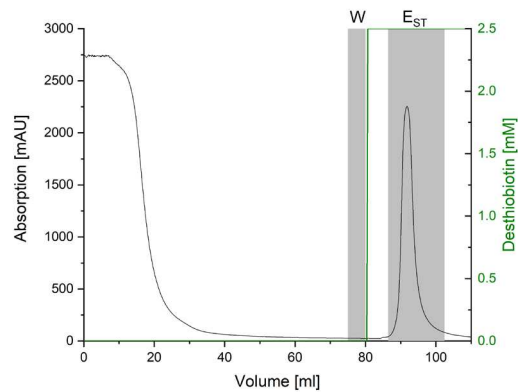


B)

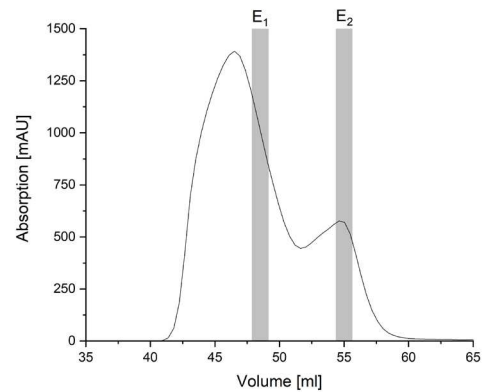
Peak	1	2	3
No detergent	225.6 ± 0.90 kDa	-	-
0.05 % Brij35 (soluble)	154.1 ± 0.97 kDa	69.7 ± 0.67 kDa	39.6 ± 0.47 kDa
0.05 % Brij35 (conjugate)	50.5 ± 0.22 kDa	54.4 ± 0.37 kDa	25.1 ± 0.29 kDa

Figure S2: SEC-MALS analysis of StrepII-TEV-CBL1 in presence or absence of Brij35 detergent. A) 200 µg StrepTrap purified protein was submitted to MALS analysis on a Superose6 increase 10/300 column. The X-axis represents the elution volume while the left Y-axis represents the UV absorption at 280 nm in mAU units and the right Y-axis represents the molecular mass calculated from light scattering. The solid traces represent the absorption at 280 nm and the dashed line represents the molecular weight. The results without detergent are depicted in black while the results in presence of 0.05 % (w/v) Brij35 are colored in red. B) The different peaks from SEC chromatogram were separately analyzed and the molecular weight for each were calculated using ASTRA 7.3.2 software (Wyatt Technology Corp.) based on the chromatograms in A). The protein sample supplemented with 0.05 % (w/v) Brij35 was analyzed as fully soluble and detergent conjugated.

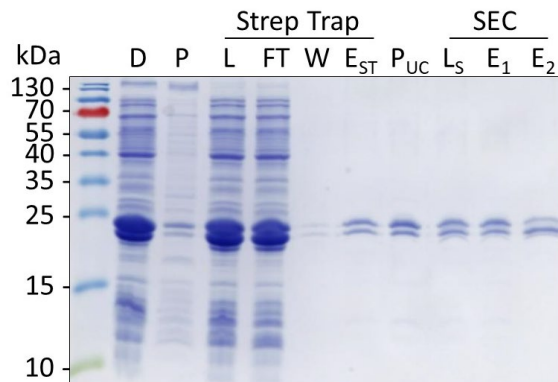
A)



B)



C)



D)

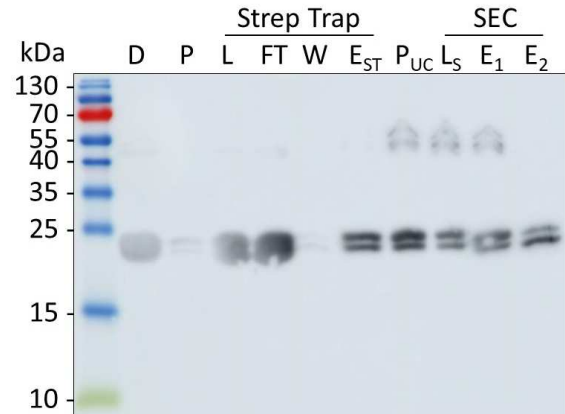


Figure S3: Purification of StrepII-TEV-CBL1. A) StrepTactin affinity chromatogram of CBL1. X-axis represents the elution volume in ml while the left Y-axis represents the UV absorption at 280 nm in mAU units and the right Y-axis represents the concentration of Desthiobiotin in mM. B) Size exclusion chromatogram of CBL1. X-axis represents the elution volume in ml while the Y-axis represents the UV absorption at 280 nm in mAU units. SEC was performed on a HiLoad Superdex75 16/600. The gray bars in A) and B) represent the fractions used for SDS samples. C) Coomassie-stained 15 % SDS gel and corresponding western blot analysis D) representing the various steps/ samples from the purification of CBL1. D = disrupted cells; P = cell debris pellet; L = load with 0.25 % (w/v) Brij35; FT = StrepTrap HP flow through; W = wash; E_{ST} = StrepTrap HP elution; P_{UC} = ultra centrifugation pellet; L_S = SEC load; E₁ = SEC Elution peak 1; E₂ = SEC Elution peak 2. The blot was developed using α -StrepII primary antibody and α -mouse-IgG-HRPO-coupled secondary antibody. The double bands at ~ 25 kDa can be assigned to CBL1 as confirmed by mass spectrometry (Figure S3 and 4).

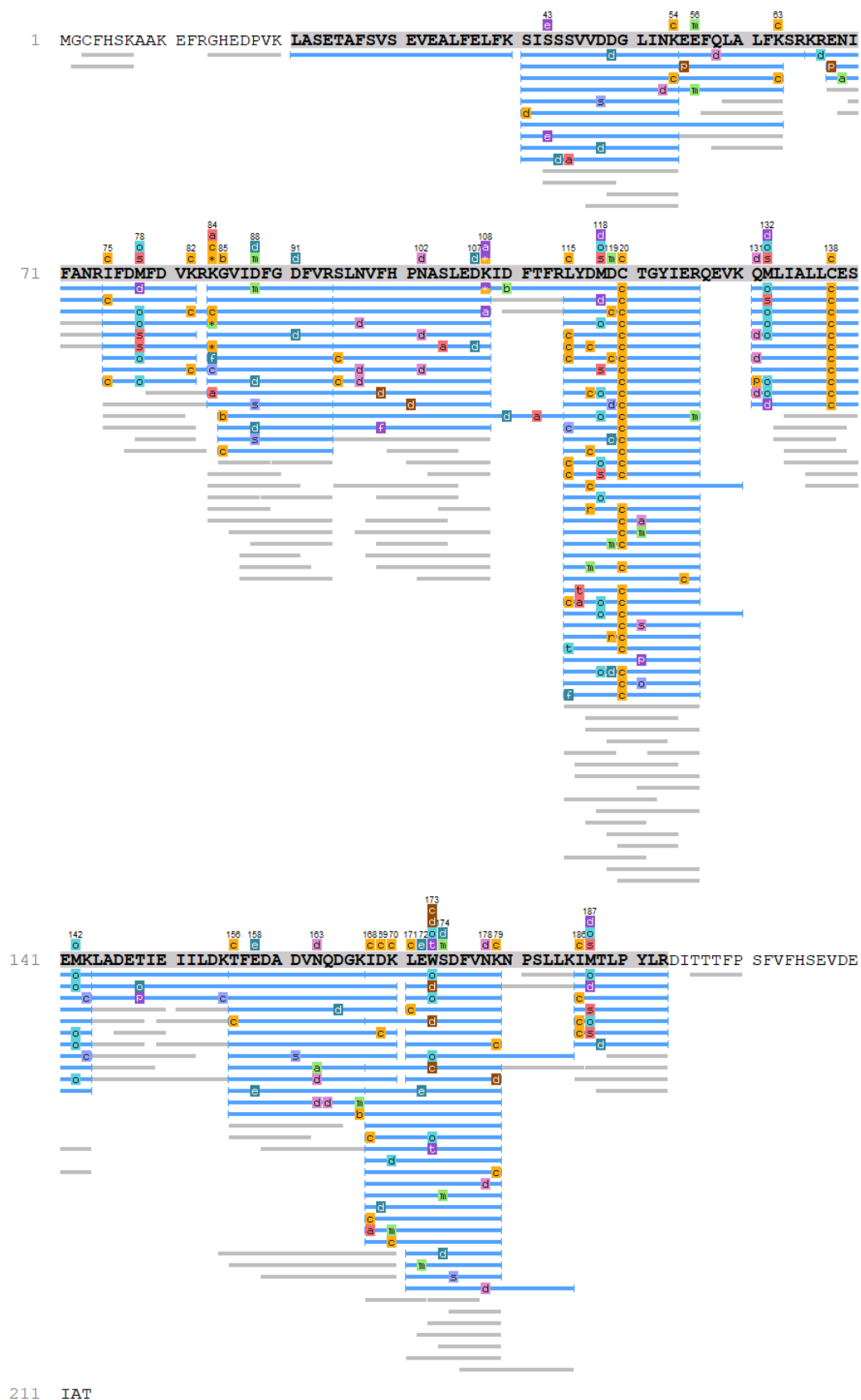


Figure S4: Mass Spectrometry analysis of StreptII-TEV-CBL1. The protein was isolated from the upper band of the 25 kDa double signal, trypsin digested and submitted to MS-coupled liquid chromatography (ESI -MS). Resulting peptides were aligned to the wildtype sequence and analyzed for posttranslational modifications (PTMs) against the SwissProt data set using Peaks Studio version 10.6. The coding for the potential PTMs can be derived from table S2.

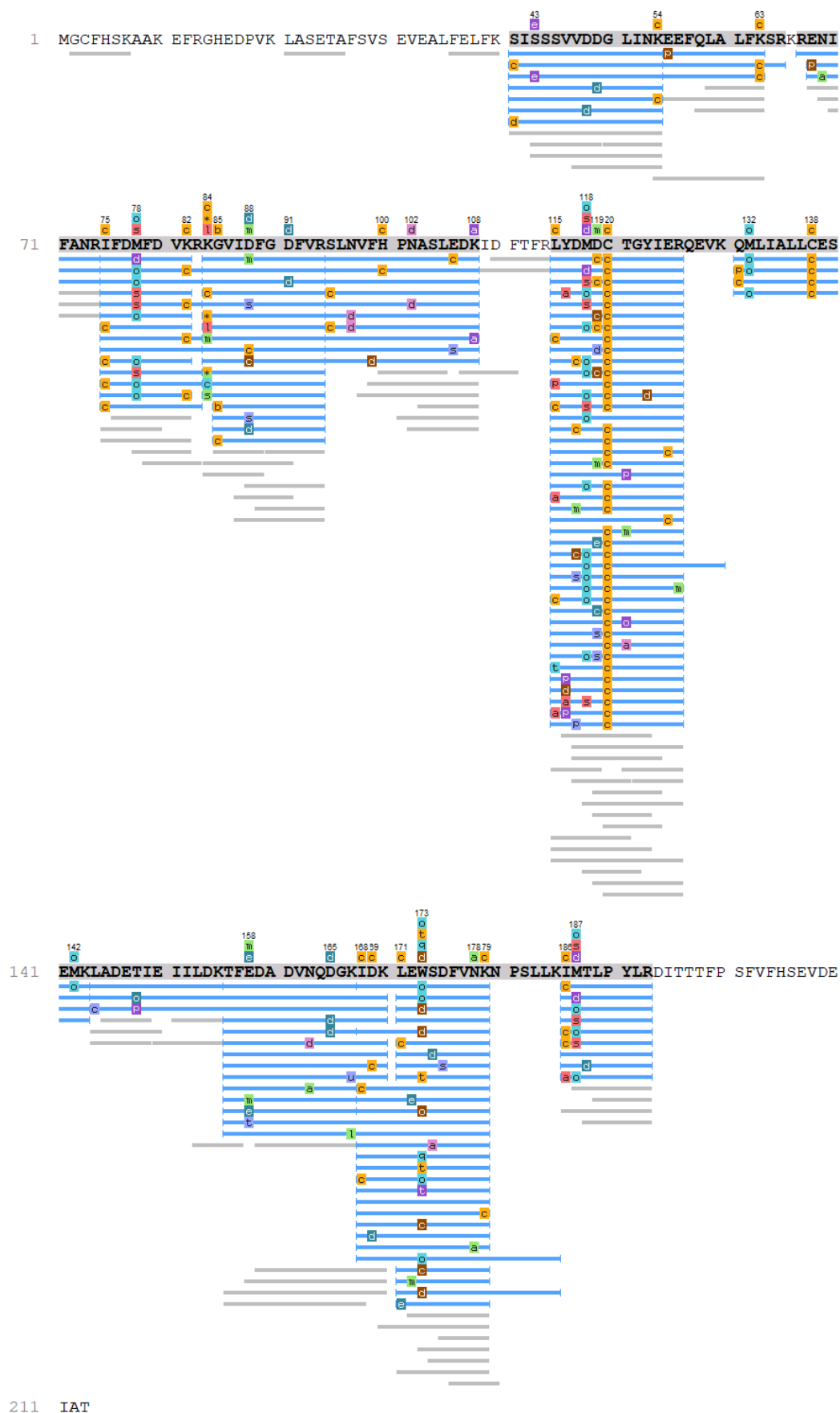
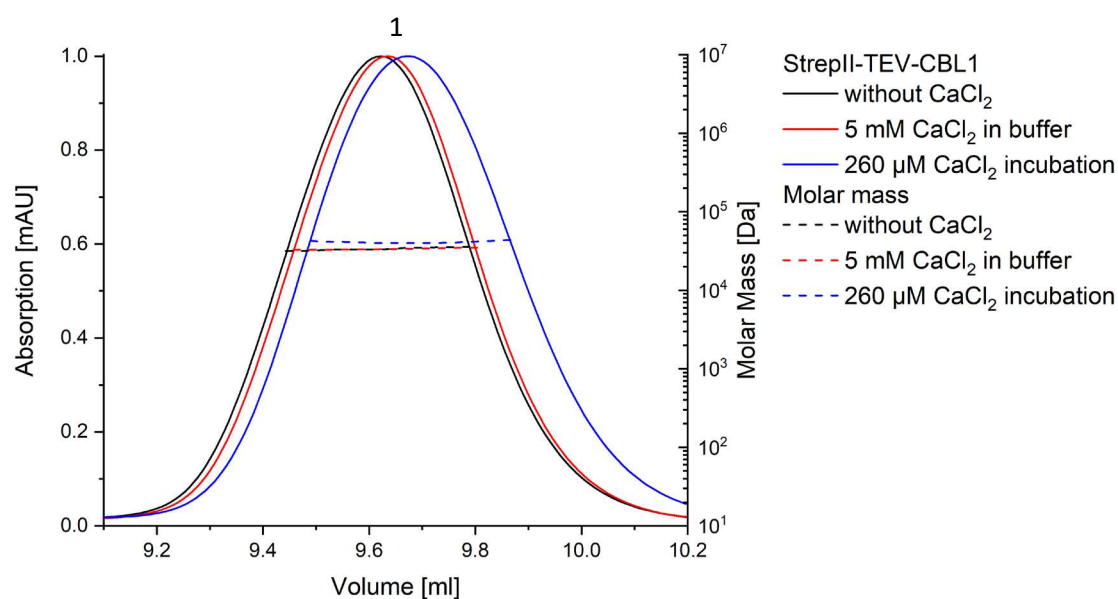


Figure S5: Mass Spectrometric analysis of StreptII-TEV-CBL1. The protein was isolated from the lower band of the 25 kDa double signal, trypsin digested and submitted to MS-coupled liquid chromatography (ESI -MS). Resulting peptides were aligned to the wildtype sequence and analyzed for posttranslational modifications (PTMs) against the SwissProt data set using Peaks Studio version 10.6. The coding for the potential PTMs can be derived from table S2.

A)



B)

Peak	1
without CaCl ₂	26.8 ± 0.77 kDa
5 mM CaCl ₂	25.4 ± 0.70 kDa
after ITC	24.2 ± 0.37 kDa

Figure S6: SEC-MALS analysis of StreptII-TEV-CBL1 protein in presence or absence of calcium chloride. A) 200 μ g of SEC purified CBL1 (Monomer) was subjected to a Superdex75 increase 10/300 column for MALS analysis, without the addition of CaCl₂ (black), in presence of 5 mM CaCl₂ in the MALS buffer (red) and CBL1 after incubation with 4.5 molar excess of CaCl₂ (blue). The X-axis represents the elution volume while the left Y-axis represents the UV absorption at 280 nm in mAU units and the right Y-axis represents the molecular mass calculated from the light scattering. The solid traces represent absorption at 280 nm while the dashed lines represent the molecular weight. B) The different peaks from SEC chromatogram were separately analyzed and the molecular weight for each were calculated using ASTRA 7.3.2 software (Wyatt Technology Corp.) based on the chromatograms in A). The protein samples were analyzed as detergent conjugated.

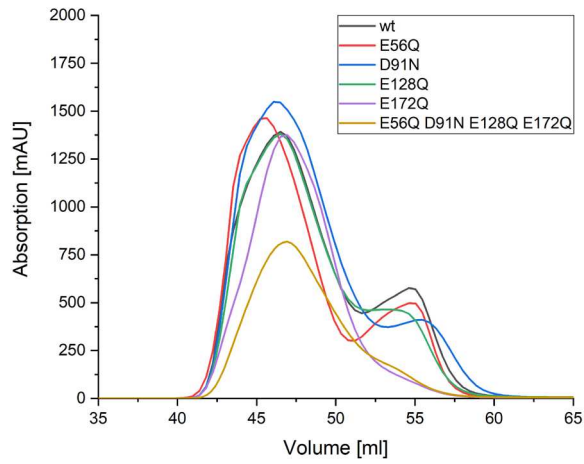
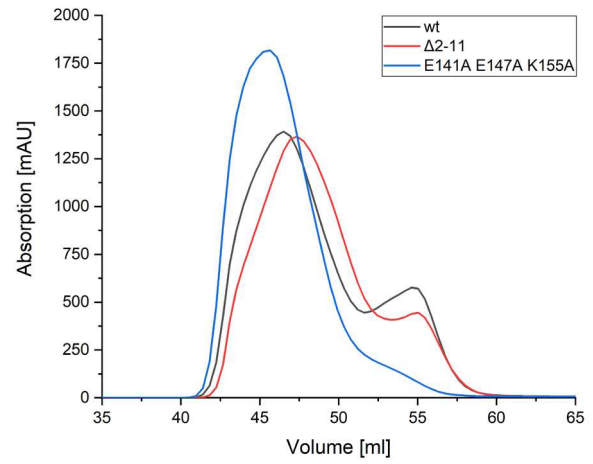
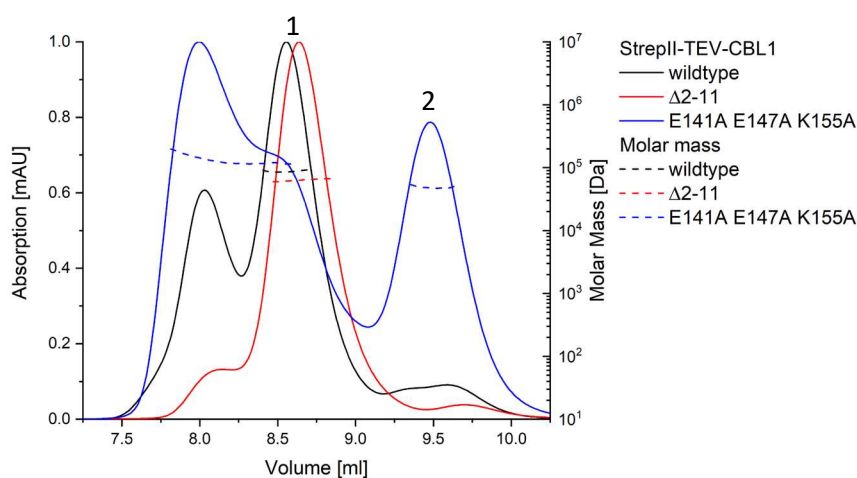
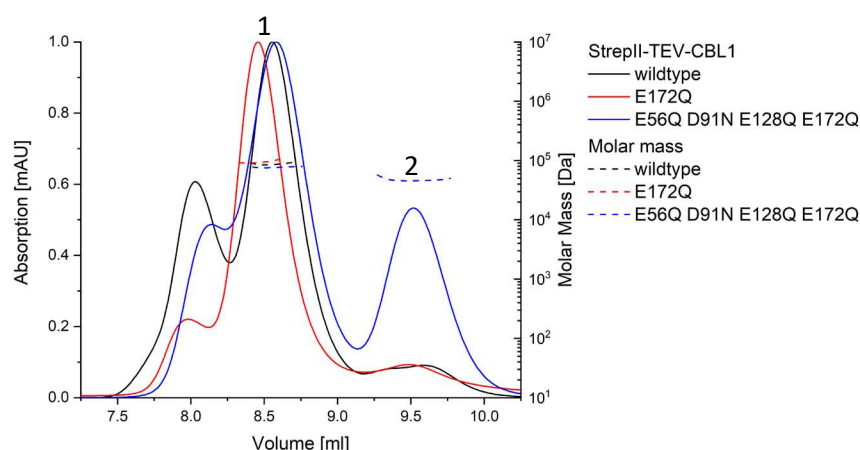
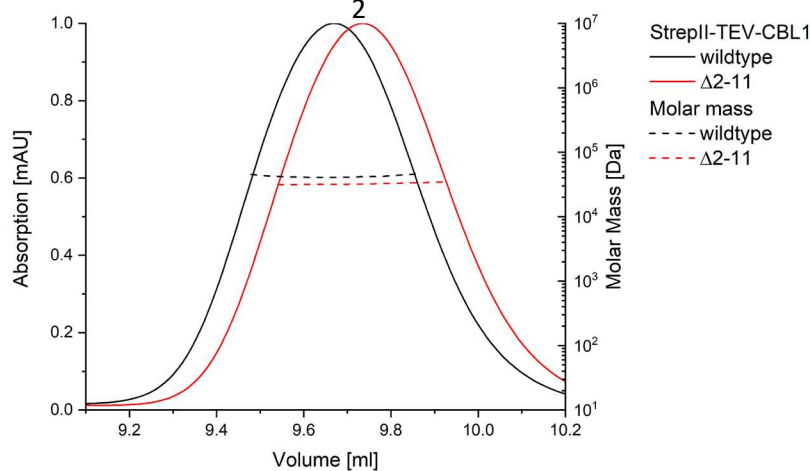
A)**B)**

Figure S7: SEC chromatograms of A) CBL1 wt (black) compared with all EF mutants (E56Q red, D91N blue, E128Q green, E172Q purple, E56Q D91N E128Q E172Q yellow) and B) CBL1 wt (black) compared with the N-terminal truncation $\Delta 2-11$ (red) and E141A E147A K155A (blue). The X-axis represents the elution volume in ml while the Y-axis represents the UV absorption at 280 nm in mAU units. The size exclusion chromatography was performed on a HiLoad Superdex75 16/600.

A)



C)

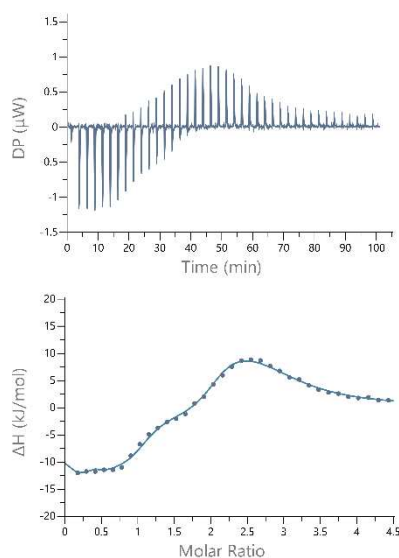


D)

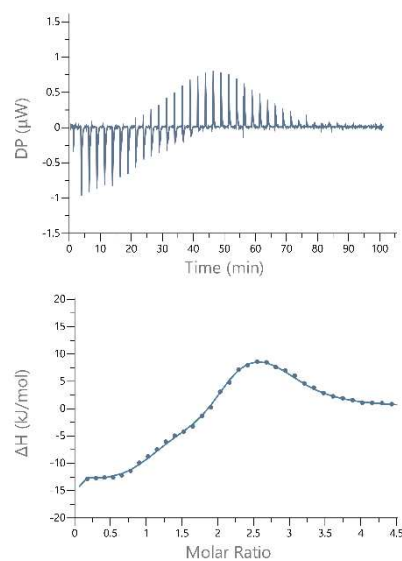
CBL1	Dimer (1)	Monomer (2)
wildtype	59.7 ± 1.22 kDa	27.1 ± 0.53 kDa
E172Q	60.7 ± 0.89 kDa	-
E56Q D91N E128Q E172Q	46.3 ± 1.55 kDa	25.8 ± 0.68 kDa
Δ2-11	53.9 ± 0.86 kDa	27.4 ± 0.60 kDa
E141A E147A K155A	114 ± 1.74 kDa	44.5 ± 0.77 kDa

Figure S8: SEC-MALS analysis of StreptII-TEV-CBL1 mutants. 200 μ g SEC purified CBL1 was subjected to a Superdex75 increase 10/300 column for MALS analysis. In section A) the protein samples of the E172Q (red) and E56Q D91N E128Q E172Q mutant (blue) are depicted. In section B) the protein samples of the Δ 2-11 (red) and E141A E147A K155A (blue) mutants are depicted. In section C) the protein samples of CBL1 Δ 2-11 (red) is depicted. For comparison the wildtype is depicted in black in A), B) and C). The X-axis represents the elution volume (ml) while the left Y-axis represents the UV absorption at 280 nm (mAU) and the right Y-axis represents the molecular mass calculated from the light scattering (Da). D) The peaks from the SEC chromatograms (Figure S6) were separately analyzed and the molecular weight for each variant was calculated using ASTRA 7.3.2 software (Wyatt Technology Corp.) based on the chromatograms in section A), B) and C).

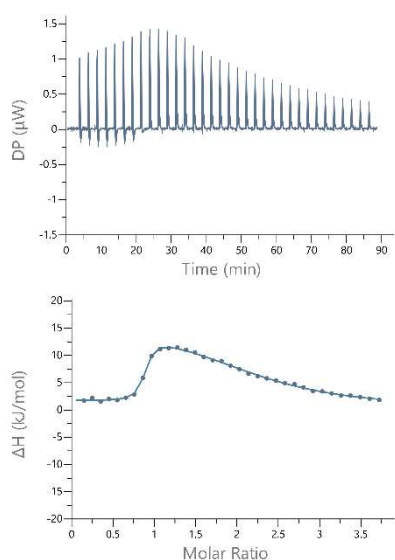
1A) wildtype CaCl_2



2B) $\Delta 2-11$ CaCl_2



2A) wildtype MnCl_2



2B) $\Delta 2-11$ MnCl_2

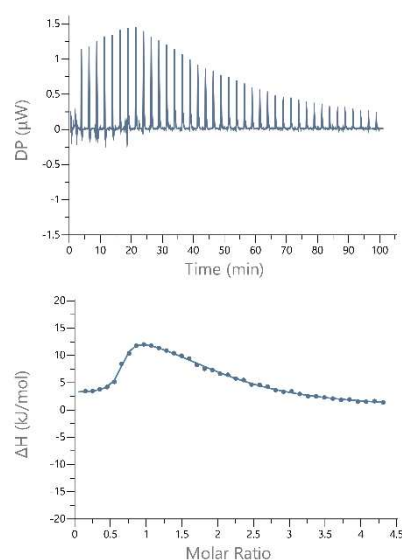


Figure S9: ITC raw data and binding isotherms of monomeric 1) and dimeric 2) $56 \mu\text{M}$ StreptII_TEV-CBL1 wildtype A) and $\Delta 2-11$ B) titrated with 1.13 mM CaCl_2 or MnCl_2 . In the upper panels the raw data is depicted. The Y-axis represents the change in heat capacity (μW) while the X-axis represents the time (min). The lower panel represents the integrated spikes in respect to time. Here the X-axis represents the molar ratio (ion: protein) while the Y-axis represents the change in heat capacity (ΔH). The data points were fitted using the fitting model which resulted in the lowest reduced Chi-Square. In the case of the CaCl_2 binding the sequential fitting model with 3 sites was used while for the MnCl_2 the two sets of sites model was used.

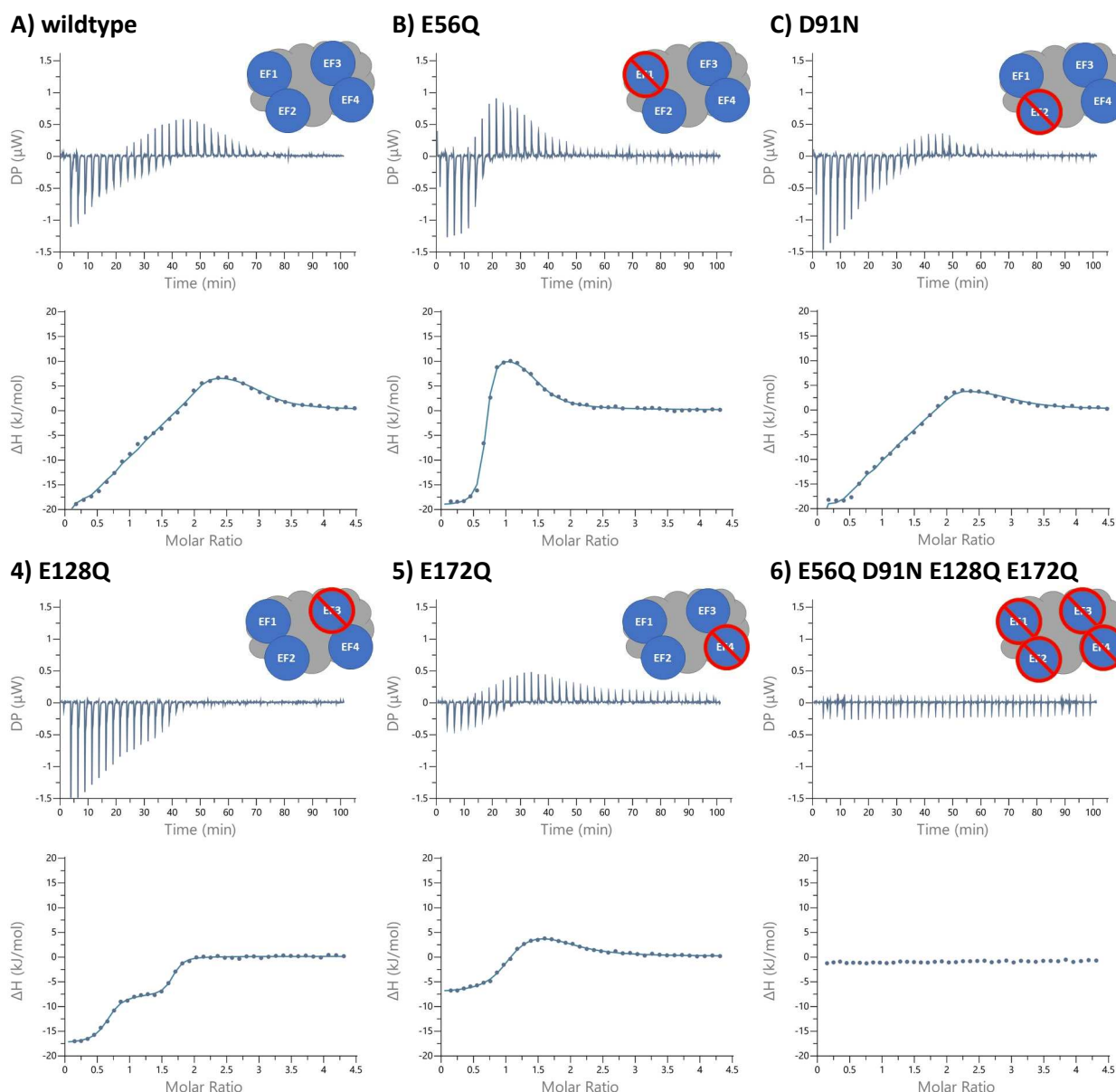


Figure S10: ITC raw data and binding isotherms of 56 μM StreptII-TEV-CBL1 wildtype and the mutants titrated with 1.13 mM CaCl_2 . In the upper panels the raw data is depicted. The Y-axis represents the change in heat capacity (μW) while the X-axis represents the time (min). The lower panel represents the integrated spikes in respect to time. Here the X-axis represents the molar ratio (ion: protein) while the Y-axis represents the change in heat capacity (ΔH). All proteins were analyzed in their dimeric form. The data points were fitted using the fitting model which resulted in the lowest reduced Chi-Square. In the case of wildtype protein and the D91N mutant, sequential fitting model with 3 sites was used while for E56Q, E128Q and E172Q mutants, two sets of sites model was used. The quadruple mutant showed no binding and therefore, the data points could not be fitted using any of the fitting models.

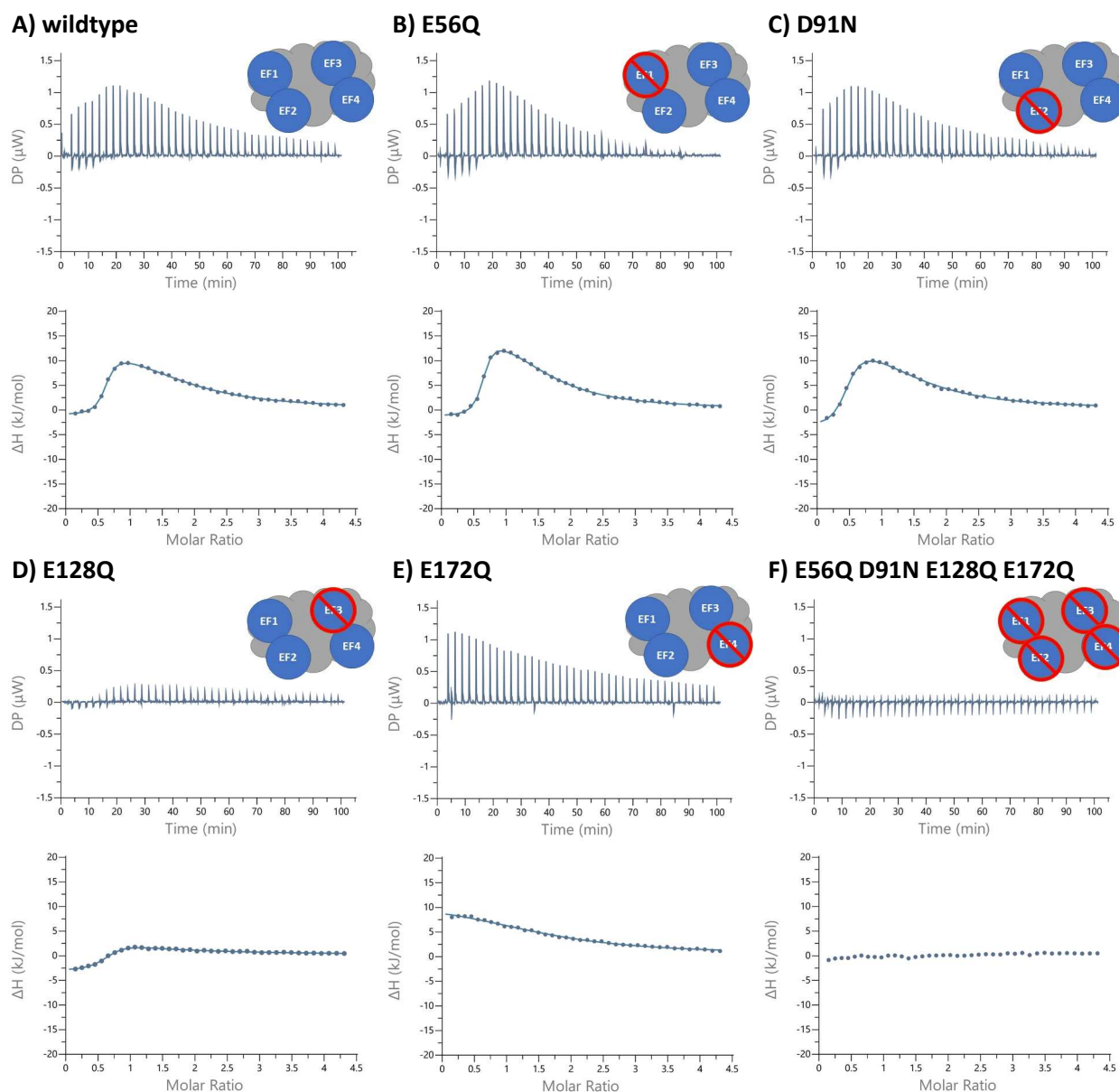


Figure S11: ITC raw data and binding isotherms of 56 μ M StreptII-TEV-CBL1 wt and the EF-hand mutants titrated with 1.13 mM MnCl_2 . In the upper panels the raw data is depicted. The Y-axis represents the change in heat capacity (μW) while the X-axis represents the time (min). The lower panel represents the integrated spikes in respect to time. Here the X-axis represents the molar ratio (ion: protein) while the Y-axis represents the change in heat capacity (ΔH). All proteins were analyzed in their dimeric form. The data points were fitted with the fitting model resulting in the lowest reduced Chi-Square. For the binding isotherms of the wt protein, the E56Q, D91N and the E128Q mutant this was the two sets of sites fitting model. The binding isotherm of the E172Q mutant was fitted with the one set of sites model. The quadruple mutant showed no binding and therefore the data points could not be fitted with any fitting model.

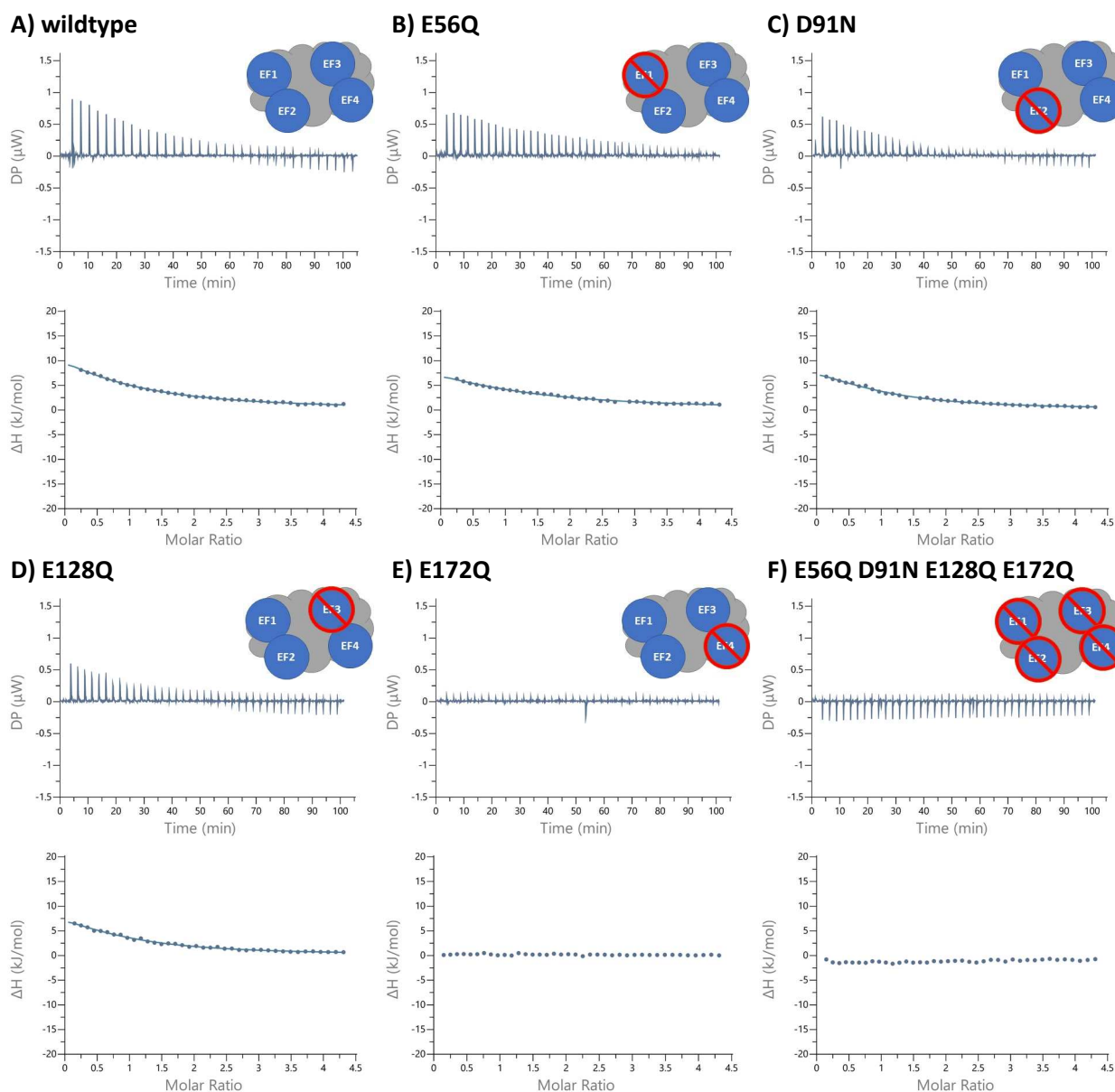


Figure S12: ITC raw data and binding isotherms of 56 μM StreptII-TEV-CBL1 wt and the EF-hand mutants titrated with 1.13 mM MgCl_2 . In the upper panels the raw data is depicted. The Y-axis represents the change in heat capacity (μW) while the X-axis represents the time (min). The lower panel represents the integrated spikes in respect to time. Here the X-axis represents the molar ratio (ion: protein) while the Y-axis represents the change in heat capacity (ΔH). The wt, E56Q, D91N, and E128Q mutant were analyzed at 25 $^{\circ}\text{C}$ in their monomeric form by adding 1 μl per titration. For the EF4 and quadruple mutant no monomeric protein could be purified, hence the dimeric protein had to be used for the ITC measurements. The data points were fitted with the one set of sites fitting model. The E172Q and the quadruple mutant showed no binding and therefore the data points could not be fitted with any fitting model.

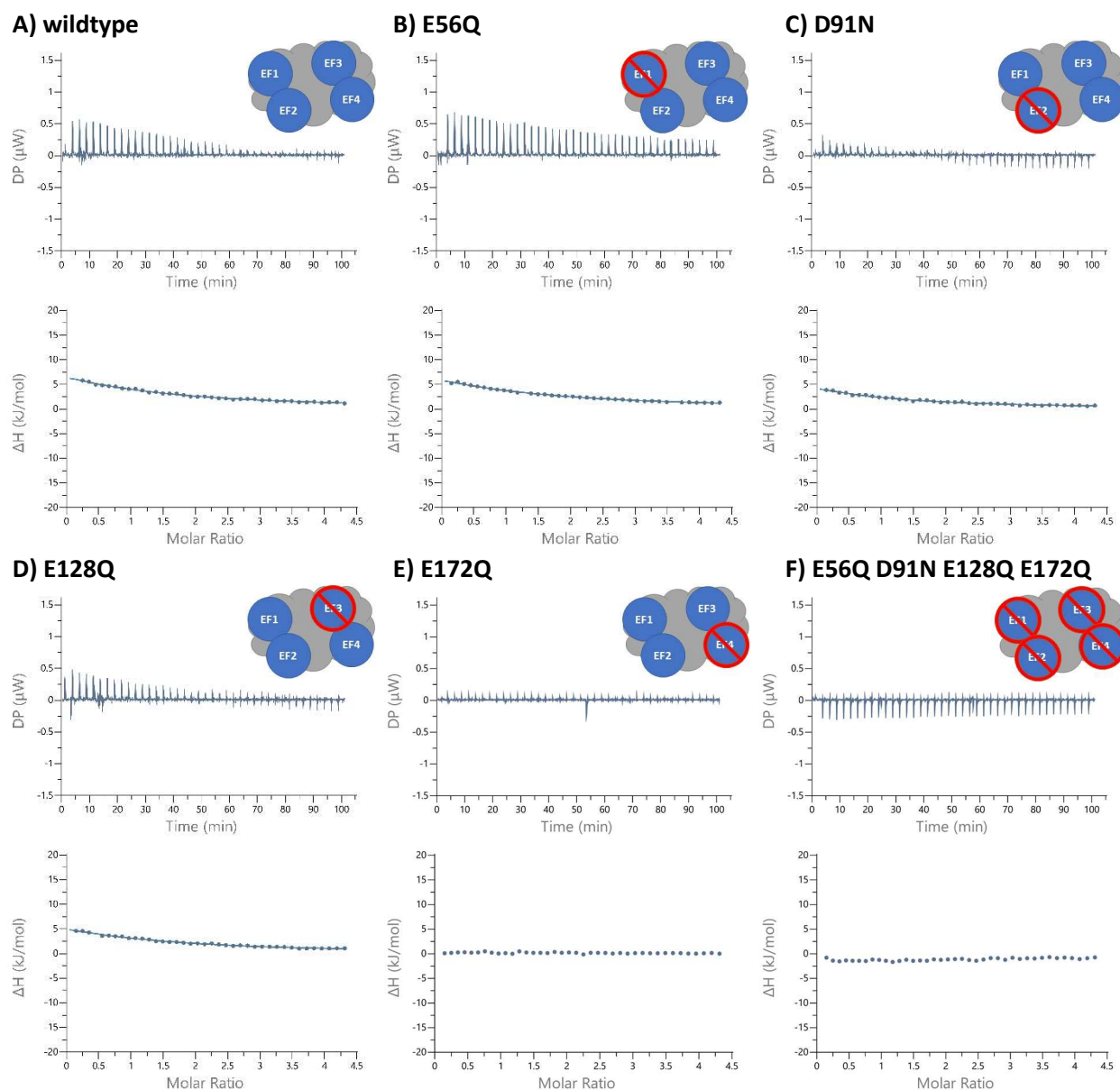


Figure S13: ITC raw data and binding isotherms of 56 μM StreptII-TEV-CBL1 wt and the EF-hand mutants titrated with 1.13 mM MgCl_2 . In the upper panels the raw data is depicted. The Y-axis represents the change in heat capacity (μW) while the X-axis represents the time (min). The lower panel represents the integrated spikes in respect to time. Here the X-axis represents the molar ratio (ion: protein) while the Y-axis represents the change in heat capacity (ΔH). All proteins were analyzed in their dimeric form. The data points were fitted with the one set of sites fitting model. The E172Q and the quadruple mutant showed no binding and therefore the data points could not be fitted with any fitting model.

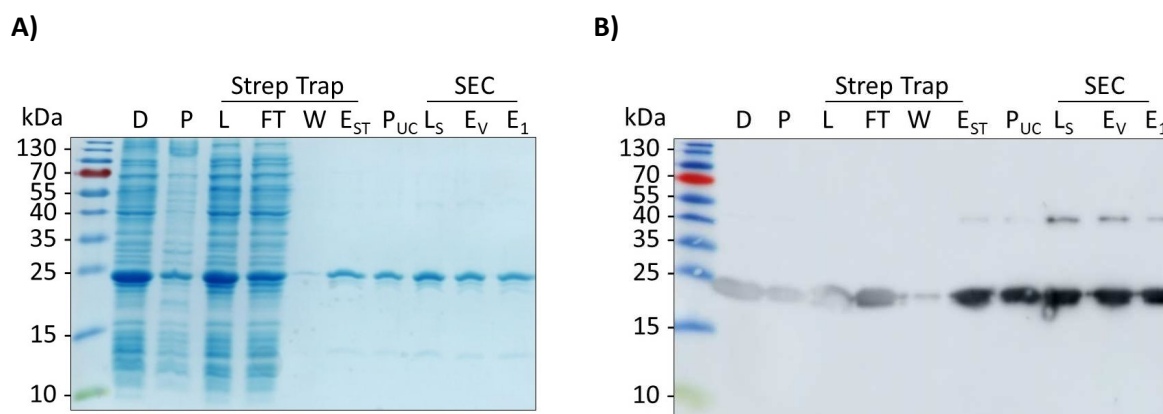
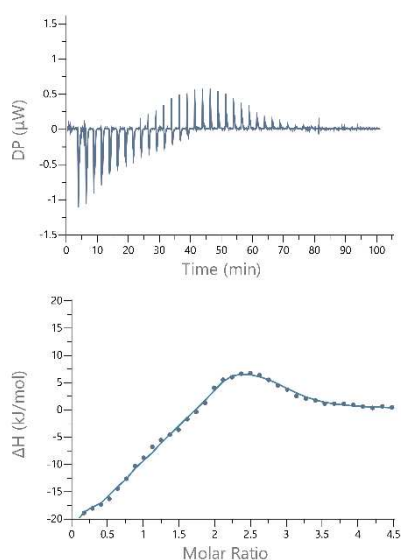


Figure S14: Purification of CBL1 E141A E147A K155A. Coomassie stained gel and Western blot. D = disrupted cells; P = cell debris pellet; L = load with 0.25 % (w/v) Brij35; FT = StrepTrap HP flow through; W = wash; E_{ST} = StrepTrap HP elution; P_{UC} = ultra centrifugation pellet; L_S = SEC load; E_V = SEC Fraction void; E₁ = SEC Fraction (Dimer). For the samples D-W 2.5 μ l were loaded. For the samples E_{ST}-E₁ 1.25 μ g protein were loaded per lane. The blot was developed using α -StrepII primary antibody and α -mouse-IgG-HRPO-coupled secondary antibody and detected by luminescence with an exposure time of 40 s.

1) wildtype Dimer



2) N141A N147A K155A

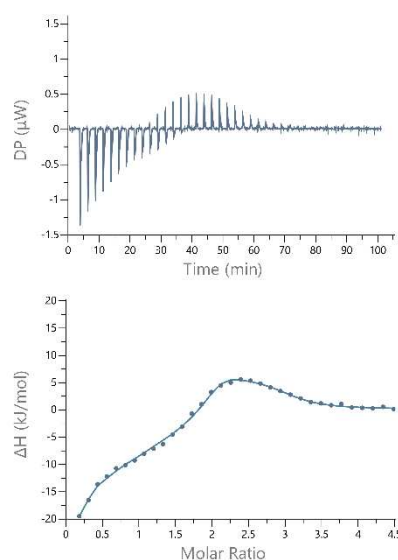


Figure S15: ITC raw data and binding isotherms of 56 μ M StrepII-TEV-CBL1 wildtype 1) and E141A E147A K155A 2) titrated with 1.13 mM CaCl₂. In the upper panels the raw data is depicted. The Y-axis represents the change in heat capacity (μ W) while the X-axis represents the time (min). The lower panel represents the integrated spikes in respect to time. Here the X-axis represents the molar ratio (ion: protein) while the Y-axis represents the change in heat capacity (Δ H). The data points were fitted using the fitting model which resulted in the lowest reduced Chi-Square. The sequential fitting model with 3 sites was used.

Table S6: List of primers used for cloning and site directed mutagenesis.

Name	Sequence 5' → 3'	Length [bp]	GC [%]	Tm [°C]
initial primer fw	TTTGCTAGCTGGAGCCACCCGCAGTTC	27	59	77
initial primer rev	TTTGTCGACTCATGTGGCAATCTCATCGACCTCC	34	50	76
TEV_CBL1_fw	TATTTTCAGGGCTGCTTCCACTCAAAG	27	44	63
TEV_CBL1_rev	CAGGTTTTCTTTTCGAACTGCGGGTG	27	48	63
CBL1-E56Q fw	TAACAAGGAGCAGTTTCAACTTG	23	39	56
CBL1-E56Q rev	ATCAGACCATCATCAACAAC	20	40	59
CBL1-D91N fw	CGATTTCGGGAACCTTGTAAGATC	24	42	60
CBL1-D91N rev	ATGACTCCTTTTCGTTTAAC	20	35	57
CBL1-E128Q fw	TGAACGACAACAGGTCAAGCAAATG	25	44	62
CBL1-E128Q rev	ATGTAACCCGTGCAGTCC	18	56	65
CBL1-E172Q fw	TGATAAATTACAGTGGAGTGATTTCG	26	35	57
CBL1-E172Q rev	ATTTTTCATCTTGATTACAG	21	35	57
CBL1 N-11 fw	GGACACGAAGACCCTGTT	18	56	64
CBL1 Nshort rev	GCCCTGAAAATACAGGTTTTTC	21	43	62
CBL1_E41A_E147A_K155A fw	CATAGAGATAATACTCGATGCAACATTTG AAGATGCAGACGTG	43	40	62
CBL1_E41A_E147A_K155A rev	GTCGCATCAGCCAGTTTCATCGCAGATTCTG CAGAGAAGCGC	41	56	65

Table S7: List of potential posttranslational modifications

	Modification	m/z
a	Acetylation (N-term)	+ 42.01
a	Acetylation (TSCYH)	+ 42.01
a	Amidation	- 0.98
a	2-amino-3-oxo-butanoic_acid	-2.02
a	Ammonia-loss (N)	- 17.03
b	Biotin polyethyleneoxide amine	+ 356.19
b	Biotinylation	+ 226.08
c	Carbamidomethylation	+ 57.02
c	Carbamidomethylation (DHKE, X@N-term)	+ 57.02
c	Carbamylation	+ 43.01
c	Carboxymethyl (KW, X@N-term)	+ 58.01
c	Carboxyl modification with ethanolamine	+ 43.04
c	Carboxylation (DKW)	+ 43.99
d	Deamidation (NQ)	+ 0.98
d	Dehydration	- 18.01
d	Deoxy	- 15.99
d	Dethiomethyl	- 48.00
d	2,3-dihydro-2,2-dimethyl-7-benzofuranol (N-methyl carbamate)	+ 58.03
d	Dihydroxy	+ 31.99
d	Dimethylation (KR)	+ 28.03
e	Ethyl amino	+ 27.05
e	Ethylation	+ 28.03
f	Fluorination	+ 17.99
f	Formylation	+ 27.99
l	Levoglandinyl-lysine pyrrole adduct	+ 316.20
l	Lysine oxidation to aminoadipic semialdehyde	- 1.03
m	Methylation (KR)	+ 14.02
m	Methylation (others)	+ 14.02
o	O3-(riboflavin phosphorlyl)	+ 438.09
o	O-Diethylphosphorylation	+ 136.03
o	O-Isopropylmethylphosphonylation	+ 120.03
o	Oxidation (HW)	+ 15.99
o	Oxidation (M)	+ 15.99
o	Oxidation to nitro	+ 44.99
p	phosphate-ribosylation	+ 212.01
p	Phosphorylation (STY)	+ 79.97
p	Propionamide (K, X@N-term)	+ 71.04
p	Pyro-glu from E	- 18.01
p	Pyro-glu from Q	- 17.03
q	Quinone	+ 29.97
r	Replacement of proton with ammonium ion	+ 17.03
s	Sodium adduct	+ 21.98
s	3-sulphanylpropanoyl	+ 88.00
s	Sulphation	+ 79.96
s	Sulphone	+ 31.99
t	Tri nitro benzene	+ 210.99
t	Triglutamyl	+ 387.13
t	Tryptophan oxidation to kynurenin	+ 3.99
t	Tryptophan oxidation to oxolactone	+ 13.98
t	Tyrosine oxidation to 2-aminotyrosine	+ 15.01
u	Ubiquitin	+ 114.04
*	Amidation, Carbamidomethylation (DHKE, X@N-term)	- 0.98/+ 57.02
*	Carbamidomethylation (DHKE, X@N-term), Carbamidomethylation (DHKE, X@N-term)	+ 57.02/+ 57.02
*	Carbamidomethylation (DHKE, X@N-term), Methylation (KR)	+ 57.02/+ 14.02

Table S8: Ca^{2+} binding parameters for EF hand 1 of CBL1 wildtype, E56Q (EF1), D91N (EF2), E128Q (EF3), E172Q (EF4), E56Q_D91N_E128Q_E172Q (quadruple), $\Delta 2-11$ (N11) and E141A_E147A_E155A (NoDimer). All values are calculated as means of at least 3 independent measurements. The errors were calculated from the standard deviation of the respective values.

Mutant	Oligomeric state	Syringe	Cell	Fit	Replicates	n1	K_D EF1	ΔH EF1	ΔG EF1	$-\Delta S$ EF1
WT	Monomer	1.13 mM	48.5 μM^*	Seq3	4	-	373 \pm 75 nM	-3.14 \pm 0.88 kJ/mol		-33.7 \pm 1.09 kJ/mol
	Dimer	1.13 mM	47.7 μM^*	Seq3	3	-	52.1 \pm 23.5 nM	3.64 \pm 1.02 kJ/mol		-45.5 \pm 2.15 kJ/mol
EF1	Monomer	1.13 mM	54.8 μM^*	TSS	6	-	-	-	-	-
	Dimer	1.13 mM	56 μM	TSS	3	-	-	-	-	-
EF2	Monomer	1.07 mM*	44.0 μM^*	Seq3	4	-	207 \pm 80.5 nM	-1.79 \pm 0.60 kJ/mol		-36.6 \pm 1.48 kJ/mol
	Dimer	1.09 mM*	53.0 μM^*	Seq3	3	-	81.2 \pm 37.0 nM	1.77 \pm 1.63 kJ/mol		-42.6 \pm 2.59 kJ/mol
EF3	Monomer	1.03 mM*	51.3 μM^*	TSS	4	1.24 \pm 0.33	353 \pm 93.0 nM	-6.62 \pm 0.26 kJ/mol	-37.0 \pm 0.73 kJ/mol	-30.4 \pm 0.80 kJ/mol
	Dimer	1.03 mM*	51.3 μM^*	TSS	4	1.34 \pm 0.36	281 \pm 73.1 nM	-8.12 \pm 0.49 kJ/mol	-37.5 \pm 0.76 kJ/mol	-29.4 \pm 1.14 kJ/mol
EF4	Dimer	1.13 mM	56 μM	TSS	6	0.85 \pm 0.16	279 \pm 104 nM	-7.33 \pm 0.22 kJ/mol	-37.6 \pm 0.98 kJ/mol	-30.3 \pm 1.12 kJ/mol
N11	Monomer	1.06 mM*	47.7 μM^*	Seq3	7	-	150 \pm 51.1 nM	-1.03 \pm 2.32 kJ/mol		-38.1 \pm 3.27 kJ/mol
	Dimer	1.08 mM*	43.8 μM^*	Seq3	5	-	59.9 \pm 33.7 nM	0.99 \pm 1.77 kJ/mol		-42.8 \pm 2.95 kJ/mol
NoDimer	Dimer	1.13 mM	51.2 μM^*	Seq3	5	-	55.5 \pm 38.9 nM	8.88 \pm 3.13 kJ/mol		-50.9 \pm 3.78 kJ/mol
Quadruple	Dimer	1.13 mM	56 μM	-	5	-	-	-	-	-

Table S9: Ca²⁺ binding parameters for EF hand 3 and 4 of CBL1 wildtype, E56Q (EF1), D91N (EF2), E128Q (EF3), E172Q (EF4), E56Q_D91N_E128Q_E172Q (quadruple), Δ2-11 (N11) and E141A_E147A_E155A (NoDimer). All values are calculated as means of at least 3 independent measurements. The errors were calculated from the standard deviation of the respective values

Mutant	Oligomeric state	Syringe	Cell	Fit	Replicates	n3	K _D EF3	ΔH EF3	ΔG EF3	-TΔS EF3	n4	K _D EF4	ΔH EF4	ΔG EF4	-TΔS EF4	Reduced Chi-Sqr.
WT	Monomer	1.13 mM	48.5 μM*	Seq3	4	-	8.60 ± 2.15 μM	15.3 ± 1.58 kJ/mol		-44.3 ± 1.36 kJ/mol	-	8.18 ± 1.85 nM	-12.5 ± 0.45 kJ/mol		-33.8 ± 0.70 kJ/mol	9.80 E-2 ± 1.51 E-2 (kJ/mol) ²
	Dimer	1.13 mM	47.7 μM*	Seq3	3	-	4.69 ± 1.48 μM	6.83 ± 1.06 kJ/mol		-37.4 ± 1.21 kJ/mol	-	13.4 ± 7.20 nM	-19.5 ± 1.35 kJ/mol		-25.8 ± 0.22 kJ/mol	2.65 E-1 ± 1.03 E-1 (kJ/mol) ²
EF1	Monomer	1.13 mM	54.8 μM*	TSS	6	0.94 ± 0.06	3.39 ± 0.88 μM	12.5 ± 1.18 kJ/mol	-31.3 ± 0.57 kJ/mol	-43.8 ± 0.99 kJ/mol	0.72 ± 0.07	8.65 ± 6.89 nM	-16.0 ± 0.67 kJ/mol	-46.6 ± 1.58 kJ/mol	-30.7 ± 1.72 kJ/mol	7.07 E-2 ± 3.06 E-2 (kJ/mol) ²
	Dimer	1.13 mM	56 μM	TSS	3	0.92 ± 0.06	3.61 ± 0.14 μM	11.9 ± 0.13 kJ/mol	-45.1 ± 1.13 kJ/mol	-25.8 ± 1.22 kJ/mol	0.68 ± 0.04	14.4 ± 7.18 nM	-19.3 ± 0.34 kJ/mol	-31.1 ± 0.09 kJ/mol	-43.0 ± 0.16 kJ/mol	6.90 E-2 ± 4.81 E-2 (kJ/mol) ²
EF2	Monomer	1.07 mM*	44.0 μM*	Seq3	4	-	5.74 ± 1.36 μM	10.6 ± 2.01 kJ/mol		-40.6 ± 1.60 kJ/mol	1	10.2 ± 2.11 nM	-15.7 ± 0.81 kJ/mol		-30.0 ± 1.10 kJ/mol	1.88 E-1 ± 3.93 E-2 (kJ/mol) ²
	Dimer	1.09 mM*	53.0 μM*	Seq3	3	-	5.11 ± 0.85 μM	5.55 ± 0.92 kJ/mol		-35.8 ± 1.35 kJ/mol	1	19.4 ± 8.11 nM	-21.4 ± 0.49 kJ/mol		-22.9 ± 1.40 kJ/mol	3.61 E-1 ± 2.62 E-1 (kJ/mol) ²
EF3	Monomer	1.03 mM*	51.3 μM*	TSS	4	-	-	-	-	-	0.90 ± 0.20	2.98 ± 1.16 nM	-12.7 ± 0.73 kJ/mol	-48.9 ± 0.91 kJ/mol	-36.2 ± 1.58 kJ/mol	3.43 E-2 ± 1.83 E-2 (kJ/mol) ²
	Dimer	1.03 mM*	51.3 μM*	TSS	4	-	-	-	-	-	0.84 ± 0.18	6.81 ± 2.44 nM	-18.8 ± 1.85 kJ/mol	-46.9 ± 1.18 kJ/mol	-28.1 ± 2.68 kJ/mol	7.35 E-2 ± 4.36 E-2 (kJ/mol) ²
EF4	Dimer	1.13 mM	56 μM	TSS	6	0.97 ± 0.13	7.01 ± 1.2 μM	5.48 ± 0.97 kJ/mol	-29.5 ± 0.42 kJ/mol	-35.0 ± 0.99 kJ/mol	-	-	-	-	-	1.90 E-2 ± 3.46 E-3 (kJ/mol) ²
N11	Monomer	1.06 mM*	47.7 μM*	Seq3	7	-	5.00 ± 1.17 μM	10.4 ± 2.84 kJ/mol		-40.8 ± 2.38 kJ/mol	-	18.4 ± 6.77 nM	-12.9 ± 1.04 kJ/mol		-31.5 ± 1.49 kJ/mol	9.79 E-2 ± 2.80 E-2 (kJ/mol) ²
	Dimer	1.08 mM*	43.8 μM*	Seq3	5	-	5.04 ± 2.51 μM	7.58 ± 3.04 kJ/mol		-38.7 ± 2.26 kJ/mol	-	11.9 ± 7.85 nM	-17.8 ± 1.56 kJ/mol		-28.4 ± 3.95 kJ/mol	3.75 E-1 ± 1.66 E-1 (kJ/mol) ²
NoDimer	Dimer	1.13 mM	51.2 μM*	Seq3	5	-	4.43 ± 2.55 μM	4.92 ± 1.50 kJ/mol		-36.1 ± 0.95 kJ/mol	-	69.6 ± 57.9 nM	-25.5 ± 3.14 kJ/mol		-16.0 ± 4.11 kJ/mol	1.03 E-1 ± 2.62 E-2 (kJ/mol) ²
Quadruple	Dimer	1.13 mM	56 μM	-	5	-	-	-	-	-	-	-	-	-	-	-

Table S10: Mn²⁺ binding parameters for CBL1 wildtype, E56Q (EF1), D91N (EF2), E128Q (EF3), E172Q (EF4), E56Q_D91N_E128Q_E172Q (quadruple) and Δ2-11 (N11). All values are calculated as means of at least 2 independent measurements. The errors were calculated from the standard deviation of the respective values. As the parameters could not be assigned to the EF hands explicitly, here they are named low and high affinity sites.

Mutant	Oligomeric states	Syringe	Cell	Fit	Replicates	n1/4	K _D EF1/4	ΔH EF1/4	ΔG EF1/4	-TΔS EF1/4	n3	K _D EF3	ΔH EF3	ΔG EF3	-TΔS EF3	Red. Chi-Sqr.
WT	Monomer	1.13 mM	56 μM	TSS	3	1.99 ± 0.09	36.3 ± 3.51 μM	14.7 ± 0.68 kJ/mol	-25.4 ± 0.25 kJ/mol	-40.1 ± 0.53 kJ/mol	0.81 ± 0.11	186 ± 61.2 nM	2.44 ± 0.21 kJ/mol	-38.6 ± 0.86 kJ/mol	-41.0 ± 1.07 kJ/mol	3.53 E-2 ± 1.17 E-2 (kJ/mol) ²
	Dimer	1.13 mM	56 μM	TSS	3	1.76 ± 0.03	21.5 ± 4.67 μM	11.9 ± 0.34 kJ/mol	-26.7 ± 0.50 kJ/mol	-38.6 ± 0.83 kJ/mol	0.62 ± 0.03	169 ± 15.5 nM	-1.72 ± 0.43 kJ/mol	-38.7 ± 0.22 kJ/mol	-37.0 ± 0.22 kJ/mol	3.17 E-2 ± 1.41 E-2 (kJ/mol) ²
EF1	Monomer	1.13 mM	56 μM	TSS	3	1.46 ± 0.06	21.6 ± 2.74 μM	15.6 ± 0.85 kJ/mol	-26.7 ± 0.33 kJ/mol	-42.3 ± 0.57 kJ/mol	0.76 ± 0.07	67.3 ± 25.7 nM	1.89 ± 0.48 kJ/mol	-41.2 ± 1.18 kJ/mol	-43.1 ± 0.79 kJ/mol	3.07 E-2 ± 4.64 E-3 (kJ/mol) ²
	Dimer	1.13 mM	56 μM	TSS	2	1.43 ± 0.04	21.2 ± 0.70 μM	14.2 ± 0.50 kJ/mol	-26.7 ± 0.10 kJ/mol	-40.9 ± 0.60 kJ/mol	0.57 ± 0.03	108 ± 43.7 nM	-0.75 ± 0.70 kJ/mol	-40.0 ± 1.10 kJ/mol	-39.3 ± 1.75 kJ/mol	2.30 E-2 ± 5.00 E-3 (kJ/mol) ²
EF2	Monomer	1.04 mM*	46.0 μM*	TSS	3	2.06 ± 0.12	24.3 ± 4.34 μM	12.8 ± 1.06 kJ/mol	-26.4 ± 0.42 kJ/mol	-39.2 ± 0.64 kJ/mol	0.88 ± 0.09	83.4 ± 16.0 nM	0.42 ± 0.11 kJ/mol	-40.9 ± 0.54 kJ/mol	-39.4 ± 2.64 kJ/mol	3.00 E-2 ± 1.00 E-2 (kJ/mol) ²
	Dimer	1.09 mM*	56 μM	TSS	3	1.76 ± 0.24	21.8 ± 5.19 μM	12.2 ± 0.95 kJ/mol	-26.7 ± 0.65 kJ/mol	-38.9 ± 0.46 kJ/mol	0.67 ± 0.28	374 ± 217 nM	-4.14 ± 0.06 kJ/mol	-37.2 ± 1.64 kJ/mol	-33.1 ± 1.60 kJ/mol	3.97 E-2 ± 1.52 E-3 (kJ/mol) ²
EF3	Monomer	0.94 mM	46.5 μM	OSS	4	1.83 ± 0.17	18.5 ± 19.3 μM	2.96 ± 1.15 kJ/mol	-28.8 ± 3.11 kJ/mol	-31.7 ± 1.98 kJ/mol	-	-	-	-	-	1.20 E-2 ± 3.57 E-3 (kJ/mol) ²
	Dimer	1.13 mM	56 μM	TSS	2	2.21 ± 0.10	148 ± 5.00 μM	2.96 ± 0.18 kJ/mol	-21.9 ± 0.10 kJ/mol	-24.9 ± 0.25 kJ/mol	0.56 ± 0.03	2.29 ± 0.59 μM	-3.12 ± 0.48 kJ/mol	-32.4 ± 0.65 kJ/mol	-29.2 ± 1.10 kJ/mol	5.80 E-3 ± 1.10 E-3 (kJ/mol) ²
EF4	Dimer	1.13 mM	56 μM	OSS	7	1.55 ± 0.22	36.1 ± 5.58 μM	10.7 ± 0.67 kJ/mol	-25.4 ± 0.37 kJ/mol	-36.1 ± 0.72 kJ/mol	-	-	-	-	-	1.63 E-2 ± 9.14 E-3 (kJ/mol) ²
N11	Monomer	1.04 mM*	51.5 μM*	TSS	5	1.97 ± 0.08	26.6 ± 3.41 μM	13.1 ± 1.17 kJ/mol	-26.1 ± 0.32 kJ/mol	39.2 ± 1.11 kJ/mol	0.70 ± 0.12	151 ± 33.1 nM	2.11 ± 1.25 kJ/mol	-39.0 ± 0.58 kJ/mol	-41.2 ± 1.41 kJ/mol	3.34 E-2 ± 1.18 E-2 (kJ/mol) ²
	Dimer	1.08 mM*	53.8 μM *	TSS	5	1.81 ± 0.20	22.9 ± 3.77 μM	11.8 ± 0.66 kJ/mol	-26.5 ± 0.43 kJ/mol	-38.3 ± 0.38 kJ/mol	0.67 ± 0.07	197 ± 58.8 nM	-1.51 ± 0.72 kJ/mol	-38.4 ± 0.86 kJ/mol	-36.9 ± 0.51 kJ/mol	4.06 E-2 ± 7.71 E-3 (kJ/mol) ²
Quadruple	Dimer	1.13 mM	56 μM	-	5	-	-	-	-	-	-	-	-	-	-	-

Table S11: Mg²⁺ binding parameters for CBL1 wildtype, E56Q (EF1), D91N (EF2), E128Q (EF3), E172Q (EF4) and E56Q_D91N_E128Q_E172Q (quadruple). All values are calculated as means of at least 2 independent measurements. The errors were calculated from the standard deviation of the respective values.

Mutant	Oligomeric state	Syringe	Cell	Fit	Replicates	n4	K _D EF4	ΔH EF4	ΔG EF4	-TΔS EF4	Red. Chi-Sqr.
WT	Monomer	1.13 mM	56 μM	OSS	4	0.88 ± 0.05	59.5 ± 11.3 μM	19.2 ± 3.28 kJ/mol	-24.2 ± 0.51 kJ/mol	-43.3 ± 2.85 kJ/mol	1.85 E-2 ± 8.62 E-3 (kJ/mol) ²
	Dimer	1.13 mM	56 μM	OSS	2	0.85 ± 0.03	67.7 ± 12.5 μM	6.81 ± 1.52 kJ/mol	-23.9 ± 0.45 kJ/mol	-30.7 ± 1.95 kJ/mol	7.40 E-3 ± 4.60 E-3 (kJ/mol) ²
EF1	Monomer	1.13 mM	56 μM	OSS	4	0.96 ± 0.14	94.2 ± 6.08 μM	20.2 ± 3.68 kJ/mol	-23.0 ± 0.15 kJ/mol	-43.2 ± 3.73 kJ/mol	1.26 E-2 ± 9.69 E-3 (kJ/mol) ²
	Dimer	1.13 mM	56 μM	OSS	2	0.86 ± 0.08	95.9 ± 7.5 μM	16.2 ± 0.30 kJ/mol	-18.8 ± 0.10 kJ/mol	-33.8 ± 0.15 kJ/mol	1.29 E-2 ± 9.50 E-4 (kJ/mol) ²
EF2	Monomer	1.13 mM	56 μM	OSS	2	1.02 ± 0.07	55.7 ± 9.35 μM	14.6 ± 1.45 kJ/mol	-24.4 ± 0.45 kJ/mol	-38.9 ± 1.10 kJ/mol	1.34 E-2 ± 5.60 E-3 (kJ/mol) ²
	Dimer	1.13 mM	56 μM	OSS	2	0.87 ± 0.11	92.6 ± 9.45 μM	11.3 ± 1.96 kJ/mol	-23.1 ± 0.25 kJ/mol	-34.4 ± 1.70 kJ/mol	8.60 E-3 ± 3.40 E-3 (kJ/mol) ²
EF3	Monomer	1.13 mM	56 μM	OSS	2	0.88 ± 0.01	55.9 ± 2.35 μM	13.8 ± 0.20 kJ/mol	-24.3 ± 0.10 kJ/mol	-38.1 ± 0.30 kJ/mol	1.65 E-2 ± 1.5 E-3 (kJ/mol) ²
	Dimer	1.13 mM	56 μM	OSS	3	1.04 ± 0.03	126 ± 43.6 μM	15.1 ± 4.37 kJ/mol	-22.4 ± 0.95 kJ/mol	-37.5 ± 3.47 kJ/mol	9.07 E-3 ± 6.08 E-3 (kJ/mol) ²
EF4	Dimer	1.13 mM	56 μM	OSS	4	-	-	-	-	-	-
Quadruple	Dimer	1.13 mM	56 μM	-	5	-	-	-	-	-	-

Discussion

The importance of plant nutrient uptake and its biochemical analysis

Plants make up one of the largest domains within eukaryotic life [1]. About half a million plant species are known on planet earth [193]. Their existence is essential for all living organisms on earth. They not only produce oxygen and fix CO₂ [193], plants as well are one of the main food sources and further provide a high variety of non-food resources like wood, paper and many more [194]. The continuous growth in human population is accompanied with severe increases in atmospheric CO₂ [195] and global warming [196] as well as an increasing need for food and non-food plant products [197, 198]. Hence a detailed understanding of plants, their growth, nutrition and the underlying biochemical processes are of high relevance to maintain sufficient supply of vegetal products and further improve agricultural yields.

Since nutrient content in soils is continuously decreasing [199, 200], the agricultural industry has to rely more and more on fertilizers [201, 202]. Plant nutrition, the uptake of nutrients and the plant responses to nutrient deprivation is a highly complex topic. Hence, elucidating the structure and function of components contributing to the complex network of nutrient uptake will help to understand the mechanisms underlying these processes [203] and to improve crop yields to comply the increasing demand on vegetal products.

Despite the fact that K⁺ is the seventh most abundant element of the earth crust [204], its bioavailability for plants is limited. Only the ionic form as K⁺ is usable for the plant. K⁺ comprises 0.1 - 0.2 % of the potassium present in soils, while 90 % and above of the soil potassium is present as unavailable minerals [205]. K⁺ deprivation comprises a form of abiotic stress for the plant and results in limitation of the plants growth and development [206]. Therefore, this study aimed for the characterization of a K⁺ uptake system from *Arabidopsis thaliana*, namely the K⁺ channel AKT1 and its activating interaction partners CIPK23 and CBL1.

Heterologous expression and purification of eukaryotic (membrane) proteins

The first step and the main prerequisite for structural and functional analysis of any protein of interest is the finding of a heterologous expression host suitable for the production of sufficient amounts of functional protein. The proteins analyzed in this study were derived from *A. thaliana*, hence an eukaryotic organism. The expression of eukaryotic proteins can be more complicated, as these proteins, compared to their prokaryotic relatives, are often higher in both structural and functional complexity and post translationally modified [207]. In general, the pro- and eukaryotic transcription and translation machinery differ in a variety of points that need to be taken into account. Not only the transcription and translation machinery, but as well the codon usage, the compartmentation as well as the lipid composition differs between pro- and eukaryotes [208-210].

E. coli is a commonly used expression host and known for its fast production of large amounts of biomass. It allows fast and easy transformation as well as selection of positive clones via antibiotics [211, 212]. For this study the prokaryotic *E. coli* expression strains C41 (DE3) and Rosetta (DE3) pLysS were chosen. While *E. coli* C41 (DE3) is a derivative of the prominent expression strain *E. coli* BL21 and specialized to overcome potential protein toxicity [213, 214], *E. coli* Rosetta (DE3) pLysS is specialized for the expression of eukaryotic proteins [215], since it encodes for codons rarely used in *E. coli* and contains the pLysS plasmid. The pLysS plasmid encodes for the T7 lysozyme, which suppresses the basal expression of proteins that are under the control the T7 promoter [216].

As an eukaryotic expression host the *S. cerevisiae* ΔPP strain was chosen. This strain comprises a deletion of the *pdr5* promoter and large parts of the *pdr5* gene (*Δpdr5promrΔpdr5*). This strain was engineered in a previous doctoral study for the homologous recombination of genes into the *pdr5* locus on the *S. cerevisiae* chromosome [217]. In *S. cerevisiae* ΔPP the proteins of interest can be produced both after induction from plasmid or constitutively after integration into the *pdr5* locus in the genome. Since pleiotropic drug resistance proteins are present in *S. cerevisiae* [218], antibiotics as selection markers cannot be used. Instead auxotrophy markers are used for selection, that enable the growth in absence of otherwise essential amino acids [219]. Hence no antibiotic agents are present and the anyway required sterility in the working procedure becomes even more important.

Lastly a cell free expression system was used for *in vitro* protein production, based on wheat germ lysate and hence with a translation machinery derived from a eukaryotic plant organism. Although in a significantly smaller scale (50 µl reaction volume) compared to cell based expression, the use of the “continuous exchange cell free” CECF expression approach further guarantees the continuous exchange between the reaction solution and the feeding solution over a semi-permeable membrane. Hence, continuous supply with required components for the synthesis is ensured as well as less accumulation of potentially toxic or inhibitory side products compared to a one-tube reaction [220, 221].

A further point that needs to be taken into account is the choice of a suitable affinity tag for the purification of the recombinant protein. The polyhistidine tag is one of the most frequently used tags. The immobilized metal-ion affinity chromatography (IMAC) purification principle relies on immobilized divalent ions like Ni^{2+} , Zn^{2+} or Co^{2+} , that are chelated to nitro acetic acid (NTA) and show high affinity towards the imidazole groups of the histidine residues of the protein tag [222, 223]. Thereby the tagged protein can be isolated from the cleared cell lysate, since sequences of multiple histidine side chains are uncommon within native protein sequences [212].

The purification procedure via StrepII-tag does rely on the interaction between StrepTactin (a modified version of the protein streptavidin) and a short octapeptide (WSHPQFEK) [224]. Hence purification via StrepII-tag does not require the presence of divalent ions, like Ni^{2+} used for the purification of his-tagged proteins. This is of advantage for metal ion binding proteins, as the possible interference of the Ni^{2+} ions with ion binding sites and undesired co-purification of Ni^{2+} can be excluded ([212, 225] and Knospe *et al.* unpublished).

The voltage gated K^+ channel AKT1

In the first chapter, the heterologous expression and subsequent isolation of the multidomain membrane protein AKT1 was attempted. Since membrane proteins are rather large in size (100 kDa for AKT1 [226]) and comprise relatively higher amounts of hydrophobic amino acids than soluble proteins (44.34 % for AKT1 compared to 39.00 % for CIPK23 [227]), the successful production of functional protein is even more challenging. Toxicity of the expressed protein towards its expression host, differing lipid compositions between the expression host and the original organism, folding errors in the secondary and tertiary structure, miss localization as well as lacking or aberrant post translational modifications are just a few potential obstacles, when expressing a eukaryotic membrane protein in a heterologous host [207, 210, 228-231].

All attempts to express and purify AKT1 were performed with a poly-histidine tag fused either to the N- or C-terminus of the channel. Since for other *A. thaliana* transmembrane proteins [232, 233] expression in *E. coli* had already been shown to work, initial attempts were made for AKT1 as well. This resulted in no expression of full length AKT1, or any detectable degradation products at all. AKT1 comprises in total four domains (TMD, CNBD, ARD and KHA). The prokaryotic translation machinery is not necessarily designed for the translation of multi-domain proteins and co-translational domain folding is rather a feature of eukaryotic organisms. In correspondence the translation in eukaryotes was found to be five to ten times slower to enable the co-translational folding [234, 235].

S. cerevisiae is a widely used expression host for eukaryotic membrane proteins [236] and it was already shown thirty years ago that AKT1 could be functionally expressed in *S. cerevisiae* [81]. While both the inducible expression from plasmids as well as the N-terminally tagged constitutive expression of AKT1 after homologous recombination worked, for non of the approaches AKT1 containing membranes could be obtained. As soon as the cells were disrupted the Western blot signal for the full length AKT1 vanished. The reasons for this instability could neither be named nor isolated during this study (see Chapter 1).

To circumvent the necessity of cell disruption, protease inhibition, membrane preparation and solubilization of AKT1, its expression in wheat germ based cell free environment was attempted. Based on the eukaryotic translation machinery and the exclusion of any protease activity, the focus of cell free expression lies only on the production of the protein of interest, instead of keeping up a whole cell metabolism [237]. This method becomes applicable for membrane protein production by the addition of detergent or liposomes to the translation reaction [238-241]. With this approach expression and initial purification success for AKT1 in the presence of Brij35 [242, 243] detergent could be achieved, but did not yield in a monodisperse peak in the SEC.

It was already stated by Drew *et al.* 2008 that some membrane proteins can be expressed sufficiently in *S. cerevisiae* still need to be produced in insect or mammalian cell lines for isolation and structural analysis, due to absence of particular lipids like cholesterol [230]. In the end this was found to be true for AKT1 as well. Not only had it been known that AKT1 could be functionally expressed in Sf9 cells 25 years ago [80], but the channel structure was resolved by Lu *et al.* in 2022 after expression and

purification of AKT1 from Sf9 insect cells [93]. Although it was not cholesterol, but phosphatidylethanolamine, that was found within the cryo EM structure of AKT1, it can be stated that lipids seem to play an essential role for the stability and functionality of the AKT1 channel. The importance of the correct and suitable lipid environment is an essential point for the successful expression and isolation of membrane proteins [244, 245]. Hence, it is questionable if the AKT1 protein that was expressed in the CECF approach in this study would have been functional, or if the lack of lipid is a potential reason for the poor purification yield.

The protein kinase CIPK23

In the second chapter, the heterologous expression and subsequent isolation of the cytosolic protein kinase CIPK23 was attempted. The protein consists of two domains linked by a junction and comprises 55 kDa in size. The expression and purification of the kinase domain (aa 24-331 35 kDa) had already been established in *E. coli* Rosetta (DE3) pLysS [125].

Hence, the initial attempts to express the full length protein were performed in the same strain as well. For CIPK23 expression with a N-terminal StrepII-tag was chosen, since the involvement of divalent ions (Mn^{2+} or Mg^{2+}) in the kinase active site is known. Hence, purification via His-tag and the potentially interfering Ni^{2+} ions was found not suitable [148]. The expression succeeded, but upon cell disruption degradation products appeared and the remaining protein eluted as aggregates in the void volume of the SEC. Same as for AKT1 degradation by a host specific protease is unlikely, since protease inhibitors against all four classes of proteases were used (see Discussion of chapter 1 and 2 for more details). Since the problem occurs as soon as the cells are broken, the reason for the degradation cannot lie in the change from a crowded *in vivo* environment to an *in vitro* environment either [212]. This is in correspondence to the finding, that the addition of the molecular crowding agent glycerol [246] could not improve the purification success. For CIPK23 structure intrinsic reasons were thought to be the cause for the instability, namely the 25 - 40 amino acid long unstructured junction that connects the kinase and regulatory domain. General complications in the stability of CIPK proteins are suggested by the CIPK23 related CIPK24, since consensus-based approaches to introduce stabilizing mutations were necessary to even purify the kinase domain of CIPK24 [125]. Another likely reason for the degradation and aggregation of CIPK23 may lie within the differences of the pro- and eukaryotic expression machinery [208]. Since CIPK23 is an eukaryotic protein, that consists of two domains, co-translational folding may be a prerequisite that can only be comprised by a eukaryotic expression host. The proper folding of the regulatory domain, that follows C-terminal to the junction, may depend on the proper folding of the preceding kinase domain. In the inactive state of the kinase the NAF domain of the regulatory domain is known to interact with the active site of the kinase domain [156]. Hence, if the kinase domain is not folded, the regulatory domain cannot properly fold as well and the protein is further destabilized.

To prevent the degradation and aggregation issues during the purification, the addition of Brij35 detergent was suggested for other CIPKs [247, 248]. Since CIPK23 is a fully soluble, cytosolic protein, this suggestion is not directly evident. The visualization of the hydrophobic surface of the AlphaFold2.0 [249, 250] structural model did not hint towards a hydrophobic patch or surface. On the other hand, the crystal structure of the CIPK23 kinase domain showed a CHAPS molecule associated to the active site of the kinase, although the protein was not purified in the presence of CHAPS [125]. Besides their different properties, Brij35 as a non-ionic detergent [251] and CHAPS [252] as an zwitterionic detergent, Brij35 was initially found to have a positive effect on the purification. Fractions containing the full length protein could be isolated, but degradation was still a problem. The mode of action how

Brij35 improves the purification is not clear. But as CIPK23 still shows degradation in presence of Brij35 and high amounts of protein remain aggregated in the void peak, it is likely that Brij just randomly attaches to the aggregated protein and keeps it in a soluble form, similar to the function of SDS in a SDS-PAGE.

Since the cell free expression showed initial success for AKT1, expression attempts were made for CIPK23 as well. Within the scope of the bachelor studies of Carolin Sebastiany the expression of StrepII-tagged CIPK23 in cell free environment showed a significantly diminished yield. Hence further cell free expression was attempted with His-tagged protein. While the degradation could be eliminated the aggregation remained despite extensive screening for optimal purification procedure [253]. Brij35 was again added during both the expression and the purification. In contrary Hashimoto *et al.* expressed CIPK23 from the same wheat germ CECF expression kit without Brij35 and showed its functionality [148]. It remains questionable if the use of Brij35 detergent in the case of CIPK23 is not rather counterproductive. The initially improved solubility of CIPK23 by addition of Brij35 may have put the project on the wrong track. In the end despite the addition of Brij35, CIPK23 could not be functionally isolated. It is questionable to what extent the addition of Brij35 might not even impair kinase activity. On the one hand the presence of CHAPS in the active site of the crystalized kinase domain may be a crystallization artifact [125], but on the other hand if Brij35 interacts with CIPK23 at that part, a blocking of the kinase active site by the detergent is likely.

The Ca²⁺ binding protein CBL1

In the third chapter, the heterologous expression and subsequent purification of the Ca²⁺ sensor CBL1 was attempted. As CBL1 is relatively small in size (26 kDa), comprises only one single domain and is not an integral membrane protein, the expression and subsequent purification from the prokaryotic expression host *E. coli* Rosetta (DE3) pLysS was attempted and could be established. The purification of CBL1 was facilitated via a N-terminal StrepII tag, since this protein is known to bind Ca²⁺ ions and for reasons described above purification via IMAC was found not suitable. The initial plasmid encoding for the N-terminally StrepII tagged CBL1 was provided by the laboratory of Prof. Dr. Jörg Kudla (WWU Münster). The choice for an N-terminal tag is retraceable, since the C-terminus of the CBLs is known to have a function in the interaction with the CIPKs [137, 185] and placing a tag to this end might have negative impact on the protein function in subsequent studies. Second, although the N-terminus is known to have a function *in vivo* by anchoring the protein to the plasma membrane, this function should not be comprised in the prokaryotic expression host *E. coli*, since *E. coli* cannot facilitate these lipid modifications [137].

Prior to this study CBL4 (and CBL2³) had already been purified from *E. coli*, with sufficient purity and homogeneity for successful crystallization [190, 191]. Based on these purification protocols the purification of CBL1 was initially attempted without the addition of detergent. Unlike CBL2 and 4 this did not yield in monodisperse and monomeric protein, but in particles of almost 10 times the expected molecular size (MALS). In contrary to the purification of CBL4 (and 2) the addition of detergent for the purification of CBL1 was attempted, whereupon these higher oligomeric states could be at least partially dissolved and functional monomeric protein could be obtained. The same phenomenon was observed for CBL9 before and during the master studies of Cigdem Günes [254]. Upon the addition of Brij35 the purification yield increased significantly from < 10 mg up to 40 - 50 mg of protein that could be submitted to SEC. Noteworthy no solubilization of the *E. coli* membranes was necessary, since CBL1

³ CBL2 belongs to another subgroup than CBL1, 4 or 9, comprises a larger N-terminal domain and is located to the tonoplast, not the plasma membrane.

(and 9) were not directly attached to the membrane. Both proteins were almost completely found in the supernatant after ultracentrifugation of the disrupted cells. Nonetheless both CBL1 (and 9) were found to comprise an intrinsic hydrophobicity strong enough to force them into higher oligomeric states if no detergent micelles were present. A possible explanation for this finding may be the lacking lipid modification, that cannot be comprised by *E. coli* [137]. For membrane proximity a certain degree of hydrophobicity of the protein is of advantage, but since the lipid anchor is lacking this hydrophobicity is not strong enough to keep the protein to the membrane and it tends to associate with other copies of itself.

The *in vivo* lipidation and membrane association of CBL1, 9 and 4 already suggests a certain degree of hydrophobicity [137, 140, 184], but gives no explanation for the deviating findings between CBL1/9 and 4. In comparison, CBL1, CBL9 as well as CBL4 comprise 43 % (CBL2 41 %) of hydrophobic amino acids within their sequence [227]. Further CBL1 and CBL4 show a sequence identity of 60.5 % (CLUSTAL O (1.2.4) Uniprot entries O81445 and O81223 [132]) and their structures⁴ can be aligned with an RMSD of 1.29 Å over 185 Cα atoms. CBL1 was found not to be a classical membrane associated protein when heterologously expressed in *E. coli* and purified, since it did not attach to the plasma membrane [255]. But it is not a fully soluble cytosolic protein either, since it needs the presence of a lipid like environment for functional isolation.

During this study, attempts to crystallize the StrepII-tagged CBL1 were made, but did not lead to the formation of any crystals. The optimal crystallization conditions are unique for each protein, but a few factors that might have had a negative influence on the crystallization attempts of CBL1 can be named. First the StrepII tag could not be cleaved due to insufficient accessibility or TEV-protease activity. On the one hand other proteins had already been crystalized with in presence of their tag, but on the other hand the presence of this unstructured and flexible peptide may have negative influences on the formation of crystals [256]. Noteworthy both CBL2 and 4 had been successfully crystalized after tag cleavage in the past. Further for both CBL2 and 4 an additional ion exchange chromatography was performed for removal of potential impurities [190, 191]. Second, for crystallization attempts the CBL1 protein that was purified in its monomeric form had to be concentrated up to 20 mg/ml. In retrospect the protein was found to form again higher oligomeric states upon concentration (SDS/ Native PAGE signals at 50 kDa and higher). Hence the protein solution was not homogeneous anymore, which is a prerequisite for successful crystallization [212]. Third the CBL1 (and 9) protein was constantly present as a double band on the SDS-PAGE. The precise reason for this finding could not be resolved, but the double band could be dissolved by alanine mutations of amino acids E141, E147 and K155 which reside in E-helix of EF hand 4 and the preceding loop. This finding is described and discussed in more detail in chapter 3. But the presence of two different species of the same protein further complicates its crystallization.

⁴ The structure of CBL1 is based on a AlphaFold2.0 model

AKT1 - The *Arabidopsis* K⁺ transporter 1

Channel or transporter?

Polar and charged substances like K⁺ ions need the aid of proteins to pass through the hydrophobic membrane bilayer. This can either be comprised by diffusion along the concentration gradient or by active transport against the concentration gradient of the transported substance. Passive diffusion is comprised by channels that allow the substrate to diffuse through the membrane via a central channel pore. Active transport requires an energy source to make the energetically unfavorable transport favorable. This can either be comprised by a direct ATP hydrolysis (e.g. ABC transporters [208]) or secondary active transport by co- or antiport of a second substrate following its concentration gradient [208, 257].

The name AKT1 is short for *Arabidopsis* K⁺ transporter 1, but AKT1 comprises the structure of a voltage gated K⁺ channel [93]. While channels classically comprise uptake along the concentration gradient, the nomination of AKT1 as transporter might result from the fact that AKT1 was found to be capable of K⁺ uptake against the K⁺ gradient across the membrane [74, 100]. The uptake of K⁺ against its concentration gradient from low K⁺ soils at first is energetically unfavorable. It becomes favorable by the generation of an electrical gradient, also known as membrane potential (ΔV_M negative inside) across the plasma membrane. A H⁺-ATPase in the plasma membrane continuously pumps positive charges (H⁺) out of the cell [60]. Therefore, the passive import of K⁺ ions via channels AKT1 gets can be comprised.

The role of the AKT1 N-terminus

About the structure and function of the AKT1 N-terminus so far little is known. In their cryo EM structure, Lu *et al.* could show that in the inactive state of the channel residues 6-14 of the N-terminus are interacting with the straight C-linkers by forming a disulfide bond between the cysteines at position 8 and 331 [93]. This interaction blocks the gating of the channel, since it hinders the transition of the C-linker from its straight to kinked conformation. Hence, it can be stated that the N-terminus has a regulatory impact on the channel and its K⁺ uptake activity.

Likely here phosphorylation plays an essential role in the regulation, since serine 26 was found to be phosphorylated by CIPK23 and essential for the K⁺ uptake activity. If the S26 phosphorylation site was impaired, the K⁺ currents are impaired too. Possibly, phosphorylation of serine 26 results in the recruitment of a reducing enzyme, like thioredoxins [258] that will result in the breakage of the disulfide bond between cysteines 8-331. Hence the interaction between the N-terminus and the C-linker will be dissolved and an opening of the channel enabled.

The AKT1 pore and its opening

When talking about the uptake mechanism, a look in the 3D structure is self evident. In 2022 Lu *et al.* successfully resolved the 3D structure of the AKT1 channel (TMD and CNBD). Thereby they state certain differences for the pore of the inactive and pre-open state of the channel. According to the authors, in the inactive state isoleucine I285, which is located in the S6 helix, forms the narrowest point of the pore. For the structure of the constitutively active mutant the pore and is further narrowed by isoleucine I285 and threonine T289. Upon this finding and the rearrangement in the cytosolic part, the authors claim this conformation as the pre-open state [93]. These statements rely on computational analysis of the pore constriction via HOLE [259].

From the structures (7WSW and 7FCV) these differences cannot be visualized. In the 3D structure of the inactive AKT1 wt channel the narrowest point of the inner pore is already formed by both the hydrophobic site chains of I285 and T289 (Figure 16.A and B). The distance determination between the C α atoms (PyMol measure tool) resulted in 7.2-7.3 Å in the closed state and 7.1 Å in the pre-open state for I285, while the C α distance of T289 remained at 6.9 Å in both states of the channel. Undoubtedly both residues are involved in the constriction of the pore, but a significant difference between the two states cannot be derived from this.

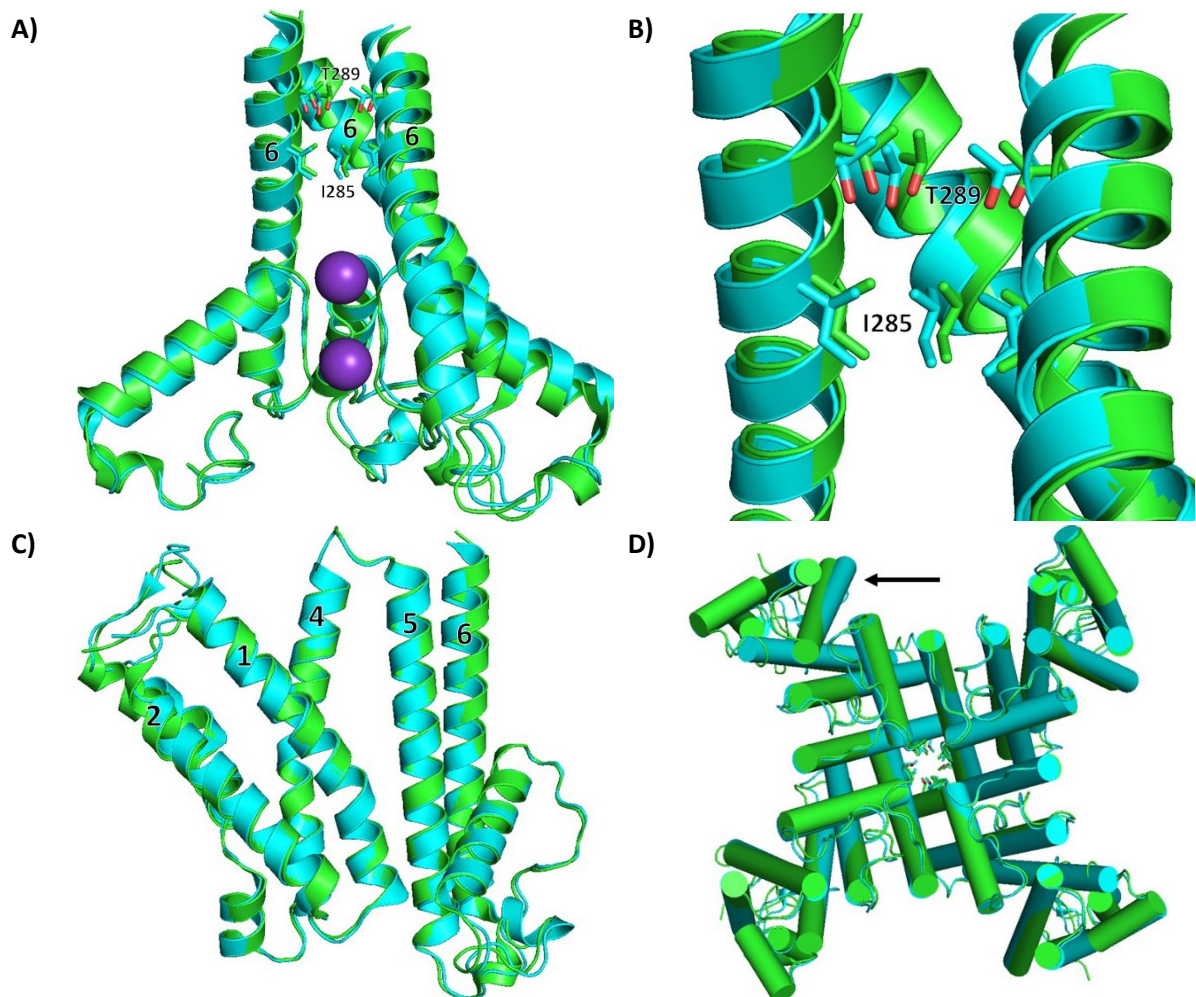


Figure 16: The voltage sensor domain of AKT1 aligned in the closed (green) and pre-open state (cyan). A) The pore of both states is constricted by I285 and T289. K⁺ ions are depicted in purple. B) Enlargement of the pore constriction. C) Alignment of a single transmembrane domain in closed and pre-open state. The transmembrane segments are labeled 1-6 D) Alignment of the entire transmembrane domain, viewed from the extracellular space. The helices are depicted as cylinders. The most significant difference between the two structures is marked by a black arrow. The alignments were performed on the basis of PDB entries 7WSW and 7FCV (aa 48- 286) [93].

Further Lu *et al.* state a “slightly counterclockwise rotation” of the voltage sensors from inactive to pre-open state [93]. Taking a look at the pore (Figure 16.B) a slight counterclockwise rotation can be visualized. It is not stated if they aligned the whole structures or just the transmembrane part, but only minor deviations within the inactive and pre-open state can be visualized when aligning the tetrameric TMDs (6,559 Å over C α -596 atoms). For the activation of the channel a conformational change within the TMD is expected and not only a repositioning of the TMDs in respect to the C-linkers and CNBDs, but the single TMDs align with an RMSD of 0.548 Å over 212 C α -atoms. No reorientation between the voltage sensor and pore domain can be visualized, as it is expected for the activation of a voltage gated K⁺ channel [25]. The whole channel might be in a pre-open state, but its worth noting that the TMD remains in the closed/ inactive state. This finding hints to a sequential opening mechanism where first the cytoplasmic part rearranges to the pre-open state and subsequently mediated by the C-linker, the transmembrane domain rearranges to open the pore.

The constitutively active mutant AKT1, that comprises the pre-open state, is not a direct phosphomimetic mutant but a mutant that was found to break the interactions in the CNBD and structurally rearranges as it is expected for an opened channel. It is obvious that upon mutations in the protomer interface (hydrogen bond between the CNBDs of protomer I and II), the interface itself and the arrangement of the protomers can be altered. But it is questionable if this is in correspondence with the precise rearrangements that happen upon phosphorylation. Since a phosphomimetic mutant (S to D) would be more obvious [260], it can only be speculated why this straight forward approach was not used. A functional impact of these mutations (S26D and S338D) could be shown [93], but expression or purification issues may be possible explanations for the use of the constitutively active D379A mutant for cryo EM studies.

The impact cyclic nucleotides on AKT1

The impact of cyclic nucleotides on the function and activity of CNBD channels differs. While the CNG channel MloK1, which was presented in the introduction, is activated by a cyclic nucleotide [84], the activity of HCN (hyperpolarization activated cyclic nucleotide gated) channels like KAT1 and AKT1 were found to be modulated by cyclic nucleotides and not required for channel activation. For both KAT1 and AKT1 cGMP shifts the activation potential to more negative values [100, 261]. The voltage gated K⁺ channel KAT1 was found to comprise a pseudo-CNBD, which already comprises a “ligand bound” conformation even in absence of a ligand [98, 262]. A comparison of the AKT1 CNBD structure with the CNBDs of MloK1 and KAT1 further underlines the assignment of AKT1 to the HCN channels (Figure 17).

In general all three structures show the same composition of secondary structure elements, 8 β -sheets with the PBC helix and the α -helical segment consisting of four α -helices. The AKT1 CNBD aligns to the structure of cAMP free MloK1 with a RMSD of 1.695 Å over 95 C $_{\alpha}$ -atoms (Figure 17.A). Here the α C helix of the AKT1 CNBD shows a different angle towards the α B helix compared to MloK1. In comparison the alignment with the cAMP bound MloK1 resulted in an RMSD of 1.587 Å over 84 C $_{\alpha}$ -atoms (Figure 17.B). Hence, the α C helix of the AKT1 CNBD is in a position between the free and ligand bound state, when comparing to the α C helix of MloK1. In comparison the AKT1 CNBD aligns with the KAT1 CNBD with an RMSD of 1.363 Å over 120 C $_{\alpha}$ -atoms (Figure 17.C). While the α C helices show the same positioning, minor deviations in helices α A and α B can be visualized. For CNBDs a conserved arginine is postulated, that interacts with the phosphate of the cyclic nucleotide [84, 108, 109]. This arginine is exchanged for glutamine in both KAT1 and AKT1. For both AKT1 and KAT1 only the structure of the cGMP free CNBD is known. While for MloK1 a precise mechanism has been stated [84], it still needs to be proven to which extend AKT1 and KAT1 CNBDs undergo conformational changes upon cGMP binding and how that is translated into a shift of the activation potential of the channel.

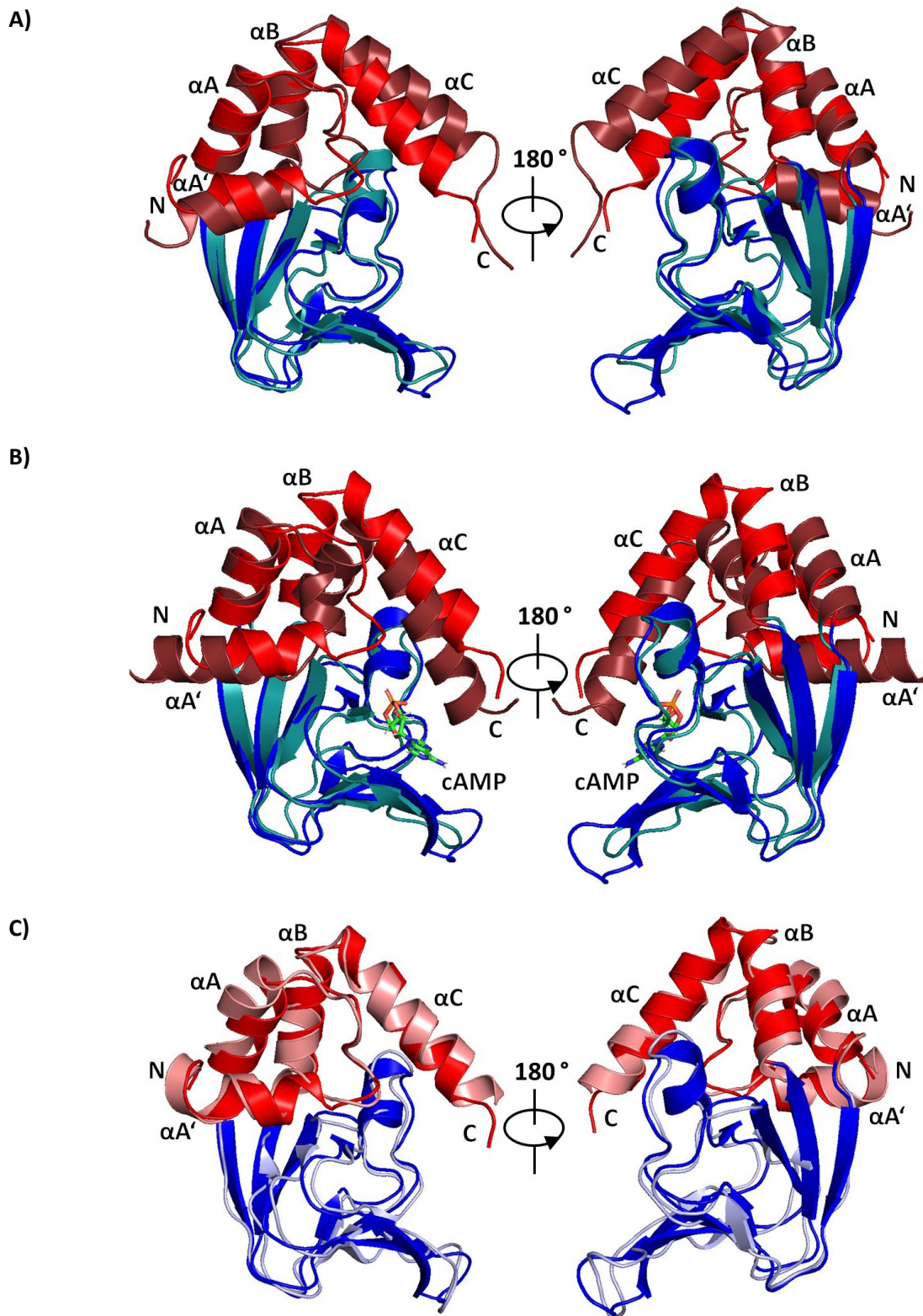


Figure 17: Cyclic nucleotide binding domains of CNG and HCN channels. A) Alignment of the AKT1 CNBD with a CNG CNBD (MloK1 cAMP free). B) Alignment of the AKT1 CNBD with a CNG CNBD (MloK1 cAMP bound). C) Alignment of the AKT1 CNBD with a HCN CNBD (KAT1 cGMP free). The core domain of the CNBD is depicted in blue (blue = AKT1; deep teal (A) = MloK1; light blue (B) = KAT1). The helical segment is depicted in red with the helices labeled accordingly (red = AKT1; dark red = MloK1; light red = KAT1). The structures of AKT1 [93], MloK1 [84] and KAT1 [98] are based on the PDB structures 7WSW, 2KXL, 2K0G and 6V1X respectively.

The CBL interacting protein kinase CIPK23

How can CIPK23 be so diverse in its interactions and yet so specific?

AKT1 is not the only target for CIPK23 and CBL1 and 9 are not the only activators. Overall CIPK23 was found to interact with 6 out of 10 CBL proteins in *A. thaliana*, namely CBL1, 2, 3, 5, 8, 9 and 10 [141, 203]. CIPK23 plays a major role in the K⁺ homeostasis within *Arabidopsis thaliana* in response to K⁺ deprivation, by promoting K⁺ uptake from the soil as well as from vacuolar storages in K⁺ limiting conditions [140, 263]. The high affinity K⁺ uptake system HAK5 in plant roots, as well KUP4 are also regulated by CIPK23 [139, 146] and TPK channels that release K⁺ from the vacuole [263]. While CBL5 is not involved in K⁺ uptake signaling [141], CBL1 and 9 in complex with CIPK23 are known to activate AKT1 *in vivo* [148] and CBL1, 8, 9 and 10 were found to activate HAK5 in combination with CIPK23 when expressed in yeast [264]. This is in correspondence with the localization of both the CBLs and K⁺ uptake proteins to the plasma membrane [137, 140]. In correspondence, the tonoplast associated CBL2 and 3 are known to recruit CIPK23 to the tonoplast for the activation of the TPK channels [140, 263]. Further CIPK23 was found to be involved in phosphorylation and hence activation of nitrate uptake system NRT1.1/CHL1 upon nitrate deficiency [265-267] as well as the anion channel SLAC1 in guard cells [268]. Here again the activation of CIPK23 is comprised by CBL1 and 9.

CIPK23 is not only involved in the activation of uptake systems, but also in the inhibition of transport systems by phosphorylation. When potentially toxic levels of substances like divalent metal ions (e.g. Zn²⁺, Mn²⁺, Co²⁺ and Cd²⁺ or ammonium) are present within the plant, CIPK23 can inactivate the broad spectrum transporter for divalent cations IRT1 and the ammonium transporter AMT1, which are responsible for the uptake of these substances [269, 270]. For IRT1 an involvement of CBL1 and 9 is suggested [271]. It is stated, that phosphorylation by CIPK23 results in subsequent degradation of the channel [272]. The AMT1 inactivation by phosphorylation of CIPK23 is only known to be induced by CBL1 [269]. In combination with CBL2 and CBL3, CIPK23 was further found to regulate the Mg²⁺ homeostasis between the cytosol and the vacuole [273]. With all the processes involved, CIPK23 can be described as a central point of regulation in nutrient household. A rising question is, how CIPK23 can operate in such a high diversity of cellular processes, but yet show a high specificity for the respective downstream interaction partners without unnecessarily activating the entire spectrum of possible interaction partners. This is not fully understood yet, but several factors are known [140].

The first point of specificity is given by the Ca²⁺ signatures. Depending on how much the Ca²⁺ level rises, different CBLs will be activated due to their presumably different Ca²⁺ affinities. Here further prove will be necessary, since so far only the Ca²⁺ affinities for CBL1 and 9 and have been determined (Chaper 3 and [254]). Surely it has been proven that the Ca²⁺ signatures are spatial and temporally specific and hence only activate a subset of the in total 10 CBLs that is expressed in the respective area of the plant [45, 51]. Such Ca²⁺ signatures in response to K⁺ deprivation were already described in the introduction in more detail. For example, the expression of CIPK23 and its CBL interaction partners is highly tissue specific and regulated. Significant expression levels of the AKT1 activating proteins CIPK23, CBL1 and CBL9 were shown in roots [274] in the same area, where the K⁺ deprivation induced Ca²⁺ signatures occur. Further the CIPK23 expression gets upregulated upon K⁺ deprivation in the soil [189].

The second point of specificity is given by the CBLs. Not only the expression and localization within the different plant tissues, but the subcellular localization of the CIPK23-CBL complex differs in dependence of the interacting CBL protein. In case of CIPK23, the upstream interaction partners CBL1, 5 and 9 are located to the plasma membrane while CBL2 and 3 are tonoplast associated, CBL10 may be either plasma membrane or tonoplast associated and CBL 8 is found in the cytosol or the nucleus [137, 141,

142, 189, 275]. Not specific, but found to be a general mechanism in the CBL-CIPK signaling network of *A. thaliana*, is the phosphorylation of the CBL C-termini, when in complex with the CIPK. In case of AKT1 the phosphorylation of the CBL1 C-terminus by CIPK23 was found to be essential for the channel activation [148].

The third point of specificity lies within the CIPK23 itself. Different catalytic efficiencies were found between the different CIPKs [148]. The phospho-mimicking CIPK24 T168D mutant (activation loop mutant) significantly increases the activity of CIPK24 kinase, while the corresponding T190D mutation in CIPK23 only had little effect on the kinase efficiency [125]. From wheat germ expressed full size proteins 8 fold lower catalytic efficiency for CIPK23 compared to CIPK24 was determined [148] and while CIPK24 shows a basal activity, CIPK23 is intrinsically inactive until activation by a CBL [125]. These differences in overall activity and the different impact of the phosphorylation of the activation loop, hint towards another point of specificity of the respective CIPK and distinguishment between the 26 CIPK proteins encoded within the *A. thaliana* genome.

The fourth point of specificity is given by the downstream targets of CIPK23. In contrast to the CBL phosphorylation, the phosphorylation pattern of CIPK23 towards its downstream target is found to be specific for each interaction, just as the interaction sites. CIPK23 and its respective downstream targets comprise interaction surfaces that are unique for each interaction. No specific CIPK23 interaction domain is known to be present in CIPK23 or its phosphorylation targets [140]. As an example, CIPK23 interacts with the ARD for AKT1 activation, while for HAK5 activation no such domain as an ARD is present (Uniport entry Q9M7K4 [132]). CIPK23 and its up- and downstream interaction partners form overall a very complex network with many factors that need to be taken into account and a deviation in just one of the above mentioned factors might already lead to an altered outcome of the initial signal.

The Calcineurin-B like protein CBL1

CBL1 and 9 – similarities and differences

CBL1 and CBL9 comprise a very high sequence identity of 89.67 % (CLUSTAL O (1.2.4), Uniprot entries O81445 und Q9LTB8 [132]), hence the question arises, how these two proteins differ. CBL1 and 9 are both known to be activated by Ca^{2+} signatures to facilitate the K^{+} uptake under low K^{+} conditions, by recruiting CIPK23 to the plasma membrane for the activation of AKT1 and HAK5 [60, 70, 73]. Further both proteins in combination with CIPK23 are involved in the inhibition of the nitrate uptake by NRT1.1 [265, 267].

For the involvements of CBL1 or 9 in response to abscisic acid, at first sight, contrary information exists. Guo *et al.* stated in 2002 that the *scabp5* gene (SOS3-like calcium binding protein 5) which is an alternative name for CBL1, and its interacting kinase PKS3 (CIPK15) are involved in the regulation of ABA responses. Their plants were hypersensitive towards ABA when the *cbl1* gene is silenced by siRNA [276]. In contrary Pandey *et al.* state that the CBL9 expression is upregulated by the presence of the plant hormone abscisic acid (ABA). Instead of siRNA gene silencing they created *cbl9* knock out plants, to prevent falsified results since *cbl1* and *cbl9* share a very high homology in their DNA sequence and the siRNA may have suppressed both *cbl1* and 9 genes. If the *cbl9* gene is knocked out, the *A. thaliana* plants become hypersensitive towards ABA, osmotic stress as well as glucose and the plants gene expression is altered [274]. They showed that CBL9 interacts with CIPK3 in the context of ABA responses [277]. This would imply no such function for CBL1 since in the described *cbl9* mutant plants only the *cbl9* gene was impaired and it seems that CBL1 cannot complement the function of CBL9 in ABA response.

The other way around was found in the presence of ammonium. Upon high ammonium in the soil, the ammonium transporter AMT1 gets inhibited by phosphorylation [278]. This phosphorylation is facilitated by the protein kinase CIPK23, whose expression gets upregulated when the external medium is supplied with ammonium. While the CBL9 expression does not change, the CBL1 expression is stimulated as well to 5 fold compared to basal expression [269]. Further *cbl9* knock out plants showed the same uptake behavior like wildtype plants, while *cipk23* and *cbl1* knockouts take up ammonium faster, due to a lack of AMT1 inhibition [269]. Hence, rather CBL1 than CBL9 is involved in the CIPK23 mediated phosphorylation and inactivation of the ammonium transporter AMT1. These findings hint towards a difference of CBL1 and 9 on the transcriptional level, since different environmental stimuli result in different expression patterns.

In order to understand how two proteins that share so much commonalities, but yet differ in some points, insights into their structure and function are indispensable. Both CBL1 and CBL9 showed the same requirement for Brij35 detergent for the purification of monomeric protein. As well, both proteins showed the same tendency to form higher oligomeric states and for both proteins the E→Q mutation of the -Z coordinate of EF hand 4 resulted in the complete absence of monomeric protein. Since the resolution of the 3D structure did not succeed in this study, the focus was put on the functional analysis of the EF hands. ITC analysis on the Ca^{2+} binding behavior have been performed on CBL1 in this study (Chapter 3) and on CBL9 during the master thesis of Cigdem Günes [254].

The alignments of the EF hand sequences of CBL1 and 9 further substantiate the already found high sequence identity between the two proteins (Figure 18.A and B). For EF hand 2 of CBL9 the same E→D mutation in the -Z coordinate can be found as for CBL1. In agreement CBL9 EF hand 2 was found not to bind Ca^{2+} just as for CBL1. Differences can only be found in EF hand 4, where 3 out of 12 amino acids

are altered in CBL9 compared to CBL1 of which only one that is involved in the Ca^{2+} coordination. The affinity of EF hand 4 is almost 4 fold lower for CBL9 compared to CBL1 (Figure 18.C). Since the affinities for both CBL1 and 9 are in a low nanomolar range, it will be occupied by Ca^{2+} under physiological conditions anyway. The EF hands that are stated to be involved in the sensing of the Ca^{2+} signatures *in vivo* (EF hand 1 and 3) show significant similarities in their affinities, which is in agreement with the joint involvement of CBL1 and 9 in several cellular signaling processes.

A)

	1	2	3	4	5	6	7	8	9	10	11	12	13	14
Consensus	X				Y		Z		-Y		-X			-Z
	S	x	x	x	I	x	D	G	L	x	N	x	x	E
EF1 CBL1	S	S	S	V	V	D	D	G	L	I	N	K	E	E
EF1 CBL9	S	S	S	V	V	D	D	G	L	I	N	K	E	E

B)

	1	2	3	4	5	6	7	8	9	10	11	12
Consensus	X		Y		Z		-Y		-X			-Z
	D	x	D	x	D	G	x	x	D	x	x	E
EF2 CBL1	D	V	K	R	K	G	V	I	D	F	G	D
EF2 CBL9	D	V	K	R	K	G	V	I	D	F	G	D
EF3 CBL1	D	M	D	C	T	G	Y	I	E	R	Q	E
EF3 CBL9	D	M	D	C	T	G	F	I	E	R	Q	E
EF4 CBL1	D	V	N	Q	D	G	K	I	D	K	L	E
EF4 CBL9	D	V	D	R	D	G	K	I	D	K	T	E

C)

	K _D EF1	K _D EF2	K _D EF3	K _D EF4
CBL1	373 ± 75.0 nM	X	8.60 ± 2.15 μM	8.18 ± 1.85 nM
CBL9	300 ± 80.0 nM	X	10.6 ± 0.90 μM	30.0 ± 3.40 nM

Figure 18: Comparison of CBL1 and CBL9. A and B) Sequence alignments of the EF hands of CBL1 and CBL9. The alignments are based on the consensus sequences stated by Batistic et al. 2009 [137]. Amino acids identical to the consensus are marked in green, while similar amino acids are colored in orange and amino acids deviating from the consensus are marked in red. C) Comparison of the Ca^{2+} binding affinities of monomeric CBL1 and 9 determined by ITC analysis of 56 μM StreptII-TEV-tagged CBL protein titrated with 1.13 mM CaCl_2 at 25 °C. For detailed information see chapter 3 and [254].

CBL-CIPK complexes are involved in plant programmed cell death

Programmed cell death (PCD) is an essential process in plants for both their development and survival. Thereby affected cells are eliminated from the organism, induced by internal developmental or external factors, like injuries or pathogens [279]. Amongst these external factors, that can lead to cell death, are also biotic or abiotic stresses [147, 280]. Upon PCD the cells morphology is changed by condensation and contraction of the cytoplasm and nucleus, nucleus fragmentation and degradation of the nuclear DNA. In difference to animal PCD no apoptotic bodies are formed, since neighboring cells do not perform phagocytosis but plants rather perform autolysis, while the cell wall remains intact [281]. This is of importance for example in the development of xylem vessels that supply the plant with water [279]. The plant vacuole plays a significant role in PCD. Here two different modes of action are known. Either the vacuole collapses and the vacuolar content is released directly into the cytosol or the vacuole fuses with the plasma membrane, which results in the release of the vacuolar content to the extracellular matrix. The vacuolar collapse will lead to immediate death of the cell, since hydrolytic proteins are released into the cytosol. Fusion of the vacuole with the plasma membrane will lead to release of those hydrolytic proteins to the extracellular matrix and thereby triggers cell death [282].

As for most cellular processes, in PCD a complex signaling and interaction network is involved. A variety of signaling molecules are known to be messengers in PCD signaling pathways, amongst others cyclic nucleotides, plant hormones, reactive oxygen and nitrogen species (ROS and RNS) as well as Ca^{2+} [283-285]. Rising cytosolic Ca^{2+} concentrations are known as a general response to initial biotic or abiotic stimuli [45, 46] as well as in programmed cell death [286]. A variety of transporters and channels are involved in Ca^{2+} influx from the extracellular space or the release of Ca^{2+} from the vacuole or ER with a mayor focus on cyclic nucleotide gated channels (CNGCs) [286-290]. Many different forms of PCD are known, well studied in plants is the hypersensitive response (HR) upon pathogen infection [291]. One of the earliest events in HR PCD is the elevation of the cytosolic Ca^{2+} concentration [292]. These signals can be sensed by Ca^{2+} sensor proteins, including members of the CaM family, CaM-like proteins, CDPKs as well as CBLs. For proteins of all these families roles in programmed cell death have been stated, amongst these CBL10 from tomatoes [286].

In tomatoes (*Solanum lycopersicum*) and *Nicotiana benthamiana* CBL10 had been found as a positive regulator of the protein kinase CIPK6, upon activation by Ca^{2+} . Thereby the CBL10-CIPK6 complex promotes the accumulation of reactive oxygen species (ROS) in pathogen induced HR PCD. The plasma membrane located NADPH oxidase RbohB was found as the downstream target of the CBL10-CIPK6 complex [182]. Thereby CBL10 senses the initial Ca^{2+} signal that gets triggered upon pathogen infection and by interaction activates the protein kinase CIPK6. Upon phosphorylation the ROS production by RbohB is promoted and the initial Ca^{2+} signal is converted into ROS accumulation and signaling [182]. Not only phosphorylation, but Ca^{2+} directly can regulate the activity of Rboh oxidases, since they comprise a N-terminal EF-hand containing domain. Hence the activation by Ca^{2+} binding and phosphorylation contribute synergistically to the activation of Rboh oxidases and ROS production [293, 294]. Such an accumulation of ROS or an oxidative burst is a characteristic in the response of plants upon pathogen infection and comprises a significant role in the signaling events during PCD [293]. ROS accumulation may result in redox modifications of PCD executing proteins like transcription factors, protein kinases (e.g. MAPKs) and antioxidant molecules [295-297].

Do CBL10-CIPK6 in *A. thaliana* contribute to PCD in the same manner as its tomato orthologues?

The question arises if the CBL10-CIPK6 complex from *A. thaliana* is involved in PCD as well. *S. lycopersicum* CBL10 shares a sequence identity of 68.6 % with CBL10 from *A. thaliana* (CLUSTAL O (1.2.4), uniprot entry: G4XMX1, Q7FRS8 [132]). Its interaction partner CIPK6 shares 70.3 % sequence identity with the *A. thaliana* counterpart (uniprot entry: G4XMX2, O65554 [132]) and both were found as orthologues [182]. In contrary to the finding that CBL10-CIPK6 interact with RbohB at the plasma membrane in *S. lycopersicum* and *N. benthamiana*, studies from 10-15 years ago claim *A. thaliana* CBL10 to be located to the tonoplast [183, 275, 298]. In combination with CIPK24 an involvement of CBL10 in salt tolerance of *A. thaliana* is stated. While CBL4(SOS3)-CIPK24(SOS2) function at the plasma membrane for Na⁺ efflux via SOS1, CBL10 in combination with CIPK24 is promoting the transfer of surplus Na⁺ to the vacuole [298, 299]. Supporting the assumption of a plasma membrane localization of CBL10, in *A. thaliana* CBL10 was found to be involved in the negative regulation of the K⁺ channel AKT1 by directly competing with CIPK23 for binding to the channel at the plasma membrane [142]. *A. thaliana in planta* experiments showed that a CBL10 overexpression strain exhibited the same phenotype as *akt1* deletion plants under low K⁺ conditions as well as decreased K⁺ uptake in both mutant strains. Similar, fluorescence based (BiFC) assays, that assigned CBL10 in combination with CIPK24 to the tonoplast, clearly showed a direct *in vivo* interaction between AKT1 and CBL10 in epidermal cells of *N. benthamiana* leaves [142]. Hence the solely assignment of CBL10 to the *A. thaliana* tonoplast appears incomplete, since CBL10 can obviously be located to the plasma membrane as well.

For *A. thaliana* CBL10 so far no interaction with CIPK6 was demonstrated, rather yeast two hybrid data by Lee *et al.* showed no interaction between these two proteins *in vitro* [138]. Instead CIPK6 was found to interact with AKT1 and contribute to its activation in combination with CBL1 in *Xenopus* two-electrode voltage-clamp experiments [138]. In contrast, *A. thaliana* CIPK6 in combination with CBL4 was found in *Xenopus* two-electrode voltage-clamp experiments to specifically interact with the inward rectifying K⁺ channel AKT2 and specifically promote its activity, but not AKT1. The CBL4-CIPK6 interaction did not result in phosphorylation of the AKT2 channel, but in CBL4 dependent translocation of the channel from the ER to the plasma membrane [300]. In contrary to *S. lycopersicum* CIPK6, *A. thaliana* CIPK6 was found to function as a negative regulator in the response to pathogen infection. While in *S. lycopersicum* the ROS production is promoted by CIPK6 interaction with RbohB, in *A. thaliana* the ROS production upon pathogen infection is comparably lower in plants that expressed *cipk6* than in plants where the *cipk6* gene was silenced [301]. Instead of CIPK6, in *A. thaliana* CIPK26 was found to be involved in ROS accumulation by interaction with RbohF at the plasma membrane as well as internal membranes [247]. Upon direct activation by Ca²⁺ and the phosphorylation by CIPK26 in complex with Ca²⁺ activated CBL1 and 9 the ROS accumulation is synergistically promoted [302]. In *A. thaliana* RbohF (and RbohD) was found to be responsible for the accumulation of ROS in response to pathogen infection and hypersensitive response [303].

In summary the orthologue proteins CBL10 and CIPK6 from *A. thaliana* and *S. lycopersicum* show significant differences in their interactions and functions between the different plant species. While in *S. lycopersicum* a clear role for CBL10 and CIPK6 in PCD upon hypersensitive response (HR) could be stated [182], similar roles for CBL1/9 and CIPK26 were found in *A. thaliana* [247]. Interestingly a interconnection between the accumulation of ROS that may lead to PCD upon HR and K⁺ uptake may be pointed out by the involvement of CBL1 and 9 in both processes. This is supported by partially overlapping expression patterns in the *A. thaliana* plant. While AKT1 expression is preliminarily located to the *A. thaliana* roots [74], RbohF was found in the roots as well as throughout the plant [304].

The role of Mn^{2+} in *A. thaliana* and points of contact with the AKT1-CIPK23-CBL1/9 network

The micronutrient Mn^{2+} is known to be essential for plant growth and reproduction. Both its deficiency and oversupply negatively affect plants by nutritional disorders or toxicity respectively [13]. Hence Mn^{2+} homeostasis is crucial for the plants survival, but so far has only been poorly investigated. The requirements of Mn^{2+} in plants are versatile, mainly Mn^{2+} functions as a co-factor in a variety of enzymes. In the previous section the creation of ROS for initiation and conduction of programmed cell death were described. In the contrary process, in the scavenging of ROS, Mn^{2+} dependent enzymes are involved [13]. Mitochondrial and peroxisomal superoxide dismutases (MnSODs) were found to use Mn^{2+} as a cofactor for disarming ROS [305, 306]. In other plant species oxalate oxidases that are responsible for creating H_2O_2 in the apoplast for pathogen defense, are dependent on Mn^{2+} [307, 308]. Differing, the homologous proteins in *A. thaliana* (GLPs) show no such function or Mn^{2+} dependence [309, 310], but rather the Mn^{2+} cation directly is thought to act as an antioxidant or in complex with phosphate (Mn-P) [13].

The main Mn^{2+} uptake system in *A. thaliana* is the plasma membrane located high affinity transporter NRAMP1, since knock out plants were found to be hypersensitive to Mn^{2+} deficiency and less Mn^{2+} is accumulated [311]. Further the broad metal spectrum transporter IRT1 is known for the Mn^{2+} uptake from the soil. This transporter was initially assigned to Fe^{2+} import in *A. thaliana* roots [312, 313]. While the regulation on transcriptional level is only influenced by iron levels (upregulation upon iron deprivation), for IRT1 an additional function as transceptor was stated. By sensing oversupply of its non-iron substrates in the cytosol, the IRT1 channel can regulate its own degradation [272]. Already described in a previous section, CIPK23 was found as a negative regulator of IRT1 [271]. Upon phosphorylation by CIPK23 the IRT1 channel gets ubiquitinated and degraded [272]. The CIPK23 kinase itself was proposed to require the presence of Mn^{2+} for autophosphorylation [148]. Hence, a connection between the sensing of surplus Mn^{2+} in the cytosol by IRT1 and the activation of the CIPK23 by Mn^{2+} to further promote the IRT1 degradation and impair the Mn^{2+} uptake by the channel can be assumed at this point.

The addition of Mn^{2+} to *in vitro* kinase activity experiments of different CIPKs was found to be more efficient than the addition of Mg^{2+} . For CIPK1, CIPK23 and CIPK24 *in vitro* auto-phosphorylation assays in presence of 0.05 to 15 mM Mn^{2+} or Mg^{2+} were performed and 1.5 to 5 mM Mn^{2+} were found to be most efficient for the autophosphorylation, while the addition of Mg^{2+} resulted in comparably weaker auto-phosphorylation in the same concentration range [148]. Similar results have been found for CIPK6, CIPK7, CIPK8, CIPK20 and CIPK26 [247, 300, 314-316]. When comparing this finding with the physiological cytosolic Mn^{2+} concentration, which is in the sub-micromolar range [317], an *in vivo* impact of Mn^{2+} on CIPK kinase activity becomes unlikely. Not only may such high concentrations be toxic, but the presence of a micronutrient in millimolar concentrations can be considered not physiological [13]. Rather the cytosolic Mg^{2+} concentration with 0.4 mM [318] is in the same order of magnitude as the concentration found in the auto-phosphorylation experiments. Hence although the activation by Mn^{2+} was found to be stronger than for Mg^{2+} *in vitro*, *in vivo* Mg^{2+} will most likely be the relevant cofactor for CIPKs.

The second point of contact between Mn^{2+} and the CBL-CIPK signaling network are the EF hands of the CBL Ca^{2+} sensors. With its atomic radius between Ca^{2+} and Mg^{2+} [319], Mn^{2+} had already been found to bind to CBL1 (this thesis) and CBL4 *in vitro* [176]. The binding affinity of the CBL1 high affinity binding site was determined by ITC to be in a physiologically relevant range of 186 ± 61.2 nM (Chapter 3) but

the assignment to the precise EF hand and hence *in vivo* impact on the Mn^{2+} binding to CLB1 could not be clarified beyond doubt. For CBL4 no precise binding affinities of Mn^{2+} were published. Here Mn^{2+} was crystallized in the EF hand 4 of CBL4. To exclude that the Mn^{2+} in EF hand 4 was a crystallization artifact, thermal denaturation experiments in combination with circular dichroism analysis were performed. The thermal denaturation temperature could be shifted in presence of both Ca^{2+} and Mn^{2+} , with the Mn^{2+} affinity one order of magnitude higher than for Ca^{2+} [176]. A functional impact on these finding so far remains elusive, but possibly CBLs could function as Mn^{2+} carriers or buffers at increasing cytosolic Mn^{2+} concentrations. Other storing or buffering mechanisms for surplus Mn^{2+} , like translocation to the vacuole, cell wall, redistribution within the plant, chelating in Mn-P complexes and complexation by organic acids, are already known [13]. So far, no impact of Mn^{2+} as a signaling molecule, in accordance with the function of Ca^{2+} , on the EF hands of CBLs or in general is stated.

The Yellow Mangaleon Sensor – a novel tool for the detection of Mn^{2+} *in vivo*

In general the precise Mn^{2+} concentrations in *A. thaliana* as well as other plant species are poorly investigated. Based on the finding that EF hand 4 of CBL4 binds Mn^{2+} with higher affinity than Ca^{2+} , the laboratory of Prof. Dr. Jörg Kudla recently created a FRET sensor for *in vivo* detection of Mn^{2+} in order to obtain a better understanding in the Mn^{2+} homeostasis in plant cells [320]. Based on the genetically encoded *Yellow Camaleon* sensor (YC3.6) [321, 322], that had already been used to visualize single action potentials in nervous cells [323], the *Yellow Mangaleon* (YM) sensor was created (Figure 19).

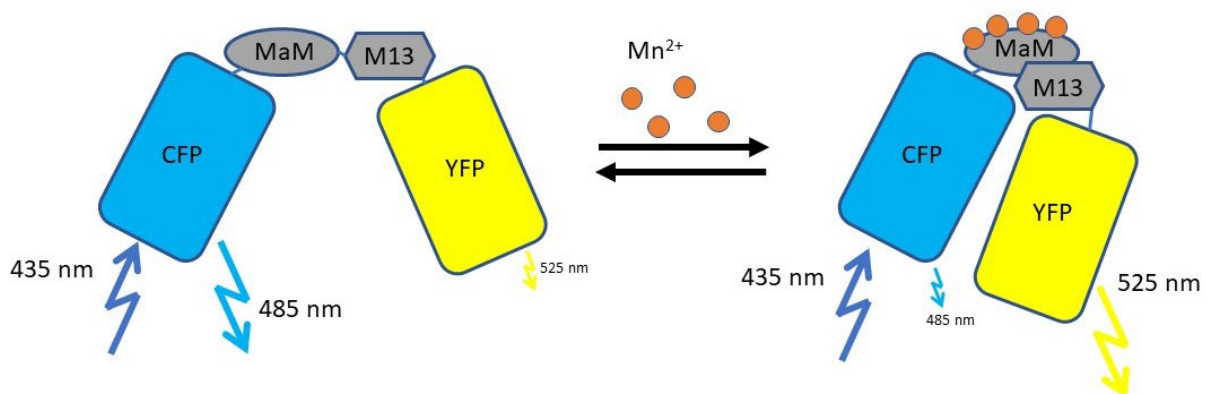


Figure 19: Schematic representation of the Yellow Mangaleon FRET sensor (Kudla unpublished). The CFP and YFP fluorophores are connected by a sensor domain, that consists of MaM and the M13 peptide. In MaM the original Ca^{2+} binding EF hands of CaM were exchanged for the fourth EF hand of CBL4 in order to bind Mn^{2+} instead of Ca^{2+} . Upon Mn^{2+} binding the M13 peptide binds to the CaM backbone and the YFP is brought in proximity to the CFP and FRET is promoted.

The YM sensor consists of CFP and YFP that are connected by the sensor domain. The sensor domain (MaM) consists of a CaM variant where all four original Ca^{2+} sensing EF hands were exchanged for the Mn^{2+} binding fourth EF hand of CBL4 from *A. thaliana* and a M13 peptide. Upon ion binding the M13 peptide binds to MaM and brings the YFP in proximity to CFP for FRET. Hence excitation of the CFP will result in specific YFP/CFP fluorescence ratios depending on the Mn^{2+} availability in the environment. This can be used as a measure for the present Mn^{2+} concentration. The function of the YM sensor *in vitro* and in HEK cells had already been given initial results pointing towards functionality and selectivity towards Mn^{2+} [320]. By ITC a clear specificity of the sensor domain towards Mn^{2+} and not Ca^{2+} could be postulated (Schmitt *et al.* unpublished). Hence the YM sensor will provide a novel tool for *in vivo* analysis of the cytosolic Mn^{2+} concentration and its potential dynamics in living plant cells.

References

1. Taiz, L., et al., *Plant physiology and development*. 2015: Sinauer Associates Incorporated.
2. Jones, C. and J. Jacobsen, *Plant nutrition and soil fertility*. Nutrient management module, 2005. **2**(11): p. 1-11.
3. Maathuis, F.J., *Physiological functions of mineral macronutrients*. Curr Opin Plant Biol, 2009. **12**(3): p. 250-8.
4. Hänsch, R. and R.R. Mendel, *Physiological functions of mineral micronutrients (Cu, Zn, Mn, Fe, Ni, Mo, B, Cl)*. Current Opinion in Plant Biology, 2009. **12**(3): p. 259-266.
5. Miller, A.J., *Plant mineral nutrition*. eLS, 2014.
6. Epstein, E. and A.J. Bloom, *Mineral nutrition of plants: principles and perspectives*. 2005, New York: Wiley & Sons.
7. Terry, N., *Photosynthesis, growth, and the role of chloride*. Plant Physiology, 1977. **60**(1): p. 69-75.
8. Xu, G., et al., *Advances in Chloride Nutrition of Plants*. 1999. p. 97-150.
9. Blevins, D.G. and K.M. Lukaszewski, *Boron in Plant Structure and Function*. Annu Rev Plant Physiol Plant Mol Biol, 1998. **49**: p. 481-500.
10. Fukuyama, K., *Structure and function of plant-type ferredoxins*. Photosynth Res, 2004. **81**(3): p. 289-301.
11. Couturier, J., et al., *The iron-sulfur cluster assembly machineries in plants: current knowledge and open questions*. Front Plant Sci, 2013. **4**: p. 259.
12. Bricker, T.M., et al., *The extrinsic proteins of Photosystem II*. Biochim Biophys Acta, 2012. **1817**(1): p. 121-42.
13. Alejandro, S., et al., *Manganese in Plants: From Acquisition to Subcellular Allocation*. Front Plant Sci, 2020. **11**: p. 300.
14. Krämer, U. and S. Clemens, *Functions and homeostasis of zinc, copper, and nickel in plants*, in *Molecular Biology of Metal Homeostasis and Detoxification*. 2005. p. 215-271.
15. Ciftci-Yilmaz, S. and R. Mittler, *The zinc finger network of plants*. Cell Mol Life Sci, 2008. **65**(7-8): p. 1150-60.
16. Yruela, I., *Copper in plants*. Brazilian Journal of Plant Physiology, 2005. **17**: p. 145-156.
17. Freyermuth, S.K., M. Bacanamwo, and J.C. Polacco, *The soybean Eu3 gene encodes an Ni-binding protein necessary for urease activity*. Plant J, 2000. **21**(1): p. 53-60.
18. Bai, C., C.C. Reilly, and B.W. Wood, *Nickel deficiency disrupts metabolism of ureides, amino acids, and organic acids of young pecan foliage*. Plant Physiol, 2006. **140**(2): p. 433-43.
19. Chen, C., D. Huang, and J. Liu, *Functions and Toxicity of Nickel in Plants: Recent Advances and Future Prospects*. CLEAN - Soil, Air, Water, 2009. **37**(4-5): p. 304-313.
20. Schwarz, G. and R.R. Mendel, *Molybdenum cofactor biosynthesis and molybdenum enzymes*. Annu Rev Plant Biol, 2006. **57**: p. 623-47.
21. Mendel, R.R., *Cell biology of molybdenum in plants*. Plant Cell Rep, 2011. **30**(10): p. 1787-97.
22. Miller, A.J. and M.D. Cramer, *Root Nitrogen Acquisition and Assimilation*. Plant and Soil, 2005. **274**(1-2): p. 1-36.
23. Chen, Y.F., Y. Wang, and W.H. Wu, *Membrane transporters for nitrogen, phosphate and potassium uptake in plants*. J Integr Plant Biol, 2008. **50**(7): p. 835-48.
24. Leghari, S.J., et al., *Role of nitrogen for plant growth and development: A review*. Advances in Environmental Biology, 2016. **10**(9): p. 209-219.
25. Jegla, T., G. Busey, and S.M. Assmann, *Evolution and Structural Characteristics of Plant Voltage-Gated K(+) Channels*. Plant Cell, 2018. **30**(12): p. 2898-2909.
26. Amtmann, A. and F. Rubio, *Potassium in Plants*, in eLS. 2012.
27. Hirsch, R.E., et al., *A role for the AKT1 potassium channel in plant nutrition*. Science, 1998. **280**(5365): p. 918-21.
28. Maathuis, F.M. and D. Sanders, *Energization of potassium uptake in Arabidopsis thaliana*. Planta, 1993. **191**(3).

29. Pittman, J.K., *Vacuolar Ca(2+) uptake*. Cell Calcium, 2011. **50**(2): p. 139-46.
30. Yang, H. and Y. Jie, *Uptake and transport of calcium in plants*. Journal of plant physiology and molecular biology, 2005. **31**(3): p. 227.
31. Knight, H., *Calcium signaling during abiotic stress in plants*. Int Rev Cytol, 2000. **195**: p. 269-324.
32. Thor, K., *Calcium-Nutrient and Messenger*. Front Plant Sci, 2019. **10**: p. 440.
33. Reddy A.S.N, R.V.S., *Calcium as a messenger in stress signal transduction*. Handbook of Plant and Crop Physiology, 2001. **Second Edition**: p. 719-756.
34. Gilroy, S. and A. Trewavas, *Signal processing and transduction in plant cells: the end of the beginning?* Nat Rev Mol Cell Biol, 2001. **2**(4): p. 307-14.
35. Yazaki, Y., Asukagawa, N., Ishikawa, Y., Ohta, E., & Sakata, M., *Estimation of Cytoplasmic Free Mg2+ Levels and Phosphorylation Potentials in Mung Bean Root Tips by In Vivo 31P NMR Spectroscopy*. Plant and cell physiology, 1988. **29**(6): p. 919-924.
36. Kleczkowski, L.A. and A.U. Igamberdiev, *Magnesium Signaling in Plants*. Int J Mol Sci, 2021. **22**(3).
37. Sirijovski, N., et al., *Substrate-binding model of the chlorophyll biosynthetic magnesium chelatase BchH subunit*. J Biol Chem, 2008. **283**(17): p. 11652-60.
38. Robinson, H., et al., *Hexahydrated magnesium ions bind in the deep major groove and at the outer mouth of A-form nucleic acid duplexes*. Nucleic Acids Res, 2000. **28**(8): p. 1760-6.
39. Schachtman, D.P., R.J. Reid, and S.M. Ayling, *Phosphorus Uptake by Plants: From Soil to Cell*. Plant Physiol, 1998. **116**(2): p. 447-53.
40. Raghothama, K.G., *Phosphorus and Plant Nutrition: An Overview*, in *Phosphorus: Agriculture and the Environment*. 2015. p. 353-378.
41. Hawkesford, M.J. and L.J. De Kok, *Managing sulphur metabolism in plants*. Plant Cell Environ, 2006. **29**(3): p. 382-95.
42. Ramani, B., H. Zorn, and J. Papenbrock, *Quantification and fatty acid profiles of sulfolipids in two halophytes and a glycophyte grown under different salt concentrations*. Z Naturforsch C J Biosci, 2004. **59**(11-12): p. 835-42.
43. Dong, Q., et al., *Ca(2+) signaling in plant responses to abiotic stresses*. J Integr Plant Biol, 2022. **64**(2): p. 287-300.
44. Berridge, M.J., P. Lipp, and M.D. Bootman, *The versatility and universality of calcium signalling*. Nat Rev Mol Cell Biol, 2000. **1**(1): p. 11-21.
45. Dodd, A.N., J. Kudla, and D. Sanders, *The language of calcium signaling*. Annu Rev Plant Biol, 2010. **61**: p. 593-620.
46. Rudd, J.J. and V.E. Franklin-Tong, *Unravelling response-specificity in Ca(2+) signalling pathways in plant cells*. New Phytol, 2001. **151**(1): p. 7-33.
47. Behera, S., et al., *Analyses of Ca2+ dynamics using a ubiquitin-10 promoter-driven Yellow Cameleon 3.6 indicator reveal reliable transgene expression and differences in cytoplasmic Ca2+ responses in Arabidopsis and rice (Oryza sativa) roots*. New Phytol, 2015. **206**(2): p. 751-60.
48. Zhu, J.K., *Abiotic Stress Signaling and Responses in Plants*. Cell, 2016. **167**(2): p. 313-324.
49. Nieves-Cordones, M., et al., *A putative role for the plasma membrane potential in the control of the expression of the gene encoding the tomato high-affinity potassium transporter HAK5*. Plant Mol Biol, 2008. **68**(6): p. 521-32.
50. Li, L., et al., *A Ca(2)+ signaling pathway regulates a K(+) channel for low-K response in Arabidopsis*. Proc Natl Acad Sci U S A, 2006. **103**(33): p. 12625-30.
51. Behera, S., et al., *Two spatially and temporally distinct Ca(2+) signals convey Arabidopsis thaliana responses to K(+) deficiency*. New Phytol, 2017. **213**(2): p. 739-750.
52. Walker, D.J., R.A. Leigh, and A.J. Miller, *Potassium homeostasis in vacuolate plant cells*. Proc Natl Acad Sci U S A, 1996. **93**(19): p. 10510-4.
53. Leigh, R.A. and R.G. Wyn Jones, *A Hypothesis Relating Critical Potassium Concentrations for Growth to the Distribution and Functions of This Ion in the Plant Cell*. New Phytologist, 1984. **97**(1): p. 1-13.

54. Wang, Y. and W.H. Wu, *Potassium transport and signaling in higher plants*. Annu Rev Plant Biol, 2013. **64**: p. 451-76.
55. Chérel, I., et al., *Molecular mechanisms involved in plant adaptation to low K(+) availability*. J Exp Bot, 2014. **65**(3): p. 833-48.
56. Maathuis, F.J., *The role of monovalent cation transporters in plant responses to salinity*. J Exp Bot, 2006. **57**(5): p. 1137-47.
57. Epstein, E., D.W. Rains, and O.E. Elzam, *Resolution of Dual Mechanisms of Potassium Absorption by Barley Roots*. Proc Natl Acad Sci U S A, 1963. **49**(5): p. 684-92.
58. Britto, D.T. and H.J. Kronzucker, *Cellular mechanisms of potassium transport in plants*. Physiol Plant, 2008. **133**(4): p. 637-50.
59. Busch, W. and M.H. Saier, Jr., *The transporter classification (TC) system, 2002*. Crit Rev Biochem Mol Biol, 2002. **37**(5): p. 287-337.
60. Nieves-Cordones, M., et al., *K⁺ uptake in plant roots. The systems involved, their regulation and parallels in other organisms*. J Plant Physiol, 2014. **171**(9): p. 688-95.
61. Spalding, E.P., et al., *Potassium uptake supporting plant growth in the absence of AKT1 channel activity: Inhibition by ammonium and stimulation by sodium*. J Gen Physiol, 1999. **113**(6): p. 909-18.
62. Nieves-Cordones, M., et al., *The Arabidopsis thaliana HAK5 K⁺ transporter is required for plant growth and K⁺ acquisition from low K⁺ solutions under saline conditions*. Mol Plant, 2010. **3**(2): p. 326-33.
63. Shabala, S. and T.A. Cuin, *Potassium transport and plant salt tolerance*. Physiol Plant, 2008. **133**(4): p. 651-69.
64. Alemán, F., et al., *Root K(+) acquisition in plants: the Arabidopsis thaliana model*. Plant Cell Physiol, 2011. **52**(9): p. 1603-12.
65. Sharma, T., I. Dreyer, and J. Riedelsberger, *The role of K(+) channels in uptake and redistribution of potassium in the model plant Arabidopsis thaliana*. Front Plant Sci, 2013. **4**: p. 224.
66. Corratgé-Faillie, C., et al., *Potassium and sodium transport in non-animal cells: the Trk/Ktr/HKT transporter family*. Cell Mol Life Sci, 2010. **67**(15): p. 2511-32.
67. Gierth, M. and P. Maser, *Potassium transporters in plants--involvement in K⁺ acquisition, redistribution and homeostasis*. FEBS Lett, 2007. **581**(12): p. 2348-56.
68. Nieves-Cordones, M., et al., *An NH₄⁺-sensitive component dominates high-affinity K⁺ uptake in tomato plants*. Plant Science, 2007. **172**(2): p. 273-280.
69. Shin, R. and D.P. Schachtman, *Hydrogen peroxide mediates plant root cell response to nutrient deprivation*. Proc Natl Acad Sci U S A, 2004. **101**(23): p. 8827-32.
70. Gierth, M., P. Maser, and J.I. Schroeder, *The potassium transporter AtHAK5 functions in K(+) deprivation-induced high-affinity K(+) uptake and AKT1 K(+) channel contribution to K(+) uptake kinetics in Arabidopsis roots*. Plant Physiol, 2005. **137**(3): p. 1105-14.
71. Rubio, F., et al., *Relative contribution of AtHAK5 and AtAKT1 to K⁺ uptake in the high-affinity range of concentrations*. Physiol Plant, 2008. **134**(4): p. 598-608.
72. Rubio, F., et al., *Studies on Arabidopsis athak5, atakt1 double mutants disclose the range of concentrations at which AtHAK5, AtAKT1 and unknown systems mediate K uptake*. Physiol Plant, 2010. **139**(2): p. 220-8.
73. Pyo, Y.J., et al., *High-affinity K(+) transport in Arabidopsis: AtHAK5 and AKT1 are vital for seedling establishment and postgermination growth under low-potassium conditions*. Plant Physiol, 2010. **153**(2): p. 863-75.
74. Lagarde, D., et al., *Tissue-specific expression of Arabidopsis AKT1 gene is consistent with a role in K⁺ nutrition*. Plant J, 1996. **9**(2): p. 195-203.
75. Tempel, B.L., et al., *Sequence of a probable potassium channel component encoded at Shaker locus of Drosophila*. Science, 1987. **237**(4816): p. 770-5.
76. Ferrús, A., et al., *Genetic analysis of the Shaker gene complex of Drosophila melanogaster*. Genetics, 1990. **125**(2): p. 383-98.
77. Schroeder, J.I., K. Raschke, and E. Neher, *Voltage dependence of K channels in guard-cell protoplasts*. Proc Natl Acad Sci U S A, 1987. **84**(12): p. 4108-12.

78. Hedrich, R., *Ion channels in plants*. Physiol Rev, 2012. **92**(4): p. 1777-811.
79. Chérel, I. and I. Gaillard, *The Complex Fine-Tuning of K(+) Fluxes in Plants in Relation to Osmotic and Ionic Abiotic Stresses*. Int J Mol Sci, 2019. **20**(3).
80. Daram, P., et al., *Tetramerization of the AKT1 plant potassium channel involves its C-terminal cytoplasmic domain*. EMBO J, 1997. **16**(12): p. 3455-63.
81. Sentenac, H., et al., *Cloning and expression in yeast of a plant potassium ion transport system*. Science, 1992. **256**(5057): p. 663-5.
82. Durell, S.R., I.H. Shrivastava, and H.R. Guy, *Models of the structure and voltage-gating mechanism of the shaker K⁺ channel*. Biophys J, 2004. **87**(4): p. 2116-30.
83. Gambale, F. and N. Uozumi, *Properties of shaker-type potassium channels in higher plants*. J Membr Biol, 2006. **210**(1): p. 1-19.
84. Schünke, S., et al., *Structural insights into conformational changes of a cyclic nucleotide-binding domain in solution from Mesorhizobium loti K1 channel*. Proc Natl Acad Sci U S A, 2011. **108**(15): p. 6121-6.
85. Long, S.B., E.B. Campbell, and R. Mackinnon, *Voltage sensor of Kv1.2: structural basis of electromechanical coupling*. Science, 2005. **309**(5736): p. 903-8.
86. Long, S.B., E.B. Campbell, and R. Mackinnon, *Crystal structure of a mammalian voltage-dependent Shaker family K⁺ channel*. Science, 2005. **309**(5736): p. 897-903.
87. Whicher, J.R. and R. MacKinnon, *Structure of the voltage-gated K(+) channel Eag1 reveals an alternative voltage sensing mechanism*. Science, 2016. **353**(6300): p. 664-9.
88. Li, M., et al., *Structure of a eukaryotic cyclic-nucleotide-gated channel*. Nature, 2017. **542**(7639): p. 60-65.
89. Lee, C.H. and R. MacKinnon, *Voltage Sensor Movements during Hyperpolarization in the HCN Channel*. Cell, 2019. **179**(7): p. 1582-1589 e7.
90. Männikkö, R., F. Elinder, and H.P. Larsson, *Voltage-sensing mechanism is conserved among ion channels gated by opposite voltages*. Nature, 2002. **419**(6909): p. 837-41.
91. Latorre, R., et al., *Molecular coupling between voltage sensor and pore opening in the Arabidopsis inward rectifier K⁺ channel KAT1*. J Gen Physiol, 2003. **122**(4): p. 459-69.
92. Doyle, D.A., et al., *The structure of the potassium channel: molecular basis of K⁺ conduction and selectivity*. Science, 1998. **280**(5360): p. 69-77.
93. Lu, Y., et al., *Structural basis for the activity regulation of a potassium channel AKT1 from Arabidopsis*. Nat Commun, 2022. **13**(1): p. 5682.
94. Nieves-Cordones, M. and I. Gaillard, *Involvement of the S4-S5 linker and the C-linker domain regions to voltage-gating in plant Shaker channels: comparison with animal HCN and Kv channels*. Plant Signal Behav, 2014. **9**(10): p. e972892.
95. Nieves-Cordones, M., et al., *Distinct amino acids in the C-linker domain of the Arabidopsis K⁺ channel KAT2 determine its subcellular localization and activity at the plasma membrane*. Plant Physiol, 2014. **164**(3): p. 1415-29.
96. James, Z.M. and W.N. Zagotta, *Structural insights into the mechanisms of CNBD channel function*. J Gen Physiol, 2018. **150**(2): p. 225-244.
97. Craven, K.B. and W.N. Zagotta, *CNG and HCN channels: two peas, one pod*. Annu Rev Physiol, 2006. **68**: p. 375-401.
98. Clark, M.D., et al., *Electromechanical coupling in the hyperpolarization-activated K(+) channel KAT1*. Nature, 2020. **583**(7814): p. 145-149.
99. Gehring, C. and I.S. Turek, *Cyclic Nucleotide Monophosphates and Their Cyclases in Plant Signaling*. Front Plant Sci, 2017. **8**: p. 1704.
100. Gaymard, F., et al., *The baculovirus/insect cell system as an alternative to Xenopus oocytes. First characterization of the AKT1 K⁺ channel from Arabidopsis thaliana*. J Biol Chem, 1996. **271**(37): p. 22863-70.
101. Brelidze, T.I., et al., *Structure of the C-terminal region of an ERG channel and functional implications*. Proc Natl Acad Sci U S A, 2013. **110**(28): p. 11648-53.
102. Carlson, A.E., et al., *Flavonoid regulation of HCN2 channels*. J Biol Chem, 2013. **288**(46): p. 33136-45.

103. Carlson, A.E., T.I. Brelidze, and W.N. Zagotta, *Flavonoid regulation of EAG1 channels*. J Gen Physiol, 2013. **141**(3): p. 347-58.
104. Samanta, A.G.D.S.K.D., *Roles of flavonoids in plants*. Int J Pharm Sci Tech, 2011. **6**(1): p. 12-35.
105. Iwashina, T., *The Structure and Distribution of the Flavonoids in Plants*. Journal of Plant Research, 2000. **113**(3): p. 287-299.
106. Flynn, G.E., et al., *Structure and rearrangements in the carboxy-terminal region of SplH channels*. Structure, 2007. **15**(6): p. 671-82.
107. Taraska, J.W., et al., *Mapping the structure and conformational movements of proteins with transition metal ion FRET*. Nat Methods, 2009. **6**(7): p. 532-7.
108. Zagotta, W.N., et al., *Structural basis for modulation and agonist specificity of HCN pacemaker channels*. Nature, 2003. **425**(6954): p. 200-205.
109. Zhou, L. and S.A. Siegelbaum, *Gating of HCN channels by cyclic nucleotides: residue contacts that underlie ligand binding, selectivity, and efficacy*. Structure, 2007. **15**(6): p. 655-70.
110. Puljung, M.C., et al., *Double electron-electron resonance reveals cAMP-induced conformational change in HCN channels*. Proc Natl Acad Sci U S A, 2014. **111**(27): p. 9816-21.
111. Goldschen-Ohm, M.P., et al., *Structure and dynamics underlying elementary ligand binding events in human pacemaking channels*. Elife, 2016. **5**.
112. Saponaro, A., et al., *Structural basis for the mutual antagonism of cAMP and TRIP8b in regulating HCN channel function*. Proc Natl Acad Sci U S A, 2014. **111**(40): p. 14577-82.
113. Jernigan, K.K. and S.R. Bordenstein, *Ankyrin domains across the Tree of Life*. PeerJ, 2014. **2**.
114. Mosavi, L.K., et al., *The ankyrin repeat as molecular architecture for protein recognition*. Protein Sci, 2004. **13**(6): p. 1435-48.
115. Mosavi, L.K., S. Williams, and Z.Y. Peng Zy, *Equilibrium folding and stability of myotrophin: a model ankyrin repeat protein*. J Mol Biol, 2002. **320**(2): p. 165-70.
116. Li, J., A. Mahajan, and M.D. Tsai, *Ankyrin repeat: a unique motif mediating protein-protein interactions*. Biochemistry, 2006. **45**(51): p. 15168-78.
117. Batchelor, A.H., et al., *The structure of GABPalpha/beta: an ETS domain- ankyrin repeat heterodimer bound to DNA*. Science, 1998. **279**(5353): p. 1037-41.
118. Foord, R., et al., *X-ray structural analysis of the yeast cell cycle regulator Swi6 reveals variations of the ankyrin fold and has implications for Swi6 function*. Nat Struct Biol, 1999. **6**(2): p. 157-65.
119. Sanchez-Barrena, M.J., et al., *Recognition and Activation of the Plant AKT1 Potassium Channel by the Kinase CIPK23*. Plant Physiol, 2020. **182**(4): p. 2143-2153.
120. Main, E.R., S.E. Jackson, and L. Regan, *The folding and design of repeat proteins: reaching a consensus*. Curr Opin Struct Biol, 2003. **13**(4): p. 482-9.
121. Mosavi, L.K., D.L. Minor, Jr., and Z.Y. Peng, *Consensus-derived structural determinants of the ankyrin repeat motif*. Proc Natl Acad Sci U S A, 2002. **99**(25): p. 16029-34.
122. Sedgwick, S.G. and S.J. Smerdon, *The ankyrin repeat: a diversity of interactions on a common structural framework*. Trends Biochem Sci, 1999. **24**(8): p. 311-6.
123. Yuan, C., et al., *Solution structure of the human oncogenic protein gankyrin containing seven ankyrin repeats and analysis of its structure--function relationship*. Biochemistry, 2004. **43**(38): p. 12152-61.
124. Chaves-Sanjuan, A., et al., *Preliminary crystallographic analysis of the ankyrin-repeat domain of Arabidopsis thaliana AKT1: identification of the domain boundaries for protein crystallization*. Acta Crystallogr F Struct Biol Commun, 2014. **70**(Pt 4): p. 509-12.
125. Chaves-Sanjuan, A., et al., *Structural basis of the regulatory mechanism of the plant CIPK family of protein kinases controlling ion homeostasis and abiotic stress*. Proc Natl Acad Sci U S A, 2014. **111**(42): p. E4532-41.
126. Very, A.A. and H. Sentenac, *Molecular mechanisms and regulation of K⁺ transport in higher plants*. Annu Rev Plant Biol, 2003. **54**: p. 575-603.
127. Ehrhardt, T., S. Zimmermann, and B. Muller-Rober, *Association of plant K⁺(in) channels is mediated by conserved C-termini and does not affect subunit assembly*. FEBS Lett, 1997. **409**(2): p. 166-70.

128. Pilot, G., et al., *Five-group distribution of the Shaker-like K⁺ channel family in higher plants*. J Mol Evol, 2003. **56**(4): p. 418-34.
129. Duby, G., et al., *AtKC1, a conditionally targeted Shaker-type subunit, regulates the activity of plant K⁺ channels*. Plant J, 2008. **53**(1): p. 115-23.
130. Wang, Y., et al., *Potassium channel alpha-subunit AtKC1 negatively regulates AKT1-mediated K⁺ uptake in Arabidopsis roots under low-K⁺ stress*. Cell Res, 2010. **20**(7): p. 826-37.
131. Geiger, D., et al., *Heteromeric AtKC1:AKT1 channels in Arabidopsis roots facilitate growth under K⁺ limiting conditions*. J Biol Chem, 2009. **284**(32): p. 21288-95.
132. Consortium, T.U., *UniProt: the Universal Protein Knowledgebase in 2023*. Nucleic Acids Research, 2022. **51**(D1): p. D523-D531.
133. Reintanz, B., et al., *AtKC1, a silent Arabidopsis potassium channel alpha -subunit modulates root hair K⁺ influx*. Proc Natl Acad Sci U S A, 2002. **99**(6): p. 4079-84.
134. Jeanguenin, L., et al., *AtKC1 is a general modulator of Arabidopsis inward Shaker channel activity*. Plant J, 2011. **67**(4): p. 570-82.
135. Wang, Y. and W.H. Wu, *Plant sensing and signaling in response to K⁺-deficiency*. Mol Plant, 2010. **3**(2): p. 280-7.
136. Wang, X.P., et al., *AtKC1 and CIPK23 Synergistically Modulate AKT1-Mediated Low-Potassium Stress Responses in Arabidopsis*. Plant Physiol, 2016. **170**(4): p. 2264-77.
137. Batistic, O. and J. Kudla, *Plant calcineurin B-like proteins and their interacting protein kinases*. Biochim Biophys Acta, 2009. **1793**(6): p. 985-92.
138. Lee, S.C., et al., *A protein phosphorylation/dephosphorylation network regulates a plant potassium channel*. Proc Natl Acad Sci U S A, 2007. **104**(40): p. 15959-64.
139. Ragel, P., et al., *The CBL-Interacting Protein Kinase CIPK23 Regulates HAK5-Mediated High-Affinity K⁺ Uptake in Arabidopsis Roots*. Plant Physiol, 2015. **169**(4): p. 2863-73.
140. Rodenas, R. and G. Vert, *Regulation of Root Nutrient Transporters by CIPK23: 'One Kinase to Rule Them All'*. Plant Cell Physiol, 2021. **62**(4): p. 553-563.
141. Xu, J., et al., *A protein kinase, interacting with two calcineurin B-like proteins, regulates K⁺ transporter AKT1 in Arabidopsis*. Cell, 2006. **125**(7): p. 1347-60.
142. Ren, X.L., et al., *Calcineurin B-like protein CBL10 directly interacts with AKT1 and modulates K⁺ homeostasis in Arabidopsis*. Plant J, 2013. **74**(2): p. 258-66.
143. Scott, J.D. and T.R. Soderling, *Serine/threonine protein kinases*. Curr Opin Neurobiol, 1992. **2**(3): p. 289-95.
144. Stancik, I.A., et al., *Serine/Threonine Protein Kinases from Bacteria, Archaea and Eukarya Share a Common Evolutionary Origin Deeply Rooted in the Tree of Life*. J Mol Biol, 2018. **430**(1): p. 27-32.
145. Edelman, A.M., D.K. Blumenthal, and E.G. Krebs, *Protein serine/threonine kinases*. Annu Rev Biochem, 1987. **56**: p. 567-613.
146. Wang, P., et al., *Mapping proteome-wide targets of protein kinases in plant stress responses*. Proc Natl Acad Sci U S A, 2020. **117**(6): p. 3270-3280.
147. Petrov, V., et al., *ROS-mediated abiotic stress-induced programmed cell death in plants*. Front Plant Sci, 2015. **6**: p. 69.
148. Hashimoto, K., et al., *Phosphorylation of calcineurin B-like (CBL) calcium sensor proteins by their CBL-interacting protein kinases (CIPKs) is required for full activity of CBL-CIPK complexes toward their target proteins*. J Biol Chem, 2012. **287**(11): p. 7956-68.
149. Guo, Y., et al., *Molecular characterization of functional domains in the protein kinase SOS2 that is required for plant salt tolerance*. Plant Cell, 2001. **13**(6): p. 1383-400.
150. Albrecht, V., et al., *The NAF domain defines a novel protein-protein interaction module conserved in Ca²⁺-regulated kinases*. EMBO J, 2001. **20**(5): p. 1051-63.
151. Ohta, M., et al., *A novel domain in the protein kinase SOS2 mediates interaction with the protein phosphatase 2C ABI2*. Proc Natl Acad Sci U S A, 2003. **100**(20): p. 11771-6.
152. Sanchez-Barrena, M.J., et al., *The structure of the C-terminal domain of the protein kinase AtSOS2 bound to the calcium sensor AtSOS3*. Mol Cell, 2007. **26**(3): p. 427-35.

153. Fujii, H. and J.K. Zhu, *An autophosphorylation site of the protein kinase SOS2 is important for salt tolerance in Arabidopsis*. Mol Plant, 2009. **2**(1): p. 183-90.
154. Jura, N., et al., *Catalytic control in the EGF receptor and its connection to general kinase regulatory mechanisms*. Mol Cell, 2011. **42**(1): p. 9-22.
155. Ng, L.M., et al., *Structural basis for basal activity and autoactivation of abscisic acid (ABA) signaling SnRK2 kinases*. Proc Natl Acad Sci U S A, 2011. **108**(52): p. 21259-64.
156. Akaboshi, M., et al., *The crystal structure of plant-specific calcium-binding protein AtCBL2 in complex with the regulatory domain of AtCIPK14*. J Mol Biol, 2008. **377**(1): p. 246-57.
157. Sanchez-Barrena, M.J., M. Martinez-Ripoll, and A. Albert, *Structural Biology of a Major Signaling Network that Regulates Plant Abiotic Stress: The CBL-CIPK Mediated Pathway*. Int J Mol Sci, 2013. **14**(3): p. 5734-49.
158. Singh, A., et al., *A protein phosphatase 2C, AP2C1, interacts with and negatively regulates the function of CIPK9 under potassium-deficient conditions in Arabidopsis*. J Exp Bot, 2018. **69**(16): p. 4003-4015.
159. Gong, D., et al., *Biochemical characterization of the Arabidopsis protein kinase SOS2 that functions in salt tolerance*. Plant Physiol, 2002. **130**(1): p. 256-64.
160. Gao, P., et al., *Expression, purification and analysis of an Arabidopsis recombinant CBL-interacting protein kinase3 (CIPK3) and its constitutively active form*. Protein Expr Purif, 2012. **86**(1): p. 45-52.
161. Nolen, B., S. Taylor, and G. Ghosh, *Regulation of protein kinases; controlling activity through activation segment conformation*. Mol Cell, 2004. **15**(5): p. 661-75.
162. Gong, D., et al., *The SOS3 family of calcium sensors and SOS2 family of protein kinases in Arabidopsis*. Plant Physiol, 2004. **134**(3): p. 919-26.
163. Li, K., et al., *AIK1, A Mitogen-Activated Protein Kinase, Modulates Abscisic Acid Responses through the MKK5-MPK6 Kinase Cascade*. Plant Physiol, 2017. **173**(2): p. 1391-1408.
164. Du, W., et al., *Phosphorylation of SOS3-like calcium-binding proteins by their interacting SOS2-like protein kinases is a common regulatory mechanism in Arabidopsis*. Plant Physiol, 2011. **156**(4): p. 2235-43.
165. Cohen, P., *The origins of protein phosphorylation*. Nat Cell Biol, 2002. **4**(5): p. E127-30.
166. Lan, W.Z., et al., *Mechanistic analysis of AKT1 regulation by the CBL-CIPK-PP2CA interactions*. Mol Plant, 2011. **4**(3): p. 527-36.
167. Kudla, J., et al., *Genes for calcineurin B-like proteins in Arabidopsis are differentially regulated by stress signals*. Proc Natl Acad Sci U S A, 1999. **96**(8): p. 4718-23.
168. Cyert, M.S. and J. Thorner, *Regulatory subunit (CNB1 gene product) of yeast Ca²⁺/calmodulin-dependent phosphoprotein phosphatases is required for adaptation to pheromone*. Mol Cell Biol, 1992. **12**(8): p. 3460-9.
169. Rusnak, F. and P. Mertz, *Calcineurin: form and function*. Physiol Rev, 2000. **80**(4): p. 1483-521.
170. Kretsinger, R.H. and C.E. Nockolds, *Carp Muscle Calcium-binding Protein*. Journal of Biological Chemistry, 1973. **248**(9): p. 3313-3326.
171. Batistic, O. and J. Kudla, *Integration and channeling of calcium signaling through the CBL calcium sensor/CIPK protein kinase network*. Planta, 2004. **219**(6): p. 915-24.
172. Kawasaki, H. and R.H. Kretsinger, *Structural and functional diversity of EF-hand proteins: Evolutionary perspectives*. Protein Sci, 2017. **26**(10): p. 1898-1920.
173. Allouche, D., J. Parello, and Y.H. Sanejouand, *Ca²⁺/Mg²⁺ exchange in parvalbumin and other EF-hand proteins. A theoretical study*. J Mol Biol, 1999. **285**(2): p. 857-73.
174. Ohki, S., M. Ikura, and M. Zhang, *Identification of Mg²⁺-binding sites and the role of Mg²⁺ on target recognition by calmodulin*. Biochemistry, 1997. **36**(14): p. 4309-16.
175. Osawa, M., et al., *Mg²⁺ and Ca²⁺ differentially regulate DNA binding and dimerization of DREAM*. J Biol Chem, 2005. **280**(18): p. 18008-14.
176. Sanchez-Barrena, M.J., et al., *The structure of the Arabidopsis thaliana SOS3: molecular mechanism of sensing calcium for salt stress response*. J Mol Biol, 2005. **345**(5): p. 1253-64.
177. Lewit-Bentley, A. and S. Rety, *EF-hand calcium-binding proteins*. Curr Opin Struct Biol, 2000. **10**(6): p. 637-43.

178. Nakayama, S., Kawasaki, H., Kretsinger, R. , *Evolution of EF-Hand Proteins*, in *Calcium Homeostasis. Topics in Biological Inorganic Chemistry*, E. Carafoli, Krebs, J., Editor. 2000, Springer, Berlin, Heidelberg.
179. Ames, J.B., et al., *Molecular mechanics of calcium-myristoyl switches*. *Nature*, 1997. **389**(6647): p. 198-202.
180. Maune, J.F., C.B. Klee, and K. Beckingham, *Ca²⁺ binding and conformational change in two series of point mutations to the individual Ca(2+)-binding sites of calmodulin*. *Journal of Biological Chemistry*, 1992. **267**(8): p. 5286-5295.
181. Nagae, M., et al., *The crystal structure of the novel calcium-binding protein AtCBL2 from Arabidopsis thaliana*. *J Biol Chem*, 2003. **278**(43): p. 42240-6.
182. de la Torre, F., et al., *The tomato calcium sensor Cbl10 and its interacting protein kinase Cipk6 define a signaling pathway in plant immunity*. *Plant Cell*, 2013. **25**(7): p. 2748-64.
183. Batistic, O., et al., *CBL-mediated targeting of CIPKs facilitates the decoding of calcium signals emanating from distinct cellular stores*. *Plant J*, 2010. **61**(2): p. 211-22.
184. Batistic, O., et al., *Dual fatty acyl modification determines the localization and plasma membrane targeting of CBL/CIPK Ca²⁺ signaling complexes in Arabidopsis*. *Plant Cell*, 2008. **20**(5): p. 1346-62.
185. Ishitani, M., et al., *SOS3 function in plant salt tolerance requires N-myristoylation and calcium binding*. *Plant Cell*, 2000. **12**(9): p. 1667-78.
186. Finn, B.E., et al., *Calcium-induced structural changes and domain autonomy in calmodulin*. *Nat Struct Biol*, 1995. **2**(9): p. 777-83.
187. Zhang, M., T. Tanaka, and M. Ikura, *Calcium-induced conformational transition revealed by the solution structure of apo calmodulin*. *Nat Struct Biol*, 1995. **2**(9): p. 758-67.
188. Kuboniwa, H., et al., *Solution structure of calcium-free calmodulin*. *Nat Struct Biol*, 1995. **2**(9): p. 768-76.
189. Cheong, Y.H., et al., *Two calcineurin B-like calcium sensors, interacting with protein kinase CIPK23, regulate leaf transpiration and root potassium uptake in Arabidopsis*. *Plant J*, 2007. **52**(2): p. 223-39.
190. Nagae, M., et al., *Crystallization and preliminary X-ray characterization of a novel calcium-binding protein AtCBL2 from Arabidopsis thaliana*. *Acta Crystallogr D Biol Crystallogr*, 2003. **59**(Pt 6): p. 1079-80.
191. Sanchez-Barrena, M.J., et al., *SOS3 (salt overly sensitive 3) from Arabidopsis thaliana: expression, purification, crystallization and preliminary X-ray analysis*. *Acta Crystallogr D Biol Crystallogr*, 2004. **60**(Pt 7): p. 1272-4.
192. Costa, T.R.D., A. Ignatiou, and E.V. Orlova, *Structural Analysis of Protein Complexes by Cryo Electron Microscopy*. *Methods Mol Biol*, 2017. **1615**: p. 377-413.
193. Kadereit, J.W., et al., *Strasburger – Lehrbuch der Pflanzenwissenschaften*. 2014.
194. Shoemaker, C.A., *Plants and Human Culture*. *Journal of Home & Consumer Horticulture*, 2010. **1**(2-3): p. 3-7.
195. Ciais, P.a.S., C. and Bala, G. and Bopp, L. and Brovkin, V. and Canadell, J. and Chhabra, A. and DeFries, R. and Galloway, J. and Heimann, M. and Jones, C. and Le Quéré, C. and Myneni, R.B. and Piao, S. and Thornton, P., *Carbon and Other Biogeochemical Cycles*, in *Climate Change 2013 – The Physical Science Basis*. 2014. p. 465-570.
196. Hansen, J., et al., *Global Surface Temperature Change*. *Reviews of Geophysics*, 2010. **48**(4).
197. Gouel, C. and H. Guimbard, *Nutrition Transition and the Structure of Global Food Demand*. *American Journal of Agricultural Economics*, 2018. **101**(2): p. 383-403.
198. Henry, R.J., *Plant resources for food, fuel and conservation*. 2009: Routledge.
199. Ruan, L., et al., *Comparative analysis of potassium deficiency-responsive transcriptomes in low potassium susceptible and tolerant wheat (Triticum aestivum L.)*. *Sci Rep*, 2015. **5**: p. 10090.
200. Rengel, Z. and P.M. Damon, *Crops and genotypes differ in efficiency of potassium uptake and use*. *Physiol Plant*, 2008. **133**(4): p. 624-36.
201. Kopittke, P.M., et al., *Global changes in soil stocks of carbon, nitrogen, phosphorus, and sulphur as influenced by long-term agricultural production*. *Glob Chang Biol*, 2017. **23**(6): p. 2509-2519.

202. Stewart, W.M., et al., *The Contribution of Commercial Fertilizer Nutrients to Food Production*. Agronomy Journal, 2005. **97**(1): p. 1-6.
203. Ragel, P., et al., *Regulation of K(+) Nutrition in Plants*. Front Plant Sci, 2019. **10**: p. 281.
204. PubChem Element Summary for AtomicNumber 19, Potassium. 2023 [cited 2023 April 3, 2023]; Available from: <https://pubchem.ncbi.nlm.nih.gov/element/Potassium>.
205. Bertsch, P.M. and G.W. Thomas, *Potassium Status of Temperate Region Soils*, in *Potassium in Agriculture*. 1985. p. 129-162.
206. Hafsi, C., A. Debez, and C. Abdelly, *Potassium deficiency in plants: effects and signaling cascades*. Acta Physiologiae Plantarum, 2014. **36**(5): p. 1055-1070.
207. Bernaudat, F., et al., *Heterologous expression of membrane proteins: choosing the appropriate host*. PLoS One, 2011. **6**(12): p. e29191.
208. Berg, J.M., J.L. Tymoczko, and L. Stryer, *Stryer Biochemie*. 7 ed. 2013: Springer-Verlag Berlin Heidelberg 2013. XLII, 1198.
209. Watson, J.D., et al., *Molekularbiologie*. Vol. 3. 2011: Pearson Deutschland GmbH.
210. Bühler, L., *Cell membranes*. 2015: Garland Science.
211. Büttner, M.G., Brigitte; Kaaden †, Oskar-Rüger; Krüger, Monika; Seidler, Tassilo; Selbitz, Hans-Joachim, *Medizinische Mikrobiologie, Infektions- und Seuchenlehre*. Vol. 8. 2007, Stuttgart: Georg Thieme Verlag KG.
212. Abts, A., et al., *Rational and Irrational Approaches to Convince a Protein to Crystallize*, in *Modern Aspects of Bulk Crystal and Thin Film Preparation*. 2012.
213. Schlegel, S., P. Genevaux, and J.W. de Gier, *De-convoluting the Genetic Adaptations of E. coli C41(DE3) in Real Time Reveals How Alleviating Protein Production Stress Improves Yields*. Cell Rep, 2015. **10**(10): p. 1758-1766.
214. Dumon-Seignovert, L., G. Cariot, and L. Vuillard, *The toxicity of recombinant proteins in Escherichia coli: a comparison of overexpression in BL21(DE3), C41(DE3), and C43(DE3)*. Protein Expr Purif, 2004. **37**(1): p. 203-6.
215. Tegel, H., et al., *Increased levels of recombinant human proteins with the Escherichia coli strain Rosetta(DE3)*. Protein Expr Purif, 2010. **69**(2): p. 159-67.
216. Addgene_Vector_Database. *Plasmid: pLysS*. [cited 2023 04.04.2023]; Available from: <https://www.addgene.org/vector-database/3494/>.
217. Ernst, R., *Molekulare Analyse von ABC-Transportern am Beispiel von Pdr5p aus S. cerevisiae und der isolierten NBD des humanen TAP1*, in *Mathematisch-Naturwissenschaftlichen Fakultät*. 2007, Heinrich-Heine Universität: Düsseldorf. p. 165.
218. Nourani, A., et al., *Multiple-drug-resistance phenomenon in the yeast Saccharomyces cerevisiae: involvement of two hexose transporters*. Mol Cell Biol, 1997. **17**(9): p. 5453-60.
219. Botstein DDavis, R., *Principles and practice of recombinant DNA research with yeast*. Strathern JN *The Molecular Biology of the Yeast Saccharomyces: Metabolism and Gene Expression*. 1982, Cold Spring Harbor: Cold Spring Harbor Laboratory Press.
220. biotechrabbit, *RTS 100 Wheat Germ CECF Kit Manual*. 2015: p. 28.
221. Schwarz, D., et al., *Preparative scale expression of membrane proteins in Escherichia coli-based continuous exchange cell-free systems*. Nat Protoc, 2007. **2**(11): p. 2945-57.
222. Porath, J., et al., *Metal chelate affinity chromatography, a new approach to protein fractionation*. Nature, 1975. **258**(5536): p. 598-9.
223. Hochuli, E., H. Dobeli, and A. Schacher, *New metal chelate adsorbent selective for proteins and peptides containing neighbouring histidine residues*. J Chromatogr, 1987. **411**: p. 177-84.
224. Voss, S. and A. Skerra, *Mutagenesis of a flexible loop in streptavidin leads to higher affinity for the Strep-tag II peptide and improved performance in recombinant protein purification*. Protein Eng, 1997. **10**(8): p. 975-82.
225. Knospe, C.V., et al., *The structure of MadC from Clostridium maddingley reveals new insights into class I lanthipeptide cyclases*. Front Microbiol, 2022. **13**: p. 1057217.
226. Gasteiger E., H.C., Gattiker A., Duvaud S., Wilkins M.R., Appel R.D., Bairoch A. *The Proteomics Protocols Handbook*. 2005; Available from: <https://web.expasy.org/protparam/>.

227. Peptide_2.0. *Peptide Hydrophobicity/Hydrophilicity Analysis Tool*. [cited 2023 April 05]; Available from: https://www.peptide2.com/N_peptide_hydrophobicity_hydrophilicity.php.
228. Gul, N., et al., *Evolved Escherichia coli strains for amplified, functional expression of membrane proteins*. J Mol Biol, 2014. **426**(1): p. 136-49.
229. Drew, D., et al., *Assembly and overexpression of membrane proteins in Escherichia coli*. Biochim Biophys Acta, 2003. **1610**(1): p. 3-10.
230. Drew, D., et al., *GFP-based optimization scheme for the overexpression and purification of eukaryotic membrane proteins in Saccharomyces cerevisiae*. Nat Protoc, 2008. **3**(5): p. 784-98.
231. Wang, D.N., et al., *Practical aspects of overexpressing bacterial secondary membrane transporters for structural studies*. Biochim Biophys Acta, 2003. **1610**(1): p. 23-36.
232. Lee, M., et al., *The ABC transporter AtABCB14 is a malate importer and modulates stomatal response to CO₂*. Nat Cell Biol, 2008. **10**(10): p. 1217-23.
233. Voet-van-Vormizeele, J. and G. Groth, *High-level expression of the Arabidopsis thaliana ethylene receptor protein ETR1 in Escherichia coli and purification of the recombinant protein*. Protein Expr Purif, 2003. **32**(1): p. 89-94.
234. Netzer, W.J. and F.U. Hartl, *Recombination of protein domains facilitated by co-translational folding in eukaryotes*. Nature, 1997. **388**(6640): p. 343-9.
235. Hartl, F.U. and M. Hayer-Hartl, *Molecular chaperones in the cytosol: from nascent chain to folded protein*. Science, 2002. **295**(5561): p. 1852-8.
236. Midgett, C.R. and D.R. Madden, *Breaking the bottleneck: eukaryotic membrane protein expression for high-resolution structural studies*. J Struct Biol, 2007. **160**(3): p. 265-74.
237. Harbers, M., *Wheat germ systems for cell-free protein expression*. FEBS Lett, 2014. **588**(17): p. 2762-73.
238. Reckel, S., et al., *Strategies for the cell-free expression of membrane proteins*. Methods Mol Biol, 2010. **607**: p. 187-212.
239. Schneider, B., et al., *Membrane protein expression in cell-free systems*. Methods Mol Biol, 2010. **601**: p. 165-86.
240. Schwarz, D., V. Dotsch, and F. Bernhard, *Production of membrane proteins using cell-free expression systems*. Proteomics, 2008. **8**(19): p. 3933-46.
241. Fogeron, M.L., et al., *Wheat Germ Cell-Free Overexpression for the Production of Membrane Proteins*. Methods Mol Biol, 2017. **1635**: p. 91-108.
242. Klammt, C., et al., *Cell-free expression as an emerging technique for the large scale production of integral membrane protein*. FEBS J, 2006. **273**(18): p. 4141-53.
243. Klammt, C., et al., *Evaluation of detergents for the soluble expression of alpha-helical and beta-barrel-type integral membrane proteins by a preparative scale individual cell-free expression system*. FEBS J, 2005. **272**(23): p. 6024-38.
244. Seddon, A.M., P. Curnow, and P.J. Booth, *Membrane proteins, lipids and detergents: not just a soap opera*. Biochim Biophys Acta, 2004. **1666**(1-2): p. 105-17.
245. Ilgu, H., et al., *Variation of the detergent-binding capacity and phospholipid content of membrane proteins when purified in different detergents*. Biophys J, 2014. **106**(8): p. 1660-70.
246. Vagenende, V., M.G. Yap, and B.L. Trout, *Mechanisms of protein stabilization and prevention of protein aggregation by glycerol*. Biochemistry, 2009. **48**(46): p. 11084-96.
247. Drerup, M.M., et al., *The Calcineurin B-like calcium sensors CBL1 and CBL9 together with their interacting protein kinase CIPK26 regulate the Arabidopsis NADPH oxidase RBOHF*. Mol Plant, 2013. **6**(2): p. 559-69.
248. Förster, S., et al., *Wounding-Induced Stomatal Closure Requires Jasmonate-Mediated Activation of GORK K(+) Channels by a Ca(2+) Sensor-Kinase CBL1-CIPK5 Complex*. Dev Cell, 2019. **48**(1): p. 87-99 e6.
249. Mirdita, M., et al., *ColabFold: making protein folding accessible to all*. Nat Methods, 2022. **19**(6): p. 679-682.
250. Jumper, J., et al., *Highly accurate protein structure prediction with AlphaFold*. Nature, 2021. **596**(7873): p. 583-589.

251. Information, N.C.f.B. *PubChem Compound Summary for CID 2724258*. 2023 [cited 2023 April 4, 2023]; Available from: <https://pubchem.ncbi.nlm.nih.gov/compound/2724258>.
252. Information, N.C.f.B. *PubChem Compound Summary for CID 107670, CHAPS*. 2023 [cited 2023 April 4, 2023]; Available from: <https://pubchem.ncbi.nlm.nih.gov/compound/Chaps>.
253. Sebastiany, C., *Studies on the CBL-interacting serine/ threonine-protein kinase CIPK23 from Arabidopsis thaliana*, in *Biochemistry I*. 2021, Heinrich-Heine-Universität Düsseldorf. p. 85.
254. Günes, C., *Investigation of the Calcineurin B-like Calcium Sensor CBL9*, in *Biochemie I*. 2022, Heinrich-Heine-Universität: Düsseldorf. p. 97.
255. Scopes, R.K., *Strategies for protein purification*. Curr Protoc Protein Sci, 2001. **Chapter 1**: p. Unit 1 2.
256. Derewenda, Z.S., *The use of recombinant methods and molecular engineering in protein crystallization*. Methods, 2004. **34**(3): p. 354-63.
257. Voet, D., J.G. Voet, and C.W. Pratt, *Lehrbuch der Biochemie*. 2019: John Wiley & Sons.
258. Meyer, Y., J.P. Reichheld, and F. Vignols, *Thioredoxins in Arabidopsis and other plants*. Photosynth Res, 2005. **86**(3): p. 419-33.
259. Smart, O.S., et al., *HOLE: a program for the analysis of the pore dimensions of ion channel structural models*. J Mol Graph, 1996. **14**(6): p. 354-60, 376.
260. Thorsness, P.E. and D.E. Koshland, *Inactivation of isocitrate dehydrogenase by phosphorylation is mediated by the negative charge of the phosphate*. Journal of Biological Chemistry, 1987. **262**(22): p. 10422-10425.
261. Hoshi, T., *Regulation of voltage dependence of the KAT1 channel by intracellular factors*. J Gen Physiol, 1995. **105**(3): p. 309-28.
262. Lee, C.H. and R. MacKinnon, *Structures of the Human HCN1 Hyperpolarization-Activated Channel*. Cell, 2017. **168**(1-2): p. 111-120 e11.
263. Tang, R.J., et al., *A calcium signalling network activates vacuolar K(+) remobilization to enable plant adaptation to low-K environments*. Nat Plants, 2020. **6**(4): p. 384-393.
264. Li, W., et al., *Plant HAK/KUP/KT K(+) transporters: Function and regulation*. Semin Cell Dev Biol, 2018. **74**: p. 133-141.
265. Ho, C.H., et al., *CHL1 functions as a nitrate sensor in plants*. Cell, 2009. **138**(6): p. 1184-94.
266. Mao, J., et al., *Mechanisms and Physiological Roles of the CBL-CIPK Networking System in Arabidopsis thaliana*. Genes (Basel), 2016. **7**(9).
267. Leran, S., et al., *Nitrate sensing and uptake in Arabidopsis are enhanced by ABI2, a phosphatase inactivated by the stress hormone abscisic acid*. Sci Signal, 2015. **8**(375): p. ra43.
268. Maierhofer, T., et al., *Site- and kinase-specific phosphorylation-mediated activation of SLAC1, a guard cell anion channel stimulated by abscisic acid*. Sci Signal, 2014. **7**(342): p. ra86.
269. Straub, T., U. Ludewig, and B. Neuhauser, *The Kinase CIPK23 Inhibits Ammonium Transport in Arabidopsis thaliana*. Plant Cell, 2017. **29**(2): p. 409-422.
270. Vert, G.A., J.F. Briat, and C. Curie, *Dual regulation of the Arabidopsis high-affinity root iron uptake system by local and long-distance signals*. Plant Physiol, 2003. **132**(2): p. 796-804.
271. Tang, R.J., et al., *The CBL-CIPK Calcium Signaling Network: Unified Paradigm from 20 Years of Discoveries*. Trends Plant Sci, 2020. **25**(6): p. 604-617.
272. Dubeaux, G., et al., *Metal Sensing by the IRT1 Transporter-Receptor Orchestrates Its Own Degradation and Plant Metal Nutrition*. Mol Cell, 2018. **69**(6): p. 953-964 e5.
273. Tang, R.J., et al., *Tonoplast CBL-CIPK calcium signaling network regulates magnesium homeostasis in Arabidopsis*. Proc Natl Acad Sci U S A, 2015. **112**(10): p. 3134-9.
274. Pandey, G.K., et al., *The calcium sensor calcineurin B-like 9 modulates abscisic acid sensitivity and biosynthesis in Arabidopsis*. Plant Cell, 2004. **16**(7): p. 1912-24.
275. Waadt, R., et al., *Multicolor bimolecular fluorescence complementation reveals simultaneous formation of alternative CBL/CIPK complexes in planta*. Plant J, 2008. **56**(3): p. 505-16.
276. Guo, Y., et al., *A calcium sensor and its interacting protein kinase are global regulators of abscisic acid signaling in Arabidopsis*. Dev Cell, 2002. **3**(2): p. 233-44.
277. Pandey, G.K., et al., *Calcineurin-B-like protein CBL9 interacts with target kinase CIPK3 in the regulation of ABA response in seed germination*. Mol Plant, 2008. **1**(2): p. 238-48.

278. Neuhauser, B., et al., *Regulation of NH₄⁺ transport by essential cross talk between AMT monomers through the carboxyl tails*. Plant Physiol, 2007. **143**(4): p. 1651-9.
279. Greenberg, J.T., *Programmed cell death: a way of life for plants*. Proc Natl Acad Sci U S A, 1996. **93**(22): p. 12094-7.
280. Pennell, R.I. and C. Lamb, *Programmed Cell Death in Plants*. Plant Cell, 1997. **9**(7): p. 1157-1168.
281. Danon, A., et al., *Plant programmed cell death: A common way to die*. Plant Physiology and Biochemistry, 2000. **38**(9): p. 647-655.
282. Hara-Nishimura, I. and N. Hatsugai, *The role of vacuole in plant cell death*. Cell Death Differ, 2011. **18**(8): p. 1298-304.
283. Locato, V. and L. De Gara, *Programmed Cell Death in Plants: An Overview*. Methods Mol Biol, 2018. **1743**: p. 1-8.
284. Orrenius, S., V. Gogvadze, and B. Zhivotovsky, *Calcium and mitochondria in the regulation of cell death*. Biochem Biophys Res Commun, 2015. **460**(1): p. 72-81.
285. Locato, V., et al., *Nitric Oxide and Reactive Oxygen Species in PCD Signaling*, in *Nitric Oxide and Signaling in Plants*. 2016. p. 165-192.
286. Ren, H., et al., *Calcium Signaling in Plant Programmed Cell Death*. Cells, 2021. **10**(5).
287. Chin, K., et al., *The Arabidopsis cyclic nucleotide-gated ion channels AtCNGC2 and AtCNGC4 work in the same signaling pathway to regulate pathogen defense and floral transition*. Plant Physiol, 2013. **163**(2): p. 611-24.
288. Moeder, W., et al., *The role of cyclic nucleotide-gated ion channels in plant immunity*. Mol Plant, 2011. **4**(3): p. 442-52.
289. Kurusu, T., et al., *Identification of a putative voltage-gated Ca²⁺ channel as a key regulator of elicitor-induced hypersensitive cell death and mitogen-activated protein kinase activation in rice*. Plant J, 2005. **42**(6): p. 798-809.
290. Boursiac, Y., et al., *Disruption of the vacuolar calcium-ATPases in Arabidopsis results in the activation of a salicylic acid-dependent programmed cell death pathway*. Plant Physiol, 2010. **154**(3): p. 1158-71.
291. Greenberg, J.T. and N. Yao, *The role and regulation of programmed cell death in plant-pathogen interactions*. Cell Microbiol, 2004. **6**(3): p. 201-11.
292. Gao, X., K.L. Cox, Jr., and P. He, *Functions of Calcium-Dependent Protein Kinases in Plant Innate Immunity*. Plants (Basel), 2014. **3**(1): p. 160-76.
293. Torres, M.A., *ROS in biotic interactions*. Physiol Plant, 2010. **138**(4): p. 414-29.
294. Ogasawara, Y., et al., *Synergistic activation of the Arabidopsis NADPH oxidase AtrbohD by Ca²⁺ and phosphorylation*. J Biol Chem, 2008. **283**(14): p. 8885-92.
295. Mittler, R., et al., *Reactive oxygen gene network of plants*. Trends Plant Sci, 2004. **9**(10): p. 490-8.
296. Mittler, R., et al., *ROS signaling: the new wave?* Trends Plant Sci, 2011. **16**(6): p. 300-9.
297. Foyer, C.H. and G. Noctor, *Redox regulation in photosynthetic organisms: signaling, acclimation, and practical implications*. Antioxid Redox Signal, 2009. **11**(4): p. 861-905.
298. Kim, B.G., et al., *The calcium sensor CBL10 mediates salt tolerance by regulating ion homeostasis in Arabidopsis*. Plant J, 2007. **52**(3): p. 473-84.
299. Yang, Y., et al., *Calcineurin B-Like Proteins CBL4 and CBL10 Mediate Two Independent Salt Tolerance Pathways in Arabidopsis*. Int J Mol Sci, 2019. **20**(10).
300. Held, K., et al., *Calcium-dependent modulation and plasma membrane targeting of the AKT2 potassium channel by the CBL4/CIPK6 calcium sensor/protein kinase complex*. Cell Res, 2011. **21**(7): p. 1116-30.
301. Sardar, A., A.K. Nandi, and D. Chattopadhyay, *CBL-interacting protein kinase 6 negatively regulates immune response to Pseudomonas syringae in Arabidopsis*. J Exp Bot, 2017. **68**(13): p. 3573-3584.
302. Kimura, S., et al., *Protein phosphorylation is a prerequisite for the Ca²⁺-dependent activation of Arabidopsis NADPH oxidases and may function as a trigger for the positive feedback*

- regulation of Ca^{2+} and reactive oxygen species. *Biochim Biophys Acta*, 2012. **1823**(2): p. 398-405.
303. Torres, M.A., J.L. Dangl, and J.D. Jones, *Arabidopsis gp91phox homologues AtrbohD and AtrbohF are required for accumulation of reactive oxygen intermediates in the plant defense response*. *Proc Natl Acad Sci U S A*, 2002. **99**(1): p. 517-22.
 304. Sagi, M. and R. Fluhr, *Production of reactive oxygen species by plant NADPH oxidases*. *Plant Physiol*, 2006. **141**(2): p. 336-40.
 305. Bowler, C., et al., *Superoxide Dismutase in Plants*. *Critical Reviews in Plant Sciences*, 2011. **13**(3): p. 199-218.
 306. Corpas, F.J., et al., *Plant peroxisomes: A nitro-oxidative cocktail*. *Redox Biol*, 2017. **11**: p. 535-542.
 307. Lane, B.G., *Oxalate, germins, and higher-plant pathogens*. *IUBMB Life*, 2002. **53**(2): p. 67-75.
 308. Requena, L. and S. Bornemann, *Barley (Hordeum vulgare) oxalate oxidase is a manganese-containing enzyme*. *Biochemical Journal*, 1999. **343**(1): p. 185-190.
 309. Membre, N., et al., *Arabidopsis thaliana germin-like proteins: common and specific features point to a variety of functions*. *Planta*, 2000. **211**(3): p. 345-54.
 310. Li, L., et al., *Genome-Wide Characterization and Expression Analysis of the Germin-Like Protein Family in Rice and Arabidopsis*. *Int J Mol Sci*, 2016. **17**(10).
 311. Cailliatte, R., et al., *High-affinity manganese uptake by the metal transporter NRAMP1 is essential for Arabidopsis growth in low manganese conditions*. *Plant Cell*, 2010. **22**(3): p. 904-17.
 312. Korshunova, Y.O., et al., *The IRT1 protein from Arabidopsis thaliana is a metal transporter with a broad substrate range*. *Plant Mol Biol*, 1999. **40**(1): p. 37-44.
 313. Vert, G., et al., *IRT1, an Arabidopsis transporter essential for iron uptake from the soil and for plant growth*. *Plant Cell*, 2002. **14**(6): p. 1223-33.
 314. Gong, D., et al., *Biochemical and functional characterization of PKS11, a novel Arabidopsis protein kinase*. *J Biol Chem*, 2002. **277**(31): p. 28340-50.
 315. Gong, D., et al., *Constitutive activation and transgenic evaluation of the function of an arabidopsis PKS protein kinase*. *J Biol Chem*, 2002. **277**(44): p. 42088-96.
 316. Luan, S., et al., *Calmodulins and calcineurin B-like proteins: calcium sensors for specific signal response coupling in plants*. *Plant Cell*, 2002. **14 Suppl**(Suppl): p. S389-400.
 317. Quiquampoix, H., Loughman, B. C., Ratcliffe, R. G. , *A 31 P-NMR Study of the Uptake and Compartmentation of Manganese by Maize Roots*. *Journal of Experimental Botany*, 1993. **44**(269): p. 1819-1827.
 318. Karley, A.J. and P.J. White, *Moving cationic minerals to edible tissues: potassium, magnesium, calcium*. *Curr Opin Plant Biol*, 2009. **12**(3): p. 291-8.
 319. *WebElements: Ionic radii of atoms and ions*. [cited 2023 23.04.]; Available from: https://webelements.com/manganese/atom_sizes.html.
 320. Wallrad, L., *Entwicklung und Charakterisierung eines ratiometrischen Mn^{2+} -Sensorproteins*, in *Institut für Biologie und Biotechnologie der Pflanzen*. 2015, Westfälische Wilhelms-Universität Münster: Münster. p. 112.
 321. Palmer, A.E., et al., *Ca^{2+} indicators based on computationally redesigned calmodulin-peptide pairs*. *Chem Biol*, 2006. **13**(5): p. 521-30.
 322. Palmer, A.E., et al., *Bcl-2-mediated alterations in endoplasmic reticulum Ca^{2+} analyzed with an improved genetically encoded fluorescent sensor*. *Proc Natl Acad Sci U S A*, 2004. **101**(50): p. 17404-9.
 323. Horikawa, K., et al., *Spontaneous network activity visualized by ultrasensitive Ca^{2+} indicators, yellow Cameleon-Nano*. *Nat Methods*, 2010. **7**(9): p. 729-32.

Acknowledgements

Zuerst möchte ich natürlich meinem Doktorvater Prof. Dr. Lutz Schmitt danken, der mir die Promotion und die Arbeit an diesem Projekt ermöglicht hat. Ich danke dir für deine stets offene Tür, die Unterstützung über die letzten Jahre und die vielen Denkanstöße, wenn die Datenlage mal wieder jenseits von rosig war. Danke dass du mich immer wieder auf den richtigen Kurs gebracht hast, wenn mein Perfektionismus die Dinge mal wieder unnötig kompliziert zu machen drohte. Vielen Dank für deine Gelassenheit und unkompliziert Art Probleme anzugehen und zu lösen. Lutz, danke dass du mir diese schöne und lehrreiche Zeit ermöglicht hast! Ebenso möchte ich dir dafür danken, dass du mir eine so interessante PostDoc Stelle vermittelt hast wo ich hoffentlich eine genauso tolle Zeit erleben darf wie in deinem Institut.

Für die freundliche Übernahme des Korreferats möchte ich Prof. Dr. Georg Groth danken.

Ebenso möchte ich Prof. Dr. Sander Smits danken. Danke für auch deine stets offene Tür, die vielen anregenden Diskussionen in den Subgroup meetings, deinen Input und deine Ideen zu meinen Experimenten sowie dein Hinterfragen meiner Daten. Ein anderer Blickwinkel und deine fundierte Kritik bei einer scheinbar aussichtslosen Datenlage war manchmal genau das was ich hören musste um voran zukommen.

Auch wenn ich Uli nicht wie viele meiner Kollegen schon im Studium kennengelernt habe, gilt doch auch ihm mein Dank. Die Möglichkeit Studenten im Praktikum und bei ihren Abschlussarbeiten zu betreuen, hat mir stets Freude bereitet. Ich konnte dadurch vieles lernen und auch an den Aufgaben wachsen.

Bei den Sekretärinnen der Biochemie Mathilde Blum, Tatjana Platz und Corinna Franzkowiak möchte ich mich für alles Organisatorische bedanken und dafür, dass sie jede bürokratische Hürde für uns Doktoranden meistern konnten.

Martina und Silke möchte ich für die Organisation unserer Labore, der Praktika und die schnelle Order von Chemikalien wie meinem Brij35 und so vielem mehr danken. Martina du bist eine unverzichtbare Ansprechpartnerin bei so vielen Fragen. Gerade mit deiner Erfahrung in Sachen Klonierung hast du mir in vielen Situationen helfen können.

Dr. Anja Stefanski möchte ich für die massenspektroskopische Analyse meines CBL1 Proteins danken. Ebenso gilt mein Dank Anette Ricken für die unzähligen AAS Messungen meiner Proteine, Stefanie und Violetta vom CSS für die Versuche meine widerspenstigen Proteine zu kristallisieren und dem Team vom CAi für die Fluoreszenz Aufnahmen von meinem AKT1 Protein.

Sakshi, thanks for all the helpful discussions and support. Your very detailed and profound comments on my paper draft were really a great help also to write this thesis.

Jens, dir möchte ich nicht nur für die unzähligen Male danken, die du mir geholfen hast den Cell disrupter fachmännisch zu zerlegen und wieder zusammenzubauen. Auch sonst konnte ich bei diversen handwerklichen Belangen auf dich zählen. Zudem warst du während der letzten Jahre stets ein super Ansprechpartner für wissenschaftliche Fragen und auch Mimimi jeglicher Art.

Eymen, dir danke ich für deine Unterstützung bei unseren Cell disruptor Aufgaben und Pflichten und natürlich auch für die gefühlt drölfzihundert MALS Messungen all meiner CBL1 und CBL9 Mutanten.

Apropos Cell disrupter. Lieber Tim, danke, dass du, auch wenn du deine Verantwortlichkeit für den Cell disrupter längst abgegeben hattest, Eymen und mir immer mit Rat und Tat und guter Laune zur Seite standest.

Liebe Julia, du und deine Bench seid der lebende Beweis für Entropie. Vielen Dank für die vielen witzigen Momente im Labor oder orientierungslos irgendwo in Düsseldorf auf der Suche nach Churros. Unsere Koch- und Lieferando-Sessions haben die Wochenendschichten doch um ein vielfaches erträglicher und lustiger gemacht.

Hans, dein wenn auch teilweise spezieller Humor hat mir doch so manchen miesen Labor-Tag erheitert. Danke für die vielen Fachsimpeleien beim morgendlichen Kaffee oder freitäglichen Feierabendbier.

Den ÄKTA Jungs Manuel und Florestan möchte ich nicht nur für Pflege und Instandhaltung unserer ÄKTAs danken, sondern auch für all die Mikro-ÄKTA Läufe meiner Proteine und für all die Male, die ihr mir beim Umgang mit den ÄKTAs geholfen habt.

Meinen Büromädels Steffi, Lea und Vivien möchte ich für die tolle gemeinsame Zeit in unserem Büro im Neubau danken. Ob Mondkalender, der Windows diskriminierende Drucker oder Ratschläge zu Experimenten, Praktika oder Studenten, es gab kaum etwas, dass nicht Thema war. Und die Investition in den Sitzsack hat sich wirklich gelohnt.

Der SMS Group um Jun.-Prof. Dr. Alexej Kedrov und seine Doktoranden Maryna, Michael, Athanasios und Max möchte ich ebenfalls meinen Dank aussprechen. Danke für euren Input und für spannende mal mehr und mal weniger wissenschaftliche Gespräche.

Den Ehemaligen Manuel, Martin, Julia, Isabelle, Marcel, Tobias möchte ich natürlich auch danken für die tolle Zeit, für die Erfahrungen, die ihr geteilt habt und das Wissen, das ihr weiter gegeben habt.

Bedanken möchte ich mich auch bei meinen Studenten Polina, Christian, Isabelle, Samet, Carolin und Cigdem, die ich während meiner Doktorandenzeit betreuen durfte. Vielen Dank für eure Begeisterung für das Thema, euren Fleiß und eure Kreativität mit der ihr wertvolle Beiträge zu meinem Projekt geleistet habt. Christian und Cigdem, ihr seit mittlerweile selbst Doktoranden in der BC1. Euch und allen anderen Neulingen wünsch ich viel Erfolg für eure Promotion und mehr „Aha“ als „Hä?“ Momente.

Generell gilt mein Dank dem gesamten BC1 Institut mit all seinen ehemaligen und aktuellen Mitgliedern. Egal ob Chefs, TAs, PostDocs oder Doktoranden, selten habe ich ein so kollegiales und sich gegenseitig unterstützendes Team erlebt, egal ob es die Gespräche an der Kaffeemaschine, die offiziellen Donnerstags und Subgroup-Meetings waren oder die „inoffiziellen“ Mario-Cart Abende, (extended) Girls nights oder Lieferando-Donnerstage. Eure Ratschläge und Tips und euer Zuspruch haben einen großen Teil dazu beigetragen, dass ich trotz teilweise sehr langer Durststrecken durchgehalten habe. Dafür möchte ich euch allen nochmal ausdrücklich danken.

Insbesondere möchte ich noch meinen Freunden danken, die mich immer unterstützt und motiviert haben und mir Mut zugesprochen haben wenn es nötig war. Vielen Dank für euer Verständnis wenn ich mal keine Zeit hatte oder vergessen habe mich zu melden. Danke, dass ihr immer ein offenes Ohr für mein Mimimi hattet auch wenn wir mittlerweile alle quer durchs ganze Land verteilt sind.

Zuletzt möchte ich noch meiner Familie danken, für ihren Rückhalt und die Unterstützung und dafür, dass ihr mir diesen Weg überhaupt ermöglicht habt.

Curriculum vitae

Personal Data

Name	Alexandra Bork
Date of Birth	07.07.1992
Place of Birth	Frankfurt am Main

University Education

Since 10/2018	Doctorate Heinrich-Heine-Universität Düsseldorf Supervisor: Prof. Dr. Lutz Schmitt Institute of Biochemistry Title: Structure and Function of the Ca ²⁺ dependent K ⁺ channel AKT1 from <i>A. thaliana</i>
10/2015 – 09/2018	Master of Science (Biochemistry)) Goethe-University Frankfurt am Main Supervisor of Master thesis : Jun. Prof. Dr. Eric Geertsma Title: ""Structure and Function of Nucleobase Transporters""
10/2012 – 09/2015	Bachelor of Science (Biochemistry) Goethe University Frankfurt am Main Supervisor of Bachelor-thesis: Prof. Dr. Klaas Martinus Pos Title: Functional Studies of RND Efflux Systems in Gram Negative Bacteria"

School education

07/2003 – 06/2012	Secondary school Schillerschule (Gymnasium) Frankfurt am Main Abitur University entrance qualification
07/1999 – 06/2003	Primary school August-Gräser Grundschule Frankfurt am Main

Declaration

Ich versichere an Eides Statt, dass die Dissertation von mir selbständig und ohne unzulässige fremde Hilfe unter Beachtung der „Grundsätze zur Sicherung guter wissenschaftlicher Praxis an der Heinrich-Heine-Universität Düsseldorf“ erstellt worden ist. Die Dissertation wurde in der vorgelegten oder in ähnlicher Form noch bei keiner anderen Fakultät eingereicht. Ich habe bisher keine erfolglosen und erfolgreichen Promotionsversuche unternommen.

Ort, Datum

Alexandra Bork